

**Journal of
Mechanics of
Materials and Structures**

Volume 13, No. 1

January 2018



JOURNAL OF MECHANICS OF MATERIALS AND STRUCTURES

msp.org/jomms

Founded by Charles R. Steele and Marie-Louise Steele

EDITORIAL BOARD

ADAIR R. AGUIAR	University of São Paulo at São Carlos, Brazil
KATIA BERTOLDI	Harvard University, USA
DAVIDE BIGONI	University of Trento, Italy
MAENGHYO CHO	Seoul National University, Korea
HUILING DUAN	Beijing University
YIBIN FU	Keele University, UK
IWONA JASIUKEWICZ	University of Illinois at Urbana-Champaign, USA
DENNIS KOCHMANN	ETH Zurich
MITSUTOSHI KURODA	Yamagata University, Japan
CHEE W. LIM	City University of Hong Kong
ZISHUN LIU	Xi'an Jiaotong University, China
THOMAS J. PENCE	Michigan State University, USA
GIANNI ROYER-CARFAGNI	Università degli studi di Parma, Italy
DAVID STEIGMANN	University of California at Berkeley, USA
PAUL STEINMANN	Friedrich-Alexander-Universität Erlangen-Nürnberg, Germany
KENJIRO TERADA	Tohoku University, Japan

ADVISORY BOARD

J. P. CARTER	University of Sydney, Australia
D. H. HODGES	Georgia Institute of Technology, USA
J. HUTCHINSON	Harvard University, USA
D. PAMPLONA	Universidade Católica do Rio de Janeiro, Brazil
M. B. RUBIN	Technion, Haifa, Israel

PRODUCTION production@msp.org

SILVIO LEVY Scientific Editor

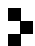
Cover photo: Ev Shafir

See msp.org/jomms for submission guidelines.

JoMMS (ISSN 1559-3959) at Mathematical Sciences Publishers, 798 Evans Hall #6840, c/o University of California, Berkeley, CA 94720-3840, is published in 10 issues a year. The subscription price for 2018 is US \$615/year for the electronic version, and \$775/year (+\$60, if shipping outside the US) for print and electronic. Subscriptions, requests for back issues, and changes of address should be sent to MSP.

JoMMS peer-review and production is managed by EditFLOW® from Mathematical Sciences Publishers.

PUBLISHED BY

 **mathematical sciences publishers**
nonprofit scientific publishing

<http://msp.org/>

© 2018 Mathematical Sciences Publishers

STUDIES ON PERFORMANCE AND FAILURE MODE OF T-SHAPED DIAPHRAGM-THROUGH CONNECTION UNDER MONOTONIC AND CYCLIC LOADING

BIN RONG, CHANGXI FENG, RUOYU ZHANG, SHUAI LIU AND GUANGCHAO YOU

This paper examines the mechanical properties of T-shaped diaphragm-through connections between CFST columns and steel beams under monotonic and cyclic loading. A monotonic test and a cyclic test on two same specimens are described. The experimental setup, connection configurations, and material properties are firstly introduced, followed by a detailed account of the results and observations from tests. The failure mode and the ultimate bearing capacity are similar in the two tests, while the connection exhibits larger yield capacity and lower ductility under cyclic loading than monotonic loading. Nonlinear finite element analysis was also employed in this investigation. The predicted results are in good agreement with the experimental ones so that the reliability of finite element analysis is verified. Diaphragm-through connection and ordinary beam-column connection are simulated and compared through FEM, and failure modes of plastic hinge at beam end and column face yielding are found respectively, which indicates a significant strengthening effect of the diaphragm and the superior mechanical properties of the diaphragm-through connection.

1. Introduction

As the hinge of force transferring, beam-column connections are the main components that transmit loads in the whole structure. Diaphragm-through connection between concrete-filled square tubular (CFST) columns and steel beams has gained a widespread usage in composite frame structures because of its good bearing capacity, ductility, seismic-resisting, and constructional convenience.

As a typical rigid beam-column connection, there are a large number of researches conducted on the diaphragm-through connection. Experimental studies on connections comprising high-strength steel and concrete were carried out by Nishiyama et al. [2004] and Fukumoto and Morita [2005] and new computing models and calculating methods of shear capacity were proposed, and the calculated results agree well with the experimental results. Finite element analyses were conducted under both monotonic loading and cyclic loading by Nie et al. [2008] and were compared with a series of cyclic loading experiments of fourteen cruciform connection specimens to analyze the mechanical behavior of these three types of connection. Rong et al. [2012] used the finite element method to analyze the tensile behavior and seismic behavior of the panel zone of diaphragm-through connections. The numerical data had a good agreement with the test results. Qin et al. [2014b] tested four full-scale specimens of existing and proposed through-diaphragm connections to concrete-filled rectangular steel tubular columns subjected to cyclic loading. The variables taken into consideration in the experiments include the geometry of the

Keywords: diaphragm-through connection, monotonic and cyclic tests, mechanical property, finite element analysis, ordinary beam-column connection, failure mode, strengthening effect of diaphragm.

through-diaphragm, the configuration of the weld access hole, horizontal stiffeners, and the methods of connecting beam webs to columns. Qin et al. [2014a] carried out theoretical studies into the behavior of the through-diaphragm to concrete-filled rectangular hollow section columns subjected to tensile force. In that study, component-based mechanical models were proposed to predict the strength of the column component of concrete-filled rectangular hollow section columns under tensile load imparted through a through-diaphragm connection, and the mechanical models were compared with a large range of experimental results and good agreement was shown between them. Based on finite element models of the internal diaphragm connection and through-diaphragm connection set up by [Yu et al. 2015], the out-of-plane deformation at the column flange, force flow pattern, and shear and moment transfer efficiency of a WF-beam to rectangular CFT column connection were discussed, and the results show that both the Poisson effect and flexibility of column flange leads to a change on the force flow pattern in the beam-column junction region and inefficient moment transferring ability through the beam web, resulting in a high level of hydrostatic stress demand at the beam flanges. Rong et al. [2016] tested four specimens under static tension loads and adapted the finite element method to study the mechanical properties and bearing capacity of diaphragm-through joints with a failure mode of panel zone; computational models of yield lines on a square steel tube and diaphragm were established based on the distribution pattern of the plastic zone, and an analytical method for the evaluation of the bearing capacity of the joint was proposed.

At present the experimental studies on diaphragm-through connection can be classified as two types: flexural capacity studies and shear capacity studies. The former refers to some researches on the flexural capacity of diaphragm-through connection based on static tension tests, while the latter refers to those hysteretic tests carried out to study the shear capacity and seismic behavior of the diaphragm-through connection. Most studies on diaphragm-through connection belong to the two types, while the study on the comparison of performance of diaphragm-through connection under monotonic and cyclic loading is little. Therefore, there is a need for further assessment and characterization of the performance of the diaphragm-through connection under monotonic and cyclic loading conditions.

This paper examines the experimental responses of two T-shaped diaphragm-through connections under monotonic and cyclic loading respectively, where T-shaped connections mean exterior connections of a frame structure. It presents and discusses the results of monotonic and cyclic tests. A detailed description of the testing arrangement and material properties is given, and the main experimental results and salient behavioral observations are discussed. The discussion focuses on the comparisons of issues related to stiffness, capacity and failure mechanisms between monotonic and cyclic tests. In addition, the relationship of failure mode and the ratio of beam width and column width is analyzed in this paper. Finally, nonlinear finite element models are also developed and validated against experimental results in this investigation. Using finite element analysis, diaphragm-through connection and ordinary beam-column connection are simulated and compared, and different failure modes of the two kinds of connection and the causes of the failure modes are studied particularly.

2. Experimental program

2.1. Test specimens. In order to investigate the behavior of a T-shaped diaphragm-through connection under monotonic and cyclic loading, two specimens named SJ1 and SJ2 with same size were designed to carry out a monotonic test and a cyclic test respectively. The specimen details are shown in Figure 1. As

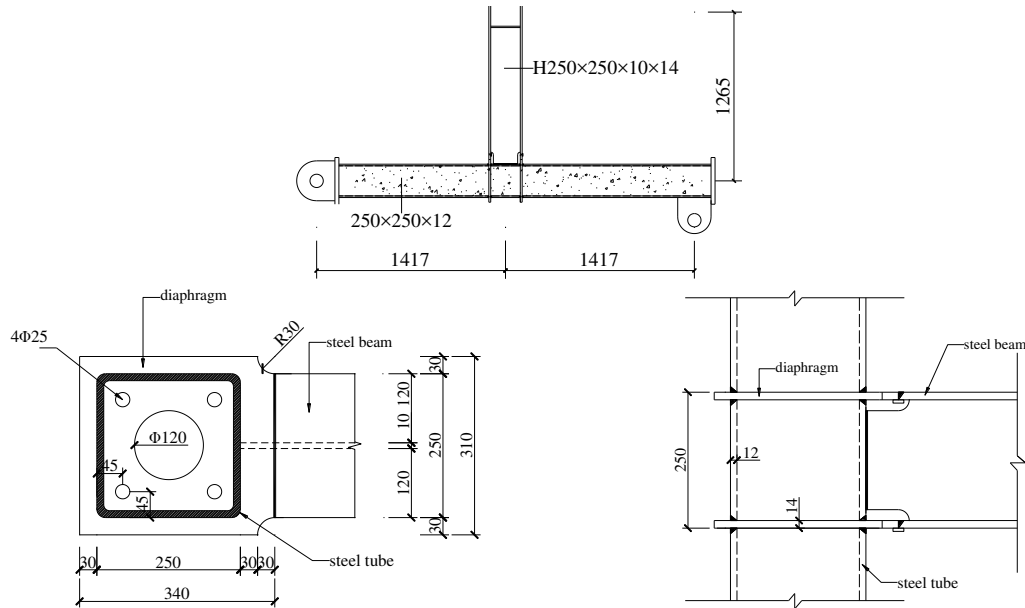


Figure 1. Details of the T-shaped diaphragm-through connection: T-shaped specimen (top), overhead view (left), and section view (right).

thickness (mm)	f_y (N/mm ²)	f_u (N/mm ²)	E_s (10 ⁵ N/mm ²)
10	272.6	352.7	2.04
12	313.7	439.8	2.01
14	252.2	414.6	2.03

Table 1. Material properties of concrete.

grade	f_c (N/mm ²)	E_c (10 ⁴ N/mm ²)
C30	38.4	3.49

Table 2. Material properties of steel.

seen in the figure, the distance between the panel zone and two hinges is equal so that the force situation of the two side columns is symmetric. The steel tubes were manufactured from cold-formed square steel tubes, and the diaphragms and beams were welded by steel plates. The C30 concrete in columns was cured for 28 days.

A material test was carried out, in which tension coupons were cut from steel tubes and steel plates and were tested to determine the material properties of the steel. The yield strength f_y , the ultimate strength f_u , and the modulus of elasticity E_s , are listed in Table 1. Concrete cubes were cast and cured in the conditions same to those of the experiments and tested under pressure load. The measured average axial compressive strength f_c and the module of elasticity E_c are listed in Table 2.

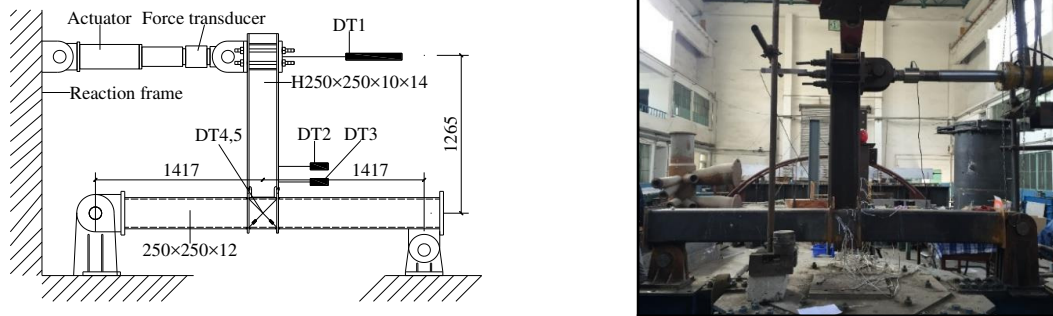


Figure 2. Test setup: schematic drawing and photo.

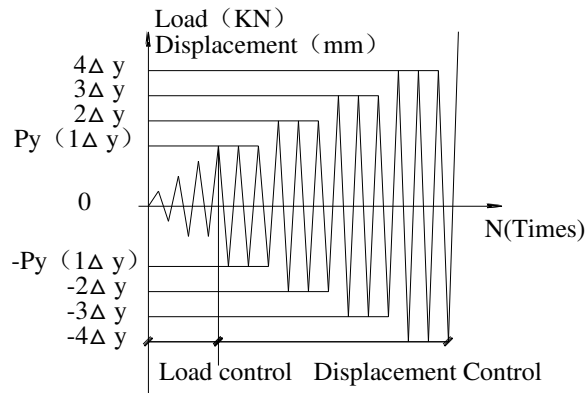


Figure 3. Regulation of cyclic loading system.

2.2. Experimental arrangement and loading procedure. The arrangement used for testing T-shaped diaphragm-through connections is shown in Figure 2. The specimens were placed horizontal on the testing frame and a 1000 kN level hydraulic actuator whose displacement range was ± 350 mm operating in load and displacement control was used to apply horizontal deformation at the free beam end. The tubular column was restrained at both ends with the aid of a hinged support and a slotted hole hinge support. DT1 (displacement transducer) was used to measure the control displacement at the free beam end corresponding to the location of horizontal actuator, while the local deformation of the restrained beam end was measured by DT2 and DT3. The diagonal displacement of the shear panel was measured by DT4 and DT5, as shown in Figure 2 (left). The mechanical testing and simulation (MTS) data collecting system was used to collect the measured data automatically.

Load-displacement hybrid control was used to control the horizontal cyclic load applied on the free beam end. Before testing, every specimen was preloaded twice to check the reaction of the test arrangement and the measuring devices. For the cyclic test, stepwise force load was applied to the beam end and recycled one time at each step loading before yield. After yield, the load would be controlled by multiplying the yield displacement Δ_y (horizontal displacement of the beam end when specimens yield), and recycled three times for each step, as shown in Figure 3 [Kataoka and El Debs 2015; Yin et al. 2016].

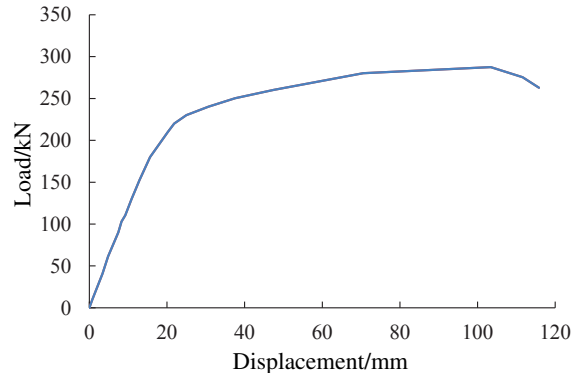


Figure 4. Load-displacement curve of SJ1.

For the monotonic test, the load system was the same as the cyclic test, except that the specimen was pushed along one direction without recycle until failure.

3. Experimental results and observations

The corresponding deformation patterns and load-displacement relationships are presented in Figures 4–7, and the main response parameters obtained from the tests are summarized in Table 3, such as the yield load p_y^e and the failure load p_u^e . A graphical method [Park et al. 2010] is employed to catch the initial stiffness and the yield load p_y^e at global connection yield. The ductility factor μ is defined as $\mu = \Delta_u/\Delta_y$, where Δ_y and Δ_u mean the yield displacement and the ultimate displacement obtained from load-displacement curve of monotonic test and skeleton curve of cyclic test respectively. In this section, the main behavioral patterns are discussed and the salient response characteristics such as stiffness, strength, and ductility factor are examined [Tizani et al. 2013]. Particular focus is given in the discussion comparing monotonic behavior and hysteretic response under cyclic loading [Elghazouli et al. 2009; Málaga-Chuquitaype and Elghazouli 2010]. In addition, the influence of the ratio of beam flange width to column flange width on failure modes of connection is discussed.

3.1. Monotonic test. SJ1 was tested under monotonic load until failure. The load-displacement curve is shown in Figure 4. It is found that SJ1 behaved in a relatively ductile manner. The curve exhibits elastic behavior at the initial stage followed by a clear extensive plastic plateau indicating good ductility. At a load of 243.1 kN corresponding to 20.6 mm displacement, the restrained end of the beam yielded but no obvious phenomenon was observed. Beyond this point, load was continued monotonously with displacement controlled by applying equal multiples of yield displacement on the free beam end. As the load increased, the compression flange of the restrained beam end started to buckle, as shown in Figure 5. The load reached its peak value of 287.5 kN corresponding to 103.4 mm displacement. Finally, the specimen failed with a plastic hinge appearing at the restrained beam end. The specimen was then unloaded and the test was terminated.

3.2. Cyclic test. In contrast to SJ1, SJ2 was loaded cyclically until failure and its failure mode was similar to that of SJ1. Figures 6 (left and right) are the hysteretic curve and the skeleton curve of SJ2 respectively. At a load of 267.5 kN corresponding to 24.1 mm displacement, there was no obvious yield

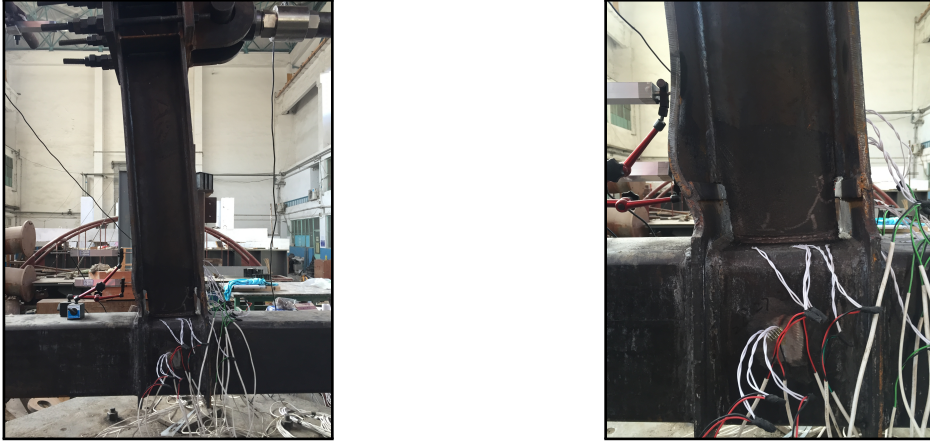


Figure 5. Behavior of SJ1.

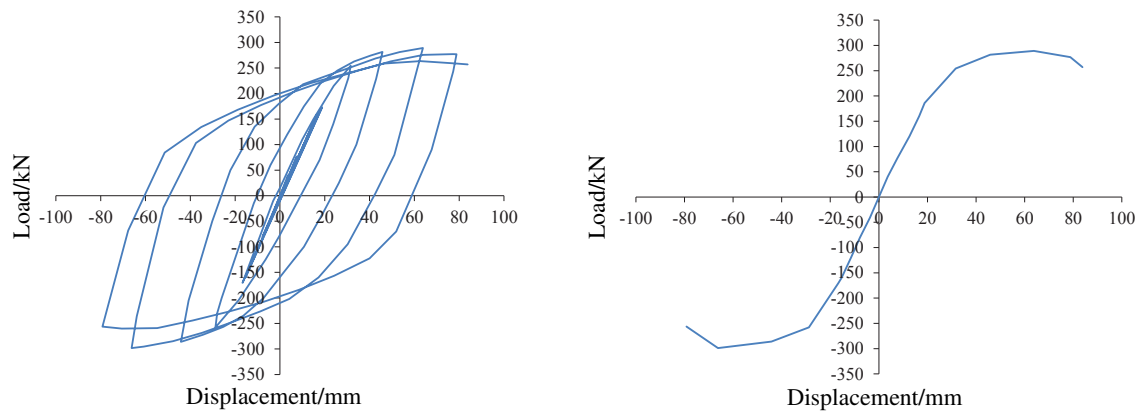


Figure 6. Load-displacement curve of SJ2: hysteretic curve (left) and skeleton curve (right).

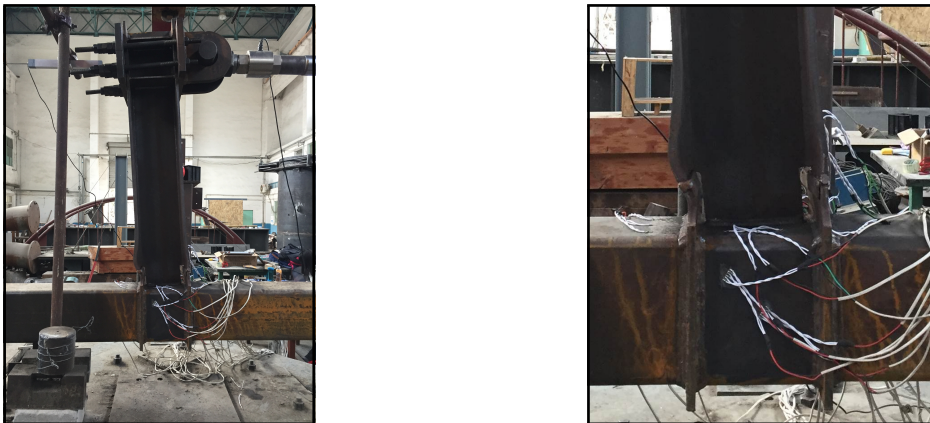


Figure 7. Behavior of SJ2.

specimen	initial stiffness (kN/m)	Δ_y (mm)	p_y^e (kN)	Δ_u (mm)	p_u^e (kN)	μ
SJ1	11.8	20.6	243.1	103.4	287.5	5.5
SJ2	11.1	24.1	267.5	63.8	289	2.6

Table 3. Summary of results.

deformation, but an inflection point was observed in the load-displacement curve. Beyond this point, load was continued cyclically with displacement controlled by applying equal multiples of yield displacement on the free end. As the load was increasing, the local buckling initiated in the flange of the restrained beam end. The peak load of SJ2 was 289 kN corresponding to 63.8 mm displacement. Finally, the plastic hinges appeared at the restrained beam end and the capacity dropped to 84% of the peak load when it was subjected to five times the yield displacement, which means the failure of SJ2. Then the specimen was unloaded and the test was terminated.

3.3. Discussion.

3.3.1. Comparison of monotonic behavior and hysteretic response. As shown in Figures 5 and 7, failure modes of SJ1 and SJ2 are both plastic hinge damage, and the failure load p_u^e of SJ1 and SJ2 are nearly equal, which indicates that different loading types, static load and seismic action, have little effect on the ultimate bearing capacity of a T-shaped diaphragm-through connection. The initial stiffness of SJ1 is approximate to SJ2, but SJ2 yielded at a larger displacement, so that the yield load p_y^e of SJ2 is a little larger than that of SJ1. In consideration of ductility factor μ illustrated in Table 3, T-shaped diaphragm-through connection under monotonic loading has better ductility than cyclic loading. In addition, SJ2 failed at a lower displacement for that cyclic test consumed more energy.

3.4. Ratio of beam flange width to column flange width. Research by [Lu 1997] showed that the ratio of beam flange width to column flange width β has great influence on the failure mechanism of a multiplanar tubular joint. It was thought that the failure mode of the connection is the punching shear failure at the column flange when β is approximately 1. According the tests described before, the ratio of beam flange width to column flange width of specimens is equal to 1, while the failure modes of SJ1 and SJ2 are not column flange damage but plastic hinge damage at the beam end, which indicates that the theory is not suitable for a diaphragm-through connection. The applicability of this theory will be discussed specifically in finite element analysis. Therefore, the limitation on the ratio of beam flange width to column flange width of a T-shaped diaphragm-through connection can be extended to 1 so that it can make full use of the bearing capacity of beam under the premise of beam damage prior to column damage.

4. Finite element analysis

In order to investigate the influences of the presence of diaphragm and the ratio of beam flange width to column flange width on failure modes of beam-column connections, a parametric finite element analysis has been undertaken using the finite element package ANSYS [Lee et al. 2012; Yu et al. 2015]. The three-dimensional finite element model DT1 in finite element analysis, designed to verify the feasibility of finite element analysis, has the same sizes and material properties as the specimens in monotonic and cyclic tests described before. Then in this study, factors that were taken into discussion include:

model	column size	beam size	β	presence of diaphragm
DT1	250 × 12	250 × 250 × 10 × 14	1	diaphragm-through
DT2		250 × 225 × 10 × 14	0.9	diaphragm-through
DT3		250 × 175 × 10 × 14	0.7	diaphragm-through
WD1		250 × 250 × 10 × 14	1	without diaphragm
WD2		250 × 225 × 10 × 14	0.9	without diaphragm
WD3		250 × 175 × 10 × 14	0.7	without diaphragm

Table 4. List of models.

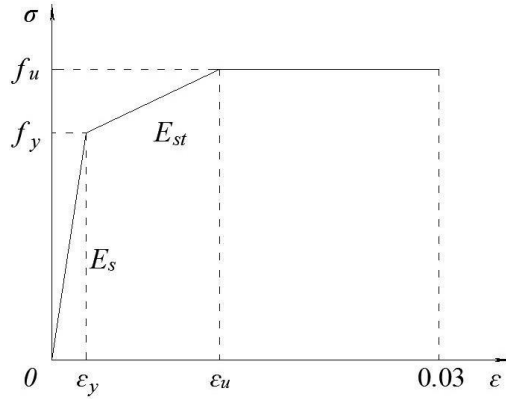


Figure 8. Constitutive law of steel members.

the presence of diaphragm and the ratio of beam flange width to column flange width. Key factors of different models are marked in Table 4. DT series are the models of diaphragm-through connections while WD series are beam-column connections without diaphragm. Two comparison series are the same in column and beam dimensions.

4.1. Finite element model.

4.1.1. Steel members modeling. The three-dimensional 20-node element SOLID 186 is adopted to model the steel tube, the diaphragm, the beam flange, and the beam web. Each node of the element has three translation degrees of freedom. This element is capable of capturing plasticity, large deflections, and large strains.

As shown in Figure 8, the trilinear stress-strain relation proposed by Nie et al. [2008] is used to model the constitutive law of the steel members, where $\varepsilon_y = f_y/E_s$ and $\varepsilon_u = 10(f_u - f_y)/E_s$. The values of the yield strength f_y , the ultimate strength f_u , and the modulus of elasticity E_s are the values found in the material test. The Poisson's ratio of the steel members is assumed as 0.3.

4.1.2. Concrete modeling. The three-dimensional 8-node element SOLID 65 is used to model the infilled concrete. Each node of the element has three translation degrees of freedom. This element is capable of capturing the effects of cracking in tension, crushing in compression, and plastic deformation.

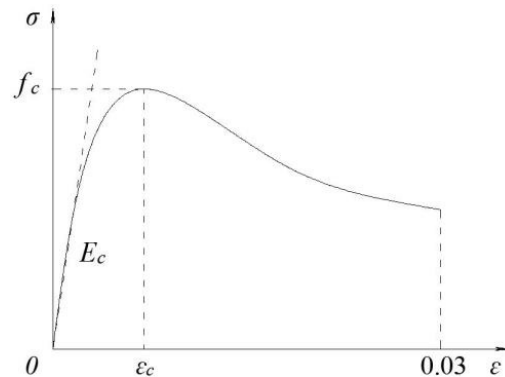


Figure 9. Constitutive law of concrete.

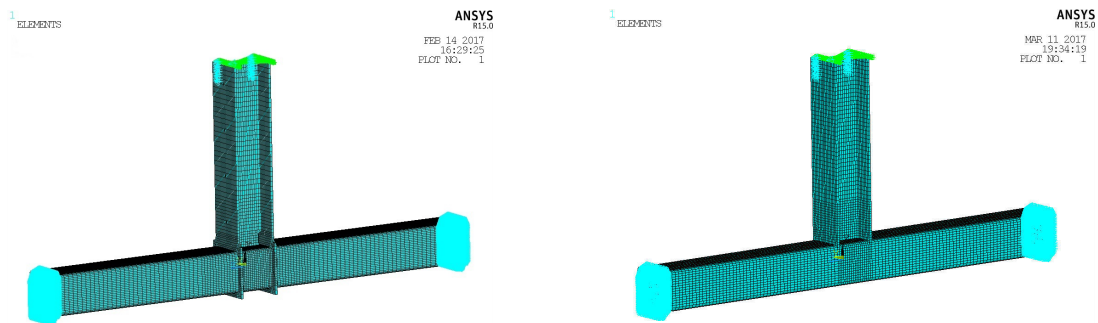


Figure 10. Finite element model: DT series (left) and WD series (right).

The constitutive law of concrete used for the infilled concrete is shown in Figure 9 [Li and Han 2012]. The values of the compressive strength σ_c and the modulus of elasticity E_c of the concrete are the values found in the material test. The Poisson's ratio of the infilled concrete is assumed equal to 0.2.

4.1.3. Modeling of the concrete-steel interface. The contact elements TARGE 170 and CONTA 174 are employed to model the contact action between the steel members and the concrete. These contact elements allow the surfaces to separate but not penetrate each other. They combine as a contact pair through sharing a real constant. The coefficient of friction between the two faces is taken as 0.25 in the analysis.

4.1.4. Modeling of loading and boundary conditions. The same loading procedures and constraints as the experiments should be used in the finite element analysis. To simulate this action, the columns were held horizontally, the top and the bottom of column were fixed and the loads were applied on the free beam end. The loads were applied as static uniform load using displacement control at each node of the loaded surfaces, and the displacement increments are identical to the increments of the monotonic test and the cyclic test. The finite element models are shown in Figure 10.

4.2. Numerical results. Among all models, the reference model DT1 was subjected to monotonic loading and cyclic loading (as the tests described before) while the others were only subjected to monotonic loading. The failure models and load-displacement relationships of DT1 and test specimens are compared

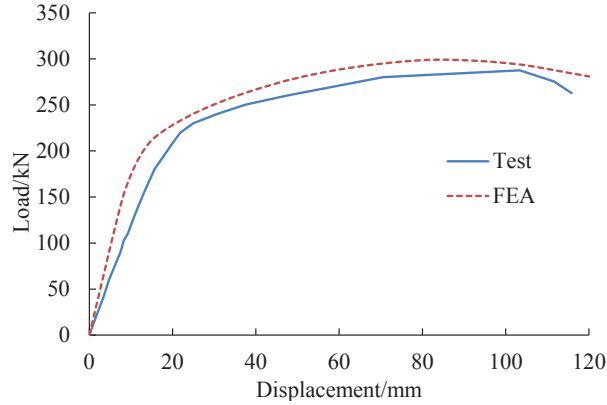


Figure 11. Comparison of load-displacement curve for SJ1.

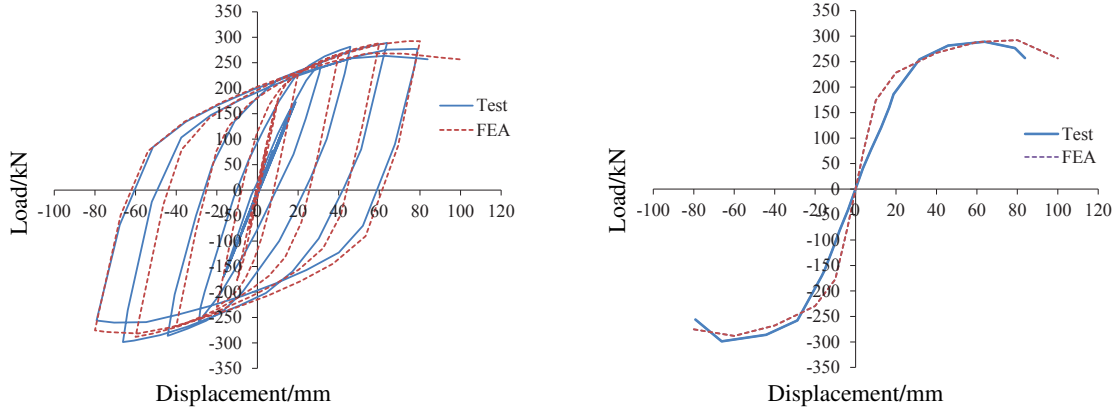


Figure 12. Comparison of load-displacement curve for SJ2: hysteric curve (left) and skeleton curve (right).

to verify the feasibility and accuracy of the finite element analysis. The influences of the presence of diaphragm and the ratio of beam flange width to column flange width on failure modes of beam-column connections are studied using experimental results and finite element analysis.

4.2.1. Model verification. In order to verify the accuracy of the finite element models, load-displacement curves obtained from the finite element model DT1 are compared with test curves in Figures 11 and 12, and it is found that all load-displacement curves match with the experimental ones well. The yield load p_y^e and the failure load p_u^e of numerical results obtained from the predicted curves by using the graphical method [Park et al. 2010] are listed in Table 5 and they are compared with the experimental ones. The analytical values are in good agreement with the experimental ones. The overall agreement between the experimental and the numerical results demonstrates the feasibility and accuracy of the finite element analysis, therefore it is reasonable to study the influences of the presence of diaphragm and the ratio of beam flange width to column flange width on failure modes of beam-column connections [Liu et al. 2012; 2014].

specimen	yield bearing capacity			ultimate bearing capacity		
	p_y^e (kN)	p_y^f (kN)	p_y^f/p_y^e	p_u^e (kN)	p_u^f (kN)	p_u^f/p_u^e
SJ1	243.1	259.9	1.069	287.5	299.1	1.040
SJ2	267.5	255.7	0.956	289	292.3	1.011

Table 5. Comparison of bearing capacity.

4.2.2. Failure modes and load-displacement curves. Typical predicted failure modes and stress contours of DT series and WD series are shown in Figure 13. The predicted failure modes of the two series are obviously different. As shown in Figure 13 (left column), the failure mode of DT series is plastic hinge damage at the beam end and it is caused by overstress of the beam end near the panel zone of the connection. The right column shows that the failure mode of WD series is column face yielding, and there is apparently large local deformation on the column flange face, which means the failure of WD series is caused by the over-deformation of the column face. Therefore, WD series are supposed to be defined as failure when local deformation of column face reaches 3% of the beam width, even though the load still increases steadily.

The load-displacement curves obtained by the finite element analysis are compared with each other in Figure 14. The predicted load-displacement curves of all models have a linear elastic behavior at the initial stage followed by inelastic behavior when the load is further increased. The curves show that the initial stiffness and the bearing capacity of DT series are obviously larger than WD series, for the diaphragm strengthens the DT series, which results in the superior mechanical properties of the diaphragm-through connection. For DT series, the failure model is plastic hinge damage at the beam end, therefore it is reasonable that the bearing capacity decreases as beam width get smaller. However, there is also a negative correlation between the bearing capacity and beam width for WD series when its failure mode is column face yielding. As illustrated in Figure 15, different beam widths cause different yield lines on the column face, and larger beam width means a larger yield region of the column face, which results in larger bearing capacity.

4.3. Discussion on failure mode of beam-column connection. According to research on beam-column connection carried out by Lu [1997] described before, the ratio of beam flange width to column flange width β greatly influences the failure mechanism of a multiplanar tubular joint. There are three kinds of failure mechanism for a column classified by β : column face yielding ($\beta \leq 0.85$), punching shear failure ($0.85 \leq \beta < 1 - 1/\gamma$), and flange failure ($\beta = 1$), where γ is the width to thickness ratio of the column. In combination with the theory, this section discusses influences of diaphragm and β of failure modes of beam-column connections through finite element analysis.

WD series are designed to verify the accuracy of the theory. Since cracks were not considered in numerical analyses and infilled concrete prevented the failure of the column flange, only column face yielding could be modeled by FEM. As shown in Figure 13, the failure modes of WD series are all column face yielding, which agrees well with the theory of Lu [1997] and verifies its accuracy for ordinary beam-column connections without diaphragm.

DT series are models of diaphragm-through connection, and there is no difference between DT series and WD series except for the presence of a diaphragm. However, failure modes of the two series are

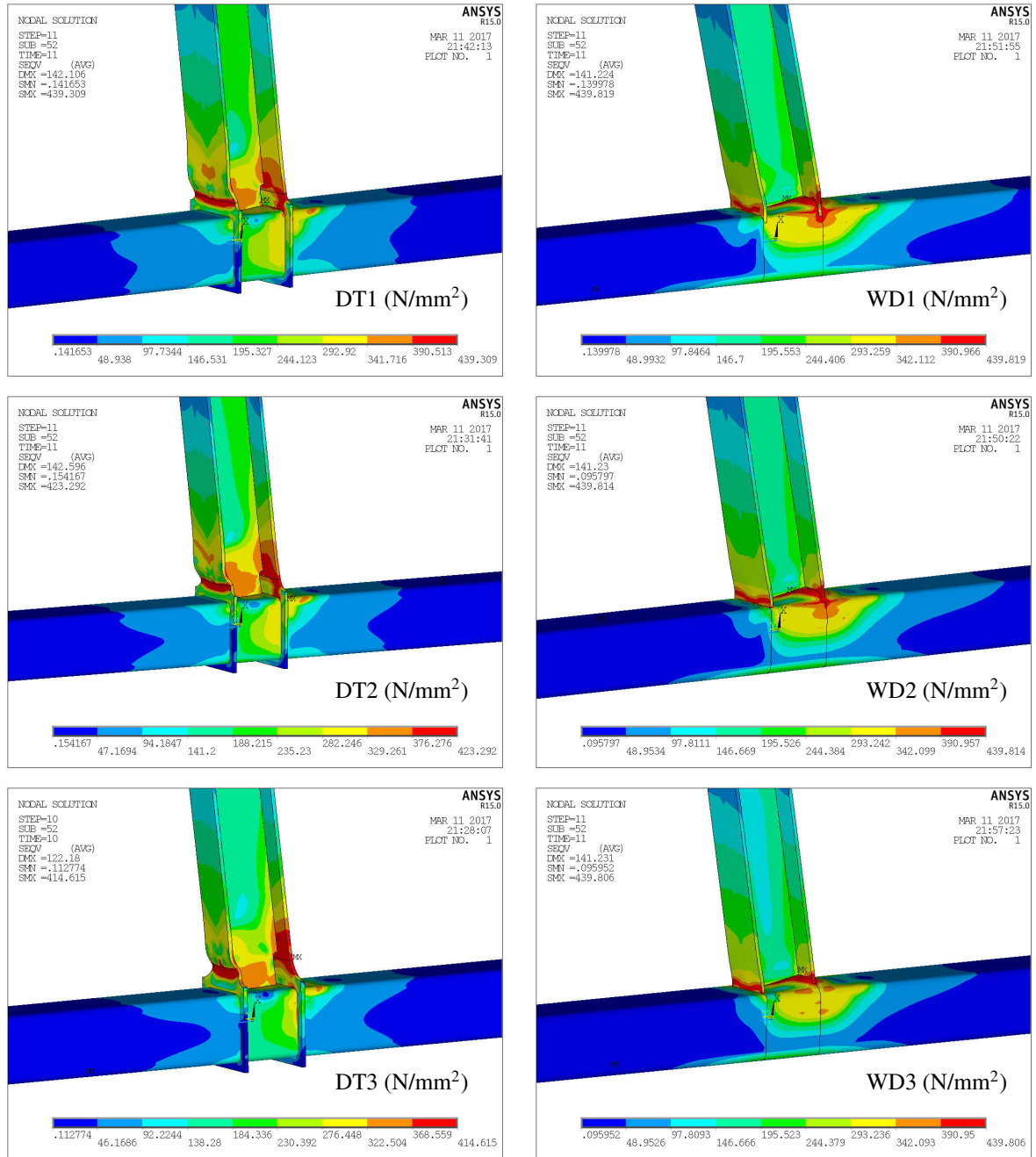


Figure 13. Failure modes and von Mises stress contour of models.

totally different. According to the theory of Lu [1997], the failure modes of DT series are also supposed to be column failure. However, failure modes of DT series are all plastic hinge at the beam end, which disagrees with the theory. Therefore, the theory of Lu [1997] is not suitable for diaphragm-through

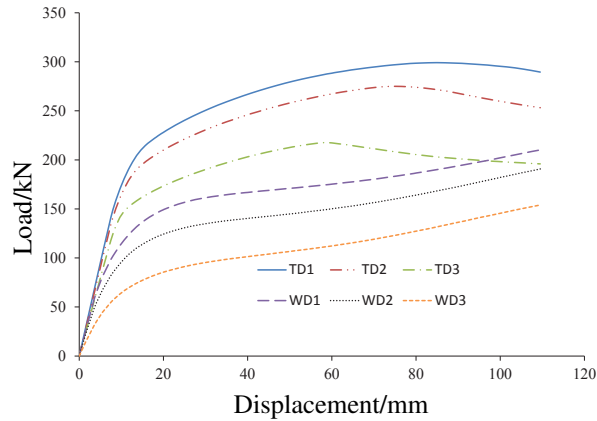


Figure 14. Load-displacement curves of models.

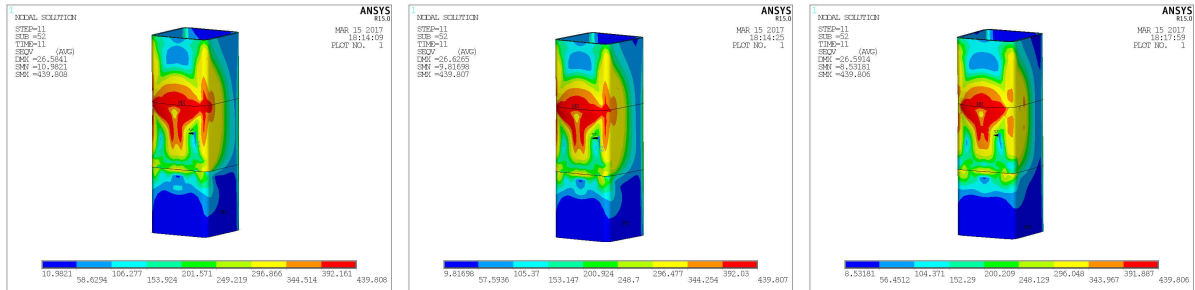


Figure 15. Column face yielding of WD series (from left to right): WD1, WD2, and WD3.

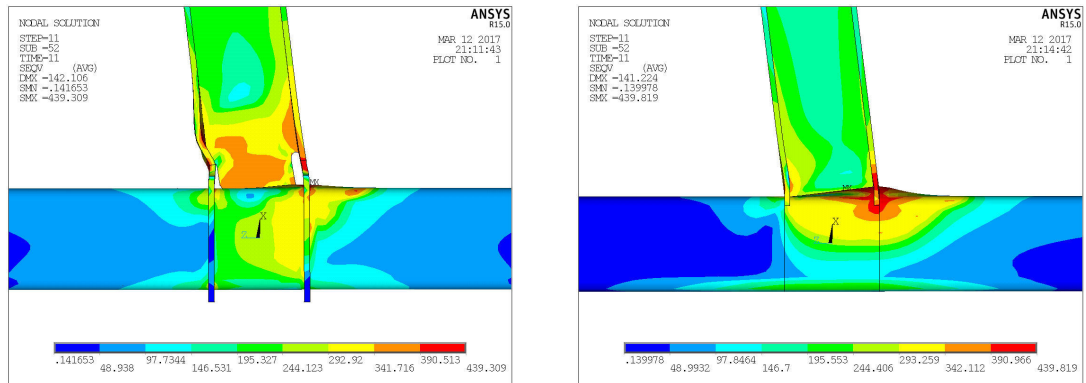


Figure 16. Failure modes of DT1 (left) and WD1 (right).

connections. Figure 16 illustrates the failure modes of DT1 and WD1 clearly; it is found that the stress level distribution for them are obviously different. For DT1, the high stress level regions of DT1 focus on the junction part of the beam and diaphragm while the stress level of the column is much lower. However, as the distribution of WD1 is revised, high stress level on the column but low stress level on the beam appear in WD1. The phenomenon demonstrates the great influence of the diaphragm on the failure mode

of beam-column connection. The diaphragm strengthens the column greatly, and it results in the turn of failure mode from column face yielding to plastic hinge damage at the beam end.

5. Conclusions

In this paper, tests and finite element analysis were undertaken to investigate mechanical properties of T-shaped diaphragm-through connections between CFST column and steel beam under monotonic and cyclic loading. The main conclusions can be drawn as follows:

- Experimental results show that the failure modes of the two specimens are both plastic hinge damage at the restrained beam end. Different loading types, static load and seismic action, have little effect on the failure mode and ultimate bearing capacity of the T-shaped diaphragm-through connection, and the connection exhibits larger yield capacity and lower ductility under cyclic loading than monotonic loading. In addition, it is also found that the failure mode of a T-shaped diaphragm-through connection whose ratio of beam flange width to column flange width is 1 is plastic hinge damage at beam end.
- According to parametric finite element analysis, which is in a good agreement with the test results, the initial stiffness and the bearing capacity of diaphragm-through connection are obviously larger than ordinary beam-column connection, and there is also a negative correlation between the bearing capacity and beam width for both the diaphragm-through connection and ordinary beam-column connection.
- The failure mode of the T-shaped diaphragm-through connection is plastic hinge damage, which is caused by overstress of the restrained beam end. However, the failure mode of the beam-column connection without diaphragm is column face yielding, which is caused by a large local deformation on the column flange face. The phenomenon demonstrates that the diaphragm strengthens the column greatly, and it results in the turn of the failure mode from column face yielding to plastic hinge damage at beam end.

Acknowledgements

The research described in this paper was financially supported by the National Natural Science Foundations of China (No. 51268054 and No. 51468061) and the Natural Science Foundation of Tianjin City, China (No. 13JCQNJJC07300). The financial supports are greatly appreciated.

References

- [Elghazouli et al. 2009] A. Y. Elghazouli, C. Málaga-Chuquitaype, J. M. Castro, and A. H. Orton, “Experimental monotonic and cyclic behavior of blind-bolted angle connections”, *Eng. Struct.* **31**:11 (2009), 2540–2553.
- [Fukumoto and Morita 2005] T. Fukumoto and K. Morita, “Elastoplastic behavior of panel zone in steel beam-to-concrete filled steel tube column moment connections”, *J. Struct. Eng.* **131**:12 (2005), 1841–1853.
- [Kataoka and El Debs 2015] M. N. Kataoka and A. L. H. d. C. El Debs, “Beam-column composite connections under cyclic loading: an experimental study”, *Mater. Struct.* **48**:4 (2015), 929–946.
- [Lee et al. 2012] S. H. Lee, Y. H. Kim, and S. M. Choi, “Shear strength formula of CFST column-beam pinned connections”, *Steel Compos. Struct.* **13**:5 (2012), 409–421.

- [Li and Han 2012] W. Li and L.-H. Han, “Seismic performance of CFST column to steel beam joint with RC slab: joint model”, *J. Constr. Steel Res.* **73** (2012), 66–79.
- [Liu et al. 2012] Y. Liu, C. Málaga-Chuquitaype, and A. Y. Elghazouli, “Response and component characterisation of semi-rigid connections to tubular columns under axial loads”, *Eng. Struct.* **41** (2012), 510–532.
- [Liu et al. 2014] Y. Liu, C. Málaga-Chuquitaype, and A. Y. Elghazouli, “Behaviour of open beam-to-tubular column angle connections under combined loading conditions”, *Steel Compos. Struct.* **16**:2 (2014), 157–185.
- [Lu 1997] L. H. Lu, *The static strength of I-beam to rectangular hollow section column connections*, Ph.D. thesis, Delft University of Technology, 1997, available at <http://tinyurl.com/staticlu>.
- [Málaga-Chuquitaype and Elghazouli 2010] C. Málaga-Chuquitaype and A. Y. Elghazouli, “Behavior of combined channel/angle connections to tubular columns under monotonic and cyclic loading”, *Eng. Struct.* **32**:6 (2010), 1600–1616.
- [Nie et al. 2008] J. Nie, K. Qin, and C. S. Cai, “Seismic behavior of connections composed of CFSSTCs and steel-concrete composite beams: finite element analysis”, *J. Constr. Steel Res.* **64**:6 (2008), 680–688.
- [Nishiyama et al. 2004] I. Nishiyama, T. Fujimoto, T. Fukumoto, and K. Yoshioka, “Inelastic force-deformation response of joint shear panels in beam-column moment connections to concrete-filled tubes”, *J. Struct. Eng.* **130**:2 (2004), 244–252.
- [Park et al. 2010] S.-H. Park, S.-M. Choi, Y.-S. Kim, Y.-W. Park, and J.-H. Kim, “Hysteresis behavior of concrete filled square steel tube column-to-beam partially restrained composite connections”, *J. Constr. Steel Res.* **66**:7 (2010), 943–953.
- [Qin et al. 2014a] Y. Qin, Z. Chen, and B. Rong, “Component-based mechanical models for axially-loaded through-diaphragm connections to concrete-filled RHS columns”, *J. Constr. Steel Res.* **102** (2014), 150–163.
- [Qin et al. 2014b] Y. Qin, Z. Chen, Q. Yang, and K. Shang, “Experimental seismic behavior of through-diaphragm connections to concrete-filled rectangular steel tubular columns”, *J. Constr. Steel Res.* **93**:1 (2014), 32–43.
- [Rong et al. 2012] B. Rong, Z. Chen, R. Zhang, A. Fafitis, and N. Yang, “Experimental and analytical investigation of the behavior of diaphragm-through joints of concrete-filled tubular columns”, *J. Mech. Mater. Struct.* **7**:10 (2012), 909–929.
- [Rong et al. 2016] B. Rong, R. Liu, R. Zhang, Z. Chen, and A. Fafitis, “Flexural bearing capacity of diaphragm-through joints of concrete-filled square steel tubular columns”, *Steel Compos. Struct.* **20**:3 (2016), 487–500.
- [Tizani et al. 2013] W. Tizani, Z. Y. Wang, and I. Hajirasouliha, “Hysteretic performance of a new blind bolted connection to concrete filled columns under cyclic loading: an experimental investigation”, *Eng. Struct.* **46** (2013), 535–546.
- [Yin et al. 2016] L. Yin, G. Tang, M. Zhang, B. Wang, and B. Feng, “Monotonic and cyclic response of speed-lock connections with bolts in storage racks”, *Eng. Struct.* **116** (2016), 40–55.
- [Yu et al. 2015] Y. Yu, Z. Chen, and X. Wang, “Effect of column flange flexibility on WF-beam to rectangular CFT column connections”, *J. Constr. Steel Res.* **106** (2015), 184–197.

Received 17 Mar 2017. Revised 7 Jul 2017. Accepted 8 Aug 2017.

BIN RONG: tjerobin@126.com
Tianjin University, Tianjin, China

CHANGXI FENG: fengchangxi95@163.com
Tianjin University, Tianjin, China

RUOYU ZHANG: zryu@163.com
Tianjin University, Tianjin, China

SHUAI LIU: lao_xs@163.com
Tianjin University, Tianjin, China

GUANGCHAO YOU: youguangchao@163.com
Tianjin University, Tianjin, China

MULTIMODAL PIEZOELECTRIC DEVICE FOR ENERGY HARVESTING FROM ENGINE VIBRATION

CLAUDIO D. GATTI, JOSÉ M. RAMIREZ, MARIANO FEBBO AND SEBASTIÁN P. MACHADO

In a conventional transport vehicle, only about 10% to 16% of the energy from the fuel is used to move it down the road. The rest of the energy is lost in the brakes, transmission, engine, accessories, rolling resistance, aerodynamic drag, and idle losses. Among all of these, the largest loss is the energy lost in the engine (approximately 63%), which is mostly wasted as vibration. Our work develops an energy harvesting device that is capable of collecting energy for different gear ratios in a car. For this reason, the structural design is oriented to create a harvesting structure with several resonant modes in a frequency bandwidth between 1600 rpm–4600 rpm, which was the range obtained through driving tests in a conventional diesel car. The harvesting device is based on a piezoelectric fiber composite beam with a high fatigue resistance placed in the middle of two mass-spring systems, which provide the multimodal character of the device. A one-dimensional analytical model based on a Lagrangian formulation is used to predict the dynamical behavior of the device. The equations provide a very good quantitative description of the system, which is also modeled with a three-dimensional finite element code (Abaqus) for numerical validation. Experimental tests are then carried out and compared with theoretical findings. The results show a very good agreement between both of them, revealing the multimodal nature of the device in the operating bandwidth, with a significant output power for different engine speeds, sufficient to feed low-power monitoring wireless systems.

1. Introduction

Energy harvesting is a subject of great importance in the scientific world. In the area of transport vehicles (land, sea, or air) that use combustion engines for propulsion, fuel consumption involves two main drawbacks. Firstly, there is environmental contamination and thus degradation of the ozone layer due to the emission of polluting gases from the incomplete combustion of fuel. From this point of view, reducing its consumption implies a reduction of greenhouse gases, and thus less damage to the atmosphere. Secondly, fossil fuels are nonrenewable natural resources. This means that in the near future there will be a fuel shortage if current consumption trends continue. In this context, it is important to implement energy harvesting techniques in order to minimize these drawbacks [Xiao and Wang 2014].

Energy harvesting can be obtained from solar, wind, tidal, kinetic, thermal sources, or mechanical vibrations, the latter being the object of study of this work. After the source has been defined, the energy can be recovered through electromagnetic devices, thermoelectric, or piezoelectric materials [IEE 1988; Erturk and Inman 2011], among others.

The use of piezoelectric materials that take advantage of mechanical deformations caused by vibration is of great interest for generating an electric potential difference. Piezoelectric materials have been used

Keywords: piezoelectric materials, vehicles, engines, vibrations, system recovery.

in different device variants, such as axial cymbals [Kim et al. 2004; 2006; Ren et al. 2010], corrugated piezoelectric springs [Harne 2013], linear [Ramirez et al. 2017; Van Blarigan et al. 2015] and nonlinear piezoelectric beams [Harne and Wang 2013], aeroelastic systems [He and Gao 2013; Bibo and Daqaq 2013], and multilayer stacks [Xu et al. 2013]. Most of them are designed to work at resonance, where the system is capable of recovering maximum energy due to the large deformations in the piezoelectric material. The main disadvantage of this approach is that the systems are efficient for a single excitation frequency (single-mode generation), which has to be coincident with one of the natural frequencies of the harvesting device. As soon as the excitation frequency moves away from this condition (off-resonance condition), the generated voltage drops abruptly. With the intention of overcoming this situation, more sophisticated proposals of energy harvesting devices have implemented multimodal systems in order to have multiple resonant modes in the range of possible excitation frequencies [Sadeqi et al. 2015; Zhu et al. 2010; Rezaei-Hosseiniabadi et al. 2016].

In the industry of transport vehicles, various energy harvesting devices have been used mainly to feed low-power wireless transmitters. Some of the most important works are based on rotational energy [Roundy 2008; Wang et al. 2010; 2013] or deformation of the tires [Lee et al. 2012]. Another important issue is energy recovery by means of the vehicle's suspension dampers [Zhang et al. 2007; 2012; Zuo and Zhang 2013], where a large amount of energy can be collected. However, there are few works that consider energy recovery from engine vibration. For example, Glynne-Jones et al. [2004] proposed an electromagnetic microgenerator mounted on the top of the engine block of a car with an average generation of $157 \mu\text{W}$. Therefore, the possibility of harvesting energy from engine vibrations using a piezoelectric generator is addressed in this paper.

There are several different issues that can be explored for developing this investigation. We will focus on the two that we consider central in this case:

- (a) the recovery of the maximum possible energy over a well-defined bandwidth, and
- (b) the long fatigue life of the piezoelectric beams.

Our proposal attempts to give a solution to these important problems. For the first issue, we propose a multimodal system with multiple resonant modes in a well-defined range of frequencies. This operating bandwidth will be defined by making a drive test in a conventional car in our city at normal speed. For the second issue, we will use a composite beam of interdigitated electrodes and piezoelectric fibers of PZT-5A [Nelson et al. 2003; Beckert and Kreher 2003; Bowen et al. 2006; Hareesh et al. 2012; Lin et al. 2013] as the harvesting device. The selected piezofiber composite has significant advantages over other conventional piezoelectric sheets. Firstly, the longitudinally oriented piezofibers give large flexibility to the sheets, and thus long fatigue life, which enables large strains and therefore more power generation [Beckert and Kreher 2003]. Secondly, the electric field is established in the longitudinal direction due to the arrangement of the interdigitated electrodes. This makes the power generation with piezoelectric charge coefficient d_{33} (polarization in same direction of stress applied) being larger than with piezoelectric charge coefficient d_{31} (polarization in perpendicular direction of stress applied) [Uchino 1997].

Considering these preliminary issues, the paper is organized as follows. In the first section, the one-dimensional structural model together with the electromechanical Lagrange's equation and their solutions are sketched. In Section 2 we define the design parameters of the harvester and perform a computational validation of the results of the first section. In Section 3, details of the experimental tests and a comparison

between analytical and experimental voltage measurements are presented. Finally, some conclusions are drawn to show the advantages of the proposed system.

2. Dynamical modeling and electromechanical equations

Figure 1, left, shows the proposed device, which consists of a composite beam with two mass-spring systems at the ends of the beam that provide the appropriate boundary conditions. By means of this model, it is possible to modify the multimodal response by varying the parameters such as the masses and springs. The composite beam consists of a central stainless steel structure with two piezoelectric fiber composites (PFCB-W14 from Advanced Cerametrics Inc.) attached to the upper and lower surfaces (see Figure 1, right). Both piezofiber composites are connected in parallel constituting a bimorph electric system. The only thing the device is subjected to is the base excitation provided by the vehicle's engine, generating a voltage difference between the electrodes of the bimorph. In Figure 1, left, $g(t)$ is the temporal base excitation, L is the length of the composite beam, $m_{1,2}$ are the masses, $k_{1,2}$ are respectively the vertical stiffnesses of the springs at the ends $x = 0$ and $x = L$, and $k_{t1,t2}$ are respectively the torsional stiffnesses of the springs at the ends $x = 0$ and $x = L$. In Figure 1, right, b_p , h_p , b_s and h_s are the width and thickness of the piezofiber composite, and the width and thickness of the stainless steel structure, respectively.

2.1. Electromechanical model of the system. The beam is modeled according to the Bernoulli–Euler formulation [Rao 2007], considering only the vertical displacement. A Lagrangian approach [Meirovitch and Parker 2010] was used to build the system of differential equations. In the following description, the x , y , and z shown in Figure 1 correspond to axes 1, 2, and 3, respectively. The idea is to have an analytical model that allows the simple dimensioning of the multimodal device according to the range of interests that will be defined later.

The vector form of the displacement field is defined (disregarding the axial displacement and including the temporal base excitation) as

$$\mathbf{u} = [u_x \ u_y \ u_z]^t = [-z \partial w(x, t) / \partial x \ 0 \ w(x, t) + g(t)]^t, \quad (1)$$

where $w(x, t)$ is the transverse displacement of the neutral axis at point x and time t .

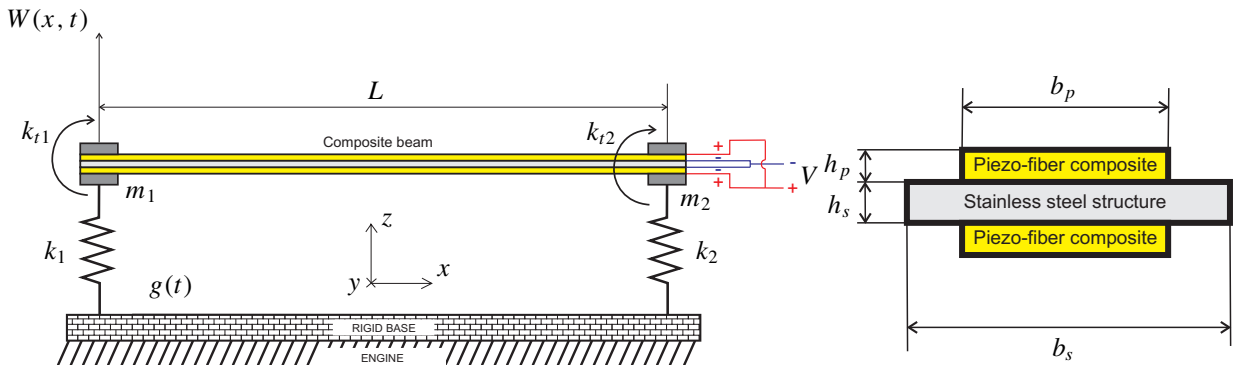


Figure 1. Harvester device. Left: scheme of the system model. Right: cross-sectional view of composite beam.

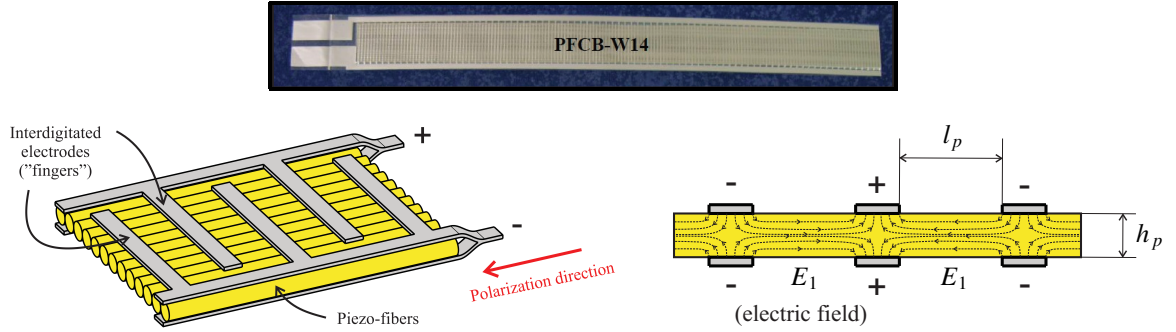


Figure 2. Schematic view of the piezofibers composite. Top: real piezofiber composite PFCB-W14 from Advanced Cerametrics Inc. (168 fingers). Left: geometric detail of only four “fingers” of the electrodes. Right: cross-sectional view of the fibers and electrodes showing the generated electric field.

The longitudinal strain is given by

$$\varepsilon_{11} = \frac{\partial u_x}{\partial x} = -z \frac{\partial^2 w(x, t)}{\partial x^2}. \quad (2)$$

From Hooke’s law, the stress generated in the steel structure is

$$\sigma_{11}^s = E_s \varepsilon_{11} = -E_s z \frac{\partial^2 w(x, t)}{\partial x^2}, \quad (3)$$

where E is the Young’s modulus of the substructure (steel beam). Based on the constitutive equation of the piezoelectric material [IEE 1988], and considering only the x component of the electric field, then

$$\sigma_{11}^p = E_p \varepsilon_{11} - \bar{e}_{11} E_1 = -E_p z \frac{\partial^2 w(x, t)}{\partial x^2} - \bar{e}_{11} E_1, \quad (4)$$

where $\bar{e}_{11} = d_{11} E_p$ is a piezoelectric constant and E_p is the Young’s modulus of the piezoelectric sheet. Furthermore, the electric field generated in the longitudinal direction E_1 can be modeled with sufficient accuracy by [Nelson et al. 2003]

$$E_1 = -\frac{v_C(t)}{l_p}, \quad (5)$$

with l_p being the distance in the x direction between the fingers of the positive and negative electrodes of each piezofiber composite (see Figure 2).

Now, the total potential energy of the system U is the sum of the potential energy of the beam U_b and springs U_{k1} and U_{k2} . i.e., $U = U_b + U_{k1} + U_{k2}$. Thus, the expression of the potential energy of the beam is given by [Erturk and Inman 2011]

$$U_b = \frac{1}{2} \left(\int_{V_s} \boldsymbol{\varepsilon}^t \boldsymbol{\sigma} \, dV_s + \int_{V_p} \boldsymbol{\varepsilon}^t \boldsymbol{\sigma} \, dV_p \right). \quad (6)$$

The first and the second volume integrals within the parentheses of (6) concern the steel structure and the piezoelectric element, respectively.

symbol	quantity	value
A_s	cross sectional area of the steel structure	$b_s h_s$
A_p	cross sectional area of the piezoelectric element ^a	$2b_s h_s$
I_s	moment of inertia of the steel structure	$\frac{1}{12}(b_s h_s^3)$
I_p	moment of inertia of the piezoelectric element ^a	$b_p h_p (\frac{2}{3}h_p^2 + h_p h_s + \frac{1}{2}h_s^2)$
J_p	coupling coefficient ^a	$[\bar{e}_{11} b_p h_p (h_p + h_s)]/l_p$
C_p	internal capacitance of the piezoelectric element ^a	$(2nb_p h_p \bar{\epsilon}_{11}^e)/l_p$

^aTotals for the entire beam (bimorph) connected in parallel.

Table 1. Geometric and electrical coefficients.

Developing the above equation yields

$$U_b = \frac{1}{2}EI \int_0^L \left(\frac{\partial^2 w(x, t)}{\partial x^2} \right)^2 dx - \frac{1}{2}J_p v_C(t) \int_0^L \frac{\partial^2 w(x, t)}{\partial x^2} dx, \quad (7)$$

where J_p is the electromechanical coupling coefficient, $EI = E_s I_s + E_p I_p$ is the flexural rigidity of the entire beam, and I_s and I_p are the cross-sectional area moments of inertia of the structure and the piezoelectric element, respectively. The calculated expressions for these geometric ratios are shown in Table 1.

Considering the vertical and torsional deformation, the elastic potential energy of the springs becomes

$$U_{ki} = \frac{1}{2} \left[k_i w(x_j, t)^2 + k_{ti} \frac{\partial w(x_j, t)}{\partial x} \right], \quad i = 1, 2, \quad x_j = 0, L, \quad (8)$$

where k_i are the vertical stiffnesses and k_{ti} are the torsional stiffnesses of the springs.

Similarly, the total kinetic energy of the system T is the sum of the kinetic energy of the beam T_b and end masses T_{m1} and T_{m2} , i.e., $T = T_b + T_{m1} + T_{m2}$. Thus, the kinetic energy of the beam is [Erturk and Inman 2011]

$$T_b = \frac{1}{2} \left(\int_{V_s} \rho_s \frac{\partial \mathbf{u}^t}{\partial t} \frac{\partial \mathbf{u}}{\partial t} dV_s + \int_{V_p} \rho_p \frac{\partial \mathbf{u}^t}{\partial t} \frac{\partial \mathbf{u}}{\partial t} dV_p \right), \quad (9)$$

where ρ_s and ρ_p represent the mass density of the steel and the piezoelectric element, respectively. After some algebra, (9) reads

$$T_b = \frac{1}{2} \rho A \int_0^L \left[\frac{\partial w(x, t)}{\partial t} \right]^2 + 2 \frac{\partial w(x, t)}{\partial t} \dot{g}(t) + \dot{g}(t)^2 dx, \quad (10)$$

where $\rho A = \rho_s A_s + \rho_p A_p$ is the mass per unit length of the beam, and A_s and A_p are the cross-sectional areas of the steel structure and the piezoelectric sheet, respectively (see Table 1).

Taking into account the rotational inertia and vertical movement, the kinetic energy of the masses becomes

$$T_{mi} = \frac{1}{2} m_i \left[\frac{\partial w(x_i, t)}{\partial t} \right]^2 + 2 \frac{\partial w(x_i, t)}{\partial t} \dot{g}(t) + \dot{g}(t)^2 + \frac{1}{2} J_i \left(\frac{\partial^2 w(x_i, t)}{\partial t \partial x} \right)^2, \quad i = 1, 2, \quad x_1 = 0, \quad x_2 = L. \quad (11)$$

The equivalent electric circuit for the PFCB-W14 piezofiber composite used in this work is schematically shown in Figure 3. It consists of a current generator and two capacitive-resistive impedances

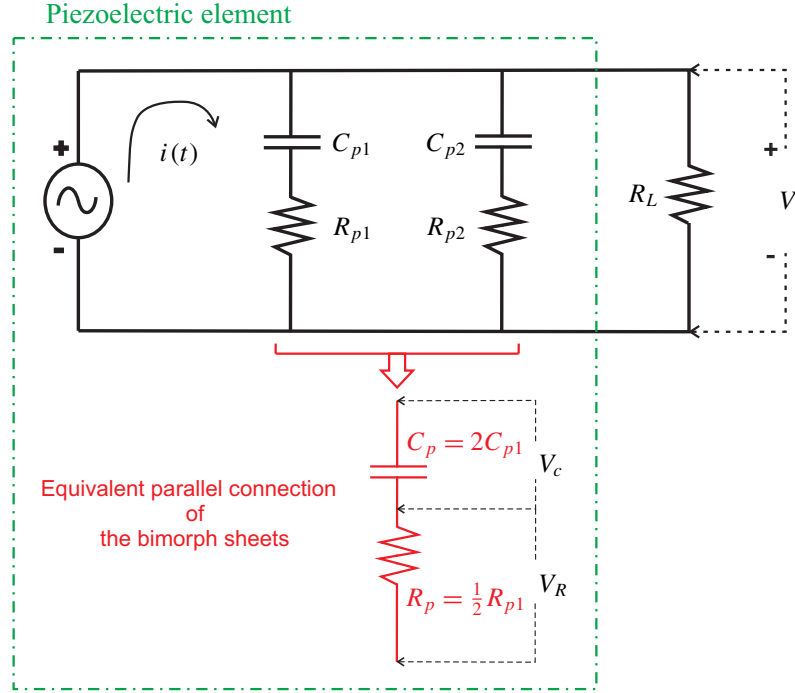


Figure 3. Equivalent electrical circuit of the PFCB-W14 piezofiber composite bimorph.

$(C_{p1,2}-R_{p1,2})$ connected in parallel, representing each piezoelectric sheet. In practical situations, the output voltage is rectified and conditioned by a DC-DC converter, for example, to store the power in a battery or a supercapacitor. However, a resistive load resistance R_L is added here as an output load in order to easily calculate the output power, which has been previously used in similar works by other authors [Erturk and Inman 2011; Ramirez et al. 2017].

In order to compute the electric potential energy, we must take into account its integral representation as expressed in [Erturk and Inman 2011]:

$$W_{ie} = \frac{1}{2} \int_{V_p} E_1 D_1 dV_p, \quad (12)$$

where the electric displacement is defined from the linear constitutive equation for piezoelectric materials as $D_1 = \bar{\epsilon}_{11}^e \epsilon_{11} + \bar{\epsilon}_{11}^e E_1$ [IEE 1988], with $\bar{\epsilon}_{11}^e$ being the permittivity of the piezoelectric sheet at constant strain.

The expression for the electric power is obtained by using D_1 and E_1 as

$$W_{ie} = \frac{1}{2} n J_p v_C(t) \int_0^{l_p} \frac{\partial^2 w(x, t)}{\partial x^2} dx + \frac{1}{2} C_p v_C(t)^2, \quad (13)$$

where C_p (see Table 1) is the total internal capacitance of both piezoelectric sheets (connected in parallel) as shown in Figure 3.

position	shear	moment
	$(E_s I_s + E_p I_p)\phi_i'''(x)$	$(E_s I_s + E_p I_p)\phi_i''(x)$
at 0	$\phi_i(x)(m_1\omega^2 - k_1)$	$\phi_i'(x)(k_{1t} - J_1\omega^2)$
at L	$\phi_i(x)(k_2 - m_2\omega^2)$	$\phi_i'(x)(J_2\omega^2 - k_{t2})$

Table 2. Boundary conditions.

The damping of the system is modeled using the Rayleigh dissipation function [Mohammad et al. 1995], whose full expression R is the sum of the energy dissipation of the beam R_b and springs R_{k1} and R_{k2} , i.e., $R = R_b + R_{k1} + R_{k2}$. Considering a modal damping coefficient for the beam $r_b = 2\xi_i m_b \omega_{ni}$, where ξ_i is the modal damping ratio, $m_b = \rho AL$ is the mass of the entire beam, and ω_{ni} is its natural frequency of the i -th vibration mode, then the final expression for the dissipation of the beam, after integrating the mass density in the total volume, is

$$R_b = \xi_i \omega_{ni} \rho A \int_0^L \frac{\partial w(x, t)^2}{\partial t} dx. \quad (14)$$

In this work, we decided to neglect the damping in the springs and attribute the total dissipation to the beam, yielding $R = R_b$.

2.2. Spatial discretization of the energy equations and electromechanical Lagrange equations. One of the commonly used procedures to obtain an analytical solution to Lagrange's equation is by the spatial discretization of the energy equations and Rayleigh dissipation function by applying the standard modal expansion method to the separation of variables [Weaver Jr. et al. 1990]. In this method, the deflection of the beam is represented as a finite sum of N generalized temporal displacements $q_i(t)$ and normalized mode shape functions $\phi_i(x)$:

$$w(x, t) = \sum_{i=1}^N \phi_i(x) q_i(t). \quad (15)$$

Mode shape functions, which satisfy the boundary conditions presented in Table 2, are given by

$$\phi_i(x) = C_1 \cos(\beta_i x) + C_2 \cosh(\beta_i x) + C_3 \sin(\beta_i x) + C_4 \sinh(\beta_i x), \quad (16)$$

where the eigenvalues β_i are related to the respective natural frequencies by

$$\omega_{ni} = (\beta_i L)^2 \sqrt{\frac{EI}{\rho AL^4}}. \quad (17)$$

Constants C_1 , C_2 , and C_3 are obtained from the boundary conditions, and C_4 is obtained from mass-normalized modal shape functions.

Finally, by applying Lagrange's formulation, the following equations are obtained:

$$\frac{d}{dt} \left(\frac{\partial T}{\partial \dot{q}_i} \right) + \frac{\partial U}{\partial q_i} + \frac{\partial R}{\partial \dot{q}_i} - \frac{\partial W_{ie}}{\partial q_i} = 0, \quad (18)$$

$$\frac{\partial U}{\partial v} - \frac{\partial W_{ie}}{\partial v} = Q_e, \quad (19)$$

where Q_e is the electrical charge whose time derivative gives the electrical current as $\dot{Q}_e = v(t)/R_L$.

After replacing U , T , W_{ie} , and R into (18) and (19), and deriving (19) with respect to time, two matrix equations are obtained that give the electromechanical behavior of the system:

$$\mathbf{M}\ddot{\mathbf{q}} + \mathbf{R}\dot{\mathbf{q}} + \mathbf{K}\mathbf{q} - \tilde{\boldsymbol{\theta}}v_C = \mathbf{f}, \quad (20)$$

$$C_p\dot{v}_c + \frac{v}{R_L} + \tilde{\boldsymbol{\theta}}^t \dot{\mathbf{q}} = 0. \quad (21)$$

In (20) the mass, damping, and stiffness matrices are defined as

$$\mathbf{M} = \begin{bmatrix} m_{11} & \cdots & 0 \\ \vdots & \ddots & \vdots \\ 0 & \cdots & m_{NN} \end{bmatrix}, \quad (22)$$

where

$$m_{ii} = \rho A \int_0^L \phi_i \phi_j \, dx + m_1 \phi_i(0) \phi_j(0) + J_1 \phi_i'(0) \phi_j'(0) + m_2 \phi_i(L) \phi_j(L) + J_2 \phi_i'(L) \phi_j'(L), \quad (23)$$

$$\mathbf{R} = \begin{bmatrix} r_{11} & \cdots & 0 \\ \vdots & \ddots & \vdots \\ 0 & \cdots & r_{NN} \end{bmatrix}, \quad (24)$$

with

$$r_{ii} = 2\xi_i \omega_{ni} \rho A \int_0^L \phi_i \phi_j \, dx + r_1 \phi_i(0) \phi_j(0) + r_2 \phi_i(L) \phi_j(L), \quad (25)$$

$$\mathbf{K} = \begin{bmatrix} k_{11} & \cdots & 0 \\ \vdots & \ddots & \vdots \\ 0 & \cdots & k_{NN} \end{bmatrix}, \quad (26)$$

where

$$k_{ii} = EI \int_0^L \phi_i'' \phi_j'' \, dx + k_1 \phi_i(0) \phi_j(0) + k_{1t} \phi_i'(0) \phi_j'(0) + k_2 \phi_i(L) \phi_j(L) + k_{2t} \phi_i'(L) \phi_j'(L). \quad (27)$$

The electromechanical coupling vector and force vector are

$$\tilde{\boldsymbol{\theta}} = [\theta_1 \cdots \theta_N]^t, \quad (28)$$

with

$$\theta_i = J_p [\phi_i'(L) - \phi_i'(0)], \quad (29)$$

$$\mathbf{f} = [f_1 \cdots f_N], \quad (30)$$

where $f_i = -\sigma_i \ddot{g}(t)$ and $\sigma_i = \rho A \int_0^L \phi_i \, dx + m_1 \phi_i(0) + m_2 \phi_i(L)$.

To solve (20) and (21), a harmonic base excitation [Meirovitch and Parker 2010] is proposed in the form of $g(t) = W_0 e^{i\omega t}$, with W_0 being the semi-amplitude of the displacement of the base.

Now, assuming a harmonic dependence of all the variables,

$$\mathbf{q} = \mathbf{Q}e^{i\omega t}, \quad (31)$$

$$v_C = V_C e^{i\omega t}, \quad (32)$$

$$v = V e^{i\omega t}, \quad (33)$$

and using $V_C = V$, the modal displacement vector \mathbf{Q} is obtained after replacing (31)–(33) into (20) and (21):

$$\mathbf{Q} = \mathbf{\Gamma}^{-1} \mathbf{F}, \quad (34)$$

where $\mathbf{F} = -\sigma \omega^2 \mathbf{W}_0$ is obtained from f_i and $g(t)$, and $\mathbf{\Gamma}$ results in

$$\mathbf{\Gamma} = -\omega^2 \mathbf{M} + i\omega \mathbf{R} + \mathbf{K} + i\omega \left[i\omega C_p \left(\frac{R_p}{R_L} + 1 \right) + \frac{1}{R_L} \right]^{-1} \tilde{\boldsymbol{\theta}} \tilde{\boldsymbol{\theta}}^t. \quad (35)$$

Finally, after obtaining the modal displacements and making use of (21) and (31)–(33), the final expression for the complex voltage applied to the load resistance R_L is

$$V = -i\omega Z_{eq} \tilde{\boldsymbol{\theta}}^t \mathbf{Q}, \quad (36)$$

where $Z_{eq} = (i\omega C_p + 1/R_L)^{-1}$ is the equivalent impedance of the entire electrical circuit model.

It is useful to present the results in the form of power for practical comparisons. In this case, the electric power in the load resistance is simply computed as

$$P = \frac{V^2}{R_L}. \quad (37)$$

3. Harvester design and computational validation

Prior to setting the experimental tests for the harvesting device, we decided to develop a three-dimensional computer model to validate the proposed analytical approach. The selection of the masses and spring sizes of the harvester, which represent its main parameters and determine its natural frequencies, were calculated from a drive test in a car on the streets of our home city of Bahía Blanca. In this way, it was possible to observe the most frequent range of engine revolutions of the car in order to determine the range of frequencies in its normal operating mode.

The test was carried out with a four-stroke Citroën C4 Diesel 1.6 HDi instrumented with a Firelog Extreme Microtex GPS data acquisition system.

Figure 4 shows the route of the drive (upper figure) and the measured working range, rpm vs. time (lower figure). Taking into account that in the case of four-stroke engines the excitation frequency is twice the rotation of the engine [Lin and Ding 2013], the spring-mass systems for the beam ends were computed with the mechanical parameters presented in Table 3. In order to do this calculation, we made the natural frequencies of this multimodal device to be inside the bandwidth defined by Figure 4.

Once the parameters of the harvester were defined, the computational model was developed using Abaqus simulation software. The finite element mesh can be observed in Figure 5. In the model, 15400 eight-node piezoelectric linear brick elements (C3D8E) were used for the piezoelectric sheets, 26477 ten-node quadratic tetrahedron elements (C3D10) for springs, and 8892 eight-node linear brick elements

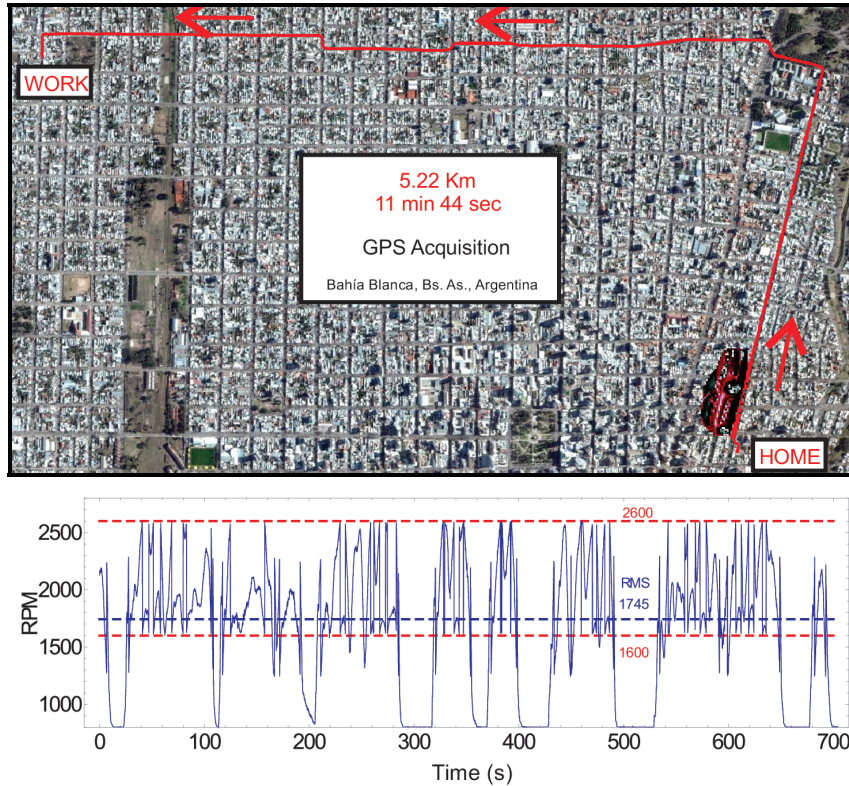


Figure 4. Rpm vs. time of a Citroën C4 engine for a short city drive.

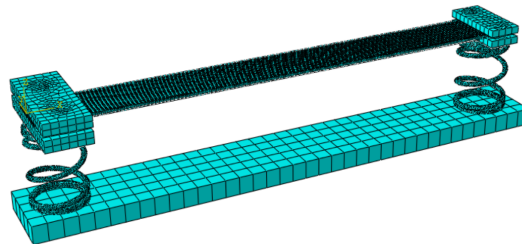


Figure 5. Abaqus 3D model of the harvesting device.

(C3D8R) for the rest of the steel parts. The test was performed in a single-step frequency mode, extracting the first seven vibrational modes. A list of the numerical values used in the calculations is presented in Tables 4 and 5.

Figure 6, left, shows a comparison between the first three flexural mode shapes obtained with analytical and Abaqus calculations. In all three cases, a very good agreement between our proposed one-dimensional model and the three-dimensional finite element method is observed. As it was one of the main objectives of the mechanical design, the first two frequencies (73 Hz and 92 Hz) are within the range of major use of the engine in the city drive.

	description	value	unit
m_1	mass at $x = 0$	19.1	gr
m_2	mass at $x = L$	6.09	gr
J_1	rotational inertia ^a at $x = 0$	3.35×10^{-7}	$\text{kg} \cdot \text{m}^2$
J_2	rotational inertia ^a at $x = L$	5.86×10^{-8}	$\text{kg} \cdot \text{m}^2$
k_1	vertical stiffness ^b at $x = 0$	5460	N/m
k_2	vertical stiffness ^b at $x = L$	3847	N/m
k_{t1}	flexural stiffness ^b at $x = 0$	0.68	$\text{N} \cdot \text{rad/m}$
k_{t2}	flexural stiffness ^b at $x = L$	1.20	$\text{N} \cdot \text{rad/m}$

^aOf the mass at the ends.

^bOf the spring at the ends.

Table 3. Mechanical parameters.

	description	steel structure	piezoelectric element
b	width (mm)	12.7	10.3
h	thickness (mm)	0.4	0.4
ρ	density (kg/m^3)	8035	3750
E	Young's modulus (GPa)	180	15.2
L	length (mm)	125	125

Table 4. Numerical parameters of the beam.

	description	value	unit
d_{11}	piezoelectric charge constant	375	pm/V
$\bar{\epsilon}_{11}^e$	electrical permittivity	13.1	nF/m
R_l	load resistance	248	$\text{k}\Omega$
C_p	internal capacitance	56.79	nF
l_p	“finger” length	0.32	mm
n	number of “fingers”	168	–

Table 5. Electrical parameters.

Figure 6, right, presents the 3D flexural mode shapes from the finite element method, together with the values of speed and gear transmission where these modes can be excited [Shigley 1972]. It is possible to observe that each natural mode is excited for many velocities or gear ratios except the third mode. This clearly demonstrates the ability of the proposed device to be in resonance for a large set of speeds.

4. Experimental validation and results

In this section, experimental tests are carried out to validate the numerical and simulation results obtained in Section 3. Figure 7, top, shows the experimental setup, consisting of a function generator (Rigol

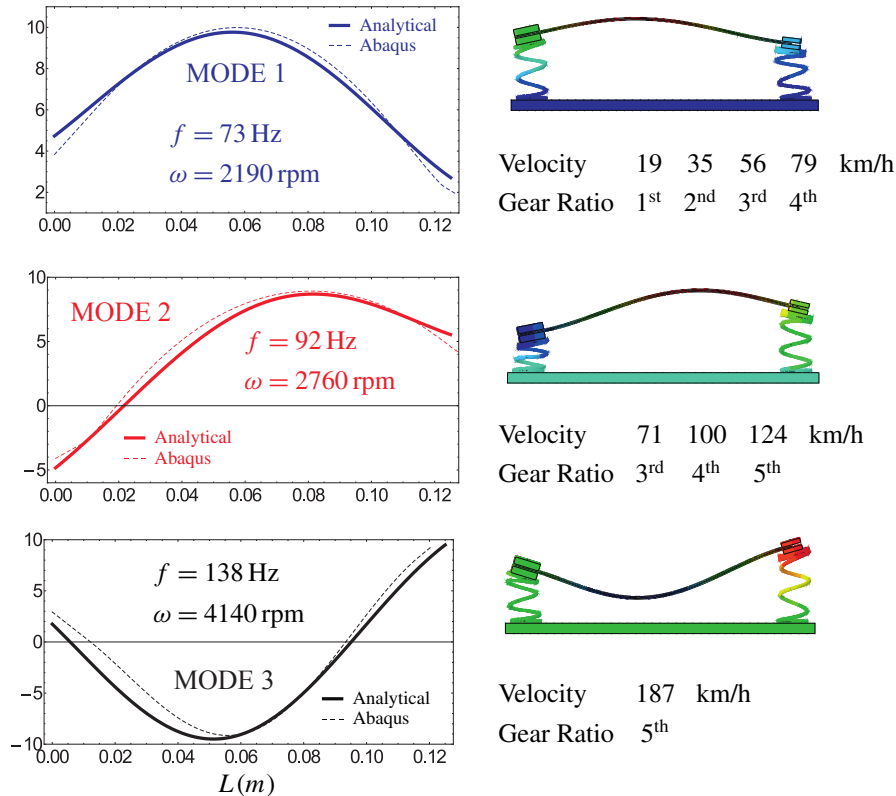


Figure 6. First three flexural mode shapes: comparison between the analytical and computational models.

DG4062) connected to a signal amplifier feeding a shaker, which excites the base of the device by variable acceleration. This acceleration signal is measured using a Wilcoxon Research 780C accelerometer, which is connected, together with the output voltage of the harvester, to a Pasco Science Workshop 750 data acquisition interface. A picture of the device is presented in Figure 7, bottom. In this last figure, the boundary conditions of the composite beam are shown in detail, where the construction method of the mass-spring systems can be observed.

Experimental data are then measured by performing a frequency sweep from 30 Hz to 180 Hz over 60 seconds. During this time interval, the accelerometer data and the piezoelectric voltage are recorded and their fast Fourier transform (FFT) are computed in order to obtain the voltage/acceleration frequency response functions in V/G units ($G = \text{gravity acceleration}$). The frequency is sweep up and down verifying the linear behavior of the device. The results for a load resistance of 248 $k\Omega$ and a peak base acceleration of 0.3 G are shown in Figure 8. This selected value of the load resistance is due to a limitation of $\pm 5 \text{ V}$ in the input voltage of the data acquisition board. As it can be observed, the experiments and theoretical results agree reasonably well for the peaks at 73 Hz (51 V/G) and 140 Hz (15 V/G), which correspond to the first and third analytically predicted vibration modes (second and fifth experimental modes), but not so well for the second peak. In the latter case, the analytical model predicts a more conservative scenario along with a shift in frequency between the analytical and experimental values.

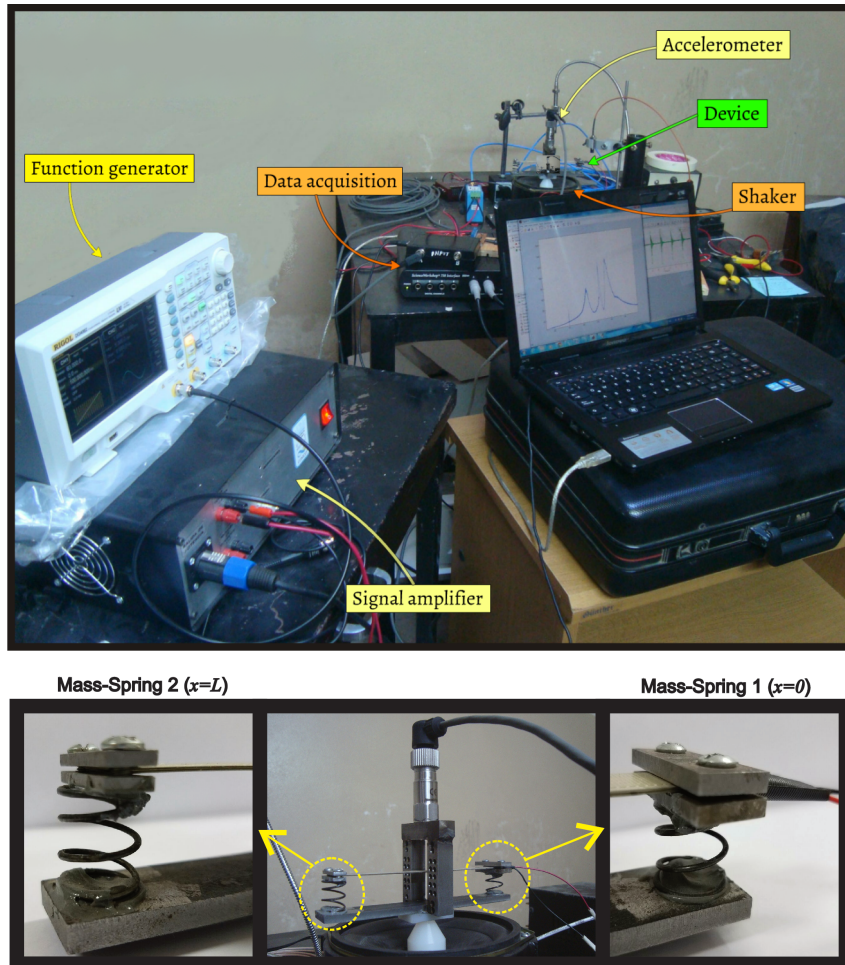


Figure 7. Experimental setup. Top: general scheme. Bottom: detailed view showing the shaker, the device and the accelerometer.

Additionally, the experiments show some additional peaks at around 60 Hz and 75 Hz (first and third modes indicated in Figure 8) that are not predicted by the analytical model. Even though it is not easy to predict the source of these discrepancies, we think that they may be due to some unmodeled effects of the actual harvesting device. Although initially the device was thought to have only vertical displacements, the size of the springs, the amount and distribution of the adhesive layer to bond them to the beam, and the imperfections in the boundary conditions (for example, the joint between the spring and the mass in the beam ends) were not taken into account in the mathematical model and hence do not fit into it.

In order to gain some insight into the source of these differences, we apply Abaqus software to determine the spatial shape in a tridimensional view of the vibration modes. The results are presented in Figure 9, where it is determined that the first peak of the experimental curve (around 60 Hz) corresponds to a lateral (y -direction) vibration mode (Figure 9, left), while the third peak of the same curve (near 75 Hz, Figure 8) corresponds to a first torsional mode of the system (Figure 9, right). As it can be deduced,

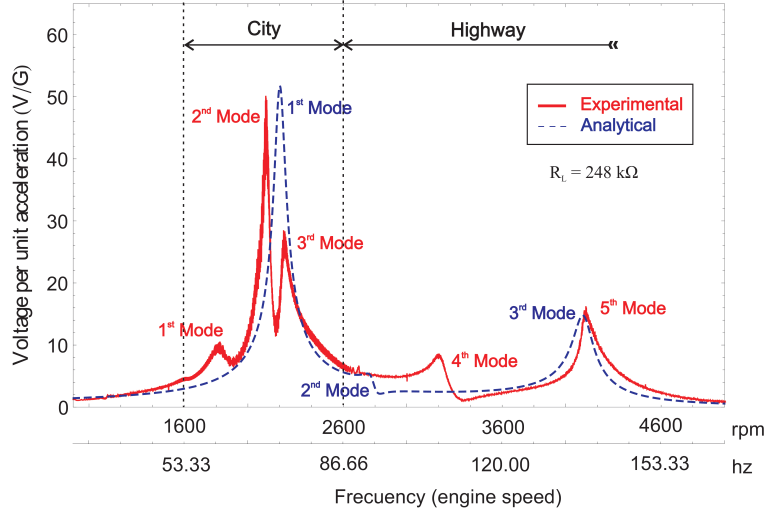


Figure 8. FFT voltage per unit acceleration of gravity in the experimental test for $R_L = 248 \text{ k}\Omega$.

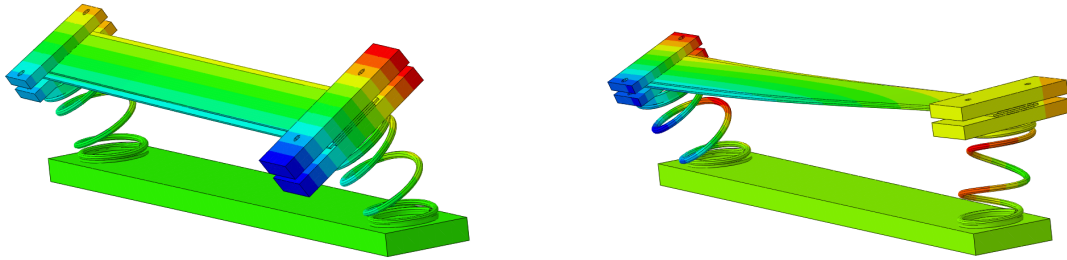


Figure 9. Additional three-dimensional modes generated using Abaqus that were not included in the analytical model. Left: first mode (lateral). Right: third mode (torsional).

it is not possible to analytically predict these additional lateral and torsional modes, and therefore they do not appear in the analytical curve presented in Figure 8. In order to fix this, a more complex model that takes into account the finite size of the springs, for example, must be proposed. However, from an energy harvesting perspective, the presence of these additional modes, although not predicted, enlarges the zone where the device is in resonance or near resonance condition, thus increasing the amount of recovered energy.

Regarding power generation for different acceleration regimes, we use an accelerometer to measure the peak acceleration, shown in Figure 10 (points), as a function of engine rotation velocity (the line represents the tendency). By means of this figure, it is possible to obtain the maximum electrical power—see (37)—for different rotational speeds. For example, at 2200 rpm the acceleration is $2.45G$ (Figure 10), and the maximum generation increases to 51 V/G (see Figure 8). For a load resistance of $248 \text{ k}\Omega$, this output represents a harvested peak power as large as 63 mW .

It must be noted that a previous work reported a similar device based on an electromagnetic rather than a piezoelectric harvester [Glynne-Jones et al. 2004]. In that approach, a microgenerator of $21 \text{ mm} \times 15 \text{ mm} \times 10 \text{ mm}$ harnessed a peak power of 3.9 mW , representing a power density of nearly 1.25 mW/cm^3 .

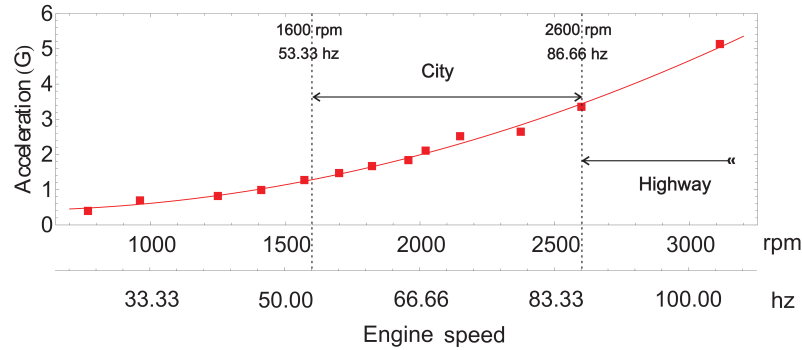


Figure 10. Engine acceleration level based on rpm.

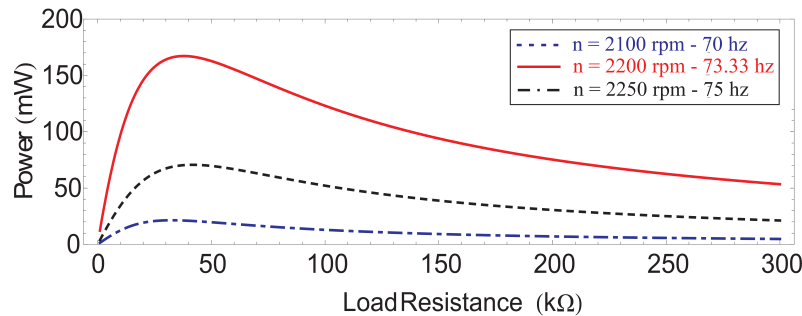


Figure 11. Electrical power as a function of load resistance for each speed measurement.

Our system, on the other hand, collected a power density of 13.5 mW/cm^3 , thus obtaining more than ten times as much. This reveals a high power density in the case of the piezoelectric device (our proposal), in agreement with previous findings [Priya 2007].

Finally, the variation in output power with load resistance R_L for different frequencies of engine rotation near the principal resonance is shown in Figure 11. It can be observed that each rotating speed has a single resistance value which maximizes the output power. For example, maximizing the load resistance at 2200 rpm yields a maximum power of 167 mW with a load resistance of 37.8 kΩ. As soon as other frequencies are considered, this maximum value decreases and the same occurs with the optimum resistance, which is a clear indication of the frequency-dependent nature of this value (see for example [Machado et al. 2015]). The same occurs for the rest of the resonances of Figure 8, indicating that a different optimal resistance can be found for those cases. This clearly suggests that the obtained output power values can be improved by an optimization procedure.

Summing up, sufficient analytical and experimental evidence are presented supporting the reliability of the proposed multimodal device to meet the requirements of energy recovery for different speed conditions, both in the city (low speeds) and highway (high speeds, see Figure 8).

5. Conclusions

In this work, an energy harvesting device that can collect energy in a car for different gear ratios is presented. The structural design provides an alternative to the common cantilever beam type of design

to harvest energy in a range of frequencies between 1600 rpm–4600 rpm, which is the range obtained in a drive test with a conventional diesel car. To this end, a piezoelectric energy harvesting device comprising a piezofiber composite with interdigitated electrodes and two mass-spring systems with large flexibility is proposed. The selected PFCB-W14 (from Advanced Cerametrics Inc.) piezobeam seems to be a good choice for both increasing harvesting energy through the use of the piezoelectric constant d_{33} and providing long fatigue life. In the mechanical design, two spring-mass systems at the ends of the beam are included to introduce multiple modes in a frequency that spans the engine's angular velocities. An analytical model based on Lagrangian formulation is developed and solved to predict the dynamic behavior of the system. In a first step towards its validation, ABAQUS software was used to compare the validity of the analytical predictions. The results show that, even though the analytical model predicted most frequencies and modes, a lateral (off-plane) and a torsional mode remained absent in the formulation due to the inability of the model to capture off-plane (vertical) modes.

A set of experiments at different engine speeds was carried out for the proposed system. The results demonstrate good agreement between analytical, computational, and experimental data, showing the accuracy of the models and the relevance of the mechanical design. As for voltage generation over the frequency bandwidth span by engine rotation, a sustained voltage generation over $10 \text{ V}/G$ is reported for the 1600 rpm–2600 rpm range (city journey), with a predicted maximum output power of 63 mW ($51 \text{ V}/G$) at 2200 rpm. For a highway journey (2600 rpm–4600 rpm), the generation is not so large, except in the vicinity of the third/fifth analytical/experimental mode, where voltage grows considerably. Finally an optimization of the load resistance is sketched, demonstrating that these large values can be also increased by a proper optimization procedure. In summary, the proposed harvesting device largely suffices the energy demand to feed low-power automotive sensors. After a comparison with other similar devices, our piezoelectric-based proposal provides a power density solution ten times larger than its electromagnetic counterpart.

Future research should study a delivery method for the harvested power to a storage device in a continuous and stabilized manner by means of AC-DC and DC-DC converters. Finally, the ultimate validation of the model will take place by mounting the device in a car and rolling it down the streets.

Acknowledgments

The authors wish to thank CONICET, ANPCyT, Departamento de Física UNS, and Secretaría de Ciencia y Tecnología UTN-FRBB.

References

- [Beckert and Kreher 2003] W. Beckert and W. S. Kreher, “Modelling piezoelectric modules with interdigitated electrode structures”, *Comput. Mater. Sci.* **26** (2003), 36–45.
- [Bibo and Daqaq 2013] A. Bibo and M. F. Daqaq, “Energy harvesting under combined aerodynamic and base excitations”, *J. Sound Vib.* **332**:20 (2013), 5086–5102.
- [Bowen et al. 2006] C. R. Bowen, L. J. Nelson, R. Stevens, M. G. Cain, and M. Stewart, “Optimisation of interdigitated electrodes for piezoelectric actuators and active fibre composites”, *J. Electroceram.* **16**:4 (2006), 263–269.
- [Erturk and Inman 2011] A. Erturk and D. J. Inman, *Piezoelectric energy harvesting*, Wiley, New Delhi, India, 2011.
- [Glynne-Jones et al. 2004] P. Glynne-Jones, M. J. Tudor, S. P. Beeby, and N. M. White, “An electromagnetic, vibration-powered generator for intelligent sensor systems”, *Sens. Actuators A Phys.* **110** (2004), 344–349.

- [Hareesh et al. 2012] P. Hareesh, I. Misri, S. Yang, and D. L. DeVoe, "Transverse interdigitated electrode actuation of homogeneous bulk PZT", *J. Microelectromechanical Sys.* **21**:6 (2012), 1513–1518.
- [Harne 2013] R. L. Harne, "Development and testing of a dynamic absorber with corrugated piezoelectric spring for vibration control and energy harvesting applications", *Mech. Syst. Signal Process.* **36**:2 (2013), 604–617.
- [Harne and Wang 2013] R. L. Harne and K. W. Wang, "A review of the recent research on vibration energy harvesting via bistable systems", *Smart Mater. Struct.* **22**:2 (2013), 23001–23012.
- [He and Gao 2013] X.-F. He and J. Gao, "Wind energy harvesting based on flow-induced-vibration and impact", *Microelectron. Eng.* **111** (2013), 82–86.
- [IEE 1988] "IEEE standard on piezoelectricity", IEEE, 1988.
- [Kim et al. 2004] H. W. Kim, A. Batra, S. Priya, K. Uchino, D. Markley, R. E. Newnham, and H. F. Hofmann, "Energy harvesting using a piezoelectric "cymbal" transducer in dynamic environment", *Japan. J. Appl. Phys.* **43**:9A (2004), 6178–6183.
- [Kim et al. 2006] H. Kim, S. Priya, and K. Uchino, "Modeling of piezoelectric energy harvesting using cymbal transducers", *Japan. J. Appl. Phys.* **45**:7 (2006), 5836–5840.
- [Lee et al. 2012] J. Lee, S. Kim, J. Oh, and B. Choi, "A self-powering system based on tire deformation during driving", *J. J. Automot. Technol.* **13**:6 (2012), 963–969.
- [Lin and Ding 2013] H. Lin and K. Ding, "A new method for measuring engine rotational speed based on the vibration and discrete spectrum correction technique", *Measurement* **46**:7 (2013), 2056–2064.
- [Lin et al. 2013] X.-J. Lin, K.-C. Zhou, X.-Y. Zhang, and D. Zhang, "Development, modeling and application of piezoelectric fiber composites", *Trans. Nonferr. Met. Soc. China* **23**:1 (2013), 98–107.
- [Machado et al. 2015] S. P. Machado, M. Febbo, F. Rubio-Marcos, L. A. Ramajo, and M. S. Castro, "Evaluation of the performance of a lead-free piezoelectric material for energy harvesting", *Smart Mater. Struct.* **24**:115011 (2015), 115011, 8 pp.
- [Meirovitch and Parker 2010] L. Meirovitch and R. Parker, *Fundamentals of vibrations*, Waveland Press, Long Grove, IL, 2010.
- [Mohammad et al. 1995] D. R. A. Mohammad, N. U. Khan, and V. Ramamurti, "On the role of Rayleigh damping", *J. Sound Vib.* **185**:2 (1995), 207–218.
- [Nelson et al. 2003] L. J. Nelson, C. R. Bowen, R. Stevens, M. Cain, and M. Stewart, "Modelling and measurement of piezoelectric fibers and interdigitated electrodes for the optimization of piezofibre composites", pp. 556–567 in *Proc. SPIE* (San Diego, California), vol. 5053, 2003.
- [Priya 2007] S. Priya, "Advances in energy harvesting using low profile piezoelectric transducers", *J. Electroceram.* **19** (2007), 167–184.
- [Ramirez et al. 2017] J. M. Ramirez, C. D. Gatti, S. P. Machado, and M. Febbo, "An experimentally validated finite element formulation for modeling 3D rotational energy harvesters", *Eng. Struct.* **153** (2017), 136–145.
- [Rao 2007] S. S. Rao, *Vibration of continuous systems*, Wiley, 2007.
- [Ren et al. 2010] B. Ren, S. W. Or, X. Zhao, and H. Luo, "Energy harvesting using a modified rectangular cymbal transducer based on $0.71\text{Pb}(\text{Mg}_{1/3}\text{Nb}_{2/3})\text{O}_3-0.29\text{PbTiO}_3$ single crystal", *J. Appl. Phys.* **107**:034501 (2010).
- [Rezaei-Hosseinabadi et al. 2016] N. Rezaei-Hosseinabadi, A. Tabesh, and R. Dehghani, "A topology and design optimization method for wideband piezoelectric wind energy harvesters", *IEEE Trans. Ind. Electron.* **63**:4 (2016), 2165–2173.
- [Roundy 2008] S. Roundy, "Energy harvesting for tire pressure monitoring systems: design considerations", pp. 9–12 in *Proc. of PowerMEMS+microEMS* (Sendai, Japan), 2008.
- [Sadeqi et al. 2015] S. Sadeqi, S. Arzanpour, and K. H. Hajikolaie, "Broadening the frequency bandwidth of a tire-embedded piezoelectric-based energy harvesting system using coupled linear resonating structure", *IEEE/ASME Trans. Mechatron.* **20**:5 (2015), 2085–2094.
- [Shigley 1972] J. E. Shigley, *Mechanical engineering design*, McGraw-Hill, 1972.
- [Uchino 1997] K. Uchino, *Piezoelectric actuators and ultrasonic motors*, Kluwer Academic Publishers, 1997.
- [Van Blarigan et al. 2015] L. Van Blarigan, J. Moehlis, and R. McMeeking, "Low dimensional modeling of a non-uniform, buckled piezoelectric beam for vibrational energy harvesting", *Smart Mater. Struct.* **24**:6 (2015), 65012–65021.

- [Wang et al. 2010] Y.-J. Wang, C.-D. Chen, and C.-K. Sung, “Design of a frequency-adjusting device for harvesting energy from a rotating wheel”, *Sens. Actuators A Phys.* **159**:2 (2010), 196–203.
- [Wang et al. 2013] Y.-J. Wang, C.-D. Chen, and C.-K. Sung, “System design of a weighted-pendulum-type electromagnetic generator for harvesting energy from a rotating wheel”, *IEEE/ASME Trans. Mechatron.* **18**:2 (2013), 754–763.
- [Weaver Jr. et al. 1990] W. Weaver Jr., S. P. Timoshenko, and D. H. Young, *Vibration problems in engineering*, Wiley, 1990.
- [Xiao and Wang 2014] H. Xiao and X. Wang, “A review of piezoelectric vibration energy harvesting techniques”, *International Review of Mechanical Engineering (IREME)* **8**:3 (2014), 609–620.
- [Xu et al. 2013] T.-B. Xu, E. J. Siochi, J. H. Kang, L. Zuo, W. Zhou, X. Tang, and X. Jiang, “Energy harvesting using a PZT ceramic multilayer stack”, *Smart Mater. Struct.* **22**:6 (2013), 65015–65029.
- [Zhang et al. 2007] Y. Zhang, K. Huang, F. Yu, Y. Gu, and D. Li, “Experimental verification of energy-regenerative feasibility for an automotive electrical suspension system”, pp. 1–5 in *IEEE Int. Conf. Veh. Electronics and Safety*, 2007.
- [Zhang et al. 2012] G. Zhang, J. Cao, and F. Yu, “Design of active and energy-regenerative controllers for DC-motor-based suspension”, *Mechatronics* **22**:8 (2012), 1124–1134.
- [Zhu et al. 2010] D. Zhu, M. J. Tudor, and S. P. Beeby, “Strategies for increasing the operating frequency range of vibration energy harvesters: a review”, *Measurement Sci. Technol.* **21**:2 (2010), 22001–22029.
- [Zuo and Zhang 2013] L. Zuo and P.-S. Zhang, “Energy harvesting, ride comfort, and road handling of regenerative vehicle suspensions”, *J. Vib. Acoust. (ASME)* **135**:1 (2013), 110021–110028.

Received 24 May 2017. Revised 19 Oct 2017. Accepted 20 Nov 2017.

CLAUDIO D. GATTI: cdgatti@frbb.utn.edu.ar

Grupo de Investigación en Multifísica Aplicada (GIMAP), Universidad Tecnológica Nacional, Bahía Blanca, Argentina

JOSÉ M. RAMIREZ: josemramire@gmail.com

Grupo de Investigación en Multifísica Aplicada (GIMAP), Universidad Tecnológica Nacional, Bahía Blanca, Argentina

MARIANO FEBBO: mfebbo@uns.edu.ar

Instituto de Física del Sur (IFISUR) and Departamento de Física, Universidad Nacional del Sur, Bahía Blanca, Argentina

SEBASTIÁN P. MACHADO: smachado@frbb.utn.edu.ar

Grupo de Investigación en Multifísica Aplicada (GIMAP), Universidad Tecnológica Nacional, Bahía Blanca, Argentina

NUMERICAL AND EXPERIMENTAL STUDY ON INCREMENTAL FORMING PROCESS OF AL/CU BIMETALS: INFLUENCE OF PROCESS PARAMETERS ON THE FORMING FORCE, DIMENSIONAL ACCURACY AND THICKNESS VARIATIONS

MOHAMMAD HONARPISHEH, MORTEZA KEIMASI AND IMAN ALINAGHIAN

In the present study, a finite element method was carried out on the single point incremental forming process of explosive-welded Al/Cu bimetal. The effect of process parameters, such as the tool diameter, vertical pitch, sheet thickness, pyramid angle, and process strategies, were investigated on the forming forces, dimensional accuracy, and thickness distribution of a truncated pyramid with FEM approaches. The results obtained from the simulation were validated by experiments. The findings indicated that by increasing the tool radius and vertical pitch size, the forming force increases and the wall thickness decreases. The finite element prediction for forming force, thickness distribution, and process strategies shown good agreement with experiments.

1. Introduction

Single point incremental forming (SPIF) is a manufacturing process whereby a metal sheet is locally deformed by series of incremental tool movements using predefined paths. The main components of a SPIF process are these: blank, blank holder, backing plate, and forming tool. This process requires a computerized forming machine such as a CNC milling machine to allow the forming tool to move along the desired path. The SPIF process is suitable for manufacturing sheet metal components for small class production or prototyping [Jeswiet et al. 2005; Mulay et al. 2017]. Manco and Ambrogio [2010] present the principal of SPIF. There are many studies on SPIF; among them is [Bao et al. 2015], where the authors investigated the formability and microstructure of AZ31B alloy in an electropulse-assisted incremental forming process. The tool diameter can highly affect failure during SPIF process; Silva et al. [2011] investigated it by forming the limit curve for a AA1050-H11 sheet. Hirt et al. [2004] presented various forming strategies to find the maximum possible wall angle and minimum geometric deviations. Reddy and Cao [2009] proposed two types of incremental forming in terms of positive and negative incremental forming, whereby negative incremental forming refers to SPIF and positive incremental forming refers to two point incremental forming. Martins et al. [2008] presented a theoretical model for tool radius to show the stress state in a SPIF process. Yamashita et al. [2008] showed that a spiral tool path provides a better wall thickness distribution. Obikawa et al. [2009] investigated the effect of a high tool rotational speed on the SPIF of aluminum foils. Thibaud et al. [2012] did a simulation on a SPIF process. They found that the forces obtained by FEM confirms measured values from experiments. Arfa et al. [2013] demonstrated the effect of process parameters on the forming forces, mechanical properties, and geometrical accuracy of SPIF parts. Petek et al. [2009] investigated the impact of the wall angle, tool rotational speed, tool step

Keywords: incremental sheet forming, force, dimensional accuracy, explosive welding, FEM.

alloy	chemical compositions (wt. %)						
	Cu	Mn	Si	Mg	Zn	Fe	Al
Al-1050	0.0292	0.0177	0.101	0.0169	0.0158	0.479	base
C-10100	99.99	< 0.0002	< 0.0004	< 0.0001	0.00042	0.0032	0.001

alloy	mechanical properties	
	hardness Vickers (Hv)	yield stress (MPa)
Al-1050	26.1	39.5
C-10100	54.3	137

Table 1. Chemical compositions and mechanical properties of Al-1050 and Copper (C-10100).

size, tool diameter, and lubrication on the forming force and plastic strain. Cui et al. [2013] used new mathematical models, such as hyperbolic cone, skew cone, and elliptical cone, to model and validate the deformation process of incremental sheet forming. Capece Minutolo et al. [2007] evaluated the maximum slope angle of simple geometries in the incremental forming process. They investigated the maximum slope angle of frustums of a pyramid and a cone. They used the FE code to have an instrument evaluate the limits of the process in regards to the geometry of the manufacturing product. Centeno et al. [2014] studied the critical analysis of necking and fracture limit strains and forming forces in single point incremental forming. Ambrogio et al. [2004] investigated the influence of the process parameters on the accuracy through a reliable statistical analysis. Honarpisheh et al. [2016a] studied experimentally and numerically of the hot incremental forming of a Ti-6Al-4V sheet using electrical current.

Explosive-welded materials are new materials which are used in different sectors, such as aerospace and food industries. Many researches have been done on the explosive welding process. Performing the postprocess on the explosive-welded multilayers is an attractive field for new researches. The effect of cold rolling [Honarpisheh et al. 2016b; Asemabadi et al. 2012] and heat treatment [Akbari Mousavi and Sartangi 2008; Honarpisheh et al. 2012] have been performed on the explosive-welded multilayers. Al/Cu multilayers are one of the materials which are investigated in some researches [Ashani and Bagheri 2009; Gulenc 2008; Sedighi and Honarpisheh 2012a; 2012b].

To the best of authors' knowledge, experimental and numerical investigations of the incremental forming process has not been reported on explosive-welded Al/Cu bimetal so far. Therefore, in the current research, the incremental forming of a truncated pyramid is studied in Al/Cu bimetal. After validating the numerical results by the experiments, the process parameters, such as pyramid angles, tool radius, sheet thickness, vertical pitch, and process strategies, were investigated.

2. Materials and method

In the current research, a parallel arrangement was used for the experimental group of explosive-welded aluminum (Al-1050) and copper (C-10100). Chemical composition and some of the mechanical properties of these materials are given in Table 1.

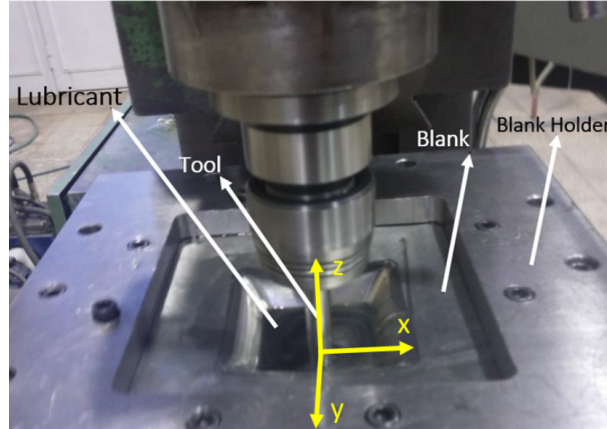


Figure 1. Incremental forming components.

A blank holder, backing plates, forming tools, and a CNC milling machine were utilized in this study. The experiments were carried out on a 3-axes CNC machine. A cylindrical punch, with a hemispherical head, was used as the tool (one-point incremental forming). The tool diameters were 10 mm and 16 mm and were made of steel Mo40 in this study. The truncated pyramids with dimensions of 72 mm × 72 mm with a 60° angle were formed in order to find the maximum depth equal to 40 mm. According to the designed equipment, square sheets (135 mm × 135 mm × 1.2 mm), were utilized during tests. The thicknesses of explosive-welded Al/Cu bimetal in the Al and Cu sheets were 0.8 mm and 0.4 mm, respectively. Figure 1 presents the used experimental setup in this study. In addition, sheet arrangement was not considered as a process parameter so a specific side of the sheet is selected for all experiments, however in future work this parameter can be studied as well. In the present study, the aluminum side of the bimetal is always in contact with the forming tool and deformation starts from that side.

In order to simulate the drawing process by finite element analysis, some of the parameters have been measured in different types of tests. In order to obtain the stress-strain curves of the used bimetal, the uniaxial tensile test performed based on ASTM-E8M standard. The tensile test was performed with a constant speed of 5 mm/min. Figure 2 illustrates the stress-strain curves of bimetal. The yield and tensile strength were 170.8 MPa and 187.2 MPa, respectively. The Coulomb friction coefficient between the tool and the sheet was equal to 0.1–0.3. These values were obtained by the experiments tests using the dynamometer forces

$$\mu = \frac{|F_h|}{|F_v|} = \frac{\sqrt{F_x^2 + F_y^2}}{F_z}, \quad (1)$$

where F_h , F_v , F_y , F_z are the horizontal force, vertical force (along forming tool axis), reaction force along x direction, reaction force along y direction, and reaction force along z direction, respectively (see Figure 1).

The spiral tool path is used to obtain the suitable strain distribution, (see Figure 3).

Lubricant was also used during the forming process to keep the temperature down at the proposed speed and stop galling as well as reducing the friction between the part and the tool. After fastening the

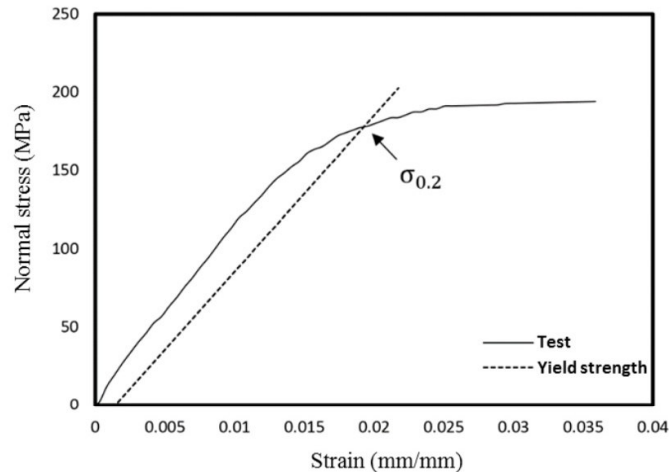


Figure 2. Stress-strain curves of explosive-welded Al/Cu bimetal before the process.

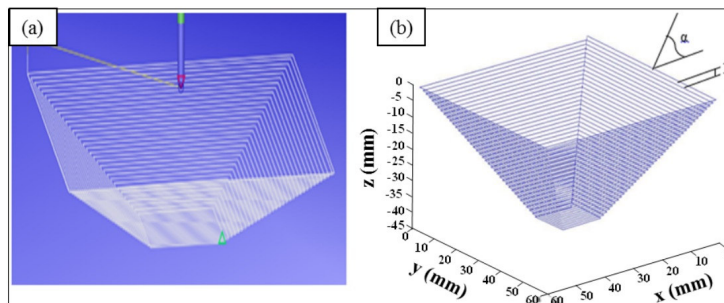


Figure 3. Schematic showing the tool path: (a) CAM software, (b) generated in the math software.

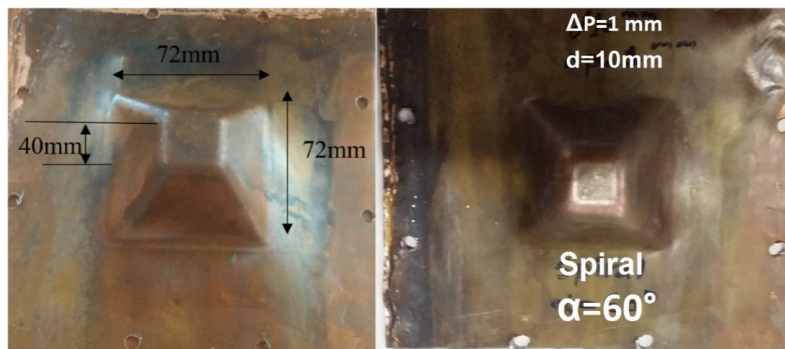


Figure 4. The formed truncated pyramid with wall angle 60° , vertical pitch 1 mm and tool diameter of: (a) 16 mm and (b) 10 mm.

blank and starting the CNC machine, the tool pushes the blank down, according to the predefined spiral path, until it reaches the maximum depth of 40 mm (see Figure 4).

tool diameters (d)	10 mm, 16 mm
vertical pitch (p)	1 mm
initial Thickness (t)	1.2 mm, 1.5 mm, 1.8 mm
rotation speed	600 rpm
height (H)	40 mm
major base	72 mm
wall angle (α)	55°, 60°, 65°
feed rate for horizontal direction (f_h)	1000 mm/min
feed rate for vertical direction (f_v)	500 mm/min

Table 2. The process parameters and geometry.

A dynamometer was used including KISTLER-9257B with six-component force sensor and a KISTLER-5017A 8 channel charge amplifier. The measuring system also includes data acquisition cards and a PC. The sampling rate of force measurement was 50 Hz. Finally, the used process parameters are summarized in Table 2. Moreover, there were two hemisphere tools with diameters (denoted by d) 10 mm and 16 mm. The wall angle of the truncated pyramid is denoted by α , which varies between 55° to 65°. Initial thickness (t) refers to thickness of the sheets before the forming process. Vertical pitch (p) is the amount of each step along z direction.

3. FEM procedures

The simulation process was performed using Abaqus finite element software. Both the explicit and implicit method can be used for this solution. However, the implicit solution showed better conformance with experimental results. On the other hand, much more computation time is required even for forming a simple shape and short tool path in implicit mode. Jeswiet et al. [2005] showed that the explicit solution needs less analysis time, and since it produces acceptable results and is suitable for generating the applicable curves, hundreds of solutions were required. In the current study, the explicit solver is employed during the entirety of FE analysis. The tool and blank holder were considered to be rigid (analytical rigid). The behavior of the stress-strain of explosive-welded Al/Cu bimetal is modeled in Figure 2. The holder was fixed and the tool can only move along the three main axes, i.e., x , y , and z along the programmed spiral path. The spiral tool path is defined in the developed VDISP subroutine; the feed rates for the horizontal direction and vertical direction were respectively 1000 mm/min and 500 mm/min.

4. Results and discussion

In this section, the numerical model and experimental results for the forming force and thickness distribution are compared. Then, the process parameters and machining strategies are numerically analyzed.

4.1. Validation the numerical model. The mesh sensitivity analysis was performed to obtain the best mesh size (see Figure 5). As it can be seen, the vertical force is relatively constant after the element number is greater than 2000.

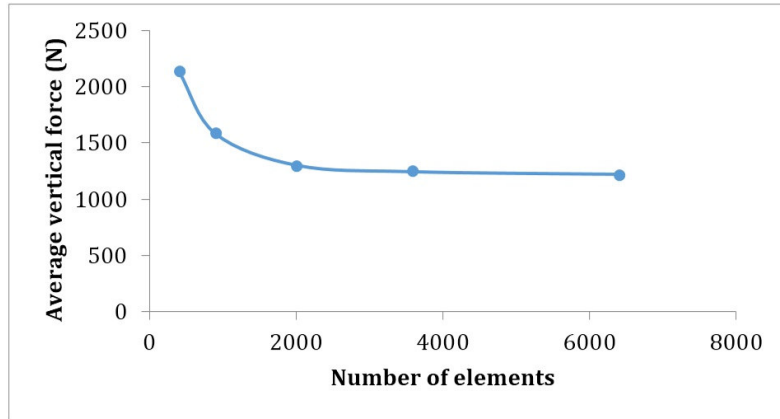


Figure 5. Mesh sensitivity analysis.

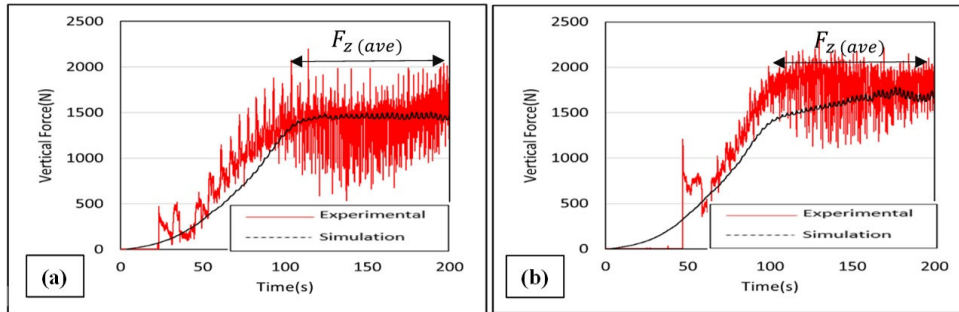


Figure 6. Experimental and numerical results of vertical force for tool diameter of: (a) 10 mm and (b) 16 mm.

To validate the numerical results, the results of the vertical forces for two diameters of forming tool are presented in Figure 6. The constant parameters are these: bimetal thickness of 1.2 mm, vertical pitch of 1 mm, and pyramid angle of 60° .

The average vertical force is useful for comparison purposes: it is calculated by taking the average of all measured or calculated F_z at a steady region (see Figure 6). The average vertical force ($F_{z(ave)}$) for a tool diameter of 10 mm for the numerical and experimental results are 1464 N and 1357 N, respectively. Moreover, the average vertical forces are 1636 N and 1730 N for a tool diameter of 16 mm using FEM and experimental approaches, respectively. The maximum error for the two presented cases is equal to 9.6%, which demonstrates the suitability of FEM for predicting the forming force.

The experimental, theoretical, and numerical formed profiles are presented in Figure 7. The deviation is due to the difference of the resultant profile or thickness from the reference state, and it can be named as an error. Moreover, the reference or theoretical state refers to a desired position where a component is expected to find the plate. Thus, the maximum deviation of the experimental and FEM results is less than 10%. Also, the thickness distribution of the formed bimetal is presented in Figure 8. The experimental profile has been measured by the help of a coordinate measuring machine (CMM).

The error between FEM and experimental results is lower than 6% in the thickness distribution.

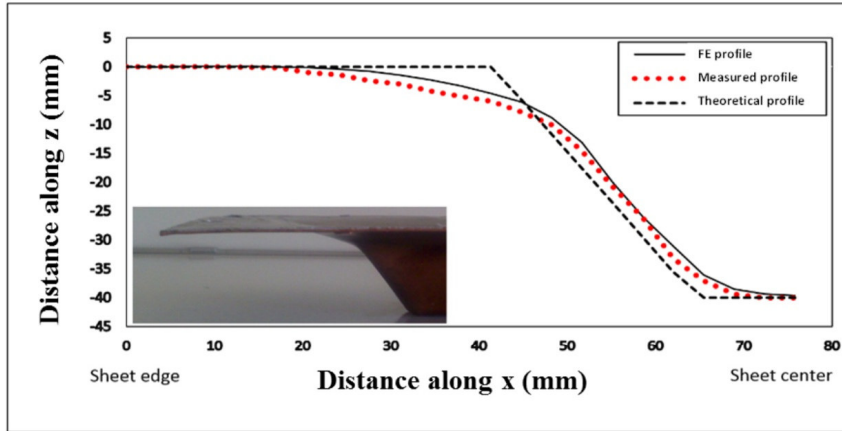


Figure 7. Comparison of the experimental, theoretical, and numerical profile for $d = 16$ mm, $p = 1$ mm, $\alpha = 60^\circ$.

4.2. FEM results of process parameters. After validating the finite element model and in order to investigate the effects of process parameters, the numerical results are presented in this section. The depth of the formed pyramids is equal to 40 mm. The starting base side of pyramids is 72 mm and the minor size of the samples depends on the value of wall inclination angle α .

Two tools with 10 mm and 16 mm diameters were used in the FEM analysis. The wall angle of the truncated pyramid was 60° and vertical pitches of 0.25 mm and 1 mm were compared together. The FEM results of vertical force and thickness distribution are presented in Figures 9 and 10.

As it can be observed in Figure 9(a), vertical forces are at a maximum for a vertical pitch of 0.25 mm when tool diameter is 16 mm, and it can be inferred that the bigger tool requires greater force in smaller pitch size. Moreover, Figure 9(b) indicates that the maximum vertical force for the vertical pitch of 1 mm is greater compared to the 0.25 mm one and it is about 2 kN. This means that a greater tool diameter and vertical pitch provide greater a reaction force. It also can be seen in Figure 10 that the thicker plate can be obtained by incremental forming using a forming tool with 10 mm diameter. This means that the lower tool diameter creates thicker parts, which is a good piece of knowledge to improve part thickness during SPIF. The two step down are presented in Figure 11.

The effect of vertical pitch on the vertical force is presented in Figure 12. It can be seen that the vertical force is greater for a tool diameter of 10 mm and a vertical pitch of 1 mm. Therefore, it is inferred that the greater tool diameter and smaller vertical pitch provides lower vertical forming force in SPIF process for the Al/Cu bimetal.

The thickness distribution for each case is seen in Figure 13. Results show that by increasing the vertical pitch, the forming force increases and the thickness distribution is more uniform, which means that a thicker SPIF part can be achieved.

The effect of the initial thickness of the bimetal on the forming force is presented in Figure 14. As could be expected, the forming force is increased by increasing the initial thickness of the bimetal. The effect of wall angles on the vertical force is presented in Figure 15. The process has been modeled at 55° , 60° , and 65° wall angles.

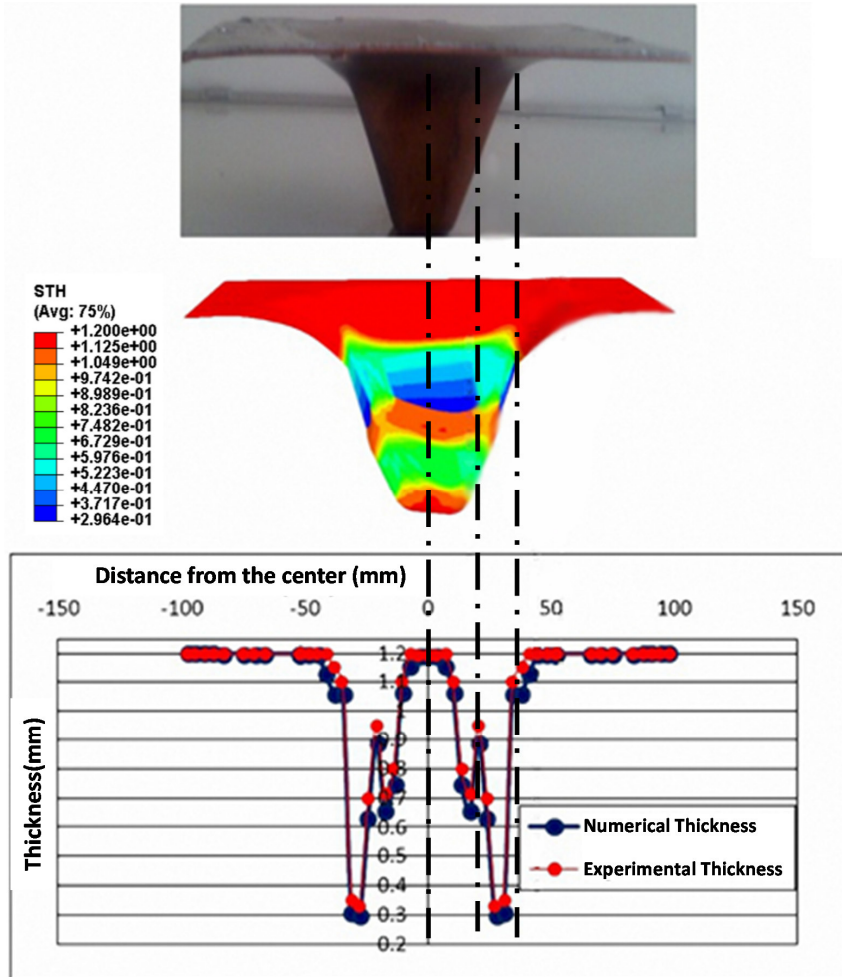


Figure 8. Comparison of the experiment and numerical thickness for $d = 16$ mm, $p = 1$ mm, $\alpha = 60^\circ$.

4.3. Effect of process strategies on dimensional accuracy and thickness distribution. The geometrical accuracy of the final products is an important issue for industrial products, especially for SPIF products. However, the nature of the SPIF process makes it difficult to achieve a high level of geometrical accuracy. Besides, different process strategies may help to achieve a high level of geometrical accuracy.

In this section, the effect of attaching a backing plate and a kinematic support as process strategies on the geometrical accuracy are investigated by FEM. The process parameters of 16 mm tool diameter, 60° wall angle, vertical pitch of 1 mm, and bimetal thickness 1.2 mm are considered for the all strategies. The process strategies are as the following:

- (1) The SPIF with a backing plate.
- (2) The SPIF without a backing plate
- (3) A counter tool is used in addition to the backing plate (see Figure 16).

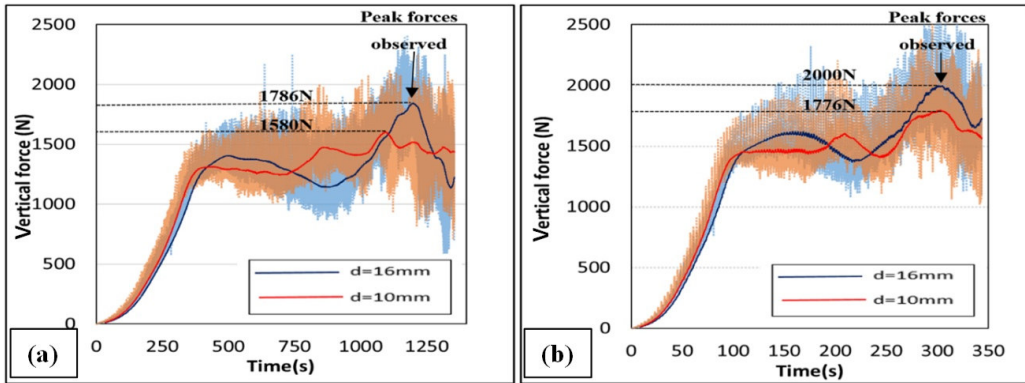


Figure 9. Vertical forces including their mean values using FEM for two tool diameters and vertical pitches of: (a) 0.25 mm (b) 1 mm.

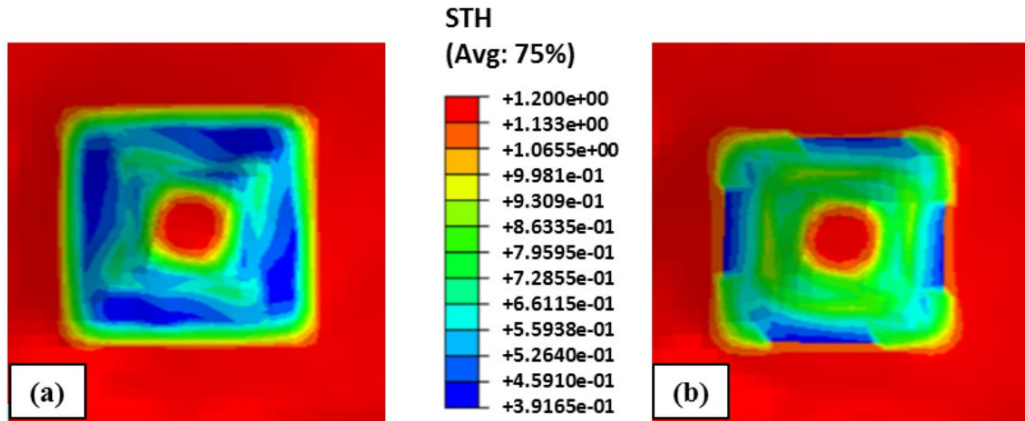


Figure 10. Thickness distributions in the vertical pitch 1 mm for tool diameter of: (a) 10 mm and (b) 16 mm.

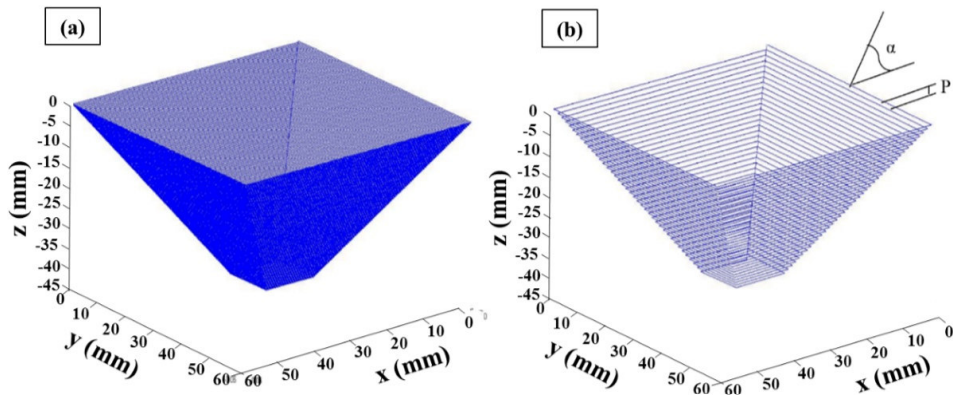


Figure 11. Tool path with step down: (a) 0.25 mm; (b) 1 mm.

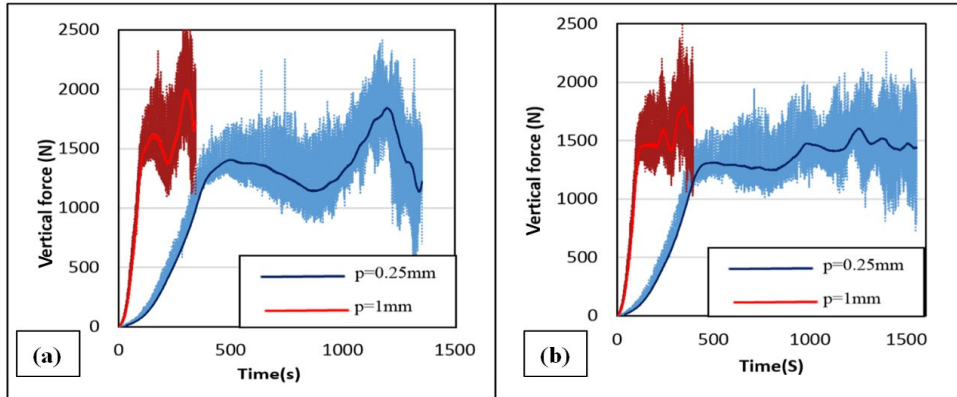


Figure 12. The effect of vertical pitches on the average vertical force in tool diameters: (a) 10 mm; (b) 16 mm.

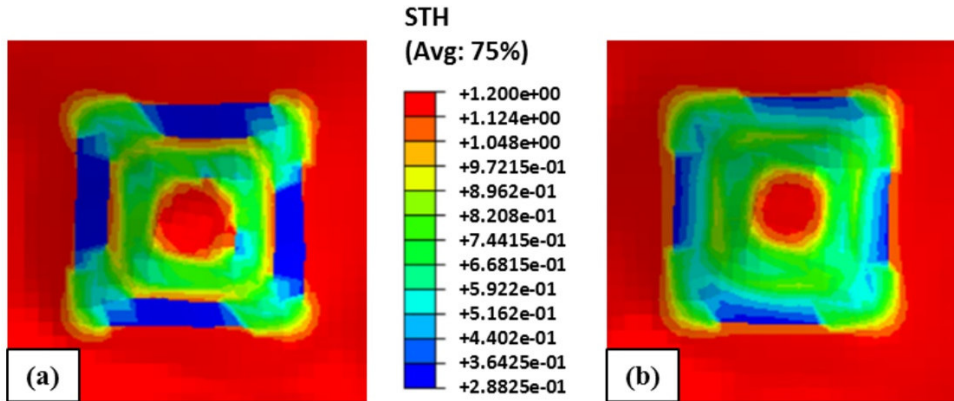


Figure 13. Thickness distributions for tool diameter 16 mm for vertical pitches: (a) 0.25 mm (b) 1 mm.

In the third strategy, a supporting counter tool is used in spite of the backing plate. The forming tool and the counter tool act in a synchronized motion and gradually form the blank sheet into the desired shape, as shown in Figure 16. The counter tool has the same geometry and dimension as the forming tool. It is modeled as a rigid body and its boundary condition is defined so that it moves in a synchronized motion with the forming tool in the XY plane and is always in contact with the bottom surface of the sheet. Surface to surface contact between the counter tool and the bottom surface of the sheet is defined and Coulomb friction is set with a friction coefficient of 0.06.

Geometrical accuracy can be represented with geometrical errors as long as the errors are at a minimum the accuracy is at a maximum. The geometrical errors are evaluated as the distance between the theoretical and FEM profiles [Micari et al. 2007]. According to this definition, two measures e_b and e_s are used to represent the geometry deviation (see Figure 17). The deviation at the upper edge is given by e_b , which represents the geometrical error resulting from the sheet bending. The deviation at the minor base is shown by e_s , which represents the sheet lifting from spring back.

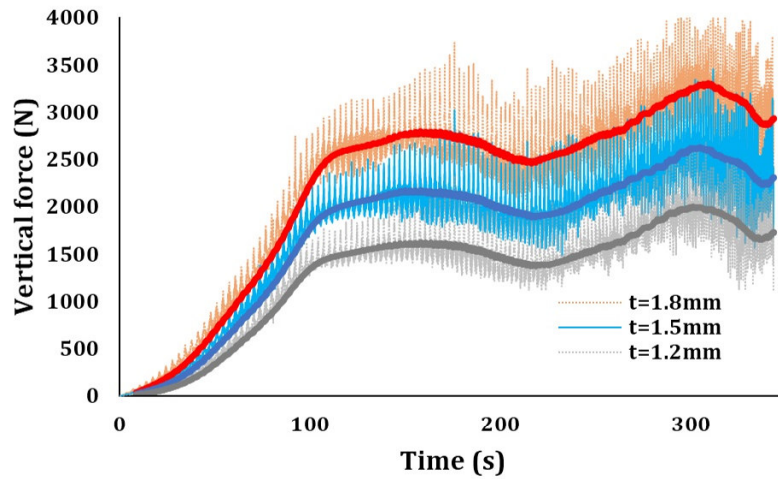


Figure 14. The effect of bimetal thickness on the vertical force curve ($d = 16$ mm, $p = 1$ mm, $\alpha = 60^\circ$).

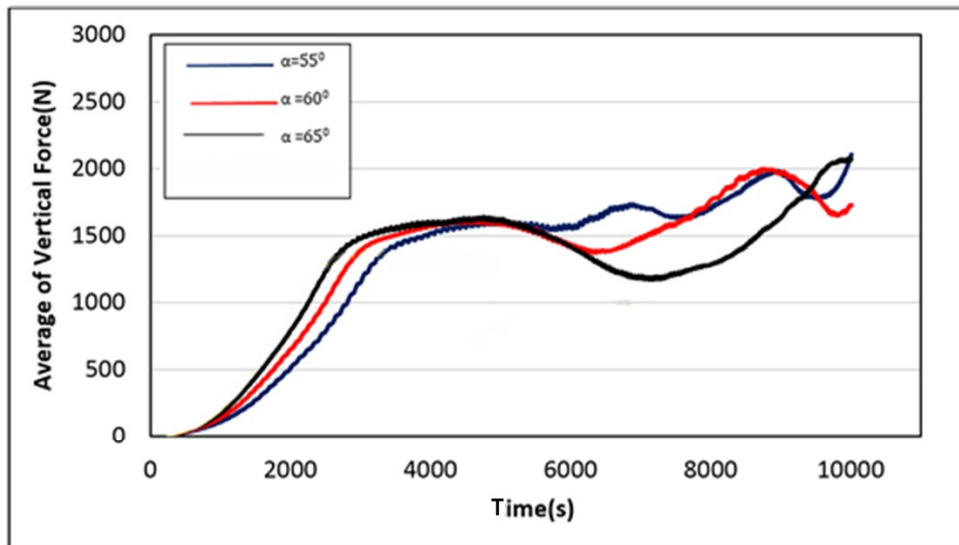


Figure 15. The effect of wall angles on the average vertical force; tool diameter (d) = 16 mm, vertical pitch (p) = 1 mm, initial thickness (t) = 1.2 mm.

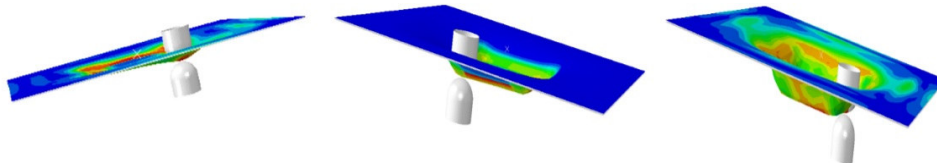


Figure 16. The configuration of the FE model of strategy 3.

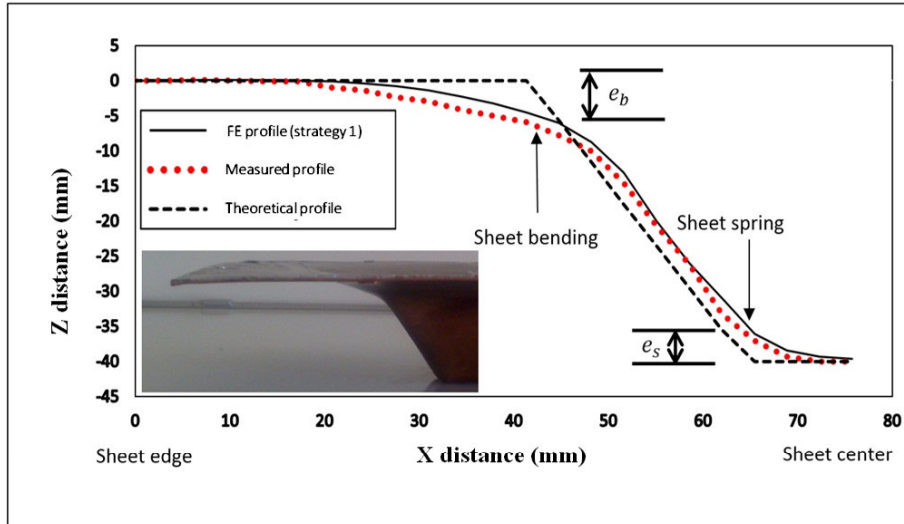


Figure 17. Deformed profile of the 60° truncated pyramid.

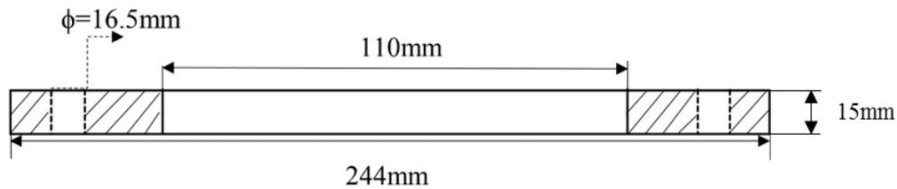


Figure 18. Dimensions (mm) and geometries of the designed backing plate.

Figure 18 shows the geometry and dimensions of the backing plate used for the truncated pyramid. All fixture components including backing plate except screws were made from CK45 steel.

The obtained values of e_b and e_s for Strategy (1) are 4.58 mm and 3.91 mm, respectively. The thickness distribution along the central plane of the deformed sheet is shown in Figure 8. It can be seen that sheet thinning increases as the truncated pyramid depth increases. At a certain point near the pyramid base, less thinning is apparent and the thickness is very close to its original value. This would be expected in Strategy (1). The reason for less thinning near the pyramid base might be that the actual slope angle is smaller than its target value due to the bending effect around the pyramid base. There is a good agreement between the FEM and the measured thickness variation.

Elastic spring back will occur locally during deformation and globally after the forming process. The resulting spring back from postprocessing, such as trimming, has not been considered in the present work. The local spring back could be reduced by using static dies as well [Franzen et al. 2008].

The elimination of the backing plate in second strategy reduces the supporting structure and maximizes this distance. Strategy (2) can illustrate the effect of the backing plate on geometrical deviations, in which deviation is the sheet bending at the major base. Figure 19 shows a comparison between Strategy (1) and (2) to indicate the impact of the backing plate on the final profile. It can be seen that the profile deviation

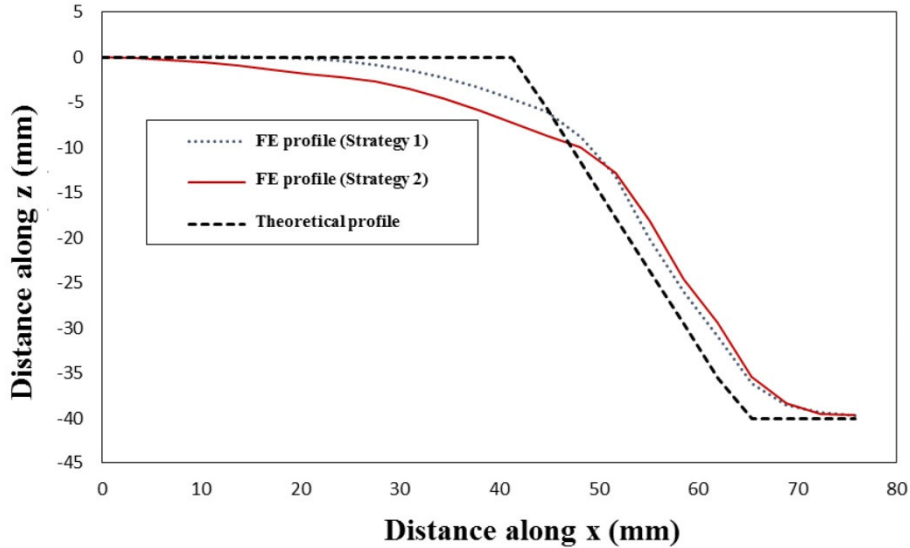


Figure 19. Effect of the backing plate on the final profile.

for Strategy (1) is less than for Strategy (2). This means Strategy (1) provides higher geometrical accuracy compared to Strategy (2).

In Strategy (3), both the counter tool and the backing plate have been used, as suggested in [Franzen et al. 2008]. In this strategy, the forming tool and the counter tool move simultaneously and incrementally form the blank sheet into the desired shape, as shown in the Figure 16. The supporting tool has the same dimensions and shape as the forming tool. Surface to surface contact was considered between the tools and sheet surfaces using Coulomb friction with a friction coefficient of 0.2.

In order to illustrate the effect of the counter tool on the geometrical errors, a comparison was performed between Strategy (1) and (3); see Figure 20. At the major base and sheet center of the truncated pyramid, there is difference between Strategy (1) and (3), which means that the kinematic supporting tool affects either the sheet bending or the spring back effect. Also it can be seen that Strategy (3) provides better geometrical accuracy compared to Strategy (1).

A significant increase in the sheet bending around the major base is obtained by Strategy (2). The backing plate can increase the sheet rigidity by introducing extra support located at the deformation zone. The results show that e_b , increases from 4.58 mm to 7.28 mm, while e_s is found to be 4.63 mm. This suggests that the backing plate can only reduce the deviation resulting from the bending effect and it cannot affect on the deviation resulting from the sheet spring back. In Strategy (3), along the pyramid wall until the minor base, there is a significant reduction in sheet spring back as a result of adding a new kinematic tool. The results show that only e_s reduces from 3.91 mm to 2.53 mm by Strategy (3). The kinematic supporting tool provides a larger localization of the deformation around the forming tool head and it also reduces the local spring back. In addition, the pyramid wall created from Strategy (3) is close to the theoretical profile and the sheet lifting of the minor base of the truncated pyramid is less than that in Strategy (2). Figure 21 shows the typical values for the different deviation measurements gained from the three strategies. The best geometrical accuracy is obtained using the Strategy (3), which includes adding a backing plate and a counter tool.

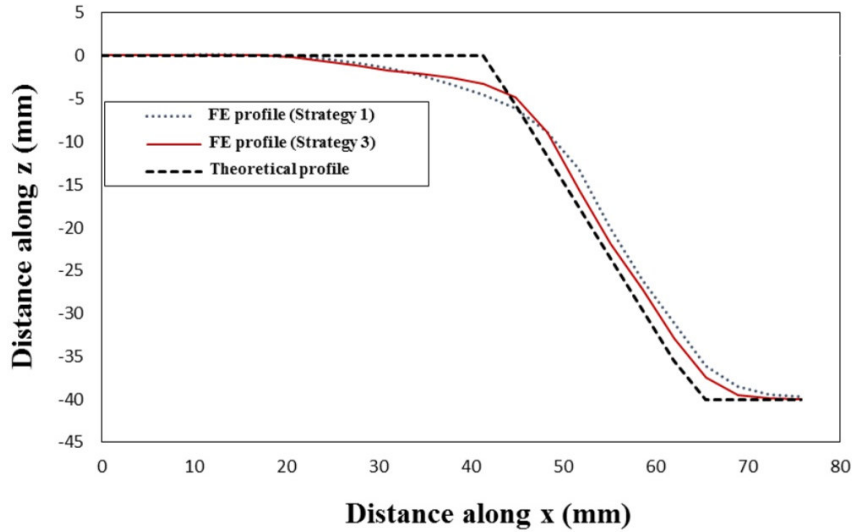


Figure 20. Effect of the kinematic supporting tool on the final profile.

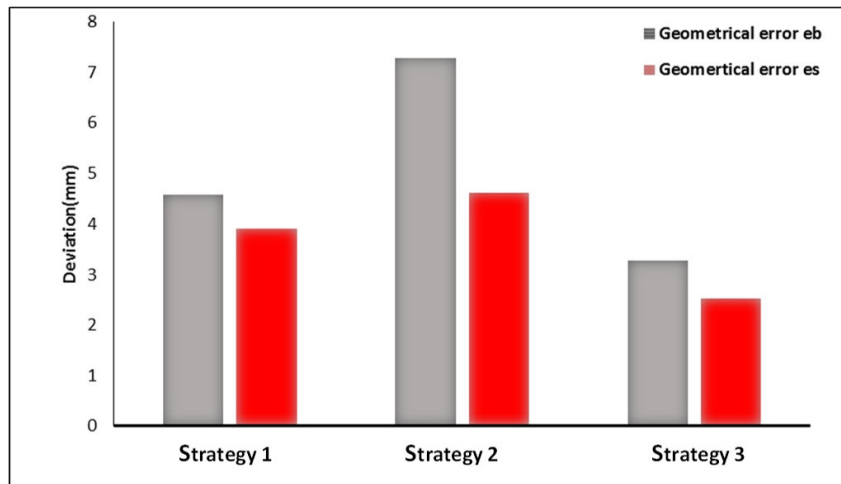


Figure 21. Summary of deviations obtained from the three strategies.

Figure 22 shows a comparison among the strategies for the vertical displacement at the end of the process, when the forming tool reaches the base of the pyramid. Figure 22(a) shows vertical displacement distribution for Strategy (1). It can be seen that there is no wrinkling for Strategy (3) (see Figure 22(c)). Moreover, SPIF with Strategy (2) produces higher wrinkling compared to other strategies.

5. Conclusion

In this study, the effects of process parameters of single point incremental forming of explosive-welded Al/Cu bimetal sheets have been numerically and experimentally investigated. The results of a truncated

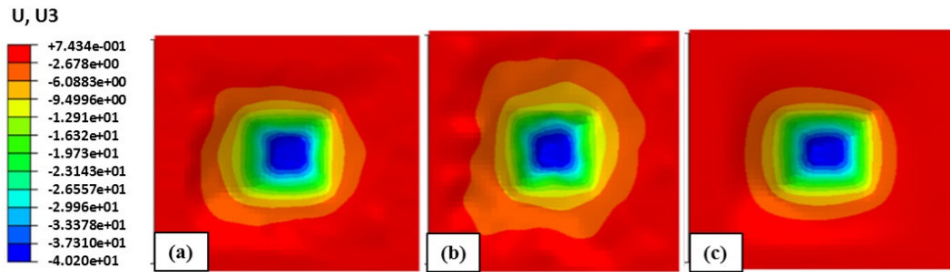


Figure 22. Contour plots for vertical distance distribution in (a) Strategy (1) (b) Strategy (2) (c) Strategy (3) of a truncated pyramidal geometry.

pyramid with depth 40 mm have been obtained for various tool diameters, vertical pitches, sheet thicknesses, pyramid wall angles, and process strategies to generate applied curves for the effective parameters on forming force, thickness distribution, and dimensional accuracy. The results are summarized in the following:

- The vertical force decreases by decreasing the tool diameter from 16 mm to 10 mm.
- The forming force increases by increasing the vertical pitch from 0.25 mm to 1 mm.
- At the beginning of SPIF process (i.e., transient region), the vertical force increases by increasing the wall angle from 55° to 65° and it gradually acts in different way: by increasing the slope angle, the force decreases (on average) when the forming tool enters the steady region.

In the second part of the work, a number of strategies were compared. In this investigation, three FE simulations of the considered process were performed for the truncated pyramidal models. For the forming of a truncated pyramid, the effects of different process strategies (i.e., the elimination of a backing plate and the addition of a kinematic supporting tool) on the geometrical accuracy were investigated. This study demonstrated the following:

- The elimination of a backing plate caused the increasing in the region closer to the major base.
- Existence a counter tool declined the deviation at the major base.
- In the strategy 3 with using a backing plate and counter tool reduced the deviation in product profile.
- In the study of a truncated pyramid, the geometrical deviations could be reduced from 7.28 mm and 4.63 mm to 3.21 mm and 2.53 mm at the major base and minor base respectively.

Acknowledgements

The authors are grateful to University of Kashan for supporting this work by giving research grant No. 682580/6.

References

- [Akbari Mousavi and Sartangi 2008] S. A. A. Akbari Mousavi and P. F. Sartangi, "Effect of post-weld heat treatment on the interface microstructure of explosively welded titanium-stainless steel composite", *Mater. Sci. Eng. A* **494**:1-2 (2008), 329–336.

- [Ambrogio et al. 2004] G. Ambrogio, I. Costantino, L. De Napoli, L. Filice, L. Fratini, and M. Muzzupappa, "Influence of some relevant process parameters on the dimensional accuracy in incremental forming: a numerical and experimental investigation", *J. Mater. Process. Technol.* **153-154** (2004), 501–507.
- [Arfa et al. 2013] H. Arfa, R. Bahloul, and H. BelHadjSalah, "Finite element modelling and experimental investigation of single point incremental forming process of aluminum sheets: influence of process parameters on punch force monitoring and on mechanical and geometrical quality of parts", *Int. J. Mater. Form.* **6:4** (2013), 483–510.
- [Asemabadi et al. 2012] M. Asemabadi, M. Sedighi, and M. Honarpisheh, "Investigation of cold rolling influence on the mechanical properties of explosive-welded Al/Cu bimetal", *Mater. Sci. Eng. A* **558** (2012), 144–149.
- [Ashani and Bagheri 2009] J. Z. Ashani and S. M. Bagheri, "Explosive scarf welding of aluminum to copper plates and their interface properties", *Materialwiss. Werkst.* **40:9** (2009), 690–698.
- [Bao et al. 2015] W. Bao, X. Chu, S. Lin, and J. Gao, "Experimental investigation on formability and microstructure of AZ31B alloy in electropulse-assisted incremental forming", *Mater. Des.* **87** (2015), 632–639.
- [Capece Minutolo et al. 2007] F. Capece Minutolo, M. Durante, A. Formisano, and A. Langella, "Evaluation of the maximum slope angle of simple geometries carried out by incremental forming process", *J. Mater. Process. Technol.* **194:1-3** (2007), 145–150.
- [Centeno et al. 2014] G. Centeno, I. Bagudanch, A. J. Martínez-Donaire, M. L. García-Romeu, and C. Valvellano, "Critical analysis of necking and fracture limit strains and forming forces in single-point incremental forming", *Mater. Des.* **63** (2014), 20–29.
- [Cui et al. 2013] Z. Cui, Z. C. Xia, F. Ren, V. Kiridena, and L. Gao, "Modeling and validation of deformation process for incremental sheet forming", *J. Manuf. Process.* **15:2** (2013), 236–241.
- [Franzen et al. 2008] V. Franzen, L. Kwiatkowski, G. Sebastiani, R. Shankar, A. E. Tekkaya, and M. Kleiner, "Dyna-die: towards full kinematic incremental forming", *Int. J. Mater. Form.* **1:1** (2008), 1163–1166.
- [Gulenc 2008] B. Gulenc, "Investigation of interface properties and weldability of aluminum and copper plates by explosive welding method", *Mater. Des.* **29:1** (2008), 275–278.
- [Hirt et al. 2004] G. Hirt, J. Ames, M. Bambach, and R. Kopp, "Forming strategies and process modelling for CNC incremental sheet forming", *CIRP Ann.* **53:1** (2004), 203–206.
- [Honarpisheh et al. 2012] M. Honarpisheh, M. Asemabadi, and M. Sedighi, "Investigation of annealing treatment on the interfacial properties of explosive-welded Al/Cu/Al multilayer", *Mater. Des.* **37** (2012), 122–127.
- [Honarpisheh et al. 2016a] M. Honarpisheh, M. J. Abdolhoseini, and S. Amini, "Experimental and numerical investigation of the hot incremental forming of Ti-6Al-4V sheet using electrical current", *Int. J. Adv. Manuf. Technol.* **83:9-12** (2016), 2027–2037.
- [Honarpisheh et al. 2016b] M. Honarpisheh, J. Niksokhan, and F. Nazari, "Investigation of the effects of cold rolling on the mechanical properties of explosively-welded Al/St/Al multilayer sheet", *Metall. Res. Technol.* **113:1** (2016), art. id. 105.
- [Jeswiet et al. 2005] J. Jeswiet, F. Micari, G. Hirt, A. Bramley, J. Dufloy, and J. Allwood, "Asymmetric single point incremental forming of sheet metal", *CIRP Ann.* **54:2** (2005), 88–114.
- [Manco and Ambrogio 2010] G. L. Manco and G. Ambrogio, "Influence of thickness on formability in 6082-T6", *Int. J. Mater. Form.* **3:1** (2010), 983–986.
- [Martins et al. 2008] P. A. F. Martins, N. Bay, M. Skjødt, and M. B. Silva, "Theory of single point incremental forming", *CIRP Ann.* **57:1** (2008), 247–252.
- [Micari et al. 2007] F. Micari, G. Ambrogio, and L. Filice, "Shape and dimensional accuracy in single point incremental forming: state of the art and future trends", *J. Mater. Process. Technol.* **191:1-3** (2007), 390–395.
- [Mulay et al. 2017] A. Mulay, S. Ben, S. Ismail, and A. Kocanda, "Experimental investigations into the effects of SPIF forming conditions on surface roughness and formability by design of experiments", *J. Brazil. Soc. Mech. Sci. Eng.* **39:10** (2017), 3997–4010.
- [Obikawa et al. 2009] T. Obikawa, S. Satou, and T. Hakutani, "Dieless incremental micro-forming of miniature shell objects of aluminum foils", *Int. J. Mach. Tool. Manuf.* **49:12-13** (2009), 906–915.

- [Petek et al. 2009] A. Petek, K. Kuzman, and J. Kopač, “Deformations and forces analysis of single point incremental sheet metal forming”, *Arch. Mater. Sci. Eng.* **35**:2 (2009), 107–116.
- [Reddy and Cao 2009] N. V. Reddy and J. Cao, “Incremental sheet metal forming: a review”, review, Indian Institute of Technology Kanpur, 2009, Available at <https://tinyurl.com/sheetreview>.
- [Sedighi and Honarpisheh 2012a] M. Sedighi and M. Honarpisheh, “Experimental study of through-depth residual stress in explosive welded Al/Cu/Al multilayer”, *Mater. Des.* **37** (2012), 577–581.
- [Sedighi and Honarpisheh 2012b] M. Sedighi and M. Honarpisheh, “Investigation of cold rolling influence on near surface residual stress distribution in explosive welded multilayer”, *Strength Mater.* **44**:6 (2012), 693–698.
- [Silva et al. 2011] M. B. Silva, P. S. Nielsen, N. Bay, and P. A. F. Martins, “Failure mechanisms in single-point incremental forming of metals”, *Int. J. Adv. Manuf. Technol.* **56**:9-12 (2011), 893–903.
- [Thibaud et al. 2012] S. Thibaud, R. B. Hmida, F. Richard, and P. Malécot, “A fully parametric toolbox for the simulation of single point incremental sheet forming process: numerical feasibility and experimental validation”, *Simul. Model. Pract. Theory* **29** (2012), 32–43.
- [Yamashita et al. 2008] M. Yamashita, M. Gotoh, and S.-Y. Atsumi, “Numerical simulation of incremental forming of sheet metal”, *J. Mater. Process. Technol.* **199**:1-3 (2008), 163–172.

Received 29 Jun 2017. Revised 5 Oct 2017. Accepted 5 Nov 2017.

MOHAMMAD HONARPISHEH: honarpishe@kashanu.ac.ir
University of Kashan, Kashan, Iran

MORTEZA KEIMASI: keimasimorteza@gmail.com
University of Kashan, Kashan, Iran

IMAN ALINAGHIAN: iman.algh@gmail.com
University of Kashan, Kashan, Iran

ORDINARY STATE-BASED PERIDYNAMICS FOR OPEN-HOLE TENSILE STRENGTH PREDICTION OF FIBER-REINFORCED COMPOSITE LAMINATES

XIAO-WEI JIANG AND HAI WANG

This study presents an ordinary state-based peridynamic model (OSB PD) for open-hole tensile strength prediction of fiber-reinforced composite laminates. The transverse Poisson's effect of composites is considered in the present OSB PD composite model, ensuring a precise capture of typical damage patterns and failure modes of composite laminates, especially when capturing the effect of thickness on damage patterns. The out-of-plane bond considers not only the adjacent plies, but also all the plies within the spherical horizon. The in-plane mesh could be much larger than the out-of-plane mesh, forming an "uneven spherical horizon". The validation of the present model is demonstrated by several numerical results. Typical damage patterns and failures modes of open-hole composite laminates under tensile loading are illustrated, and the effect of thickness on damage patterns is also discussed.

1. Introduction

Aircraft structures are ideal applications of fiber-reinforced composite laminates, due to their high specific stiffness/strength, low coefficient of thermal expansion, and excellent fatigue resistance [Camanho and Lambert 2006]. For the design of composite structures, open-hole tensile strength is a fundamental datum for structural design allowables [ASTM 2011]. In the building block approach for designing composite structures, testing and analysis are both needed due to the overall consideration of cost and reliability [US-DoD 2002]. Conventional analysis methods, normally the finite element method (FEM), have been widely used in open-hole tensile strength predictions of fiber-reinforced composite laminates [Camanho et al. 2007; Hallett et al. 2009; Chen et al. 2013; Aidi and Case 2015; Su et al. 2015; Bao and Liu 2016; Bartan et al. 2016; Moure et al. 2016; Mohammadi et al. 2017]. However, as stated in [Askari et al. 2006; Xu et al. 2008; Kilic et al. 2009; Oterkus and Madenci 2012a; 2012b; Hu et al. 2015; Diyaroglu et al. 2016; Hu and Madenci 2016; Sun and Huang 2016; Yu et al. 2016], conventional analysis methods based on classical continuum mechanics require that the displacement field of the body should be continuously differential for the spatial displacement derivatives of partial differential equations; this requirement contradicts the inherent discontinuity that exists in fracture and damage. Besides, conventional analysis methods, including FEM, usually need a preset damage path, which might not be available for complex loading conditions.

As an alternative to conventional analysis methods, the peridynamic (PD) theory of solid mechanics, which attempts to unite the mathematical modeling of continuous media, cracks, and particles within a single framework, was introduced [Silling 2000; Silling et al. 2007; Silling and Lehoucq 2010]. Peridynamic theory replaces the partial differential equation of the classical theory of solid mechanics with

Keywords: peridynamics, composite laminates, ordinary state-based, open-hole Strength, damage, delamination.

integral or integral-differential equations, and “spontaneous” formation of fracture and damage could be simulated without any prior knowledge of damage path. These two features suggest great potential advantages of PD in the analysis of composite structures. Matrix cracking, fiber breakage, and delamination: these typical damage modes of composites could bring about severe discontinuities in structures during the loading process. Besides, in most cases, a preset for the damage path of these damage modes is impossible or leads to a huge expense. For example, in order to precisely capture the delamination damage of composite laminates based on FEM, a cohesive zone element (CZE) has to be preset between each adjacent ply, which could result in huge computation cost and convergence problems.

The application of the peridynamic theory into the analysis of composite structures is emerging. Askari et al. [2006] analyzed the damage and failure of composite panels under static and dynamics loads. Xu et al. [2007; 2008] predicted in detail the delamination and matrix damage process in composite laminates under biaxial loads and low-velocity impact. Kilic et al. [2009] predicted the damage in center-cracked laminates with different fiber orientations. Oterkus et al. [2010] present an approach based on the merger of classical continuum theory and peridynamic theory to predict failure simulations in bolted composite lap joints. Hu et al. [2011; 2012] proposed a homogenization-based peridynamic model for simulating fracture and damage in fiber-reinforced composites, and analyzed the dynamic effects induced by different types of dynamic loading. Oterkus and Madenci [2012a; 2012b] present an application of PD theory in the analysis of fiber-reinforced composite materials subjected to mechanical and thermal loading conditions. Damage growth patterns of preexisting cracks in fiber-reinforced composite laminates subjected to tensile loading were computed. Oterkus et al. [2012] present an analysis approach based on a merger of the finite element method and the peridynamic theory. The validity of the approach is established through qualitative and quantitative comparisons against the test results for a stiffened composite curved panel with a central slot under combined internal pressure and axial tension. Hu et al. [2014] developed a PD composite model that accounts for the variation of bond *micromodulus* based on the angle between the bond direction and fiber orientation. As an extension of this model, Hu et al. [2015] developed an energy-based approach to simulate delamination under different fracture mode conditions. Furthermore, Hu and Madenci [2016] present a new bond-based peridynamic modeling of composite laminates without any limitation to specific fiber orientation and material properties in order to consider arbitrary laminate layups. Sun and Huang [2016] proposed a peridynamic rate-dependent constitutive equation and a new interlayer bond describing interlayer interactions of fiber-reinforced composite laminates.

The above peridynamic models for the analysis of composite structures are bond-based peridynamics. Comparatively, ordinary state-based (OSB) peridynamic models for the analysis of composite structures are quite few. Colavito, Madenci, and Oterkus [Colavito 2013; Colavito and Barut 2013; Madenci and Oterkus 2014] presented an OSB peridynamic laminate theory (PDLT) for composite structures. This OSB PDLT was used by Hu et al. [2016] for progressive damage predictions in open-hole quasi-isotropic laminates under tension and compression, and by Diyaroglu et al. [2016] to predict nonlinear transient deformation and damage behavior of composites under shock or blast types of loadings due to explosions. However, the transverse Poisson’s effect is neglected in this OSB PDLT model. The out-of-plane horizon of this OSB PDLT model considers only the adjacent layers, and two different types of out-of-plane bonds, the normal bonds and the shear bonds, are introduced in this OSB PDLT model. For a symmetric-layup composite laminate under in-plane tensile loading, which has no coupling between bending and extension, the out-of-plane deformation caused by transverse Poisson’s ratio ν_{13} and ν_{23} is neglected

by this OSB PDLT model. This neglect might make this OSB PDLT model insensitive to the effect of thickness on damage patterns of composite laminates, especially for delamination damage.

In the present paper, we are trying to present an ordinary state-based peridynamic (OSB PD) composite model for the open-hole tensile strength prediction of fiber-reinforced composite laminates that considers the transverse Poisson's effect of composites. A spherical horizon, instead of the adjacent-layer horizon in the previous OSB PDLT model, for out-of-plane bonds is used. The out-of-plane normal bond and shear bond in the previous OSB PDLT model are also abandoned. The deformation caused by transverse Poisson's ratios ν_{13} and ν_{23} of composites is taken into account in the present OSB PD composite model, ensuring a precise capture of typical damage patterns and failure modes of composite laminates, especially when capturing the effect of thickness on damage patterns. Although each ply has to be meshed, the in-plane mesh could be much larger than the out-of-plane mesh, forming an "uneven spherical horizon". The validation of the present model is demonstrated by several numerical results. Typical damage patterns and failures modes of open-hole composite laminates under tensile loading are illustrated, and the effect of thickness on damage patterns is also discussed. The numerical analysis is carried out via PGI CUDA FORTRAN compiler (GPU-parallel computing), on the P100 cluster node at the High Performance Computing Center (HPCC) of Shanghai Jiao Tong University.

2. Ordinary state-based peridynamic model for composite laminates

2.1. Governing equation. Starting from the work done by Colavito, Madenci and Oterkus [Colavito 2013; Colavito and Barut 2013; Madenci and Oterkus 2014], the governing equation of the present ordinary state-based (OSB PD) peridynamic model for composite laminates can be expressed by

$$\rho_{(k)}^{(n)} \ddot{\mathbf{u}}_{(k)}^{(n)} = \sum_{j=1}^{\infty} [\mathbf{t}_{(k)(j)} - \mathbf{t}_{(j)(k)}] V_{(j)} + \mathbf{b}_{(k)}^{(n)}, \quad (1)$$

where $\rho_{(k)}^{(n)}$ is the density of material point $\mathbf{x}_{(k)}^{(n)}$, $\ddot{\mathbf{u}}_{(k)}^{(n)}$ is instantaneous acceleration of $\mathbf{x}_{(k)}^{(n)}$, and n denotes the layer number of laminates, as shown in Figure 1. Furthermore, $\mathbf{b}_{(k)}^{(n)}$ is the external load density; $\mathbf{t}_{(k)(j)}$ and $\mathbf{t}_{(j)(k)}$ are the PD force densities between $\mathbf{x}_{(k)}^{(n)}$ and $\mathbf{x}_{(j)}$, where $\mathbf{x}_{(j)}$ includes both in-plane material points and out-of-plane material points. The PD force density can be expressed as

$$\mathbf{t}_{(k)(j)} = A_{(k)(j)} \frac{\mathbf{y}_{(j)} - \mathbf{y}_{(k)}^{(n)}}{|\mathbf{y}_{(j)} - \mathbf{y}_{(k)}^{(n)}|}, \quad (2)$$

$$\mathbf{t}_{(j)(k)} = B_{(j)(k)} \frac{\mathbf{y}_{(k)}^{(n)} - \mathbf{y}_{(j)}}{|\mathbf{y}_{(k)}^{(n)} - \mathbf{y}_{(j)}|}, \quad (3)$$

with

$$A_{(k)(j)} = 2ad \frac{\delta}{|\mathbf{x}_{(j)} - \mathbf{x}_{(k)}^{(n)}|} \Lambda_{(k)(j)} \theta_{(k)} + 2\delta bs_{(k)(j)} + 2\delta(\mu_F b_F + \mu_T b_T) s_{(k)(j)}^{(n)(n)}, \quad (4)$$

$$B_{(j)(k)} = 2ad \frac{\delta}{|\mathbf{x}_{(k)}^{(n)} - \mathbf{x}_{(j)}|} \Lambda_{(k)(j)} \theta_{(j)} + 2\delta bs_{(j)(k)} + 2\delta(\mu_F b_F + \mu_T b_T) s_{(j)(k)}^{(n)(n)}, \quad (5)$$

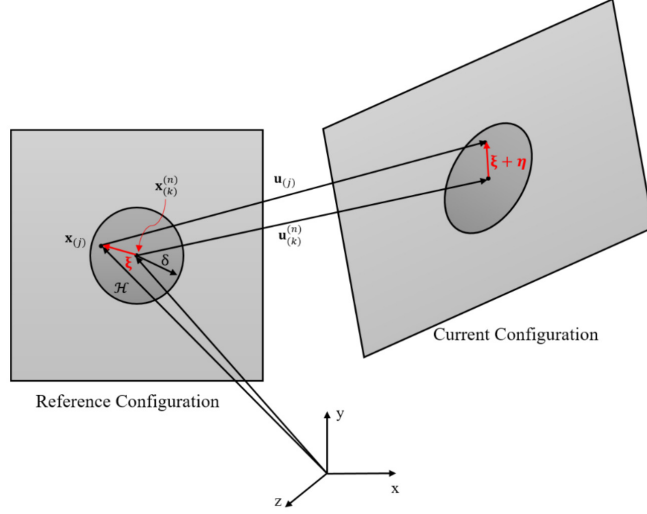


Figure 1. Peridynamic notations.

and

$$s_{(k)(j)} = \frac{|\mathbf{y}_{(j)} - \mathbf{y}_{(k)}^{(n)}| - |\mathbf{x}_{(j)} - \mathbf{x}_{(k)}^{(n)}|}{|\mathbf{x}_{(j)} - \mathbf{x}_{(k)}^{(n)}|}, \quad (6)$$

$$s_{(k)(j)}^{(n)(n)} = \frac{|\mathbf{y}_{(j)}^{(n)} - \mathbf{y}_{(k)}^{(n)}| - |\mathbf{x}_{(j)}^{(n)} - \mathbf{x}_{(k)}^{(n)}|}{|\mathbf{x}_{(j)}^{(n)} - \mathbf{x}_{(k)}^{(n)}|}, \quad (7)$$

and

$$\mu_F = \begin{cases} 1 & (\mathbf{x}_{(j)}^{(n)} - \mathbf{x}_{(k)}^{(n)}) \parallel \text{fiber direction,} \\ 0 & \text{otherwise,} \end{cases} \quad (8)$$

$$\mu_T = \begin{cases} 1 & (\mathbf{x}_{(j)}^{(n)} - \mathbf{x}_{(k)}^{(n)}) \perp \text{fiber direction,} \\ 0 & \text{otherwise,} \end{cases} \quad (9)$$

where $s_{(k)(j)}$ is the stretch of bonds, $s_{(k)(j)}^{(n)(n)}$ denotes the in-plane fiber direction bond stretch. In (4) and (5), δ is the radius of the horizon zone. The direction cosines of the relative position vectors between the material points $\mathbf{x}_{(k)}^{(n)}$ and $\mathbf{x}_{(j)}$ in the undeformed and deformed states are defined as

$$\Lambda_{(k)(j)} = \frac{\mathbf{y}_{(j)} - \mathbf{y}_{(k)}^{(n)}}{|\mathbf{y}_{(j)} - \mathbf{y}_{(k)}^{(n)}|} \cdot \frac{\mathbf{x}_{(j)} - \mathbf{x}_{(k)}^{(n)}}{|\mathbf{x}_{(j)} - \mathbf{x}_{(k)}^{(n)}|}. \quad (10)$$

The three-dimensional PD dilatation $\theta_{(k)}$ can be expressed as

$$\theta_{(k)} = d \sum_{j=1}^{\infty} \delta s_{(k)(j)} \Lambda_{(k)(j)} V_{(j)}. \quad (11)$$

The PD material parameters a , d characterize the effect of dilation, and b , b_F , b_T are associated with the deformation of material points in arbitrary directions (in-plane fiber direction and in-plane transverse

direction, respectively). These parameters are related to material properties of composite laminates, horizon radius, and ply direction. The main derivation procedures to get these PD material parameters are illustrated in Section 2.2, and the detailed derivation process will be given in the Appendix. Here we directly give the derived results as

$$a = \frac{1}{2}(C_{33} - 3C_{55}), \quad (12)$$

$$d = \frac{9}{4\pi\delta^4}, \quad (13)$$

$$b = \frac{15C_{55}}{2\pi\delta^5}, \quad (14)$$

$$b_F = \frac{C_{11} - C_{33}}{2\delta \sum_{j=1}^J |\mathbf{x}_{(j)}^{(n)} - \mathbf{x}_{(k)}^{(n)}| V_{(j)}^{(n)}}, \quad (15)$$

$$b_T = \frac{C_{22} - C_{33}}{2\delta \sum_{j=1}^J |\mathbf{x}_{(j)}^{(n)} - \mathbf{x}_{(k)}^{(n)}| V_{(j)}^{(n)}}, \quad (16)$$

where C_{11} , C_{22} , C_{33} , and C_{55} are coefficients of composite material stiffness matrix \mathbf{C} , and are defined as

$$C_{11} = \frac{1 - \nu_{23}\nu_{32}}{E_2 E_3 \Delta}, \quad C_{22} = \frac{1 - \nu_{13}\nu_{31}}{E_1 E_3 \Delta}, \quad C_{33} = \frac{1 - \nu_{12}\nu_{21}}{E_1 E_2 \Delta}, \quad C_{55} = G_{31}, \quad (17)$$

$$\Delta = \frac{1 - \nu_{12}\nu_{21} - \nu_{23}\nu_{32} - \nu_{13}\nu_{31} - 2\nu_{21}\nu_{32}\nu_{13}}{E_1 E_2 E_3}. \quad (18)$$

It may be worth noting that the present OSB PD composite model differs from the OSB PDLT model by using a spherical horizon for out-of-plane bonds, and the transverse Poisson's effect is taken into account, as shown in the parameters in (12)–(18).

2.2. Derivation of PD material parameters. Derivation of the PD material parameters for the present OSB PD composite model follows a similar procedure for deriving the OSB PDLT model presented by Colavito, Madenci, and Oterkus [Colavito 2013; Colavito and Barut 2013; Madenci and Oterkus 2014]. Nevertheless, it might be worth noting that as the normal bond and shear bond in the OSB PDLT model are abandoned in the present OSB PD composite model, the out-of-plane spherical horizon is used and transverse Poisson's effect is considered, so the derivation involving out-of-plane bonds shall be different from OSB PDLT's derivation process.

The PD strain energy density of the present OSB PD composite model for composite laminates can be expressed as

$$W_{(k)}^{(n)} = a\theta_{(k)}^2 + b \sum_{j=1}^{\infty} \delta |\mathbf{x}_{(j)} - \mathbf{x}_{(k)}| s_{(k)(j)}^2 V_{(j)} + b_F \sum_{j=1}^J \delta |\mathbf{x}_{(j)}^{(n)} - \mathbf{x}_{(k)}^{(n)}| s_{(k)(j)}^{(n)(n)2} V_{(j)}^{(n)} + b_T \sum_{j=1}^J \delta |\mathbf{x}_{(j)}^{(n)} - \mathbf{x}_{(k)}^{(n)}| s_{(k)(j)}^{(n)(n)2} V_{(j)}^{(n)}. \quad (19)$$

The PD material parameters in (4), (5), and (14) can be derived by comparing the PD strain energy density and the strain energy density of continuum mechanics under simple loading conditions. In the

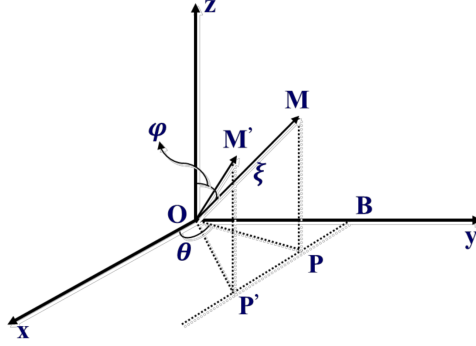


Figure 2. Transverse pure shear loading on xz -plane (γ_{13}).

present model, we derive these parameters by assuming a unidirectional composite laminate under four simple loading conditions:

- (1) transverse pure shear loading on xz -plane (γ_{13});
- (2) transverse tensile loading (ε_{33});
- (3) in-plane uniaxial tension in x direction (ε_{11});
- (4) in-plane uniaxial tension in y direction (ε_{22}).

Here we only show the main derivation procedure, and the detailed derivation processes are presented in the Appendix.

2.2.1. Transverse pure shear loading on xz -plane (γ_{13}). Under this loading condition, we assume $\gamma_{13} = \zeta$ and all other strains equal zero. From three-dimensional elasticity of orthotropic composite materials, we get

$$\theta_{(k)}^{CM} = 0, \quad W_{(k)}^{CM} = \frac{1}{2} C_{55} \zeta^2. \quad (20)$$

Firstly, the stretch of bonds $s_{(k)(j)}$ in (6) should be calculated under $\gamma_{13} = \zeta$. As shown in Figure 2, under this simple loading condition, material point M moves to M' :

$$\begin{aligned} OM' &= \sqrt{OM^2 + M'P'^2} = \sqrt{OB^2 + BP'^2 + M'P'^2} \\ &= \sqrt{(\xi \sin \varphi \sin \theta)^2 + (\xi \sin \varphi \cos \theta + \zeta \xi \cos \varphi)^2 + (\xi \cos \varphi)^2} \\ &= \sqrt{\xi^2 + 2\xi \sin \varphi \cos \theta \zeta \xi \cos \varphi + (\zeta \xi \cos \varphi)^2} \\ &\approx \sqrt{\xi^2 + 2\xi \sin \varphi \cos \theta \zeta \xi \cos \varphi}. \end{aligned} \quad (21)$$

$$\begin{aligned} s_{(k)(j)} &= \frac{OM' - OM}{OM} = \frac{\sqrt{\xi^2 + 2\xi \sin \varphi \cos \theta \zeta \xi \cos \varphi} - \xi}{\xi} = \sqrt{1 + \zeta 2 \sin \varphi \cos \theta \cos \varphi} - 1 \\ &\approx 1 + \frac{1}{2} \zeta 2 \sin \varphi \cos \theta \cos \varphi - 1 = \zeta \sin \varphi \cos \varphi \cos \theta. \end{aligned} \quad (22)$$

Then the PD strain energy can be derived as

$$\begin{aligned}
W_{(k)}^{(n)} &= a\theta_{(k)}^2 + b \sum_{j=1}^{\infty} \delta |\mathbf{x}_{(j)} - \mathbf{x}_{(k)}| s_{(k)(j)}^2 V_{(j)} + b_F \sum_{j=1}^J \delta |\mathbf{x}_{(j)}^{(n)} - \mathbf{x}_{(k)}^{(n)}| s_{(k)(j)}^{(n)2} V_{(j)}^{(n)} \\
&\quad + b_T \sum_{j=1}^J \delta |\mathbf{x}_{(j)}^{(n)} - \mathbf{x}_{(k)}^{(n)}| s_{(k)(j)}^{(n)2} V_{(j)}^{(n)} \\
&= b \sum_{j=1}^{\infty} \delta |\mathbf{x}_{(j)} - \mathbf{x}_{(k)}| s_{(k)(j)}^2 V_{(j)} = b \sum_{j=1}^{\infty} \delta \xi (\zeta \sin \varphi \cos \varphi \cos \theta)^2 V_{(j)} \\
&= \zeta^2 b \delta \int_0^{2\pi} \int_0^{\pi} \int_0^{\delta} \xi \sin^2 \varphi \cos^2 \varphi \cos^2 \theta \xi^2 \sin \varphi \, dr \, d\varphi \, d\theta = \zeta^2 b \frac{\pi^2}{15} \delta^5.
\end{aligned} \tag{23}$$

Comparing with (23), we get

$$b = \frac{1/2 C_{55} \zeta^2}{\zeta^2 \pi / 15 \delta^5} = \frac{15 C_{55}}{2\pi \delta^5}. \tag{24}$$

2.2.2. Transverse tensile loading (ε_{33}). Setting $\varepsilon_{33} = \zeta$ and conducting the same procedure in Section 2.2.1, we get

$$\theta_{(k)}^{CM} = \zeta, \quad W_{(k)}^{CM} = \frac{1}{2} C_{33} \zeta^2, \tag{25}$$

$$s_{(k)(j)} = \zeta \cos^2 \varphi, \tag{26}$$

$$\theta_{(k)} = \zeta d \frac{4}{9} \pi \delta^4, \quad W_{(k)}^{(n)} = a \zeta^2 + \zeta^2 \frac{3}{2} C_{55}. \tag{27}$$

Comparing (28) and (30), we get

$$d = \frac{9}{4\pi \delta^4}, \quad a = \frac{1}{2} (C_{33} - 3C_{55}). \tag{28}$$

2.2.3. In-plane uniaxial tension in x -direction (ε_{11}). Similarly, setting $\varepsilon_{11} = \zeta$, we get

$$\theta_{(k)}^{CM} = \zeta, \quad W_{(k)}^{CM} = \frac{1}{2} C_{11} \zeta^2, \tag{29}$$

$$s_{(k)(j)} = \zeta \sin^2 \varphi \cos^2 \theta, \tag{30}$$

$$\theta_{(k)} = \zeta d \frac{4}{9} \pi \delta^4, \quad W_{(k)}^{(n)} = a \zeta^2 + \zeta^2 b \frac{\pi}{5} \delta^5 + \zeta^2 b_F \delta \sum_{j=1}^J |\mathbf{x}_{(j)}^{(n)} - \mathbf{x}_{(k)}^{(n)}| V_{(j)}^{(n)}. \tag{31}$$

Substituting a and b , and comparing (32) and (34), we get

$$d = \frac{9}{4\pi \delta^4}, \quad b_F = \frac{1/2 (C_{11} - C_{33})}{\delta \sum_{j=1}^J |\mathbf{x}_{(j)}^{(n)} - \mathbf{x}_{(k)}^{(n)}| V_{(j)}^{(n)}}. \tag{32}$$

2.2.4. In-plane uniaxial tension in y -direction (ε_{22}). Similarly, setting $\varepsilon_{22} = \zeta$, we get

$$\theta_{(k)}^{CM} = \zeta, \quad W_{(k)}^{CM} = \frac{1}{2} C_{22} \zeta^2, \tag{33}$$

$$s_{(k)(j)} = \zeta \sin^2 \varphi \cos^2 \theta, \tag{34}$$

$$\theta_{(k)} = \zeta d \frac{4}{9} \pi \delta^4, \quad W_{(k)}^{(n)} = a \zeta^2 + \zeta^2 b \frac{\pi}{5} \delta^5 + \zeta^2 b_T \delta \sum_{j=1}^J |\mathbf{x}_{(j)}^{(n)} - \mathbf{x}_{(k)}^{(n)}| V_{(j)}^{(n)}. \tag{35}$$

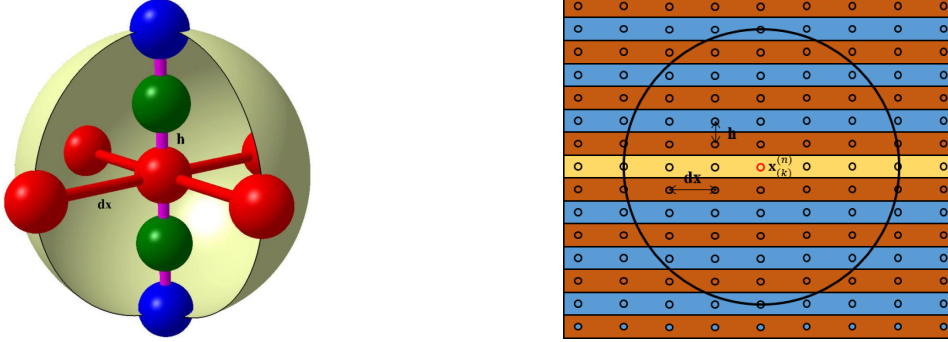


Figure 3. “Uneven spherical horizon” for OSB PD composite model of composite laminates. Left: 3D view, $\delta = dx$, $dx = 2h$. Right: 2D view, $\delta = 3dx$, $dx = 2h$.

Substituting a and b , and comparing (36) and (39), we can get

$$d = \frac{9}{4\pi\delta^4}, \quad b_T = \frac{1/2(C_{22} - C_{33})}{\delta \sum_{j=1}^J |\mathbf{x}_{(j)}^{(n)} - \mathbf{x}_{(k)}^{(n)}| V_{(j)}^{(n)}}. \quad (36)$$

2.3. Uneven spherical horizon. The present OSB PD composite model of composite laminates uses a spherical horizon for out-of-plane bonds. The out-of-plane bonds consider not only the adjacent plies, but also all the plies within the spherical horizon. In order to precisely capture the delamination damage between plies of composite laminates, each ply has to be meshed. In the present model, an uneven mesh is adopted for computational efficiency. The in-plane mesh could be much larger than the out-of-plane mesh, forming an “uneven spherical horizon”, as shown in Figure 3. The effect of a truncated spherical horizon near the boundaries must be considered. In the present OSB PD composite model, we use the similar surface effect correction procedure as stated in [Madenci and Oterkus 2014], which calculates the surface effect correction factors by comparing the theoretical PD dilatation and strain energy density with numerically discrete PD dilatation and strain energy density under simple loading conditions. For material points which have complete spherical horizon, this correction factor is around 1. For those with a truncated spherical horizon near boundaries, such as top and bottom surfaces of laminates, the correction factor is around 2. By adding these surface effect correction factors into the equation, the surface effect can be significantly reduced.

2.4. Failure criteria. The failure criteria used in the present model is similar to other PD models [Hu et al. 2014; 2016]. When the bond stretch between two material points exceeds a critical value, the interaction between these two material points is irreversibly removed. The critical stretches for the in-plane fiber bonds, in-plane matrix bonds, and the remaining arbitrary bonds are shown in Figure 4, and their values can be calculated by

$$\begin{aligned} s_0^{\text{ft}} &= X^T / E_1, & s \geq 0 & \text{ (fiber bonds),} \\ s_0^{\text{fc}} &= X^C / E_1, & s < 0 & \text{ (fiber bonds),} \\ s_0^{\text{mt}} &= Y^T / E_2, & s \geq 0 & \text{ (matrix bonds and arbitrary bonds),} \\ s_0^{\text{mc}} &= Y^C / E_2, & s < 0 & \text{ (matrix bonds and arbitrary bonds),} \end{aligned} \quad (37)$$

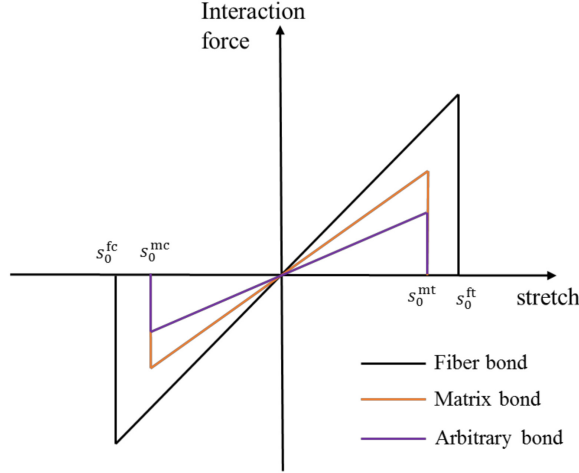


Figure 4. Force-stretch relationships for peridynamic interactions.

where X^T , X^C , Y^T , Y^C are strengths of composite materials.

Local damage at a material point is defined as the weighted ratio of the number of eliminated interactions to the total number of initial interactions of the material point with its family members. The local damage at a point can be quantified as [Silling and Askari 2005; Diyaroglu et al. 2016]

$$\varphi(\mathbf{x}, t) = 1 - \frac{\int_H \mu(\mathbf{x}' - \mathbf{x}, t) dV'}{\int_H dV'}. \quad (38)$$

The status variable μ is defined as

$$\mu = \begin{cases} 1 & s < s_c \quad (\text{no damage}), \\ 0 & s \geq s_c \quad (\text{damage}). \end{cases} \quad (39)$$

To be specific for the present model, three kinds of typical damage modes of composite laminates can be captured: fiber breakage, in-plane matrix cracking, and delamination. These damage modes are indicated by

$$\begin{aligned} \varphi_{\text{fiber breakage}} &= 1 - \frac{\sum_{j=1}^J \mu_{(k)(j)}^{(n)(n)}}{J}, & \varphi_{\text{matrix cracking}} &= 1 - \frac{\sum_{j=1}^{N_{(k)}^{(n)}} \mu_{(k)(j)}^{(n)(n)}}{N_{(k)}^{(n)}}, \\ \varphi_{\text{out-of-plane upper}}^{(n)} &= 1 - \frac{\sum_{j=1}^{N_{(k)}^{(\text{upper})}} \mu_{(k)(j)}^{(n)(n)}}{N_{(k)}^{(\text{upper})}}, & \varphi_{\text{out-of-plane lower}}^{(n+1)} &= 1 - \frac{\sum_{j=1}^{N_{(k)}^{(\text{lower})}} \mu_{(k)(j)}^{(n)(n)}}{N_{(k)}^{(\text{lower})}}, \\ \varphi_{\text{delamination}}^{(n)(n+1)} &= \frac{1}{2} (\varphi_{\text{out-of-plane upper}}^{(n)} + \varphi_{\text{out-of-plane lower}}^{(n+1)}), \end{aligned} \quad (40)$$

where J is the number of fiber material points inside the horizon, $N_{(k)}^{(n)}$ is the number of in-plane matrix material points inside the horizon, $N_{(k)}^{(\text{upper})}$ is the number of upper side out-of-plane material points inside the horizon, and $N_{(k)}^{(\text{lower})}$ is the number of lower side out-of-plane material points inside the horizon.

3. Numerical implementation

Although the peridynamic governing equation is in dynamic form, it can still be used to solve quasistatic or static problems by using the adaptive dynamic relaxation (ADR) method [Kilic and Madenci 2010].

According to the ADR method, (1) at the n -th iteration can be rewritten as

$$\ddot{\mathbf{U}}^n(\mathbf{X}, t^n) + c^n \dot{\mathbf{U}}^n(\mathbf{X}, t^n) = \mathbf{D}^{-1} \mathbf{F}^n(\mathbf{U}^n, \mathbf{U}^m, \mathbf{X}, \mathbf{X}'), \quad (41)$$

where \mathbf{D} is the fictitious diagonal density matrix and c is the damping coefficient, which can be expressed by

$$c^n = 2\sqrt{((\mathbf{U}^n)^T \mathbf{K}^n \mathbf{U}^n) / ((\mathbf{U}^n)^T \mathbf{U}^n)}, \quad (42)$$

in which ${}^1\mathbf{K}^n$ is the diagonal ‘‘local’’ stiffness matrix, which is given as

$${}^1K_{ii}^n = -(F_i^n / \lambda_{ii} - F_i^{n-1} / \lambda_{ii}) / (\Delta t \dot{u}_i^{n-1/2}), \quad (43)$$

where F_i^n is the value of force vector \mathbf{F}^n at material point \mathbf{x} , which includes both the peridynamic force state vector and external forces. Here, λ_{ii} is the diagonal elements of \mathbf{D} which should be large enough for numerical convergence.

By utilizing central-difference explicit integration, displacements and velocities for the next time step can be obtained:

$$\dot{\mathbf{U}}^{n+1/2} = \frac{((2 - c^n \Delta t) \dot{\mathbf{U}}^{n-1/2} + 2 \Delta t \mathbf{D}^{-1} \mathbf{F}^n)}{(2 + c^n \Delta t)} \quad (44)$$

and

$$\dot{\mathbf{U}}^{n+1} = \mathbf{U}^n + \Delta t \dot{\mathbf{U}}^{n+1/2}. \quad (45)$$

To start the iteration process, we assume that $\mathbf{U}^0 \neq 0$ and $\dot{\mathbf{U}}^0 = 0$, so the integration can be started by

$$\dot{\mathbf{U}}^{1/2} = \frac{\Delta t \mathbf{D}^{-1} \mathbf{F}^0}{2}. \quad (46)$$

Due to the large computational cost of the PD model, GPU-parallel computing is introduced. The PGI CUDA FORTRAN compiler, PGI/16.10 Community Edition, is used for compiling. The P100 cluster node at the High Performance Computing Center (HPCC) of Shanghai Jiao Tong University is applied for running the GPU-parallel program. The P100 cluster node has two NVIDIA Tesla P100 graphic cards (3584 CUDA Cores, 16 GB graphic memory), two Intel Xeon E5-2680 CPUs, and 96 GB memory. The GPU block threads are fixed to 256, and the number of blocks depends on the total number of parallel processes [Ruetsch and Fatica 2013].

4. Numerical results

4.1. Deformation of composite laminated plate. As shown in Figure 5, a composite laminated plate [45/0/45] under tensile loading is simulated both by the present OSB PD composite model and FEM. The dimensions of the composite laminated plate are $L = 12.5$ mm and $W = 6.25$ mm. The thickness of the plate is 0.375 mm, with 0.125 mm for each ply. The material is the fiber-reinforced composite from [Madenci and Oterkus 2014]. The material properties of the composite are: $\rho = 8000$ kg/m³, elastic modulus in the fiber direction $E_1 = 159.96$ GPa, elastic modulus in transverse direction $E_2 = 8.96$ GPa,

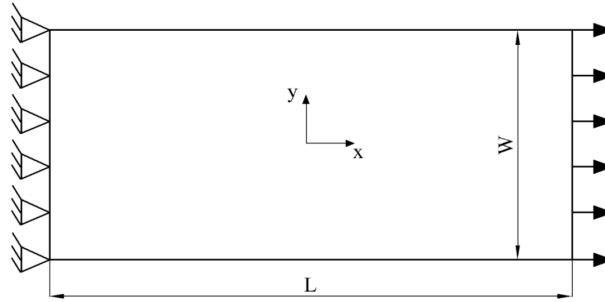


Figure 5. Composite laminated plate [45/0/45] under tensile loading.

in-plane Poisson's ratio $\nu_{12} = 0.33$, and in-plane shear modulus $G_{12} = 3.0054$ GPa. The mesh of the PD model is $100 \times 50 \times 3$, with $dx = h = 0.125$ mm, and horizon $\delta = 3 dx$.

Under the tensile loading condition, with 0.2 mm displacement at the right end, the deformation of the composite laminated plate is presented in Figure 6. The simulation results of the displacement fields in three directions, U1, U2, and U3, are all compared between PD and FEM. The variation of the in-plane and out-of-plane displacement in the three directions are compared with FEM results in Figure 7. It can be seen from these figures that deformation simulation of the present OSB PD composite model fits the FEM results well. The influence of fiber direction on the displacement fields, especially U2, is precisely captured by the present model. The out-of-plane deformation caused by transverse Poisson's effect is accurately captured by the present OSB PD composite model, as shown in Figure 7, bottom. It should be noted that as FEM and PD use different mesh methods, the calculated points have different coordinates. This is the reason that PD is unable to fit a curved tendency with three mesh points, as seen in Figure 7, bottom. Better results can be seen when a composite laminate with large number plies is simulated, as shown in Figure 12, bottom.

4.2. Deformation of composite laminated plate with open-hole. As shown in Figure 8, the deformation of a composite laminated plate with an open-hole is considered. With the same plate dimension, material system, mesh, and loading condition as Section 4.1, the composite laminated plate with an open-hole in this section only has an additional hole with radius $R = 0.5$ mm. Similarly, simulation results of displacement fields, U1, U2, and U3, by both PD and FEM are presented in Figure 9. The variation of the in-plane and out-of-plane displacement in the three directions are compared with FEM results in Figure 10. All the deformation results of the present OSB PD composite model fit the FEM results well. The influence of the fiber direction on the displacement field can also be precisely captured. The effect of the hole on the deformation is also obviously observed by comparing Figure 6 and Figure 9. Also, the out-of-plane deformation caused by transverse Poisson's effect is accurately captured by the present OSB PD composite model, as shown in Figure 10, bottom.

In order to illustrate that the present OSB PD composite model is also valid for calculating the deformation of composite laminates with a large number plies, an 8-layer $[90/45/0/-45]_S$ composite laminate with an open-hole is simulated. The dimensions, material system, and loading condition are similar to the case in Figure 8, and only the ply number is changed. The deformation contour is compared with FEM results in Figure 11. The variation of the in-plane and out-of-plane displacement in the three

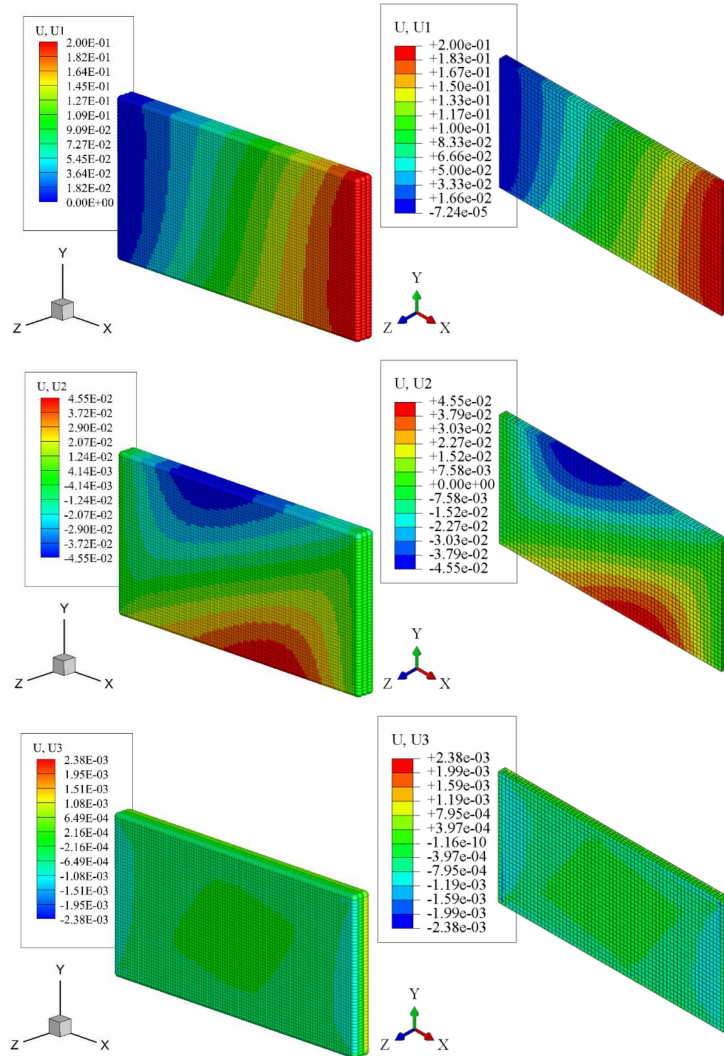


Figure 6. Comparison of the deformation of composite laminated plate [45/0/45] (mm). Left: PD. Right: FEM.

directions are compared with FEM results in Figure 12. It can be seen from these figures that the calculated deformation results by the present OSB PD composite model fit the FEM results well. The out-of-plane deformation shown in Figure 12, bottom, is mainly induced due to the transverse Poisson's effect, as the layup is symmetric and there is no bending-extension coupling under tensile loading. This transverse deformation will be neglected if the transverse Poisson's ratio ν_{13} and ν_{23} is not introduced into the PD model.

4.3. Open-hole strength prediction of fiber-reinforced composite laminates. Three different experiments for open-hole tensile strength of fiber-reinforced composite laminates from the literature are simulated by the present OSB PD composite model. The specimen schematic is shown in Figure 13,

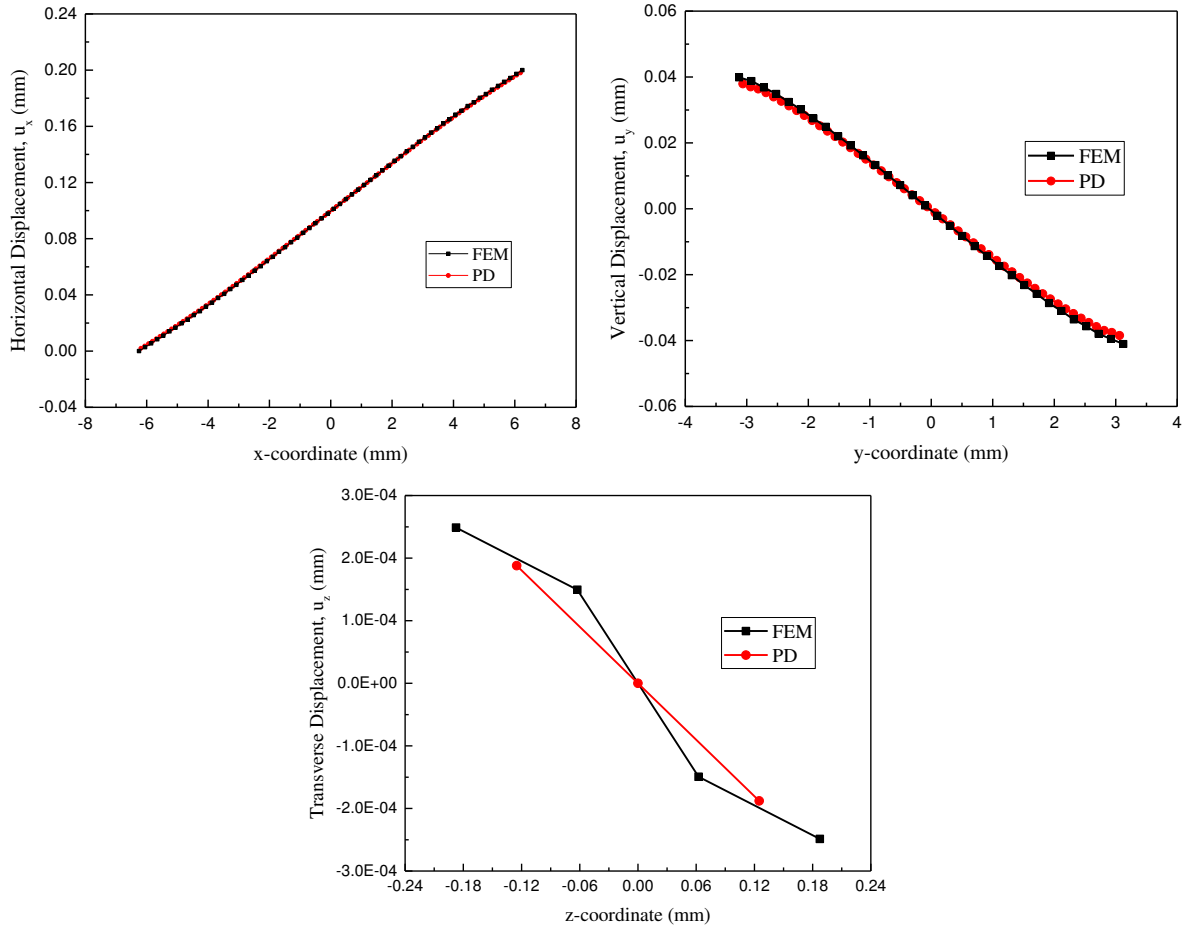


Figure 7. Comparison of the deformation of a composite laminated plate [45/0/45] under tensile loading. Left: along x -axis for midply ($y = 0, z = 0$). Right: along y -axis for midply ($x = 0, z = 0$). Bottom: along z -axis ($x = 0, y = 0$).

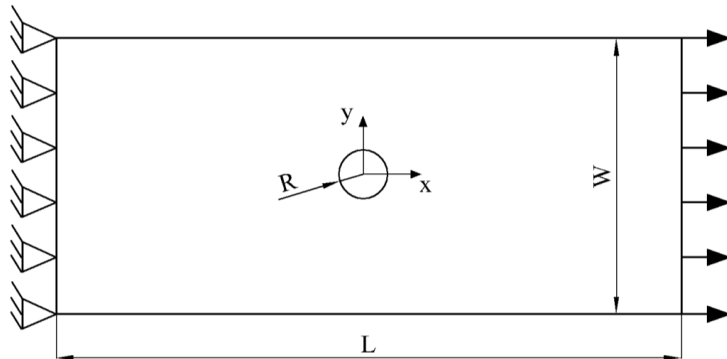


Figure 8. Composite laminated plate [45/0/45] with open-hole under tensile loading.

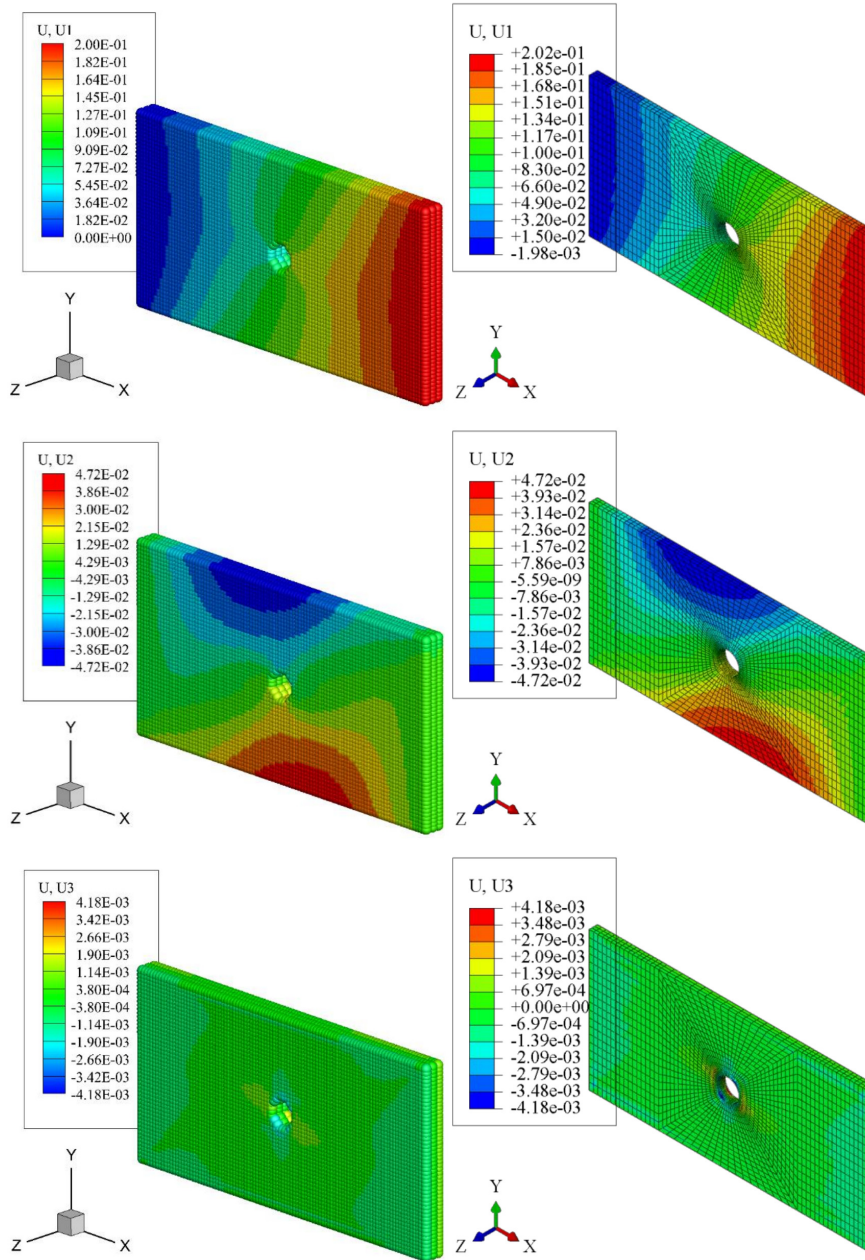


Figure 9. Comparison of the deformation of composite laminated plate [45/0/45] with open-hole (mm). Left: PD. Right: FEM.

bottom. These experiments are renamed in the present paper as specimen A1, A2, and A3. The specimen configurations are shown in Table 1. The material properties of IM7/977-3 and IM7/8552 are shown in Table 2 and Table 3, respectively.

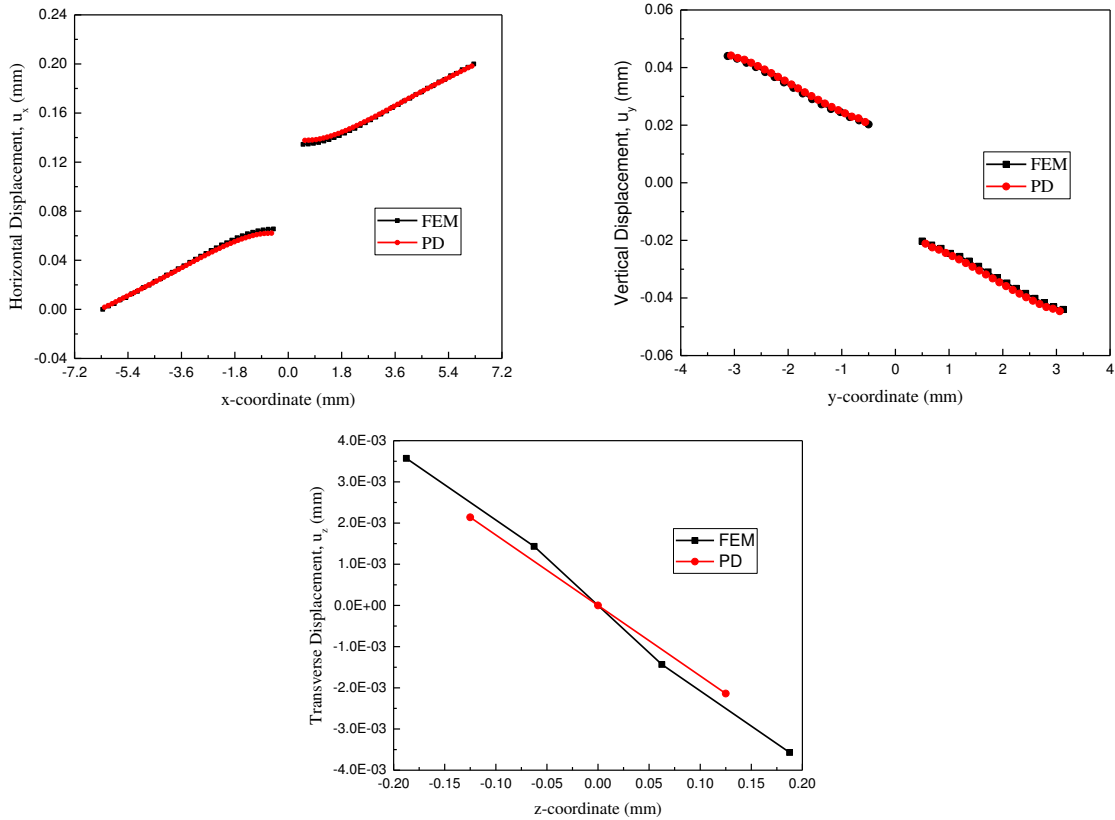


Figure 10. Comparison of the deformation of a composite laminated plate [45/0/45] with an open-hole. Left: along x -axis for midply ($y = 0, z = 0$). Right: along y -axis for midply ($x = 0, z = 0$). Bottom: along z -direction at the hole edge in the 45° direction ($x = \sqrt{2}R/2, y = \sqrt{2}R/2$).

specimen	material system	L	W	D	thickness	layup	h/ply
A1	IM7/977-3	138.43	38.1	6.35	2	[0/45/90/−45] _{2s}	0.125
A2	IM7/8552	64	16	3.175	1	[90/45/0/−45] _s	0.125
A3	IM7/8552	64	16	3.175	2	[90 ₂ /45 ₂ /0 ₂ /−45 ₂] _s	0.125

Table 1. Specimen configuration of composite laminates with an open-hole: data for A1 are from [Hu and Madenci 2016], whereas data for A2 and A3 are from [Hallett et al. 2007]. All dimensions are in units of mm.

E_1 (GPa)	E_2 (GPa)	G_{12} (GPa)	ν_{12}	X^T (MPa)	X^C (MPa)	Y^T (MPa)	Y^C (MPa)
164.3	8.977	5.02	0.32	2905	1680	100	247

Table 2. Material properties of IM7/977-3 [Hu and Madenci 2016] ($\rho = 1603 \text{ kg/m}^3$).

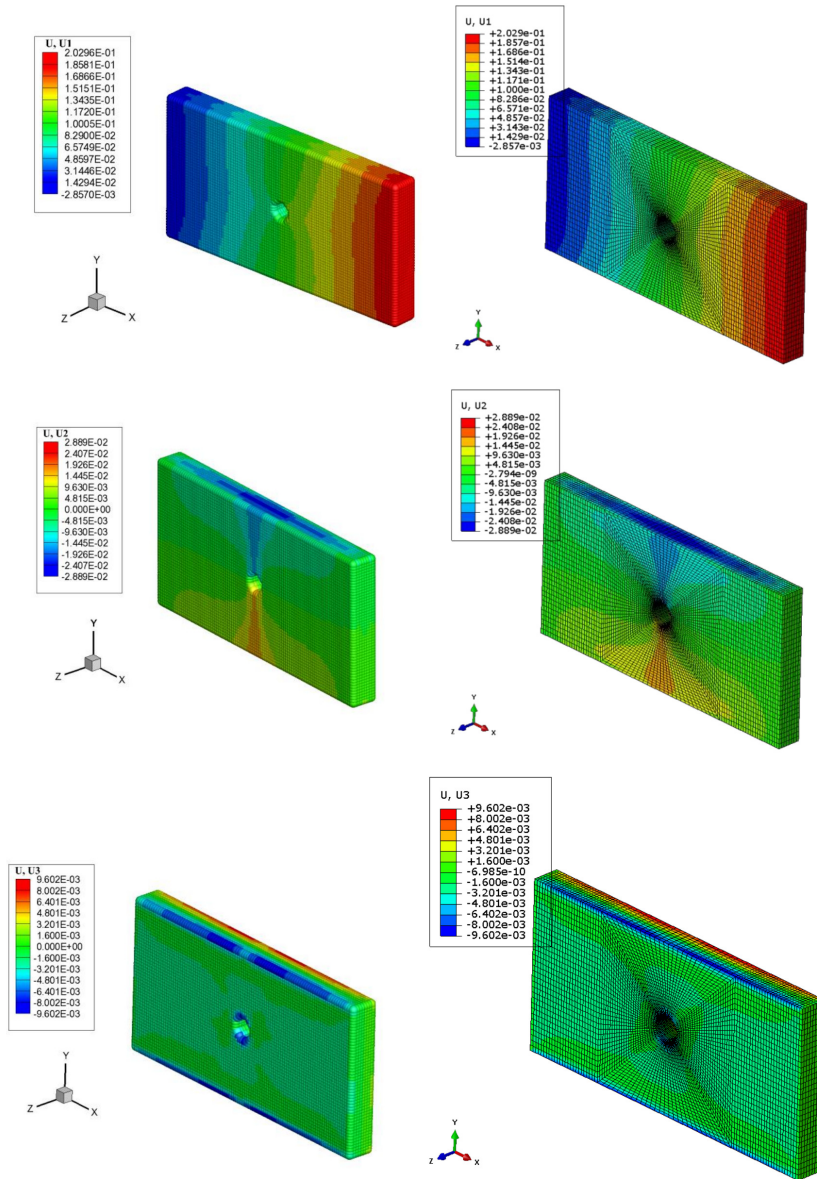


Figure 11. Comparison of the deformation of a composite laminated plate [90/45/0/-45]_s with an open-hole. Left: PD. Right: FEM.

E_1 (GPa)	E_2 (GPa)	G_{12} (GPa)	ν_{12}	X^T (MPa)	X^C (MPa)	Y^T (MPa)	Y^C (MPa)
161	11.38	5.17	0.32	2905	1680	100	247

Table 3. Material properties of IM7/8552 [Camanho and Lambert 2006; Hallett et al. 2007].

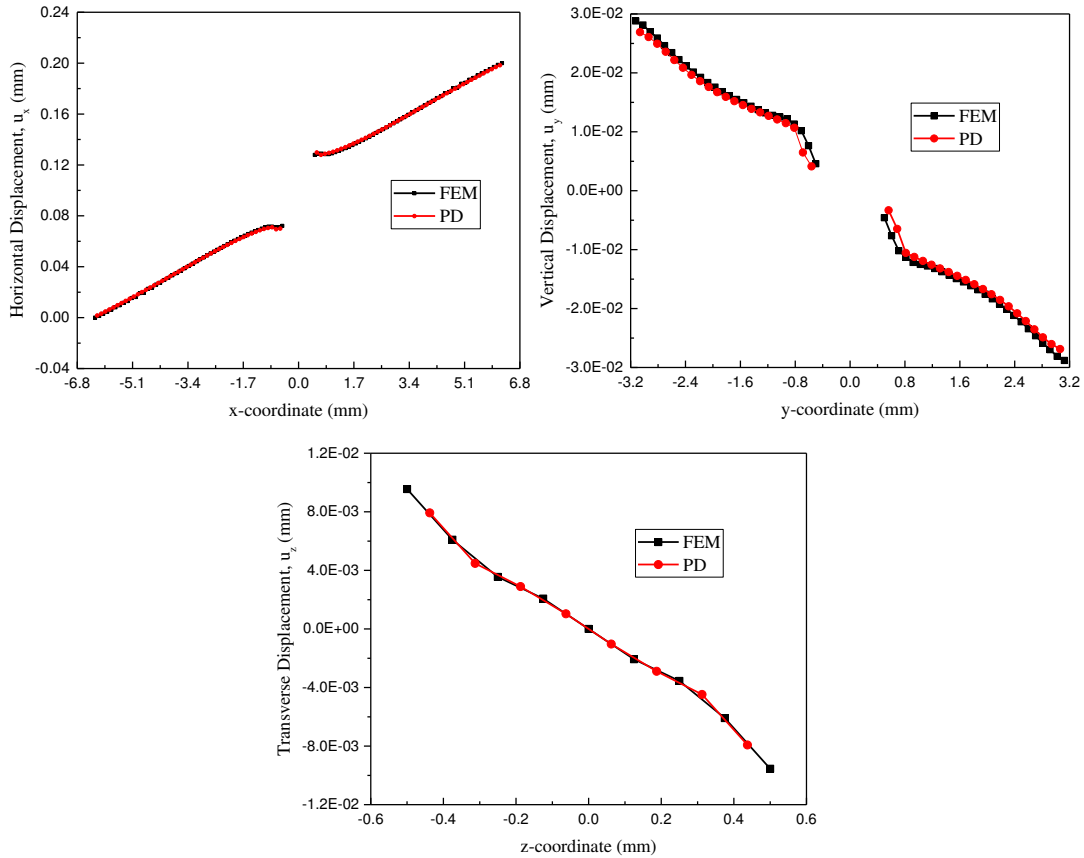


Figure 12. Comparison of the deformation of a composite laminated plate $[90/45/0/-45]_S$ with an open-hole. Left: along x -axis for midply ($y = 0, z = 0$). Right: along y -axis for midply ($x = 0, z = 0$). Bottom: along z direction at the hole edge in the 90° direction ($x = 0, y = R$).

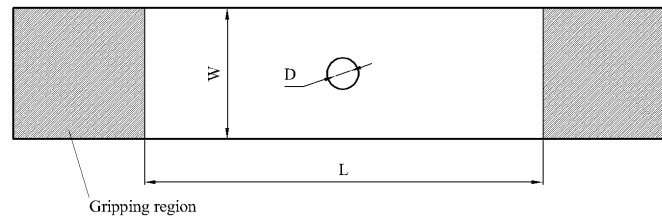


Figure 13. Schematic of open-hole tensile test specimen.

To further the verification of the deformation, the displacement field of specimen A1, with layup $[0/45/90/-45]_{2S}$, is compared with FEM results. Tensile loading of 0.5 mm at the right end of the specimen is applied. The deformation contour is shown in Figure 14, and the variation of the in-plane and out-of-plane displacement in three directions are presented in Figure 16. The vertical and transverse

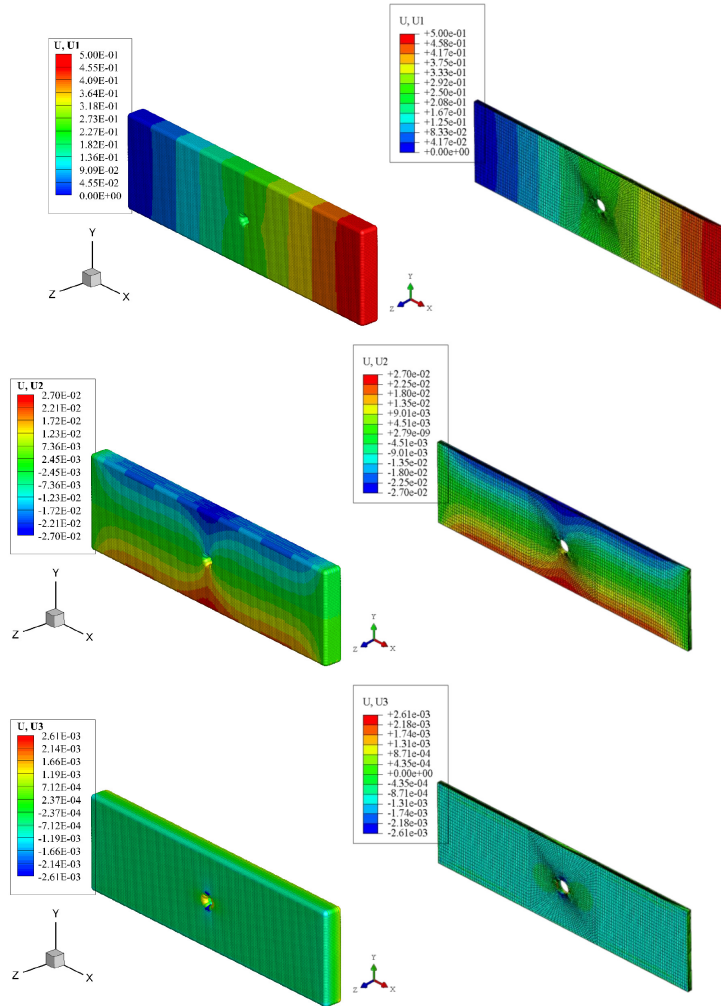


Figure 14. Comparison of the deformation of $[0/45/90/-45]_{2S}$ open-hole composite laminate under tensile loading in x -direction. Left: PD. Right: FEM.

deformation results in Figure 16, right, and Figure 16, bottom, are not as good as the results in Figure 12, right, and Figure 12, bottom. This is mainly due to the usage of an uneven mesh for in-plane and out-of-plane material points. For this specimen A1, $dx \approx 5h$. As using the uneven mesh largely increases the computational efficiency, this slight mismatch between the PD results and FEM results is acceptable. The transverse deformation contour around the hole is also presented in Figure 15. It is interesting to find that for the top surface of the laminate $[0/45/90/-45]_{2S}$, the transverse displacement u_z in the 0° direction along the hole edge is positive, while the transverse Poisson's ratio tends to induce a negative displacement for the top surface. It is not possible to capture this phenomenon if the transverse Poisson's ratios ν_{13} and ν_{23} are not introduced into the PD model.

Open-hole tensile strength prediction results and mesh conditions are shown in Table 4. "Uneven spherical horizon" is adopted as $dx > h$, and the horizon $\delta = 3dx$. It can be seen from the table that the

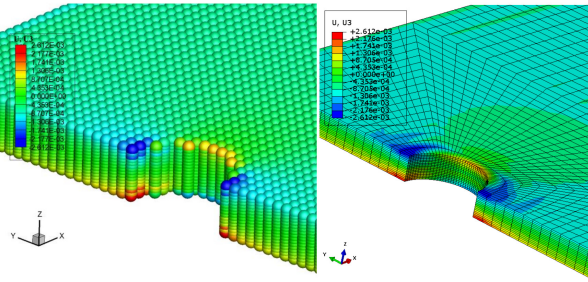


Figure 15. Comparison of the deformation of $[0/45/90/-45]_{2S}$ open-hole composite laminate under tensile loading in x -direction, transverse displacement field around the hole. Left: PD. Right: FEM.

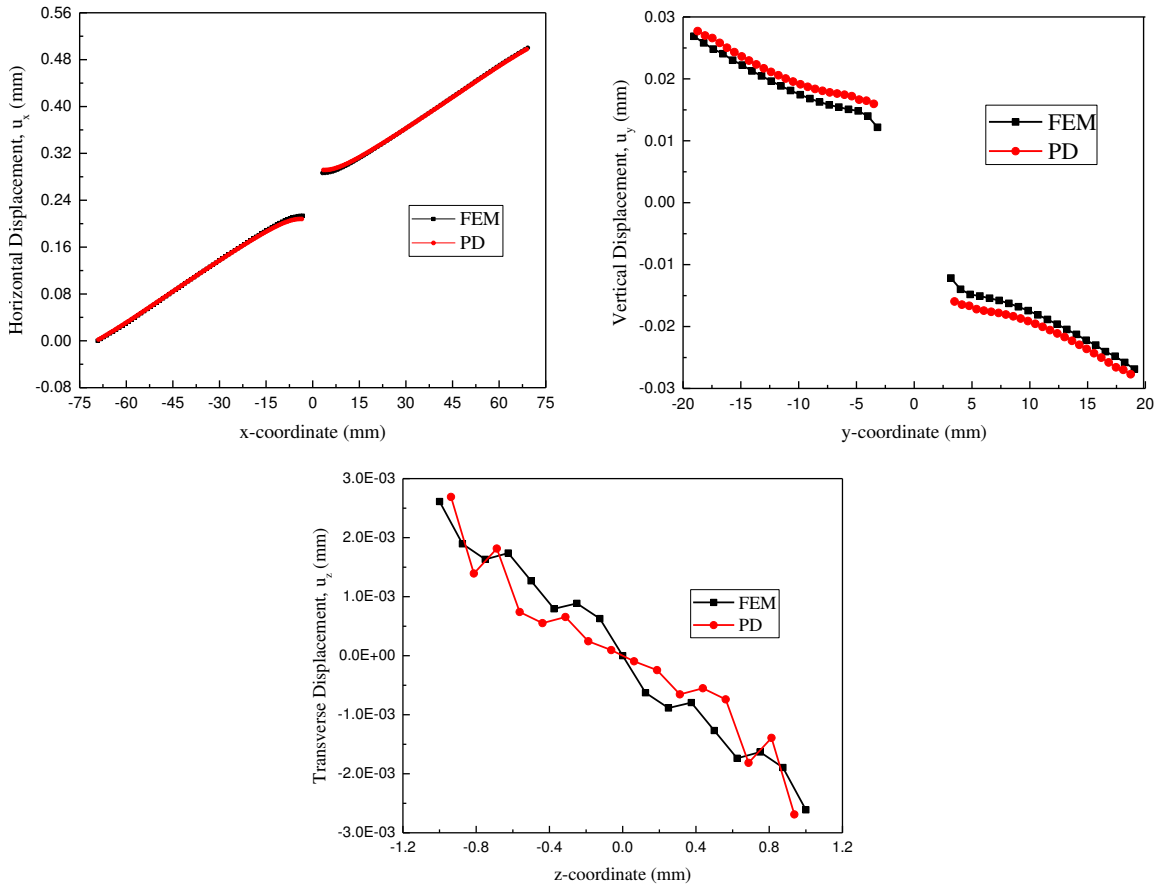


Figure 16. Comparison of the deformation of $[0/45/90/-45]_{2S}$ open-hole composite laminate under tensile loading in x -direction. Left: along x -axis for midply ($y = 0, z = 0$). Right: along y -axis for midply ($x = 0, z = 0$). Bottom: along z -direction at the hole in the 90° direction ($x = 0, y = R$).

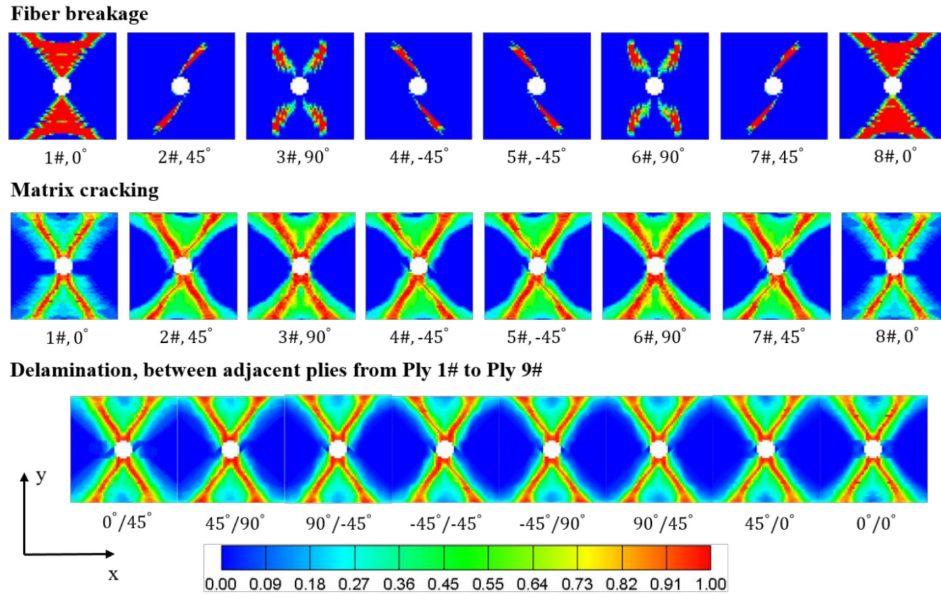


Figure 17. Damage patterns at final failure in each ply of $[0/45/90/-45]_{2S}$ open-hole composite laminate under tensile loading in x -direction.

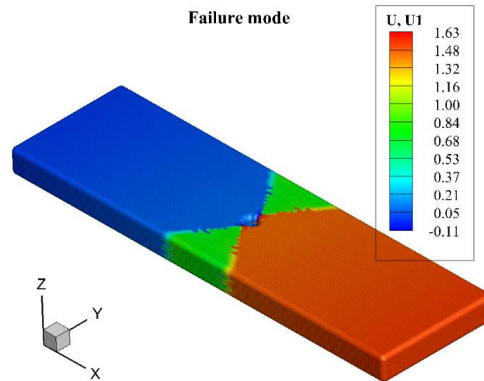


Figure 18. Displacement field in x -direction u (mm) at final failure of $[0/45/90/-45]_{2S}$ open-hole composite laminate under tensile loading in x -direction.

strength prediction results simulated by the preset OSB PD composite model fit the experimental results well. Damage patterns and failure modes of these specimens are presented in Figures 17–22. Three typical damage modes, fiber breakage, matrix cracking, and delamination, are calculated according to (40). These damage patterns illustrated in Figures 17, 19, and 21 represent a square area around the open-hole of each ply, and the dimension of the square equals the width of the specimen. Final failure modes of the specimens are characterized by the final displacement field in x -direction, as shown in Figures 18, 20, and 22.

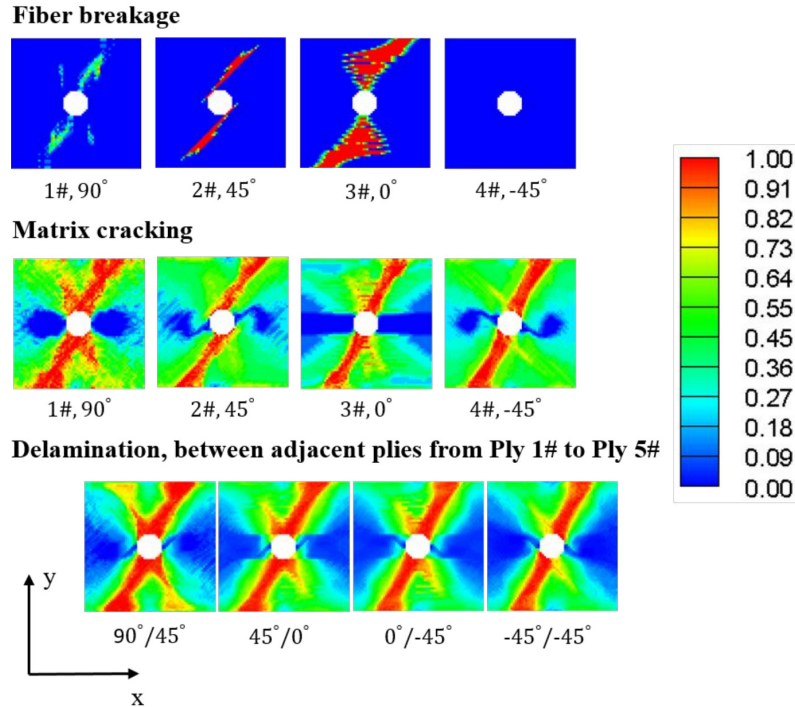


Figure 19. Damage patterns at final failure in each ply of $[90/45/0/-45]_S$ open-hole composite laminate under tensile loading in x -direction.

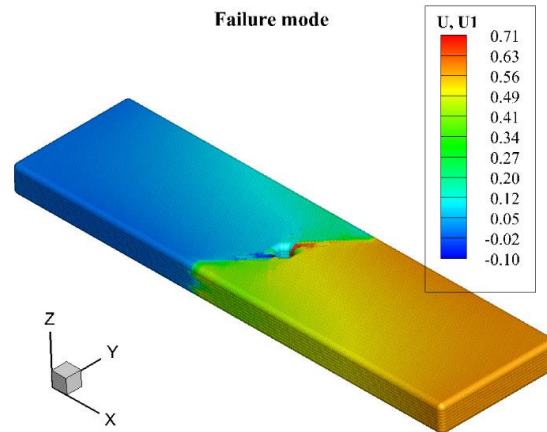


Figure 20. Displacement field in x -direction u (mm) at final failure of $[90/45/0/-45]_S$ open-hole composite laminate under tensile loading in x -direction.

For the open-hole composite laminate specimen A1, with layup $[0/45/90/-45]_{2S}$, it can be seen from Figure 17 that fiber breakage mainly happens in 0° plies, and for the 45° and -45° plies, the damage direction is consistent with their fiber direction. Matrix cracking and delamination damage form a cross

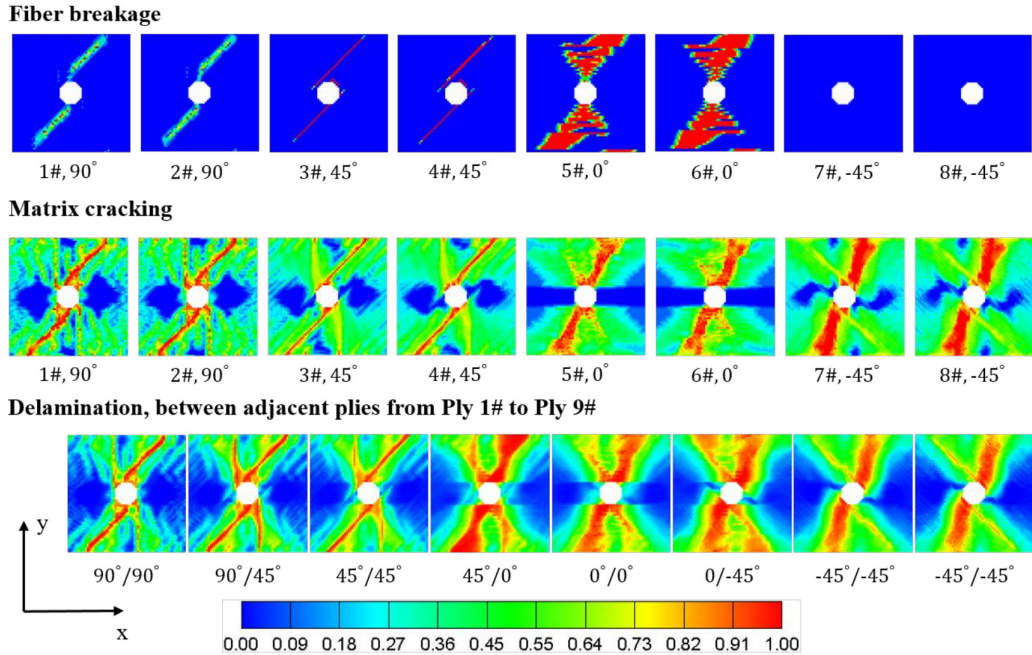


Figure 21. Damage patterns at final failure in each ply of $[90_2/45_2/0_2/-45_2]_S$ open-hole composite laminate under tensile loading in x -direction.

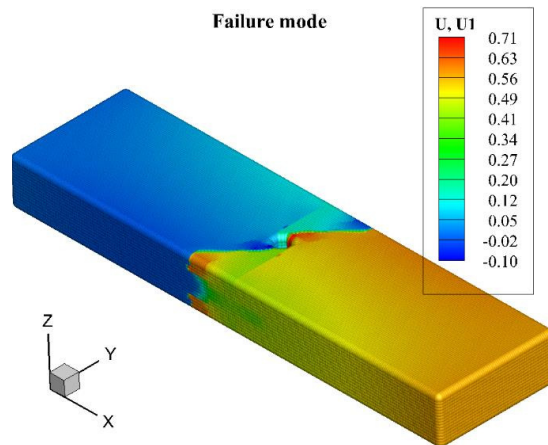


Figure 22. Displacement field in x -direction u (mm) at final failure of $[90_2/45_2/0_2/-45_2]_S$ open-hole composite laminate under tensile loading in x -direction.

$\pm 45^\circ$ area around the open-hole, and matrix cracking in 90° plies are obvious. Figure 18 presents the final failure mode of A1. The specimen fails around the open-hole with cross $\pm 45^\circ$ fracture surface.

For an open-hole composite laminate specimen A2, with layout $[90/45/0/-45]_S$, it can be seen from Figure 19 that similarly to A1, fiber breakage mainly happens in 0° plies, and the damage direction is consistent with their fiber direction for 45° plies. It is interesting that in ply #4 of A2, with fiber direction

specimen	mesh	dx (mm)	h (mm)	experiment (MPa)	PD (MPa)	relative error
A1	$218 \times 60 \times 16$	0.635	0.125	554	590.55	6.6%
A2	$256 \times 64 \times 8$	0.25	0.125	481	462.7	-3.8%
A3	$256 \times 64 \times 16$	0.25	0.125	474	431.25	-9.02%

Table 4. Open-hole tensile strength prediction of fiber-reinforced composite laminates

-45° , fiber breakage does not happen. This damage pattern is also detected in A3, as shown in Figure 21; the -45° plies #7 and #8 do not exhibit fiber breakage. Matrix cracking in A2 is severe, and the effect of fiber direction on matrix cracking can be obviously observed by comparing plies #2 and #4 in Figure 19. Delamination between adjacent plies of A2 changes from surface to midplane in the specimen. From Figure 20, we can also observe an obvious 45° fracture surface as the final failure mode of A2.

Specimen A3, with layup $[90_2/45_2/0_2/-45_2]_s$, is directly double the layup of A2. Comparing Figure 19 and Figure 21, we can see that although they both have the same layup proportion, the damage patterns change with an increase in thickness. Comparing the three damage modes of A2 and A3 respectively, we find that the most significant change between A2 and A3 is delamination damage, which indicates that delamination is the most sensitive damage mode to thickness change, and in order to precisely capture the delamination damage, the transverse Poisson's effect should be considered. The final fracture surface of A3 is similar to A2, as shown in Figure 22. From the simulation results of A2 and A3, we can see that the present OSB PD model for composite laminates can capture the effect of thickness on damage patterns, especially for delamination damage.

From the results above, we can conclude that the present OSB PD composite model is validated in open-hole tensile strength prediction of fiber-reinforced composite laminates, and is able to precisely capture the typical damage patterns and failure modes of composite laminates, especially when capturing the effect of thickness on damage patterns.

5. Conclusion

Open-hole strength prediction of fiber-reinforced composite laminates is a fundamental problem in the analysis of composite structures. An ordinary state-based peridynamic (OSB PD) model for open-hole tensile strength prediction is proposed. The transverse Poisson's effect of composites is considered in the present OSB PD composite model, ensuring a precise capture of typical damage patterns and failure modes of composite laminates, especially when capturing the effect of thickness on damage patterns. The out-of-plane bond considers not only the adjacent plies, but also all the plies within the spherical horizon. Although each ply has to be meshed, the in-plane mesh could be much larger than the out-of-plane mesh, forming an "uneven spherical horizon". The validation of the present model is demonstrated by several numerical results. The deformation of a composite laminated plate without and with an open-hole is simulated by both PD and FEM, and the deformation results of the present OSB PD composite model fit the FEM results well. Three different experiments for the open-hole tensile strength of fiber-reinforced composite laminates from the literature are simulated by the present model. By comparing the simulation results with experimental results and discussing the predicted damage patterns and final failure modes, we can conclude that the present OSB PD composite model is validated in open-hole tensile strength

prediction of fiber-reinforced composite laminates, and is able to precisely capture the typical damage patterns and failure modes of composite laminates, especially when capturing the effect of thickness on damage patterns.

Acknowledgments

The authors are indebted to Professor Hui-Shen Shen of Shanghai Jiao Tong University for his considerable support. The study in the present paper is supported by Center for HPC, Shanghai Jiao Tong University.

Appendix

The PD material parameters a , d , b , b_F , and b_T can be derived by comparing the PD strain energy density and the strain energy density of continuum mechanics under simple loading conditions. In the present OSB PD composite model, we derive these parameters by assuming a unidirectional composite laminate under four simple loading conditions:

(1) Transverse pure shear loading on xz -plane (γ_{13}):

$$\begin{aligned}
\gamma_{13} &= \zeta, \quad \theta_{(k)}^{CM} = 0, \quad W_{(k)}^{CM} = \frac{1}{2} C_{55} \zeta^2, \quad s_{(k)(j)} = \zeta \sin \varphi \cos \varphi \cos \theta. \\
W_{(k)}^{(n)} &= a \theta_{(k)}^2 + b \sum_{j=1}^{\infty} \delta |\mathbf{x}_{(j)} - \mathbf{x}_{(k)}| s_{(k)(j)}^2 V_{(j)} + b_F \sum_{j=1}^J \delta |\mathbf{x}_{(j)}^{(n)} - \mathbf{x}_{(k)}^{(n)}| s_{(k)(j)}^{(n)2} V_{(j)} \\
&\quad + b_T \sum_{j=1}^J \delta |\mathbf{x}_{(j)}^{(n)} - \mathbf{x}_{(k)}^{(n)}| s_{(k)(j)}^{(n)2} V_{(j)} \\
&= b \sum_{j=1}^{\infty} \delta |\mathbf{x}_{(j)} - \mathbf{x}_{(k)}| s_{(k)(j)}^2 V_{(j)} = b \sum_{j=1}^{\infty} \delta \xi (\zeta \sin \varphi \cos \varphi \cos \theta)^2 V_{(j)} \\
&= \zeta^2 b \delta \int_0^{2\pi} \int_0^{\pi} \int_0^{\delta} \xi \sin^2 \varphi \cos^2 \varphi \cos^2 \theta \xi^2 \sin \varphi \, dr \, d\varphi \, d\theta \\
&= \zeta^2 b \delta \int_0^{2\pi} \cos^2 \theta \, d\theta \int_0^{\pi} \sin^3 \varphi \cos^2 \varphi \, d\varphi \int_0^{\delta} \xi^3 \, dr. \\
\int_0^{2\pi} \cos^2 \theta \, d\theta &= \pi, \quad \int_0^{\pi} \sin^3 \varphi \cos^2 \varphi \, d\varphi = \frac{4}{15}, \quad \int_0^{\delta} \xi^3 \, dr = \frac{1}{4} \delta^4. \\
W_{(k)}^{(n)} &= \zeta^2 b \delta \pi \times \frac{4}{15} \times \frac{1}{4} \delta^4 = \zeta^2 b \frac{\pi^2}{15} \delta^5. \\
b &= \frac{1/2 C_{55} \zeta^2}{\sum_{j=1}^{\infty} \delta |\mathbf{x}_{(j)} - \mathbf{x}_{(k)}| s_{(k)(j)}^2 V_{(j)}} = \frac{1/2 C_{55} \zeta^2}{\zeta^2 \pi / 15 \delta^5} = \frac{15 C_{55}}{2 \pi \delta^5}. \tag{A.1}
\end{aligned}$$

(2) Transverse tensile loading (ε_{33}):

$$\varepsilon_{33} = \zeta, \quad \theta_{(k)}^{CM} = \zeta, \quad W_{(k)}^{CM} = \frac{1}{2} C_{33} \zeta^2, \quad s_{(k)(j)} = \zeta \cos^2 \varphi.$$

$$\begin{aligned}
\theta_{(k)} &= d \sum_{j=1}^{\infty} \delta s_{(k)(j)} \Lambda_{(k)(j)} V_{(j)} = d \sum_{j=1}^{\infty} \delta \zeta \cos^2 \varphi V_{(j)} = \zeta d \delta \int_0^{2\pi} \int_0^{\pi} \int_0^{\delta} \cos^2 \varphi \xi^2 \sin \varphi \, dr \, d\varphi \, d\theta \\
&= \zeta d \delta \int_0^{2\pi} d\theta \int_0^{\pi} \cos^2 \varphi \sin \varphi \, d\varphi \int_0^{\delta} \xi^2 \, dr. \\
\int_0^{\pi} \cos^2 \varphi \sin \varphi \, d\varphi &= \frac{2}{3}, \quad \theta_{(k)} = \zeta d \delta 2\pi \times \frac{2}{3} \times \frac{1}{3} \delta^3 = \zeta d \frac{4}{9} \pi \delta^4. \\
d &= \frac{\zeta}{\sum_{j=1}^{\infty} \delta s_{(k)(j)} \Lambda_{(k)(j)} V_{(j)}} = \frac{\zeta}{\zeta \frac{4}{9} \pi \delta^4} = \frac{9}{4\pi \delta^4}. \tag{A.2}
\end{aligned}$$

$$\begin{aligned}
W_{(k)}^{(n)} &= a\theta_{(k)}^2 + b \sum_{j=1}^{\infty} \delta |\mathbf{x}_{(j)} - \mathbf{x}_{(k)}| s_{(k)(j)}^2 V_{(j)} + b_F \sum_{j=1}^J \delta |\mathbf{x}_{(j)}^{(n)} - \mathbf{x}_{(k)}^{(n)}| s_{(k)(j)}^{(n)2} V_{(j)}^{(n)} \\
&\quad + b_T \sum_{j=1}^J \delta |\mathbf{x}_{(j)}^{(n)} - \mathbf{x}_{(k)}^{(n)}| s_{(k)(j)}^{(n)2} V_{(j)}^{(n)}
\end{aligned}$$

$$= a\theta_{(k)}^2 + b \sum_{j=1}^{\infty} \delta |\mathbf{x}_{(j)} - \mathbf{x}_{(k)}| s_{(k)(j)}^2 V_{(j)} = a\zeta^2 + b \sum_{j=1}^{\infty} \delta \xi (\zeta \cos^2 \varphi)^2 V_{(j)}$$

$$= a\zeta^2 + \zeta^2 b \delta \int_0^{2\pi} \int_0^{\pi} \int_0^{\delta} \xi \cos^4 \varphi \xi^2 \sin \varphi \, dr \, d\varphi \, d\theta$$

$$= a\zeta^2 + \zeta^2 b \delta \int_0^{2\pi} d\theta \int_0^{\pi} \cos^4 \varphi \sin \varphi \, d\varphi \int_0^{\delta} \xi^3 \, dr.$$

$$\int_0^{\pi} \cos^4 \varphi \sin \varphi \, d\varphi = \frac{2}{5}.$$

$$W_{(k)}^{(n)} = a\zeta^2 + \zeta^2 b \delta 2\pi \times \frac{2}{5} \times \frac{1}{4} \delta^4 = a\zeta^2 + \zeta^2 b \frac{1}{5} \pi \delta^5 = a\zeta^2 + \zeta^2 \frac{15C_{55}}{2\pi \delta^5} \frac{1}{5} \pi \delta^5 = a\zeta^2 + \zeta^2 \frac{3}{2} C_{55}.$$

$$a = \frac{1}{2} (C_{33} - 3C_{55}). \tag{A.3}$$

(3) In-plane uniaxial tension in x direction (ε_{11}),

$$\varepsilon_{11} = \zeta, \quad \theta_{(k)}^{CM} = \zeta, \quad W_{(k)}^{CM} = \frac{1}{2} C_{11} \zeta^2,$$

$$s_{(k)(j)} = \zeta \sin^2 \varphi \cos^2 \theta.$$

$$\theta_{(k)} = d \sum_{j=1}^{\infty} \delta s_{(k)(j)} \Lambda_{(k)(j)} V_{(j)} = d \sum_{j=1}^{\infty} \delta \zeta \sin^2 \varphi \cos^2 \theta V_{(j)}$$

$$= \zeta d \delta \int_0^{2\pi} \int_0^{\pi} \int_0^{\delta} \sin^2 \varphi \cos^2 \theta \xi^2 \sin \varphi \, dr \, d\varphi \, d\theta$$

$$= \zeta d \delta \int_0^{2\pi} \cos^2 \theta d\theta \int_0^{\pi} \sin^3 \varphi \, d\varphi \int_0^{\delta} \xi^2 \, dr.$$

$$\begin{aligned}
& \int_0^{2\pi} \cos^2 \theta \, d\theta = \pi, \quad \int_0^\pi \sin^3 \varphi \, d\varphi = \frac{4}{3}. \\
\theta_{(k)} &= \zeta \, d\delta \int_0^{2\pi} \cos^2 \theta \, d\theta \int_0^\pi \sin^3 \varphi \, d\varphi \int_0^\delta \xi^2 \, dr = \zeta \, d\delta \pi \times \frac{4}{3} \times \frac{1}{3} \delta^3 = \zeta \, d \frac{4}{9} \pi \delta^4. \\
d &= \frac{\zeta}{\sum_{j=1}^{\infty} \delta s_{(k)(j)} \Lambda_{(k)(j)} V_{(j)}} = \frac{\zeta}{\zeta \, 4/9 \pi \delta^4} = \frac{9}{4\pi \delta^4}, \\
W_{(k)}^{(n)} &= a\theta_{(k)}^2 + b \sum_{j=1}^{\infty} \delta |\mathbf{x}_{(j)} - \mathbf{x}_{(k)}| s_{(k)(j)}^2 V_{(j)} + b_F \sum_{j=1}^J \delta |\mathbf{x}_{(j)}^{(n)} - \mathbf{x}_{(k)}^{(n)}| s_{(k)(j)}^{(n)2} V_{(j)}^{(n)} \\
&\quad + b_T \sum_{j=1}^J \delta |\mathbf{x}_{(j)}^{(n)} - \mathbf{x}_{(k)}^{(n)}| s_{(k)(j)}^{(n)2} V_{(j)}^{(n)} \\
&= a\zeta^2 + b \sum_{j=1}^{\infty} \delta \xi (\zeta \sin^2 \varphi \cos^2 \theta)^2 V_{(j)} + b_F \sum_{j=1}^J \delta |\mathbf{x}_{(j)}^{(n)} - \mathbf{x}_{(k)}^{(n)}| (\zeta \cos^2 \theta)^2 V_{(j)}^{(n)} \\
&= a\zeta^2 + \zeta^2 b \delta \int_0^{2\pi} \int_0^\pi \int_0^\delta \xi \sin^4 \varphi \cos^4 \theta \xi^2 \sin \varphi \, dr \, d\varphi \, d\theta + \zeta^2 b_F \delta \sum_{j=1}^J |\mathbf{x}_{(j)}^{(n)} - \mathbf{x}_{(k)}^{(n)}| V_{(j)}^{(n)} \\
&= a\zeta^2 + \zeta^2 b \delta \int_0^{2\pi} \cos^4 \theta \, d\theta \int_0^\pi \sin^5 \varphi \, d\varphi \int_0^\delta \xi^3 \, dr + \zeta^2 b_F \delta \sum_{j=1}^J |\mathbf{x}_{(j)}^{(n)} - \mathbf{x}_{(k)}^{(n)}| V_{(j)}^{(n)}. \\
&\quad \int_0^{2\pi} \cos^4 \theta \, d\theta = \frac{3}{4}\pi, \quad \int_0^\pi \sin^5 \varphi \, d\varphi = \frac{16}{15}. \\
W_{(k)}^{(n)} &= a\zeta^2 + \zeta^2 b \delta \int_0^{2\pi} \cos^4 \theta \, d\theta \int_0^\pi \sin^5 \varphi \, d\varphi \int_0^\delta \xi^3 \, dr + \zeta^2 b_F \delta \sum_{j=1}^J |\mathbf{x}_{(j)}^{(n)} - \mathbf{x}_{(k)}^{(n)}| V_{(j)}^{(n)} \\
&= a\zeta^2 + \zeta^2 b \delta \times \frac{3}{4}\pi \times \frac{16}{15} \times \frac{1}{4} \delta^4 + \zeta^2 b_F \delta \sum_{j=1}^J |\mathbf{x}_{(j)}^{(n)} - \mathbf{x}_{(k)}^{(n)}| V_{(j)}^{(n)} \\
&= a\zeta^2 + \zeta^2 b \frac{\pi}{5} \delta^5 + \zeta^2 b_F \delta \sum_{j=1}^J |\mathbf{x}_{(j)}^{(n)} - \mathbf{x}_{(k)}^{(n)}| V_{(j)}^{(n)} \\
&\quad a + b \frac{\pi}{5} \delta^5 + b_F \delta \sum_{j=1}^J |\mathbf{x}_{(j)}^{(n)} - \mathbf{x}_{(k)}^{(n)}| V_{(j)}^{(n)} = \frac{1}{2} C_{11}. \tag{A.4}
\end{aligned}$$

Substituting a and b from (A.3) and (A.1), (A.4) becomes

$$\begin{aligned}
& \frac{1}{2}(C_{33} - 3C_{55}) + \frac{15C_{55}}{2\pi\delta^5} \times \frac{\pi}{5} \delta^5 + b_F \delta \sum_{j=1}^J |\mathbf{x}_{(j)}^{(n)} - \mathbf{x}_{(k)}^{(n)}| V_{(j)}^{(n)} = \frac{1}{2} C_{11}, \\
& \frac{1}{2}(C_{11} - 3C_{55}) + \frac{3}{2} C_{55} + b_F \delta \sum_{j=1}^J |\mathbf{x}_{(j)}^{(n)} - \mathbf{x}_{(k)}^{(n)}| V_{(j)}^{(n)} = \frac{1}{2} C_{11},
\end{aligned}$$

$$b_F = \frac{1/2 (C_{11} - C_{33})}{\delta \sum_{j=1}^J |\mathbf{x}_{(j)}^{(n)} - \mathbf{x}_{(k)}^{(n)}| V_{(j)}}. \quad (\text{A.5})$$

(4) In-plane uniaxial tension in y direction (ε_{22}):

$$\varepsilon_{22} = \zeta, \quad \theta_{(k)}^{CM} = \zeta, \quad W_{(k)}^{CM} = \frac{1}{2} C_{22} \zeta^2,$$

$$s_{(k)(j)} = \zeta \sin^2 \varphi \sin^2 \theta.$$

$$\theta_{(k)} = d \sum_{j=1}^{\infty} \delta s_{(k)(j)} \Lambda_{(k)(j)} V_{(j)} = d \sum_{j=1}^{\infty} \delta \zeta \sin^2 \varphi \sin^2 \theta V_{(j)}$$

$$= \zeta d \delta \int_0^{2\pi} \int_0^{\pi} \int_0^{\delta} \sin^2 \varphi \sin^2 \theta \xi^2 \sin \varphi dr d\varphi d\theta$$

$$= \zeta d \delta \int_0^{2\pi} \sin^2 \theta d\theta \int_0^{\pi} \sin^3 \varphi d\varphi \int_0^{\delta} \xi^2 dr.$$

$$\int_0^{2\pi} \sin^2 \theta d\theta = \pi, \quad \int_0^{\pi} \sin^3 \varphi d\varphi = \frac{4}{3}.$$

$$\theta_{(k)} = \zeta d \delta \int_0^{2\pi} \sin^2 \theta d\theta \int_0^{\pi} \sin^3 \varphi d\varphi \int_0^{\delta} \xi^2 dr = \zeta d \delta \pi \times \frac{4}{3} \times \frac{1}{3} \delta^3 = \zeta d \frac{4}{3} \pi \delta^4.$$

$$d = \frac{\zeta}{\sum_{j=1}^{\infty} \delta s_{(k)(j)} \Lambda_{(k)(j)} V_{(j)}} = \frac{\zeta}{\zeta \frac{4}{9} \pi \delta^4} = \frac{9}{4\pi \delta^4}.$$

$$W_{(k)}^{(n)} = a \theta_{(k)}^2 + b \sum_{j=1}^{\infty} \delta |\mathbf{x}_{(j)} - \mathbf{x}_{(k)}| s_{(k)(j)}^2 V_{(j)} + b_F \sum_{j=1}^J \delta |\mathbf{x}_{(j)}^{(n)} - \mathbf{x}_{(k)}^{(n)}| s_{(k)(j)}^{(n)2} V_{(j)}^{(n)}$$

$$+ b_T \sum_{j=1}^J \delta |\mathbf{x}_{(j)}^{(n)} - \mathbf{x}_{(k)}^{(n)}| s_{(k)(j)}^{(n)2} V_{(j)}^{(n)}$$

$$= a \zeta^2 + b \sum_{j=1}^{\infty} \delta \xi (\zeta \sin^2 \varphi \sin^2 \theta)^2 V_{(j)} + b_T \sum_{j=1}^J \delta |\mathbf{x}_{(j)}^{(n)} - \mathbf{x}_{(k)}^{(n)}| (\zeta \sin^2 \theta)^2 V_{(j)}^{(n)}$$

$$= a \zeta^2 + \zeta^2 b \delta \int_0^{2\pi} \int_0^{\pi} \int_0^{\delta} \xi \sin^4 \varphi \sin^4 \theta \xi^2 \sin \varphi dr d\varphi d\theta + \zeta^2 b_T \delta \sum_{j=1}^J |\mathbf{x}_{(j)}^{(n)} - \mathbf{x}_{(k)}^{(n)}| V_{(j)}^{(n)}$$

$$= a \zeta^2 + \zeta^2 b \delta \int_0^{2\pi} \sin^4 \theta d\theta \int_0^{\pi} \sin^5 \varphi d\varphi \int_0^{\delta} \xi^3 dr + \zeta^2 b_T \delta \sum_{j=1}^J |\mathbf{x}_{(j)}^{(n)} - \mathbf{x}_{(k)}^{(n)}| V_{(j)}^{(n)}.$$

$$\int_0^{2\pi} \sin^4 \theta d\theta = \frac{3}{4} \pi, \quad \int_0^{\pi} \sin^5 \varphi d\varphi = \frac{16}{15}.$$

$$W_{(k)}^{(n)} = a \zeta^2 + \zeta^2 b \delta \int_0^{2\pi} \sin^4 \theta d\theta \int_0^{\pi} \sin^5 \varphi d\varphi \int_0^{\delta} \xi^3 dr + \zeta^2 b_T \delta \sum_{j=1}^J |\mathbf{x}_{(j)}^{(n)} - \mathbf{x}_{(k)}^{(n)}| V_{(j)}^{(n)}$$

$$\begin{aligned}
&= a\zeta^2 + \zeta^2 b\delta \times \frac{3}{4}\pi \times \frac{16}{15} \times \frac{1}{4}\delta^4 + \zeta^2 b_T \delta \sum_{j=1}^J |\mathbf{x}_{(j)}^{(n)} - \mathbf{x}_{(k)}^{(n)}| V_{(j)}^{(n)} \\
&= a\zeta^2 + \zeta^2 b \frac{\pi}{5} \delta^5 + \zeta^2 b_T \delta \sum_{j=1}^J |\mathbf{x}_{(j)}^{(n)} - \mathbf{x}_{(k)}^{(n)}| V_{(j)}^{(n)}. \\
&\quad a + b \frac{\pi}{5} \delta^5 + b_T \delta \sum_{j=1}^J |\mathbf{x}_{(j)}^{(n)} - \mathbf{x}_{(k)}^{(n)}| V_{(j)}^{(n)} = \frac{1}{2} C_{22}. \tag{A.6}
\end{aligned}$$

Substituting a and b from (A.3) and (A.1), (A.6) becomes

$$\begin{aligned}
&\frac{1}{2}(C_{33} - 3C_{55}) + \frac{15C_{55}}{2\pi\delta^5} \times \frac{\pi}{5} \delta^5 + b_T \delta \sum_{j=1}^J |\mathbf{x}_{(j)}^{(n)} - \mathbf{x}_{(k)}^{(n)}| V_{(j)}^{(n)} = \frac{1}{2} C_{22}, \\
&\frac{1}{2}(C_{33} - 3C_{55}) + \frac{3}{2} C_{55} + b_T \delta \sum_{j=1}^J |\mathbf{x}_{(j)}^{(n)} - \mathbf{x}_{(k)}^{(n)}| V_{(j)}^{(n)} = \frac{1}{2} C_{22}, \\
&\quad b_T = \frac{1/2 (C_{22} - C_{33})}{\delta \sum_{j=1}^J |\mathbf{x}_{(j)}^{(n)} - \mathbf{x}_{(k)}^{(n)}| V_{(j)}^{(n)}}. \tag{A.7}
\end{aligned}$$

References

- [Aidi and Case 2015] B. Aidi and S. W. Case, “Experimental and numerical analysis of notched composites under tension loading”, *Appl. Compos. Mater.* **22**:6 (2015), 837–855.
- [Askari et al. 2006] E. Askari, J. Xu, and S. A. Silling, “Peridynamic analysis of damage and failure in composites”, in *44th AIAA aerospace sciences meeting and exhibition* (Reno), 2006.
- [ASTM 2011] “Standard test method for open-hole tensile strength of polymer matrix composite laminates”, standard, American Society for Testing and Materials (ASTM) International, West Conshohocken, PA, 2011.
- [Bao and Liu 2016] H. Bao and G. Liu, “Progressive failure analysis on scaled open-hole tensile composite laminates”, *Compos. Struct.* **150** (2016), 173–180.
- [Bartan et al. 2016] B. Bartan, B. Acar, and A. Kayran, “Three-dimensional delamination analysis in composite open hole tensile specimens with cohesive zone method”, in *57th AIAA/ASCE/AHS/ASC structures, structural dynamics, and materials conference*, 2016.
- [Camanho and Lambert 2006] P. P. Camanho and M. Lambert, “A design methodology for mechanically fastened joints in laminated composite materials”, *Compos. Sci. Technol.* **66**:15 (2006), 3004–3020.
- [Camanho et al. 2007] P. P. Camanho, P. Maimí, and C. G. Dávila, “Prediction of size effects in notched laminates using continuum damage mechanics”, *Compos. Sci. Technol.* **67**:13 (2007), 2715–2727.
- [Chen et al. 2013] B. Y. Chen, T. E. Tay, P. M. Baiz, and S. T. Pinho, “Numerical analysis of size effects on open-hole tensile composite laminates”, *Compos. A Appl. Sci. Manuf.* **47** (2013), 52–62.
- [Colavito 2013] K. Colavito, *Peridynamics for failure and residual strength prediction of fiber-reinforced composites*, electronic dissertation, University of Arizona, 2013, available at <http://arizona.openrepository.com/arizona/handle/10150/311300>.
- [Colavito and Barut 2013] K. Colavito and A. E. M. Barut, “Residual strength of composite laminates with a hole by using peridynamic theory”, in *54th AIAA/ASME/ASCE/AHS/ASC structures, structural dynamics, and materials conference* (Boston), 2013.
- [Diyaroglu et al. 2016] C. Diyaroglu, E. Oterkus, E. Madenci, T. Rabczuk, and A. Siddiq, “Peridynamic modeling of composite laminates under explosive loading”, *Compos. Struct.* **144** (2016), 14–23.

- [Hallett et al. 2007] S. Hallett, W.-G. Jiang, and M. Wisnom, “The effect of stacking sequence on thickness scaling of tests on open hole tensile composite specimens”, in *48th AIAA/ASME/ASCE/AHS/ASC structures, structural dynamics, and materials conference* (Honolulu), 2007.
- [Hallett et al. 2009] S. R. Hallett, B. G. Green, W. G. Jiang, and M. R. Wisnom, “An experimental and numerical investigation into the damage mechanisms in notched composites”, *Compos. A Appl. Sci. Manuf.* **40**:5 (2009), 613–624.
- [Hu and Madenci 2016] Y. L. Hu and E. Madenci, “Bond-based peridynamic modeling of composite laminates with arbitrary fiber orientation and stacking sequence”, *Compos. Struct.* **153** (2016), 139–175.
- [Hu et al. 2011] W. K. Hu, Y. D. Ha, and F. Bobaru, “Modeling dynamic fracture and damage in a fiber-reinforced composite lamina with peridynamics”, *Int. J. Multiscale Comput. Eng.* **9**:6 (2011), 707–726.
- [Hu et al. 2012] W. K. Hu, Y. D. Ha, and F. Bobaru, “Peridynamic model for dynamic fracture in unidirectional fiber-reinforced composites”, *Comput. Methods Appl. Mech. Eng.* **217** (2012), 247–261.
- [Hu et al. 2014] Y. L. Hu, Y. Yu, and H. Wang, “Peridynamic analytical method for progressive damage in notched composite laminates”, *Compos. Struct.* **108** (2014), 801–810.
- [Hu et al. 2015] Y. L. Hu, N. V. De Carvalho, and E. Madenci, “Peridynamic modeling of delamination growth in composite laminates”, *Compos. Struct.* **132** (2015), 610–620.
- [Hu et al. 2016] Y. L. Hu, E. Madenci, and N. D. Phan, “Peridynamics for predicting tensile and compressive strength of notched composites”, in *57th AIAA/ASCE/AHS/ASC structures, structural dynamics, and materials conference* (San Diego), 2016.
- [Kilic and Madenci 2010] B. Kilic and E. Madenci, “An adaptive dynamic relaxation method for quasi-static simulations using the peridynamic theory”, *Theor. Appl. Fract. Mech.* **53**:3 (2010), 194–204.
- [Kilic et al. 2009] B. Kilic, A. Agwai, and E. Madenci, “Peridynamic theory for progressive damage prediction in center-cracked composite laminates”, *Compos. Struct.* **90**:2 (2009), 141–151.
- [Madenci and Oterkus 2014] E. Madenci and E. Oterkus, *Peridynamic theory and its applications*, Springer, New York, 2014.
- [Mohammadi et al. 2017] R. Mohammadi, M. A. Najafabadi, M. Saeedifar, J. Yousefi, and G. Minak, “Correlation of acoustic emission with finite element predicted damages in open-hole tensile laminated composites”, *Compos. B Eng.* **108** (2017), 427–435.
- [Moure et al. 2016] M. M. Moure, S. K. García-Castillo, S. Sánchez-Sáez, E. Barbero, and E. J. Barbero, “Influence of ply cluster thickness and location on matrix cracking evolution in open-hole composite laminates”, *Compos. B Eng.* **95** (2016), 40–47.
- [Oterkus and Madenci 2012a] E. Oterkus and E. Madenci, “Peridynamic analysis of fiber-reinforced composite materials”, *J. Mech. Mater. Struct.* **7**:1 (2012), 45–84.
- [Oterkus and Madenci 2012b] E. Oterkus and E. Madenci, “Peridynamic theory for damage initiation and growth in composite laminate”, pp. 355 in *Advances in fracture and damage mechanics X*, vol. 488–489, edited by Z. Tonkovic and M. H. Aliabadi, 2012.
- [Oterkus et al. 2010] E. Oterkus, A. Barut, and E. Madenci, “Damage growth prediction from loaded composite fastener holes by using peridynamic theory”, in *51st AIAA/ASME/ASCE/AHS/ASC structures, structural dynamics, and materials conference* (Orlando), 2010.
- [Oterkus et al. 2012] E. Oterkus, E. Madenci, O. Weckner, S. Silling, P. Bogert, and A. Tessler, “Combined finite element and peridynamic analyses for predicting failure in a stiffened composite curved panel with a central slot”, *Compos. Struct.* **94**:3 (2012), 839–850.
- [Ruetsch and Fatica 2013] G. Ruetsch and M. Fatica, *CUDA Fortran for scientists and engineers: best practices for efficient CUDA Fortran programming*, Elsevier, Burlington, MA, 2013.
- [Silling 2000] S. A. Silling, “Reformulation of elasticity theory for discontinuities and long-range forces”, *J. Mech. Phys. Solids* **48**:1 (2000), 175–209.
- [Silling and Askari 2005] S. A. Silling and E. Askari, “A meshfree method based on the peridynamic model of solid mechanics”, *Comput. Struct.* **83**:17–18 (2005), 1526–1535.

- [Silling and Lehoucq 2010] S. A. Silling and R. B. Lehoucq, “Peridynamic theory of solid mechanics”, pp. 73–168 in *Advances in applied mechanics*, vol. 44, edited by H. Aref and E. van der Giessen, 2010.
- [Silling et al. 2007] S. A. Silling, M. Epton, O. Weckner, J. Xu, and E. Askari, “Peridynamic states and constitutive modeling”, *J. Elasticity* **88**:2 (2007), 151–184.
- [Su et al. 2015] Z. C. Su, T. E. Tay, M. Ridha, and B. Y. Chen, “Progressive damage modeling of open-hole composite laminates under compression”, *Compos. Struct.* **122** (2015), 507–517.
- [Sun and Huang 2016] C. Y. Sun and Z. X. Huang, “Peridynamic simulation to impacting damage in composite laminate”, *Compos. Struct.* **138** (2016), 335–341.
- [US-DoD 2002] *Composite materials handbook*, Army Research Laboratory, Weapons and Materials Research Directorate, 2002.
- [Xu et al. 2007] J. F. Xu, A. Askari, O. Weckner, H. Razi, and S. Silling, “Damage and failure analysis of composite laminates under biaxial loads”, in *48th AIAA/ASME/ASCE/AHS/ASC structures, structural dynamics, and materials conference* (Honolulu), 2007.
- [Xu et al. 2008] J. F. Xu, A. Askari, O. Weckner, and S. Silling, “Peridynamic analysis of impact damage in composite laminates”, *J. Aerosp. Eng. (ASCE)* **21**:3 (2008), 187–194.
- [Yu et al. 2016] Y. Yu, S. S. Liu, S. L. Zhao, and Z. Yu, “The nonlinear inplane behavior and progressive damage modeling for laminate by peridynamics”, in *ASME 2016 international mechanical engineering congress and exposition* (Phoenix), 2016.

Received 5 Jul 2017. Revised 20 Nov 2017. Accepted 23 Dec 2017.

XIAO-WEI JIANG: jiangxiaowei@sjtu.edu.cn

School of Aeronautics and Astronautics, Shanghai Jiao Tong University, Shanghai, China

HAI WANG: wanghai601@sjtu.edu.cn

School of Aeronautics and Astronautics, Shanghai Jiao Tong University, Shanghai, China

STABILITY OF COSSERAT SOLIDS: SIZE EFFECTS, ELLIPTICITY AND WAVES

RODERIC S. LAKES

We consider stability in Cosserat solids. To obtain restrictions on elastic constants based on positive definite strain energy, energy terms are tacitly assumed to be independent. In finite-size objects, however, the terms are linked in Cosserat materials. Therefore, in contrast to classical solids, the stability of Cosserat solids appears to depend on the size and shape of the specimen, provided strong ellipticity is satisfied. Stability in the presence of stored energy is possible. Solids with microstructure and stored energy offer the potential to facilitate attainment of extreme behavior in the presence of spatial gradients. Snap-through buckling in torsion is envisaged by analogy to the axial buckling concept used for composites with negative stiffness inclusions. It is possible to support compressive load in a stable manner but to dissipate energy in the presence of spatial gradients as in torsion or bending.

1. Introduction

Extremely high values of physical properties such as mechanical damping [Lakes 2001; Lakes et al. 2001], stiffness [Jaglinski et al. 2007], and piezoelectric sensitivity [Wang and Lakes 2001] can be attained in systems at the margins of stability, in bistable systems that undergo hysteresis, and in composites with inclusions of negative stiffness. Thus far, metastable and unstable systems have been understood in the context of classical elasticity. However, many such materials are heterogeneous with a coarse structure size. Such materials can be modeled as Cosserat solids.

Cosserat elasticity [Cosserat and Cosserat 1909; Mindlin 1965b] incorporates sensitivity to gradients of rotation by virtue of the coupling between rotations and stresses. The constitutive equations for linear isotropic Cosserat elasticity, also called micropolar elasticity [Eringen 1968] in the presence of microinertia, are as follows:

$$\sigma_{ij} = 2G\epsilon_{ij} + \lambda\epsilon_{kk}\delta_{ij} + \kappa e_{ijk}(r_k - \phi_k), \quad (1)$$

$$m_{ij} = \alpha\phi_{k,k}\delta_{ij} + \beta\phi_{i,j} + \gamma\phi_{j,i}. \quad (2)$$

There are two rotation variables: ϕ_m is the rotation of points, called microrotation, and $r_k = \frac{1}{2}e_{klm}u_{m,l}$ is the “macro” rotation based on the antisymmetric part of gradient of displacement u_i . Here, e_{jkm} is the permutation symbol. In contrast to classical elasticity, the stress σ_{ij} (force per unit area) in Cosserat elasticity can be asymmetric. The theory incorporates a couple stress m_{ij} (a torque per unit area) which balances the distributed moment associated with asymmetric stress.

Isotropic Cosserat solids have six elastic constants: λ , G , α , β , γ , κ . Constants λ and G have the same meaning as in classical elasticity. The Cosserat elasticity constants α , β , γ provide sensitivity to the

Keywords: Cosserat, stability, micropolar.

rotation gradient. The Cosserat constant κ governs the coupling between local rotation and the rotation associated with displacement gradients.

Various other generalized continuum theories are available. We use Cosserat elasticity in our laboratory [Lakes 1986; Rueger and Lakes 2016] because suitable solutions of boundary value problems are available for interpreting experiments.

In the present research, real wave velocity and strong ellipticity are assumed and the size dependence of the stability of circular cylinders is explored. The rationale is to provide groundwork for developing gradient sensitive heterogeneous materials with extreme dissipative properties.

2. Range of elastic constants

An assumption of positive definite strain energy leads to restrictions on the elastic constants. For classical isotropic elasticity, the shear modulus $G > 0$ and $3\lambda + 2G > 0$. For Cosserat solids, these additional restrictions apply [Eringen 1968; 1999]: $\kappa > 0$, $\gamma > 0$, $-\gamma < \beta < \gamma$, and $3\alpha + \beta + \gamma > 0$.

As for physical interpretation, positive definite strain energy corresponds in classical elasticity to positive shear modulus and positive bulk modulus. Positive moduli are required for a sample of material to be stable in the absence of constraint.

An assumption of strong ellipticity corresponds to a weaker set of conditions. For classical elasticity, they are $G > 0$ and $\lambda + 2G > 0$.

Strong ellipticity is associated with the requirement that waves have a real velocity. For longitudinal waves to have a real velocity, $\lambda + 2G$ must be greater than 0 in both classical and Cosserat elasticity. For transverse waves in Cosserat solids to have a real velocity at low frequency, G must be greater than 0; in the high frequency limit [Eringen 1968], $G + \frac{1}{2}\kappa > 0$. A second set of transverse waves can exist above a critical frequency. The wave speed v_3 is real if $\gamma > 0$ and $\kappa > 0$; the high frequency limit is $c_4 = \sqrt{\gamma/\rho j}$, where ρ is density and j is microinertia. For such waves to exist at high frequency, γ must be greater than 0. There are also dispersive microrotation waves that exist above a critical frequency governed by microinertia. Such waves can exist if $\alpha + \beta + \gamma > 0$. As for surface waves, their speed is dominated by the shear modulus G ; for Cosserat solids there is a contribution from κ . So the stability condition based on plane waves presented [loc. cit.] includes $\lambda + 2G > 0$, $G > 0$, $G + \frac{1}{2}\kappa > 0$, $\kappa > 0$, $\alpha + \beta + \gamma > 0$, and $\gamma > 0$.

It was suggested [Neff et al. 2016; 2017] that the criteria for real wave velocity in a Cosserat solid are $\lambda + 2G > 0$, $G > 0$, and $\kappa > 0$. For strong ellipticity, the usual classical condition $\lambda + 2G > 0$ is supplemented in the Cosserat case [Jeong and Neff 2010] with $G + \kappa > 0$, $\gamma > 0$, and $\alpha + \beta + \gamma > 0$.

2.1. Stability of classical solids. Negative values of λ (but not too negative) are consistent with stability; this entails a negative Poisson's ratio $\nu = \lambda/(2(\lambda + G))$, which is certainly possible [Lakes 1987]. The stability criterion for Poisson's ratio of unconstrained objects is $-1 < \nu < 0.5$.

Suppose $G < 0$; strain energy is not positive definite. An unconstrained block of material is then unstable to shear deformation because the restoring force is reversed. The structural rigidity or spring constant for shear becomes negative. Any small perturbation causes the block to diverge from its initial state. Similarly, a negative bulk modulus $B = \lambda + \frac{2}{3}G < 0$ entails a volume change instability of unconstrained blocks.

It is possible for a solid to have a negative bulk modulus, corresponding to a strain energy that is not positive definite. Such a solid may be stabilized by constraint at the boundaries. The material contains

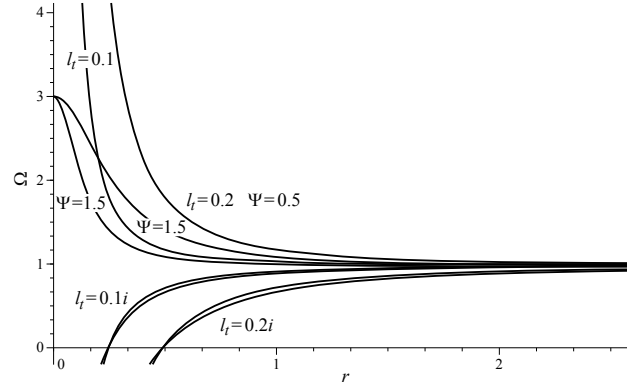


Figure 1. Size effect, rigidity ratio of a round bar vs. radius r , in torsion for $N = 0.5$ and for various ℓ_t^2 including negative values for $\Psi = \pm 0.5$ and for $\Psi = \pm 1.5$. When the normalized torsion rigidity Ω becomes negative, the bar is unstable in torsion.

stored elastic energy. The effects of constrained negative bulk modulus have been demonstrated in the laboratory [Moore et al. 2006].

If strong ellipticity fails, then the material exhibits bands of heterogeneous deformation, as is the case in solid-to-solid phase transformations.

In the following we show that for Cosserat solids, materials with nonpositive definite strain energy may be stable without constraint if the specimen is sufficiently large in size.

2.2. Stability of Cosserat solids. As with classical solids, a Poisson's ratio within the range $-1 < \nu < 0.5$ is consistent with the stability of a Cosserat solid in the absence of constraint via positive definite strain energy. The constant β can be negative provided $|\beta/\gamma| < 1$. The criterion $3\alpha + \beta + \gamma > 0$ allows negative (but not too negative) values of α .

To obtain the restrictions on elastic constants based on positive definite strain energy, it is assumed that modes of deformation are independent. In classical elasticity, volumetric and shear deformation are indeed independent. Such deformations can occur homogeneously without any strain gradient. In Cosserat elasticity it is assumed [Eringen 1968] that the strain ϵ_{ij} , rotation difference $r_k - \phi_k$, and rotation gradient $\phi_{i,j}$ can be varied independently. For a particular specimen geometry, however, these variables are coupled via the equilibrium equations and by the boundary conditions for the specimen. Deformation modes that involve a strain gradient are coupled to a rotation gradient. The specifics depend on specimen size and shape as follows.

Consider the torsional structural rigidity ratio Ω . This is the Cosserat rigidity of a round rod of radius r of a Cosserat solid divided by the corresponding classical rigidity. The classical torsional rigidity is $M/\theta = G[(\pi/2)r^4]$; M is the applied moment and θ is the angular displacement per length. If elastic constants obey positive definiteness, there are size effects in which slender rods appear stiffer than thicker ones. The rigidity (Figure 1) depends on the characteristic length for torsion, defined as $\ell_t = \sqrt{(\beta + \gamma)/2G}$.

Suppose $\beta/\gamma < -1$, or equivalently $\beta + \gamma < 0$, which violates positive definite strain energy. Elastic constants $\lambda, G, \gamma, \kappa$ are assumed to be positive. Then $(\ell_t/r)^2$ becomes negative; ℓ_t is imaginary. This

is admissible [Mindlin 1965a], given the form of the energy function. Physically in the present context, negative Cosserat constants corresponding to an imaginary characteristic length entail a destabilizing influence. Then in (3), the second term provides a negative contribution to the structural rigidity because $(\ell_t/r)^2 < 0$. The structural rigidity Ω remains positive, however, if the rod is sufficiently thick (Figure 1). Observe that one must have $\alpha + \beta + \gamma > 0$ or the Bessel functions have imaginary arguments, which suggests instability. Recall the same criterion was required for microrotation waves to exist above a characteristic frequency and to satisfy strong ellipticity. Plots are shown in Figure 1 for several values of polar ratio $\Psi = (\beta + \gamma)/(\alpha + \beta + \gamma)$. To maintain $\alpha + \beta + \gamma > 0$, we assume $\Psi < 0$ when $\ell_t^2 < 0$. This corresponds to large positive α . Allowing $\beta/\gamma < -1$ can cause torsional instability only for sufficiently slender rods. Thicker ones are stabilized by the classical term. The stiffening effect does not allow $G < 0$ for slender rods because they would be unstable to deformation in simple shear. The exact solution for torsion of a round rod is [Gauthier and Jahsman 1975]

$$\Omega = \left(1 + 6 \left\{ \frac{\ell_t}{r} \right\}^2\right) \left[\frac{1 - \frac{4}{3}\Psi\chi}{1 - \Psi\chi} \right], \quad (3)$$

in which $\chi = I_1(pr)/prI_0(pr)$, $p^2 = 2\kappa/(\alpha + \beta + \gamma)$, and I_0, I_1 are modified Bessel functions of the first kind. Recall that Ω is the ratio of torsional rigidity of the Cosserat solid to that of a classical solid.

The case $N = 1$ (in which $N = \sqrt{\kappa/(2G + \kappa)}$), see (4), is simpler; the same phenomena occur as well. For Cosserat elasticity in the regime $N = 1$, we have $M/\theta = G[(\pi/2)r^4](1 + 6(\ell_t/r)^2)$. Here, G is the true shear modulus in the absence of gradients.

$$\Omega = 1 + 6 \left(\frac{\ell_t}{r} \right)^2. \quad (4)$$

The case $N = 1$ is called couple stress elasticity. Stability for anisotropic couple stress solids has been analyzed [Gourgiotis and Bigoni 2016a; 2016b; Bigoni and Gourgiotis 2016]. Strong ellipticity does not imply real wave propagation in such couple stress solids, in contrast to classical solids; similarly for the reverse. Also in the vicinity of the ellipticity criterion, the couple stress solid exhibits folding and faulting patterns not present in the classical case.

We remark that for $\Psi = 1.5$, its upper limit, $\alpha < 0$, assuming positive definite strain energy. For small N , the rigidity softens below classical values but remains positive, as shown in Figure 2, in harmony with the stability criterion of positive definiteness. This region was not explored in [Gauthier and Jahsman 1975] and is not known experimentally. The effect of N is not obvious in (3), however the limit of small N can be visualized via expansion of the Bessel functions for small argument. In the limit $\chi \rightarrow \frac{1}{2}$, then for $\Psi = 1.5$ and small N , the rigidity ratio $\Omega \rightarrow 0$. To approach the limit of classical elasticity for a given range of radius r , $\alpha, \beta, \gamma \rightarrow 0$, which is not plotted in Figure 2.

As for bending, size effects in rigidity also occur, see (5) and (6). As with torsion, allowing $\ell_t^2 < 0$ (hence $\beta/\gamma < -1$) can cause instability only for sufficiently slender rods (Figure 3). Thicker ones are stabilized by the classical term. The rigidity ratio for bending of a Cosserat elastic circular rod of radius r is [Krishna Reddy and Venkatasubramanian 1978]

$$\Omega = 1 + 8 \left(\frac{\ell_b}{r} \right)^2 \frac{(1 - (\beta/\gamma)^2)}{(1 + \nu)} + \frac{8N^2}{(1 + \nu)} \left[\frac{(\beta/\gamma + \nu)^2}{\zeta(\delta r) + 8N^2(1 - \nu)} \right] \quad (5)$$

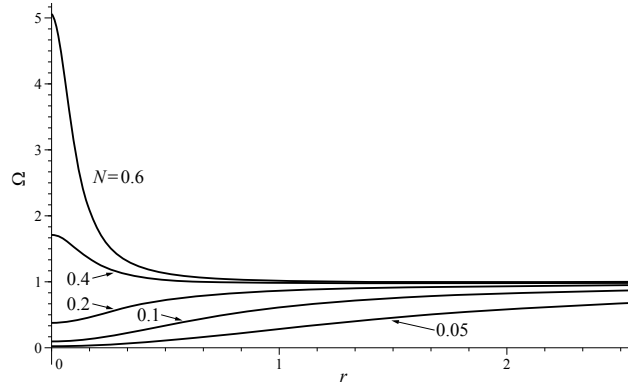


Figure 2. Size effect, rigidity ratio Ω of a round bar vs. radius r , in torsion for $\ell_t = 0.1$ and for $\Psi = 1.5$, where the upper limit assumes positive definite energy. Curves are shown for $N = 0.6, 0.4, 0.2, 0.1, 0.05$.

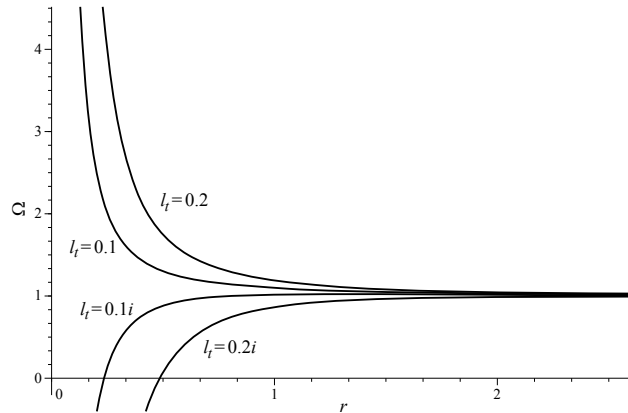


Figure 3. Size effect, rigidity ratio Ω of a round bar vs. radius r , in bending for $N = 0.5$, for $\ell_b = 0.2$ and for various ℓ_t^2 including negative values. When the normalized bending rigidity Ω becomes negative, the bar is unstable in bending.

with $\ell_b = \sqrt{\gamma/4G}$ as a characteristic length for bending, $N = \sqrt{\kappa/(2G + \kappa)}$ as the coupling number, and ν as Poisson's ratio. Also $\delta = N/\ell_b$ and $\zeta(\delta r) = (\delta r)^2 [((\delta r)I_0((\delta r)) - I_1((\delta r)))/((\delta r)I_0(\delta r) - 2I_1(\delta r))]$. The classical bending rigidity is $M/\theta = E[(\pi/4)r^4]$.

The Bessel term vanishes for $\beta/\gamma = -\nu$ and is small for $N \ll 1$. In this regime we have the following simpler form (this form also applies for $(\ell_b/r)^2 \ll 1$ but is not as good an approximation):

$$\Omega = 1 + 8 \left(\frac{\ell_b}{r} \right)^2 \frac{(1 - (\beta/\gamma)^2)}{(1 + \nu)}. \quad (6)$$

As for other instability modes, the bar is stable under perturbations in extension because Young's modulus E is positive and there are no rotation gradients. The rigidity depends only on E and not on any Cosserat constants. Similarly the bar is stable under perturbations in uniform shear because the shear

modulus G is positive and simple shear is also spatially uniform. Similarly a positive bulk modulus B provides stability with respect to homogeneous volumetric deformation. Sausage deformation involves shear but the gradients in rotation are small compared to the gradients in torsion and bending so such deformation is unlikely to cause instability. Also, sausage deformation could initiate from an instability in surface wave speed. However, this wave speed depends primarily on G and has a correction involving κ with no effect of β or γ , so the cases considered are stable with respect to surface waves. We do not, however, know *all* possible instability modes.

Observe that the threshold radius for instability is similar in torsion and in bending. In contrast to classical solids, the stability of unconstrained Cosserat solids appears to depend on the size and shape of the specimen.

3. Experiment

Stored energy may be achieved via an initial compressive strain, sufficient to buckle some of the cell ribs. Such a deformation was input to a square cross section bar of foam of dimensions $50 \times 50 \times 161$ mm. An open-cell polyurethane foam with cells about 4 mm across and density 0.026 g/cc was used. Cyclic sinusoidal deformation at 1 Hz in torsion was applied using a tension-torsion frame with a sensitive torque cell. Calculated peak shear engineering strain was $\pm 20\%$. Torsion hysteresis was measured with and without precompression.

Axial precompression was found to result in softening of the apparent torsion rigidity and an increase in the damping $\tan \delta$. For no precompression, $\tan \delta = 0.12$. For 5% precompression (the typical threshold for rib buckling), $\tan \delta = 0.11$, and the effective shear modulus softened to 85% of the value for no compression. For 7.5% precompression, $\tan \delta = 0.19$, and the effective shear modulus softened to 77% of the value for no compression. For 10% precompression, $\tan \delta = 0.21$, and the effective shear modulus softened to 74% of the value for no compression.

Resolution was insufficient to reveal hypothetical regions of local negative structural rigidity. Rib buckling is known to occur, leading to multiple snap-through events. Softening of moduli and increase in damping due to such mechanisms are known in other contexts [Lakes et al. 2001].

The experiment reveals coupling between axial precompression and an increase in torsional damping and softening of torsional rigidity. Ordinarily, in cellular solids the damping $\tan \delta$ is independent of the foam cell geometry. If the frequency is sufficiently low so that stress-induced air flow does not contribute to the damping, foam damping is equal to that of the polymer from which it is made. The damping increase in the present experiment occurs when the threshold for cell rib buckling is exceeded, so the increase is interpreted in the context of instability. However, to explicitly demonstrate a Cosserat aspect of these phenomena, a protocol to measure size effects with and without precompression would require higher resolution than is currently available.

4. Composites and applications

Composite materials with negative stiffness inclusions are well known [Lakes 2001]; they allow extreme values of mechanical damping or of stiffness as shown by experiment [Lakes et al. 2001; Jaglinski et al. 2007]. In distributed composites, negative stiffness is achieved by incipient phase transformation of inclusions. In lumped or discrete systems, negative stiffness is achieved by the postbuckling of structural



Figure 4. Torsional snap through element with negative incremental torsional rigidity. Left, top view; right, perspective view.

elements. The negative stiffness, which involves relaxing the requirement of positive definite strain energy, is stabilized by constraint within a composite or a structure. Thus far the approach [Lakes 2001; Lakes et al. 2001; Jaglinski et al. 2007] has been classical.

Nonpositive definite strain energy entails stored elastic energy in the material. If the material is a Cosserat solid, energy may be stored in the rotational degrees of freedom in an unconstrained object. It is possible to store energy in the material by controlled microbuckling of ribs, as has been done in foams and composites. Stored energy may also be incorporated via a prestrain or during the fabrication of the composite.

As for purely rotational freedom, we envisage torsional snap-through elements (Figure 4) as inclusions. Such a discrete element, either used alone with rotational constraint or embedded in a classical matrix, can be stable while containing stored energy in a neutral position. Torsional snap through elements contribute a negative torsion rigidity; in a composite, the total rigidity can be positive by virtue of the stiffness of the surrounding matrix material. Torsion through the element's negative stiffness region can give rise to partial softening of the torsion rigidity: hysteresis, and mechanical damping, corresponding to similar phenomena observed in classical composites with negative stiffness inclusions. Consequently, there is the potential to support compressive load in a stable manner but to dissipate energy in the presence of spatial gradients as in torsion or bending.

Composites based on Cosserat solids outside the usual range of elastic constants offer the potential of extreme values of damping of torsional waves independently of the ability to support axial load. In the context of waves, material properties can approach the margins of strong ellipticity. Wave cut off may be manipulated by the control of gradient sensitivity rather than by adding extra inertia, as is done in most "metamaterials".

5. Discussion

Stability of materials has been studied in the context of positive definite strain energy and of ellipticity. If a classical material has positive definite strain energy then it is stable in the absence of constraint. If it obeys strong ellipticity then it is stable with respect to the formation of bands of heterogeneous deformation and with respect to instability associated with waves.

More restrictive views than the assumption of positive definiteness have been taken. In classical elasticity, it had been believed, and even stated in textbooks, that Poisson's ratio of isotropic solids must be positive; negative values are now well known [Lakes 1987]. In Cosserat solids it had been claimed

that $\frac{1}{2}\kappa < G$ but this claim was shown to be incorrect [Cowin 1970]. Also, allowing the full stable range of Cosserat constants implies that torsion and bending stiffness can diverge as rod radius becomes small. This has been considered to be mathematically unpalatable and also can present difficulties in obtaining stable fits of experimental data to analytical curves [Neff et al. 2010]. If, however, $\Psi = 1.5$ and $\beta = \gamma$, then the structural rigidity is bounded as the radius becomes small. Size effect experiments on isotropic dense foam [Lakes 1986] are consistent with such a notion. However, a definitive experimental test of the concept has not been done; some known Cosserat solids such as bone are highly anisotropic, and open cell foams and lattices can exhibit various degrees of anisotropy as well as strong size effects.

The value of β/γ (pertinent to stability limits) can be probed as follows. For square section bars, the cross section shape changes in bending as shown both theoretically and experimentally. Classical linear tilt of lateral surfaces becomes a sigmoid shape in Cosserat solids [Lakes and Drugan 2015]. Experiment shows that for an open cell foam, $\beta/\gamma > 0$ and is consistent with $\beta/\gamma = 1$. If β/γ were to be sufficiently negative, the curve of lateral surfaces would be of opposite sign.

By contrast, views less restrictive than positive definiteness have been taken. For example, continuum models were compared with corresponding structural lattice analyses. It was argued, based on such a comparison, that stability conditions should be applied to volume elements considerably larger than the structural length scale of the material to be studied [Brulin and Hjalmar 1981]. This concept leads to stability conditions weaker than those obtained from positive definite strain energy in Cosserat solids. However, the role of boundary conditions in objects of finite size was not considered, in contrast to the perspective taken here.

As for experiment, torsional damping increases when axial precompression suffices to buckle ribs. This could be useful in vibration damping applications but is not definitive in a Cosserat interpretation. As for waves, transmitted longitudinal wave amplitude in a foam is reduced by compression below and near the cut off frequency [Balch and Lakes 2017].

6. Conclusion

In contrast to classical solids, the stability of Cosserat solids appears to depend on the size and shape of the specimen provided strong ellipticity is satisfied. For Cosserat solids, materials with nonpositive definite strain energy due to stored energy in the rotational freedom may be stable without constraint if the specimen is sufficiently large in size.

7. Acknowledgements

We gratefully acknowledge support of this research by the National Science Foundation via Grant CMMI-1361832 and by ARO US Army Research Office under Grant W911NF-13-1-0484. We thank Professor R. Vanderby for the use of the tension torsion device and Ron and Jeff for their effort with the experiments.

References

- [Balch and Lakes 2017] S. P. Balch and R. S. Lakes, “Amelioration of waves and micro-vibrations by micro-buckling in open celled foam”, *Cell. Polymers* **36**:1 (2017), 1–12.
- [Bigoni and Gougiotis 2016] D. Bigoni and P. A. Gougiotis, “Folding and faulting of an elastic continuum”, *Proc. R. Soc. Lond. A* **472**:2187 (2016), art. id. 20160018.

- [Brulin and Hjalmar 1981] O. Brulin and S. Hjalmar, “Stability conditions in continuum models of discrete systems”, pp. 209–212 in *Continuum models of discrete systems, IV* (Stockholm, 1981), edited by O. Brulin and R. K. T. Hsieh, North-Holland, Amsterdam, 1981.
- [Cosserat and Cosserat 1909] E. Cosserat and F. Cosserat, *Théorie des corps déformables*, Hermann, Paris, 1909.
- [Cowin 1970] S. C. Cowin, “An incorrect inequality in micropolar elasticity theory”, *Z. Angew. Math. Phys.* **21**:3 (1970), 494–497.
- [Eringen 1968] A. C. Eringen, “Theory of micropolar elasticity”, pp. 621–729 in *Fracture, II: Mathematical fundamentals*, edited by H. Liebowitz, Academic Press, New York, 1968.
- [Eringen 1999] A. C. Eringen, *Microcontinuum field theories, I: Foundations and solids*, Springer, 1999.
- [Gauthier and Jahsmann 1975] R. D. Gauthier and W. E. Jahsmann, “A quest for micropolar elastic constants”, *J. Appl. Mech. (ASME)* **42**:2 (1975), 369–374.
- [Gourgiotis and Bigoni 2016a] P. A. Gourgiotis and D. Bigoni, “Stress channelling in extreme couple-stress materials, I: Strong ellipticity, wave propagation, ellipticity, and discontinuity relations”, *J. Mech. Phys. Solids* **88** (2016), 150–168.
- [Gourgiotis and Bigoni 2016b] P. A. Gourgiotis and D. Bigoni, “Stress channelling in extreme couple-stress materials, II: Localized folding vs. faulting of a continuum in single and cross geometries”, *J. Mech. Phys. Solids* **88** (2016), 169–185.
- [Jagliniski et al. 2007] T. Jagliniski, D. Kochmann, D. Stone, and R. S. Lakes, “Composite materials with viscoelastic stiffness greater than diamond”, *Science* **315**:5812 (2007), 620–622.
- [Jeong and Neff 2010] J. Jeong and P. Neff, “Existence, uniqueness and stability in linear Cosserat elasticity for weakest curvature conditions”, *Math. Mech. Solids* **15**:1 (2010), 78–95.
- [Krishna Reddy and Venkatasubramanian 1978] G. V. Krishna Reddy and N. K. Venkatasubramanian, “On the flexural rigidity of a micropolar elastic circular cylinder”, *J. Appl. Mech. (ASME)* **45**:2 (1978), 429–431.
- [Lakes 1986] R. S. Lakes, “Experimental microelasticity of two porous solids”, *Int. J. Solids Struct.* **22**:1 (1986), 55–63.
- [Lakes 1987] R. S. Lakes, “Foam structures with a negative Poisson’s ratio”, *Science* **235**:4792 (1987), 1038–1040.
- [Lakes 2001] R. S. Lakes, “Extreme damping in composite materials with a negative stiffness phase”, *Phys. Rev. Lett.* **86**:13 (2001), 2897–2900.
- [Lakes and Drugan 2015] R. S. Lakes and W. J. Drugan, “Bending of a Cosserat elastic bar of square cross section: theory and experiment”, *J. Appl. Mech. (ASME)* **82**:9 (2015), art. id. 091002.
- [Lakes et al. 2001] R. S. Lakes, T. Lee, A. Bersie, and Y. C. Wang, “Extreme damping in composite materials with negative-stiffness inclusions”, *Nature* **410** (2001), 565–567.
- [Mindlin 1965a] R. D. Mindlin, “Second gradient of strain and surface-tension in linear elasticity”, *Int. J. Solids Struct.* **1**:4 (1965), 417–438.
- [Mindlin 1965b] R. D. Mindlin, “Stress functions for a Cosserat continuum”, *Int. J. Solids Struct.* **1**:3 (1965), 265–271.
- [Moore et al. 2006] B. Moore, T. Jagliniski, D. S. Stone, and R. S. Lakes, “Negative incremental bulk modulus in foams”, *Philos. Mag. Lett.* **86**:10 (2006), 651–659.
- [Neff et al. 2010] P. Neff, J. Jeong, and A. Fischle, “Stable identification of linear isotropic Cosserat parameters: bounded stiffness in bending and torsion implies conformal invariance of curvature”, *Acta Mech.* **211**:3-4 (2010), 237–249.
- [Neff et al. 2016] P. Neff, A. Madeo, G. Barbagallo, M. V. d’Agostino, R. Abreu, and I.-D. Ghiba, “Real wave propagation in the isotropic relaxed micromorphic model”, lecture notes, INSA-Lyon, 2016, available at <https://tinyurl.com/techrepleff>.
- [Neff et al. 2017] P. Neff, A. Madeo, G. Barbagallo, M. V. d’Agostino, R. Abreu, and I.-D. Ghiba, “Real wave propagation in the isotropic-relaxed micromorphic model”, *Proc. R. Soc. Lond. A* **473**:2197 (2017), art. id. 20160790.
- [Rueger and Lakes 2016] Z. Rueger and R. S. Lakes, “Experimental Cosserat elasticity in open-cell polymer foam”, *Philos. Mag.* **96**:2 (2016), 93–111.
- [Wang and Lakes 2001] Y. C. Wang and R. S. Lakes, “Extreme thermal expansion, piezoelectricity, and other coupled field properties in composites with a negative stiffness phase”, *J. Appl. Phys.* **90**:12 (2001), 6458–6465.

Received 14 Sep 2017. Revised 7 Nov 2017. Accepted 14 Nov 2017.

RODERIC S. LAKES: lakes@engr.wisc.edu

Department of Engineering Physics, University of Wisconsin-Madison, Madison, WI, United States

EXTREME COSSERAT ELASTIC CUBE STRUCTURE WITH LARGE MAGNITUDE OF NEGATIVE POISSON'S RATIO

CARLOS ANDRADE, CHAN SOO HA AND RODERIC S. LAKES

A structure consisting of pivoting cubes is presented. It has zero Young's modulus and zero bulk modulus. Poisson's ratio has large negative values in all directions; the structure exhibits anisotropy in Poisson's ratio. The structure is compliant in tension but rigid in torsion and bending. The Cosserat characteristic length tends to infinity.

1. Introduction

A 3D negative Poisson's ratio material based on transformed open cell polyurethane foam was reported in [Lakes 1987a]; it had a Poisson's ratio -0.7 . It is possible to approach the isotropic lower limit -1 via structures or lattices with hinges. Negative Poisson's ratio was analyzed in a model of rods, hinges and springs [Almgren 1985]; a value of -1 was calculated. A Poisson's ratio of -1 can be achieved in 2D structures containing rotating rigid units such as squares [Grima et al. 2005] connected by ideal hinges. Negative Poisson's ratio was also studied in 2D systems with rotating hexamers [Wojciechowski 1987; 1989] in the context of thermodynamic stability.

More recent designs with bars linked by ideal pivots allow the structure to undergo arbitrarily large volumetric strain with zero bulk modulus [Milton 2013]. Negative Poisson's ratio materials have been called "dilatational" [Milton 1992] because they easily undergo volume changes but are difficult to shear.

It is possible to approach the isotropic lower limit -1 at small strain in the analysis of a hierarchical two phase composite [Milton 1992] if there is sufficient contrast between constituent properties. A 2D chiral lattice [Prall and Lakes 1997] exhibits a Poisson's ratio -1 over a range of strain as shown by experiment and analysis.

In the present research, we develop a structure made of cubes connected by pivots at their corners. Poisson's ratio and sensitivity to gradients are studied.

2. Cube structure

A structure is envisaged of cubes of side length a connected by pivots at the corners; see Figure 1.

Views of the $3 \times 3 \times 3$ cube structure along principal directions are shown in Figure 2. The rear layers of the cubes are fully hidden. Deformation results in tilting of the cubes at the pivot points. This tilt causes void space to appear in the structure giving rise to a volume change. Transverse expansion of the structure under tension implies a negative Poisson's ratio.

2.1. Analysis and interpretation.

Keywords: auxetic, negative Poisson's ratio, Cosserat, metamaterial.



Figure 1. Cube structure, oblique view.

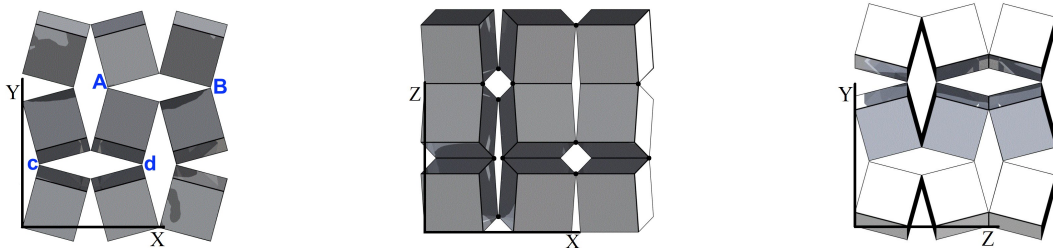


Figure 2. Cube structure, principal direction view.

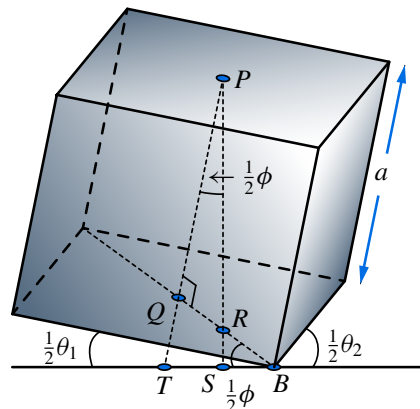


Figure 3. Analysis of cube structure deformation using two angles.

2.1.1. Elastic moduli and Poisson's ratio: two angles. We assume that the cubes are rigid and the pivots are ideal and allow frictionless rotation in all directions. Tensile deformation of the structure freely occurs in each axial direction: Young's modulus $E = 0$. Consequently, changes in volume occur with no resistance so the bulk modulus is zero. Shear forces in the X direction (Figure 2, left) on adjacent layers cause no deformation because the cube tilt cannot accommodate such motion. Shear forces in the Y direction (Figure 2, center) cause no deformation because the edges are in contact, forming a hinge.

Consequently, the structure resists shear in all directions but allows tensile deformation, suggesting an extremal negative Poisson's ratio.

Strain ϵ depends on cube tilt angle ϕ , beginning at zero, as follows. Two angles are considered for simplicity and transparency; the third angle shown in Figure 2 right appears to be small and is neglected for the present. In Figure 3 consider the change in the length of a vertical line element during deformation. Points A and B (Figure 2, left) are at pivoted corners; distance a is the cube width. After deformation the vertical line from P , center of top face, intersects the bottom cube face at R ; because tilt occurs in two orthogonal directions, the intersection is along a diagonal. Points B , S , and T , not necessarily collinear, are in a horizontal plane. The change in length is $\Delta L = PS - a$. The corresponding strain is $\epsilon_{yy} = (PS - a)/a$.

In triangle PQR , $\cos \frac{1}{2}\phi = PQ/(PR) = a/(PR)$. In triangle BQT , $\tan \frac{1}{2}\phi = QT/(BQ)$ so $QT = a\frac{1}{2}\sqrt{2}\tan \frac{1}{2}\phi$. Also, $PT = a + QT = a(1 + \frac{1}{2}\sqrt{2}\tan \frac{1}{2}\phi)$, but in triangle PST , $\cos \frac{1}{2}\phi = PS/(PT)$ so $PS = PT \cos \frac{1}{2}\phi$ with $PT = a + QT$. $PS = a(1 + \frac{1}{2}\sqrt{2}\tan \frac{1}{2}\phi) \cos \frac{1}{2}\phi$.

So the strain in terms of tilt angle is

$$\epsilon_{yy} = \left(1 + \frac{1}{2}\sqrt{2}\tan \frac{1}{2}\phi\right) \cos \frac{1}{2}\phi - 1. \quad (1)$$

If the angle is sufficiently large, the force has a line of action passing through a pivot. The force generates no moment to cause further rotation. For ϵ_{xx} as seen in the XY plane, the geometry is similar. However, viewed in the z direction, the effect of θ_1 alone gives the following in the linear regime of small angle:

$$\epsilon_{xx}^{\theta_1} = \frac{1}{2}\tan \frac{1}{2}\phi, \quad (2)$$

but θ_2 rotates the corresponding point on the right face center down, reducing the distance, yielding a strain

$$\epsilon_{xx} = +\frac{1}{2\sqrt{2}}\tan \frac{1}{2}\phi. \quad (3)$$

The Poisson's ratio is, for small angle,

$$\nu_{xy} = -\frac{\epsilon_{xx}}{\epsilon_{yy}} = -\frac{\left(\frac{1}{2\sqrt{2}}\tan \frac{1}{2}\phi\right)}{\left(1 + \frac{\sqrt{2}}{2}\tan \frac{1}{2}\phi\right) \cos \frac{1}{2}\phi - 1}. \quad (4)$$

From the definition, $\nu_{yx} = 1/\nu_{xy}$. For small angle, $\nu_{xy} = -\frac{1}{2}$, $\nu_{yx} = -2$. The structure is therefore anisotropic even though Young's modulus $E = 0$ in all directions.

As for ϵ_{zz} as seen in the YZ plane, $\epsilon_{zz} = \epsilon_{xx}$ by virtue of a similar construction (neglecting tilt in the third orthogonal direction). So $\nu_{zx} = -1$, $\nu_{xz} = -1$.

This analysis makes the simplifying assumption that tilt in the third direction is small compared with tilt in the two directions considered. Tilt in all three directions is considered in the numerical approach below.

2.1.2. Bending. The classical bending rigidity of a bar is $M\mathcal{R} = EI$ with \mathcal{R} as the principal bending radius of curvature and I is the area moment of inertia. Moment M is about the y axis; the z axis is along the bar. The rigidity depends only on Young's modulus E not on Poisson's ratio ν . The effect

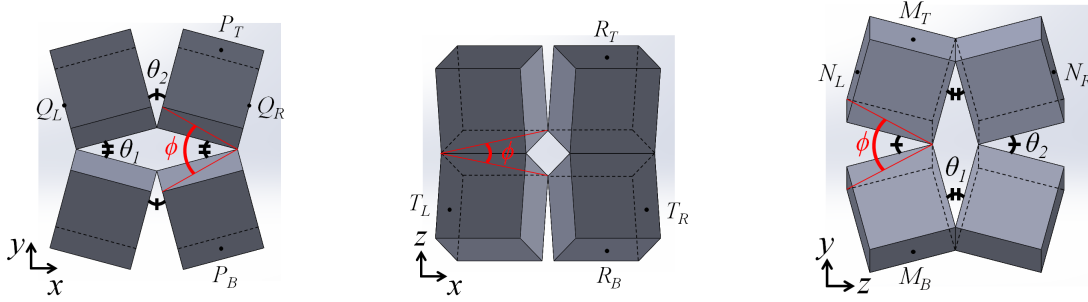


Figure 4. Cube structure viewed along the principal directions. All points are located at the center of cube faces. Here, ϕ is an angle between diagonal lines of adjacent cubes; θ_1 and θ_2 represent angles between cube edges when the structure is viewed in the corresponding principal directions. For the structure shown, $\phi = 42.17^\circ$, $\theta_1 = 30^\circ$ and $\theta_2 = 28.96^\circ$.

of Poisson's ratio is to alter the deformation field. For positive Poisson's ratio the cross sections curve oppositely to the principal bending curve, the familiar anticlastic curvature. A negative Poisson's ratio causes curvature in the same direction as the bending curve, synclastic curvature [Lakes 1987a]. The three-dimensional displacement field for pure bending of a linear elastic homogeneous, isotropic bar of rectangular section is

$$u_x = -\frac{z^2 + \nu(x^2 - y^2)}{2R}, \quad u_y = -\nu\frac{xy}{R}, \quad u_z = \frac{xz}{R}. \quad (5)$$

So if Young's modulus E tends to zero, it should be easy to bend the bar with no effort regardless of Poisson's ratio, provided the bar obeys classical elasticity.

The cube structure, while easy to deform in tension ($E = 0$), is rigid in bending. To visualize this, in the XY plane in the left image in Figure 2, expansion of a line along direction AB due to bending due to a Z moment is accompanied by contraction along line cd . The pivoted cube structure requires either expansion or contraction in all directions, so the structure is rigid to bending. Lines AB and cd are in different planes but that does not affect the argument because the classical motion has the same sign on the front and back.

Bending differs from axial extension in that bending entails gradients in strain and rotation. Classical elasticity is insensitive to gradients but Cosserat elasticity allows such sensitivity. Rigidity of the structure to bending combined with a zero tensile Young's modulus implies a Cosserat characteristic length that tends to infinity. Again, the cubes are assumed to be rigid and the pivots are assumed to be ideal.

2.1.3. Elastic moduli and Poisson's ratio: numerical model, three angles. Figure 4 illustrates views of the structure along the principal directions and points on the center of cube faces that were used to compute Poisson's ratio via a numerical model. Moreover, θ_1 and θ_2 represent angles between cube edges when the structure is viewed in the corresponding principal directions.

To determine the effect of motion in all three angles, the cube structure was modeled by SolidWorks commercial CAD software. In this analysis, a cube structure was modeled with a cube side length

of 10 mm and with various inclined angles ϕ of 7.07, 14.13, 21.18, 42.17, 62.74, and 82.56 degrees. Poisson's ratio in the principal directions was obtained as follows. The "mate" feature in SolidWorks was used to make hinge constraints on corners. Distance was then measured using the software. The effect is purely geometrical so there was no need to use tools such as ANSYS APDL.

To obtain Poisson's ratio of the cube structure, strain and Poisson's ratio were determined in terms of the distances. First, strains in the principal directions due to the angle ϕ were computed, as given in the following equations:

In xy plane,

$$\epsilon_{xx} = \frac{|\overline{Q_{R,x}Q_{L,x}}| - 2a}{2a}, \quad (6a)$$

$$\epsilon_{yy} = \frac{|\overline{P_{T,y}P_{B,y}}| - 2a}{2a}. \quad (6b)$$

In xz plane,

$$\epsilon_{xx} = \frac{|\overline{T_{R,x}T_{L,x}}| - 2a}{2a}, \quad (6c)$$

$$\epsilon_{zz} = \frac{|\overline{R_{T,z}R_{B,z}}| - 2a}{2a}. \quad (6d)$$

In yz plane,

$$\epsilon_{zz} = \frac{|\overline{N_{R,z}R_{L,z}}| - 2a}{2a}, \quad (6e)$$

$$\epsilon_{yy} = \frac{|\overline{M_{T,y}M_{B,y}}| - 2a}{2a}. \quad (6f)$$

In the above, a is the cube side length and $|\overline{Q_{R,x}Q_{L,x}}|$ denotes a distance between Q_R and Q_L in the x direction in the xy plane after deformation; ϵ_{xx} is then equal to $(|\overline{Q_{R,x}Q_{L,x}}| - 2a)/2a$. With strains found in (6), Poisson's ratio in the principal directions are

$$\nu_{xy} = -\frac{\epsilon_{xx}}{\epsilon_{yy}} = -\frac{|\overline{Q_{R,x}Q_{L,x}}| - 2a}{|\overline{P_{T,y}P_{B,y}}| - 2a}, \quad (7a)$$

$$\nu_{xz} = -\frac{\epsilon_{xx}}{\epsilon_{zz}} = -\frac{|\overline{T_{R,x}T_{L,x}}| - 2a}{|\overline{R_{T,z}R_{B,z}}| - 2a}, \quad (7b)$$

$$\nu_{zy} = -\frac{\epsilon_{zz}}{\epsilon_{yy}} = -\frac{|\overline{N_{R,z}R_{L,z}}| - 2a}{|\overline{M_{T,y}M_{B,y}}| - 2a}. \quad (7c)$$

From numerical results, it was found that $\epsilon_{xx,num}$ from the xy and the xz planes were identical (i.e., $\epsilon_{xx,num}^{xy-plane} = \epsilon_{xx,num}^{xz-plane}$). Similarly, $\epsilon_{yy,num}$ in the xy plane agreed exactly with the one in the yz plane, and $\epsilon_{zz,num}$ were the same for the xz and the yz planes (i.e., $\epsilon_{yy,num}^{xy-plane} = \epsilon_{yy,num}^{yz-plane}$ and $\epsilon_{zz,num}^{xz-plane} = \epsilon_{zz,num}^{yz-plane}$). This confirms that cube structures modeled by the employed CAD software were correctly designed and interpreted since the computed strains were the same regardless of views in different principal directions.

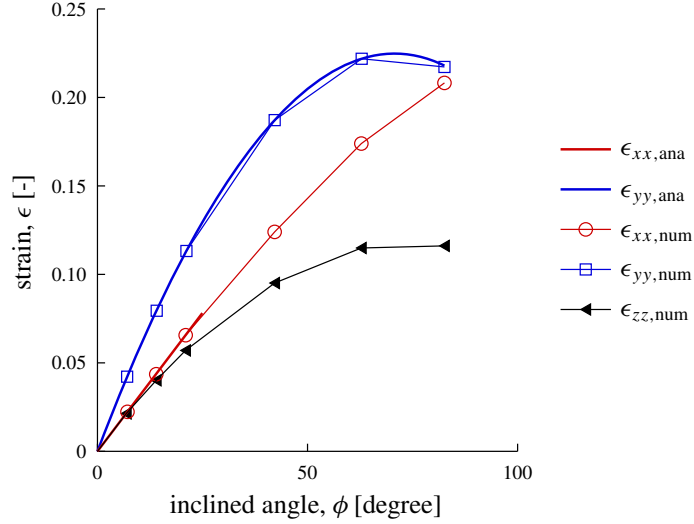


Figure 5. Strains of a cube structure as a function of the angle ϕ .

As a result, the superscript of strains obtained numerically were omitted in this paper as follows, unless stated otherwise.

A comparison of strains between analytical and numerical approaches was made, as shown in Figure 5.

The strain ϵ_{yy} between these two approaches agreed well with one another throughout the range of ϕ . The strain ϵ_{xx} also agreed over the narrower range of strain consistent with the simplifying assumptions in that analysis including neglect of the effect of the tilt in the third orthogonal direction and of higher nonlinearity.

As illustrated in Figure 4, left, and Figure 4, right, the effect of the orthogonal tilt is small when the angle ϕ is small. From this, it was expected that $\epsilon_{xx,num}$ and $\epsilon_{zz,num}$ be similar when ϕ is small, and this can be observed in Figure 5. In this regime (i.e., for small ϕ), strains are almost linear as a function of angle. In contrast, nonlinearity occurs when ϕ is large. The effect of the tilt in the third orthogonal direction can be quantified by θ_1 and θ_2 that represent angles between adjacent cube edges when the structure is viewed in the corresponding principal directions. For small ϕ , these two angles are similar.

In summary, for small strain, the Poisson's ratios ν_{zx} and ν_{xz} obtained by two-angle analysis and three-angle numerical methods are equal with a value of -1 , as illustrated in Figure 6. For other directions, the simple analysis and numerical results agree with the appropriate small angle range.

3. Physical model

Physical models were made to aid visualization and to illustrate the concepts. An initial model was made with cubes cut from polymer foam. A design was assembled digitally using Solidworks 2016. Cubes were prepared using Solidworks in .stl (StereoLithography) format for export to a 3D printer. The method was fused deposition method (FDM). The print resolution (i.e., the minimum size of a stand alone feature) was 0.5 mm. These cubes, 2 cm wide, were manufactured using a Dimension Elite 3D printer, and made of Stratasys ABSplus P430 thermoplastic. Pivots can be made by 3D printing but

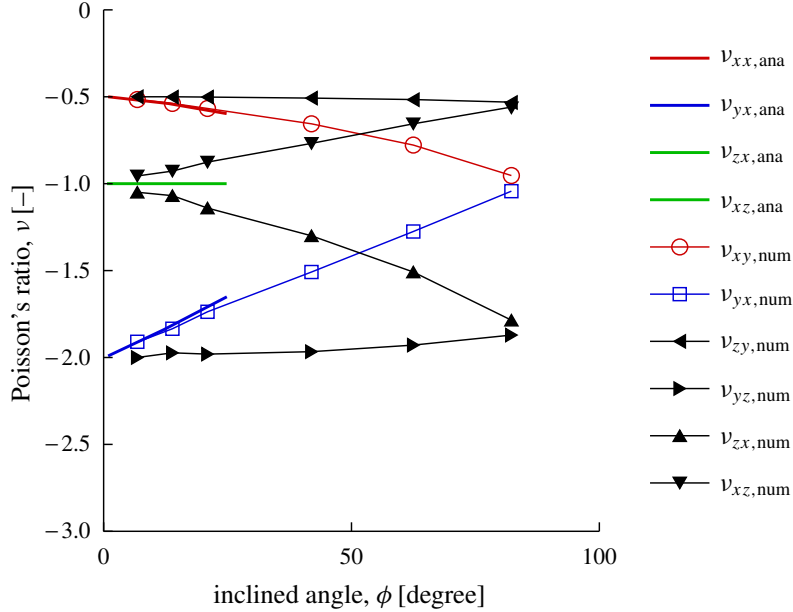


Figure 6. Poisson's ratio in all the principal directions.

they are subject to considerable friction which would interfere with the demonstration of the concept. Therefore a fibrous tape was cut into a dog-bone shape. Segments were taped to adjacent cubes, leaving the slender portion as a pivot. A $3 \times 3 \times 6$ model was made with Z as the long direction.

The physical model was observed to be easy to stretch provided only one or two cubes on each end were held gently and allowed to rotate. The structure expanded fully in tension under its own weight. The model was rigid to torsion as well as to shear in different directions. The model was also rigid to cantilever bending. In both cases, slight movement associated with slack in the pivots was observed.

4. Discussion

Several negative Poisson's ratio structures with rotating hinged elements are known. In addition to rotating squares [Grima et al. 2005], one can have rotating rhombi [Attard and Grima 2008], triangles [Grima and Evans 2006], edge connected cuboids of different sizes [Attard and Grima 2012], and complex hinged structures [Milton 2013]. Such pivoted structures, including the present one, exhibit a hard nonlinearity when the structural elements come into contact and when the lattice is fully extended. Even so, the geometry of hinged structures has been used to help explain [Attard and Grima 2008] the negative Poisson's ratio of materials in which the effects arise on the molecular scale.

For the present ideal structure with rigid cubes and frictionless pivots, Young's modulus is zero in tension provided the end cubes are allowed to rotate as is the case in stress control. Although tensile deformation freely occurs, the structure is rigid in bending and torsion. Classical elasticity cannot account for such behavior but Cosserat [Cosserat and Cosserat 1909] (micropolar [Eringen 1968]) elasticity, which allows sensitivity to gradients, can do so. Cosserat theory provides characteristic length parameters as elastic constants. If the specimen size is not too much greater than the characteristic length, size effects are observed in bending and torsion; the effective modulus in bending exceeds the true Young's modulus

in tension. Such effects are known in a variety of foams including negative Poisson's ratio foam [Rueger and Lakes 2016]. However the range of Poisson's ratio is the same in Cosserat solids as in classical ones so coarse cell structure is not needed to control the Poisson's ratio [Lakes 1987b]. The cube structure will be rigid to bending and torsion independent of how small the cubes are in comparison with the specimen size, provided the cubes are rigid and the pivots are ideal. This implies a characteristic length that is infinitely large. Such singular behavior arises from the geometrical constraints in a highly idealized structure. Similar singular behavior likely occurs in other negative Poisson's ratio hinged structures and in structures made using sliding elements [Gourgiotis and Bigoni 2016]. Extremely large Cosserat effects leading to folding and faulting can occur in highly anisotropic materials that admit couple stress [Bigoni and Gourgiotis 2016]. Three-dimensional structures are of particular interest because in 3D, classical bending can occur either via shear at constant volume, as in rubbery materials, or via local volume change with constant shape, as when Poisson's ratio tends to -1 . A material or structure that does not allow bending cannot be classically elastic.

5. Conclusions

A structure of pivoting cubes is presented. It has negative Poisson's ratio of large magnitude in each direction and a tensile modulus of zero. It is rigid to bending, therefore it is not classically elastic. The structure behaves as an extreme Cosserat solid.

Acknowledgements

We gratefully acknowledge support of this research by the National Science Foundation via Grant CMMI-1361832 and by the SURE program.

References

- [Almgren 1985] R. F. Almgren, "An isotropic three-dimensional structure with Poisson's ratio $= -1$ ", *J. Elasticity* **15**:4 (1985), 427–430.
- [Attard and Grima 2008] D. Attard and J. N. Grima, "Auxetic behaviour from rotating rhombi", *Phys. Status Solidi B* **245**:11 (2008), 2395–2404.
- [Attard and Grima 2012] D. Attard and J. N. Grima, "A three-dimensional rotating rigid units network exhibiting negative Poisson's ratios", *Phys. Status Solidi B* **249**:7 (2012), 1330–1338.
- [Bigoni and Gourgiotis 2016] D. Bigoni and P. A. Gourgiotis, "Folding and faulting of an elastic continuum", *Proc. R. Soc. Lond. A* **472**:2187 (2016), art. id. 20160018.
- [Cosserat and Cosserat 1909] E. Cosserat and F. Cosserat, *Théorie des corps déformables*, Hermann et Fils, Paris, 1909.
- [Eringen 1968] A. C. Eringen, "Theory of micropolar elasticity", pp. 621–729 in *Fracture: an advanced treatise, II: Mathematical fundamentals*, edited by H. Liebowitz, Academic Press, New York, 1968.
- [Gourgiotis and Bigoni 2016] P. A. Gourgiotis and D. Bigoni, "Stress channelling in extreme couple-stress materials, I: Strong ellipticity, wave propagation, ellipticity, and discontinuity relations", *J. Mech. Phys. Solids* **88** (2016), 150–168.
- [Grima and Evans 2006] J. N. Grima and K. E. Evans, "Auxetic behavior from rotating triangles", *J. Mater. Sci.* **41**:10 (2006), 3193–3196.
- [Grima et al. 2005] J. N. Grima, A. Alderson, and K. E. Evans, "Auxetic behaviour from rotating rigid units", *Phys. Status Solidi B* **242**:3 (2005), 561–575.
- [Lakes 1987a] R. S. Lakes, "Foam structures with a negative Poisson's ratio", *Science* **235**:4792 (1987), 1038–1040.

- [Lakes 1987b] R. S. Lakes, "Negative Poisson's ratio materials", *Science* **238**:4826 (1987), 551.
- [Milton 1992] G. W. Milton, "Composite materials with Poisson's ratios close to -1 ", *J. Mech. Phys. Solids* **40**:5 (1992), 1105–1137.
- [Milton 2013] G. W. Milton, "Complete characterization of the macroscopic deformations of periodic unimode metamaterials of rigid bars and pivots", *J. Mech. Phys. Solids* **61**:7 (2013), 1543–1560.
- [Prall and Lakes 1997] D. Prall and R. S. Lakes, "Properties of a chiral honeycomb with a Poisson's ratio of -1 ", *Int. J. Mech. Sci.* **39**:3 (1997), 305–314.
- [Rueger and Lakes 2016] Z. Rueger and R. S. Lakes, "Cosserrat elasticity of negative Poisson's ratio foam: experiment", *Smart Mater. Struct.* **25**:5 (2016), art. id. 054004.
- [Wojciechowski 1987] K. W. Wojciechowski, "Constant thermodynamic tension Monte Carlo studies of elastic properties of a two-dimensional system of hard cyclic hexamers", *Mol. Phys.* **61**:5 (1987), 1247–1258.
- [Wojciechowski 1989] K. W. Wojciechowski, "Two-dimensional isotropic system with a negative Poisson ratio", *Phys. Lett. A* **137**:1-2 (1989), 60–64.

Received 28 Nov 2017. Revised 18 Dec 2017. Accepted 22 Dec 2017.

CARLOS ANDRADE: carlos.andrade.von@gmail.com
University of Wisconsin, Madison, WI, United States

CHAN SOO HA: ha3@wisc.edu
University of Wisconsin, Madison, WI, United States

RODERIC S. LAKES: rlakes@wisc.edu
Department of Engineering Physics, University of Wisconsin-Madison, Madison, WI, United States

ELECTROMECHANICAL FIELDS IN A NONUNIFORM PIEZOELECTRIC SEMICONDUCTOR ROD

GUANGYING YANG, JIANKE DU, JI WANG AND JIASHI YANG

We study electromechanical fields in a piezoelectric semiconductor rod nonuniformly doped with impurities producing holes and electrons. The phenomenological theory of piezoelectric semiconductors consisting of the equations of piezoelectricity and the conservation of charge for holes and electrons is used, which was reduced to a one-dimensional model for thin rods in a previous paper. In this paper the one-dimensional theory is linearized for low electric potential or voltage. Solutions from the linearized one-dimensional equations are obtained for three specific doping profiles: linear doping, piecewise linear doping with fundamentally important applications in PN junctions, and sinusoidal doping. Various electromechanical fields produced by the doping are calculated and examined. The results are fundamental to piezoelectric semiconductor devices or piezotronics.

1. Introduction

Piezoelectric materials can be dielectrics (insulators) or semiconductors although most of the time they are used as dielectrics. Historically, there were early attempts on making piezoelectric semiconductor devices decades ago but the research essentially became dormant (see the review [Hickernell 2003]). However, relatively recently, various piezoelectric semiconductor nanostructures have been synthesized such as ZnO fibers, tubes, belts, spirals and films [Wang 2003; 2010; Kumar and Kim 2011; Lee et al. 2012; 2014]. They can be made into single structures [Gao and Wang 2009; Hu et al. 2010; Araneo et al. 2012; Ji et al. 2013] or in arrays [Shen et al. 2010; Chen et al. 2007; Yoo et al. 2009; Xue et al. 2010], and have been used to make energy harvesters for converting mechanical energy into electrical energy [Gao et al. 2007; Choi et al. 2009; Romano et al. 2011; Asthana et al. 2014; Liao et al. 2014], field effect transistors [Wang 2003; 2010; Wang et al. 2006], acoustic charge transport devices [Büyükköse et al. 2014], as well as strain, gas, humidity and chemical sensors [Wang 2003; Yu et al. 2010]. The study of piezoelectric semiconductor materials and devices is growing rapidly and has formed a new research area called piezotronics. It also presents a new class of coupled-field problems in mechanics.

For device application, the basic behaviors of piezoelectric semiconductors regarding the motion of charge carriers under the action of the electric potential produced by mechanical loads through piezoelectric coupling can be described by a phenomenological theory [Hutson and White 1962] consisting of the equations of linear piezoelectricity [Auld 1973] and the conservation of charge for electrons and holes [Pierret 1983]. Because of the anisotropy of piezoelectric materials, the electromechanical couplings in them, and the nonlinearity associated with the drift currents of electrons and holes which are the products of the unknown carrier concentrations and the unknown electric field [Pierret 1983], theoretical analyses of piezoelectric semiconductor devices normally present considerable mathematical challenges. In spite

Keywords: piezoelectric, semiconductor, piezotronics.

of the mathematical difficulties, researchers have studied a series of useful problems of piezoelectric semiconductors including thickness vibration of plates [Wauer and Suherman 1997; Li et al. 2015], propagation of plate and surface waves [Collet 2008; Gu and Jin 2015], electromechanical fields around a hole [Zhang and Hu 2014] and in an inclusion [Yang et al. 2006], fields near cracks [Yang 2005; Hu et al. 2007; Sladek et al. 2014a; 2014b; Zhao et al. 2016a; 2016b; Fan et al. 2016], fields and waves in a rod with excessive electrons [Zhang et al. 2016a; 2016b], static extension of a fiber [Zhang et al. 2017a; 2017b], static bending of a fiber [Gao and Wang 2007; 2009; Fan et al. 2017; Zhang et al. \geq 2018], and structural theories of plates [Yang and Zhou 2005], shells [Yang et al. 2005], and rods [Li et al. \geq 2018].

In this paper we study electromechanical fields in a nonuniformly doped piezoelectric semiconductor rod. We consider three specific doping profiles. The case of linear doping is for the most basic understanding of nonuniform doping. The case of piecewise linear doping is for the understanding of the formation of a PN junction and the prediction of its structure and fields, which is fundamentally important in piezotronics applications. The case of sinusoidal doping is for some further understanding of nonuniform doping with potentials in applications.

2. Phenomenological theory of piezoelectric semiconductors

This section presents a brief summary of the three-dimensional theory of piezoelectric semiconductors. We use the Cartesian tensor notation. The indices i, j, k , and l assume 1, 2, and 3. A comma followed by an index indicates a partial derivative with respect to the coordinate associated with the index. A superimposed dot represents a time derivative. The theory consists of [Auld 1973; Pierret 1983]

$$T_{ji,j} = \rho \ddot{u}_i, \quad D_{i,i} = \rho^e = q(p - n + N_D^+ - N_A^-), \quad J_{i,i}^p = -q \dot{p}, \quad J_{i,i}^n = q \dot{n}, \quad (1)$$

where \mathbf{T} is the stress tensor, ρ the mass density, \mathbf{u} the mechanical displacement vector, \mathbf{D} the electric displacement vector, ρ^e the charge density, $q = 1.6 \times 10^{-19}$ C the electronic charge, p and n the concentrations of holes and electrons, N_D^+ and N_A^- the concentrations of impurities of donors and accepters, and J_i^p and J_i^n the hole and electron current densities. Equation (1)₁ is the stress equation of motion or the linear momentum equation (Newton's law). Equation (1)₂ is the charge equation of electrostatics (Gauss's law). Equations (1)₃ and (1)₄ are the conservation of charge for electrons and holes, respectively which are also called continuity equations. Constitutive relations accompanying (1) can be written in the form [Auld 1973; Pierret 1983]

$$\begin{aligned} S_{ij} &= s_{ijkl}^E T_{kl} + d_{kij} E_k, & D_i &= d_{ikl} T_{kl} + \varepsilon_{ik}^T E_k, \\ J_i^p &= qp\mu_{ij}^p E_j - qD_{ij}^p p_{,j}, & J_i^n &= qn\mu_{ij}^n E_j + qD_{ij}^n n_{,j}, \end{aligned} \quad (2)$$

where \mathbf{S} is the strain tensor, \mathbf{E} the electric field vector, s_{ijkl}^E the elastic compliance, d_{kij} the piezoelectric constants, ε_{ij}^T the dielectric constants, μ_{ij}^n and μ_{ij}^p the carrier mobility, D_{ij}^n and D_{ij}^p the carrier diffusion constants. The equations on the first line of (2) are the usual constitutive relations for piezoelectric materials. Those on the second line are for hole and electron currents including both drift currents under an electric field and diffusion currents due to concentration gradients. The strain \mathbf{S} and the electric field \mathbf{E} are related to the mechanical displacement \mathbf{u} and the electric potential φ through

$$S_{ij} = \frac{1}{2}(u_{i,j} + u_{j,i}), \quad E_i = -\varphi_{,i}. \quad (3)$$

3. One-dimensional equations for the extension of a rod

Consider the piezoelectric semiconductor rod shown in Figure 1. The shape of the cross section A of the rod may be arbitrary. The rod is assumed to be long and thin, i.e., its length is much larger than the characteristic dimension of the cross section. It is made from a piezoelectric semiconductor crystal of class 6 mm. The c -axis of the crystal is along the axis of the rod. The lateral surface of the rod is free. The electric field in the surrounding free space is neglected.

We are interested in the extensional deformation of the rod which can be described by a set of one-dimensional equations for the axial displacement u_3 and the axial stress $T_3 = T_{33}$. In the one-dimensional model, (1) reduces to [Zhang et al. 2017a]

$$\begin{aligned} \frac{\partial T_3}{\partial x_3} &= \rho \ddot{u}_3, & \frac{\partial D_3}{\partial x_3} &= \rho^e = q(p - n + N_D^+ - N_A^-), \\ q\dot{p} &= -\frac{\partial J_3^p}{\partial x_3}, & q\dot{n} &= \frac{\partial J_3^n}{\partial x_3}. \end{aligned} \quad (4)$$

The relevant one-dimensional constitutive relations are [Zhang et al. 2017a]

$$\begin{aligned} T_3 &= \bar{c}_{33} S_3 - \bar{e}_{33} E_3, & D_3 &= \bar{e}_{33} S_3 + \bar{\epsilon}_{33} E_3, \\ J_3^p &= qp\mu_{33}^p E_3 - qD_{33}^p \frac{\partial p}{\partial x_3}, & J_3^n &= qn\mu_{33}^n E_3 + qD_{33}^n \frac{\partial n}{\partial x_3}. \end{aligned} \quad (5)$$

Here, \bar{c}_{33} , \bar{e}_{33} , and $\bar{\epsilon}_{33}$ are the effective one-dimensional elastic, piezoelectric, and dielectric constants. They are related to the usual three-dimensional material constants s_{pq}^E , ϵ_{ij}^T and d_{ip} through

$$\bar{c}_{33} = 1/s_{33}^E, \quad \bar{e}_{33} = d_{33}/s_{33}^E, \quad \bar{\epsilon}_{33} = \epsilon_{33}^T - d_{33}^2/s_{33}^E. \quad (6)$$

The appearance of the effective one-dimensional material constants in (5) is because of the introduction of the one-dimensional stress relaxation condition that for thin rods we approximately have $T_1 = T_2 = 0$. The mobility and diffusion constants in (5), μ_{33}^p , μ_{33}^n , D_{33}^p , and D_{33}^n , satisfy the Einstein relation

$$\frac{\mu_{33}^p}{D_{33}^p} = \frac{\mu_{33}^n}{D_{33}^n} = \frac{q}{k_B T}, \quad (7)$$

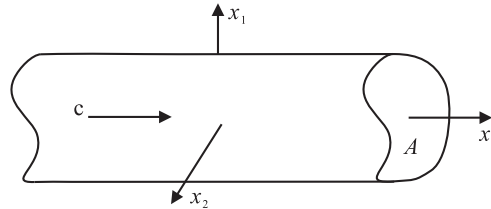


Figure 1. A piezoelectric semiconductor rod of crystals of class 6 mm.

where k_B is the Boltzmann constant and T the absolute temperature. The relevant strain-displacement relation and the electric field-potential relation are

$$S_3 = \frac{\partial u_3}{\partial x_3}, \quad E_3 = -\frac{\partial \varphi}{\partial x_3}. \quad (8)$$

4. Static fields in a rod

Consider a rod in equilibrium. From (4)₁,

$$T_3 = C_1, \quad (9)$$

where C_1 is an integration constant. From (5)₁,

$$S_3 = \frac{1}{\bar{c}_{33}}(C_1 + \bar{e}_{33}E_3). \quad (10)$$

Substituting (10) and (8)₂ into (5)₂, we obtain

$$D_3 = \frac{\bar{e}_{33}}{\bar{c}_{33}}C_1 + \left(\bar{\epsilon}_{33} + \frac{\bar{e}_{33}^2}{\bar{c}_{33}}\right)E_3 = \frac{\bar{e}_{33}}{\bar{c}_{33}}C_1 - \epsilon_{33}\varphi_{,3}. \quad (11)$$

From (4)_{3,4}, J_3^p and J_3^n are constants. When the rod is electrically isolated at its two ends without currents, which we assume to be the case in this paper, these constants are zero. From (5)_{3,4} and (8)₂,

$$J_3^p = -qp\mu_{33}^p \frac{\partial \varphi}{\partial x_3} - qD_{33}^p \frac{\partial p}{\partial x_3} = 0, \quad J_3^n = -qn\mu_{33}^n \frac{\partial \varphi}{\partial x_3} + qD_{33}^n \frac{\partial n}{\partial x_3} = 0. \quad (12)$$

With the use of (7), we rewrite (12) as

$$\frac{1}{p} \frac{\partial p}{\partial x_3} = -\frac{q}{k_B T} \frac{\partial \varphi}{\partial x_3}, \quad \frac{1}{n} \frac{\partial n}{\partial x_3} = \frac{q}{k_B T} \frac{\partial \varphi}{\partial x_3}. \quad (13)$$

Equation (13) can be integrated to produce

$$p = p_0 \exp\left(-\frac{q}{k_B T} \varphi\right), \quad n = n_0 \exp\left(\frac{q}{k_B T} \varphi\right), \quad (14)$$

where p_0 and n_0 are integration constants. Physically they are the values of p and n at $\varphi = 0$. The substitution of (11) and (14) into (4)₂ gives the following single equation governing the electric potential:

$$-\epsilon_{33}\varphi_{,33} = q \left[p_0 \exp\left(-\frac{q}{k_B T} \varphi\right) - n_0 \exp\left(\frac{q}{k_B T} \varphi\right) + N_D^+(x_3) - N_A^-(x_3) \right]. \quad (15)$$

For small φ , we make the following approximation (14):

$$p \cong p_0 \left(1 - \frac{q}{k_B T} \varphi\right), \quad n \cong n_0 \left(1 + \frac{q}{k_B T} \varphi\right), \quad (16)$$

which can describe small carrier concentration variations. Substituting (16) into (15), we obtain a linear equation for the potential:

$$\varphi_{,33} = -\frac{q}{\epsilon_{33}} \left[p_0 - n_0 - (p_0 + n_0) \frac{q}{k_B T} \varphi + N_D^+(x_3) - N_A^-(x_3) \right], \quad (17)$$

which can be further written as

$$\varphi_{,33} - \kappa^2 \varphi = -\frac{q}{\varepsilon_{33}} [p_0 - n_0 + N_D^+(x_3) - N_A^-(x_3)], \quad (18)$$

where

$$\kappa^2 = \frac{q}{\varepsilon_{33}} (p_0 + n_0) \frac{q}{k_B T}. \quad (19)$$

The general solution to (18) can be written as

$$\varphi = C_2 \sinh \kappa (x_3 + L) + C_3 \sinh \kappa (x_3 - L) + \frac{q}{\kappa^2 \varepsilon_{33}} (p_0 - n_0) + \varphi^p(x_3), \quad (20)$$

where C_2 and C_3 are integration constants, and φ^p is a particular solution of the nonhomogeneous equation

$$\varphi_{,33}^p - \kappa^2 \varphi^p = -\frac{q}{\varepsilon_{33}} [N_D^+(x_3) - N_A^-(x_3)]. \quad (21)$$

Once φ is known, p and n can be obtained from (16). With φ known, for the mechanical displacement, from (10), we have

$$u_{3,3} = \frac{1}{\bar{c}_{33}} (C_1 - \bar{e}_{33} \varphi_{,3}). \quad (22)$$

Integrating (22), we obtain

$$u_3 = \frac{1}{\bar{c}_{33}} (C_1 x_3 - \bar{e}_{33} \varphi) + C_4, \quad (23)$$

where C_4 is an integration constant.

We consider a free rod with the following boundary conditions:

$$T_{33}(\pm L) = 0, \quad J_3^p(\pm L) = 0, \quad J_3^n(\pm L) = 0, \quad D_3(\pm L) = 0. \quad (24)$$

When $C_1 = 0$, (24)₁ is satisfied. The satisfaction of (24)_{2,3} is ensured by (12). Only (24)₄ remains which, according to (11), translates into

$$\varphi_{,3}(\pm L) = 0. \quad (25)$$

From (20), it can be seen that (25) determines C_2 and C_3 formally in terms of p_0 and n_0 . Then (24) is completely satisfied. We need additional conditions to determine the remaining integration constants C_4 , p_0 , and n_0 . Since (4), (5), (8), and (24) are invariant under a rigid-body translation of the rod in the x_3 direction, to fix the rigid-body displacement so that the displacement is unique, we choose the center of the rod as a reference for the displacement and impose

$$u_3(0) = 0. \quad (26)$$

Equation (26) formally determines C_4 . At this point, (24)–(26) are all satisfied, and C_1 – C_4 are all formally determined. There are two undetermined constants left, i.e., p_0 and n_0 . Similar to (26), we also choose the center of the rod as the reference of the electric potential and set

$$\varphi(0) = 0. \quad (27)$$

Equation (27) determines a relationship between p_0 and n_0 . To completely determine p_0 and n_0 , we specify the total holes in the rod by the global charge neutrality condition

$$\int_{-L}^L (p - N_A^-) dx_3 = 0. \quad (28)$$

Since (4)₂ and (24)₄ imply that

$$\int_{-L}^L (p - n + N_D^+ - N_A^-) dx_3 = 0, \quad (29)$$

(28) and (29) further imply that

$$\int_{-L}^L (-n + N_D^+) dx_3 = 0. \quad (30)$$

Therefore (28) is the only independent charge neutrality condition. Equations (27) and (28) determine p_0 and n_0 .

5. Uniform and linear doping

For some basic understanding of the effect of a nonuniform doping, we begin with the simple case of uniform and linear doping. Let

$$N_A^-(x_3) = b_1 x_3 + c_1, \quad N_D^+(x_3) = b_2 x_3 + c_2. \quad (31)$$

Hence,

$$N_D^+(x_3) - N_A^-(x_3) = b x_3 + c, \quad b = b_2 - b_1, \quad c = c_2 - c_1. \quad (32)$$

In this case a particular solution of (21) is simply

$$\varphi^p = \frac{q}{\varepsilon_{33} k^2} (b x_3 + c). \quad (33)$$

Therefore, the effects of a uniform or linear doping on the electric potential and p as well as n according to (16) are also uniform and linear. We also notice that in this case (27) and (28) take the following forms:

$$(p_0 - n_0) + c = 0, \quad (34)$$

$$p_0 = \frac{3c_1 n_0}{6n_0 - 3c_2}. \quad (35)$$

In the special case of a linear doping only with $c_1 = c_2 = 0$, i.e., without the uniform doping term, we have $p_0 = n_0 = 0$.

6. Piecewise linear doping and PN junction

PN junctions are the fundamental building blocks of many piezoelectric semiconductor devices [Lee et al. 2012; 2014; Chung et al. 2012]. The understanding of PN junctions in these materials and the prediction of the electromechanical fields near a PN junction are fundamentally important to the development of piezoelectric semiconductor devices. PN junctions between two piezoelectric semiconductor half spaces and between a circular cylinder and its surrounding material were analyzed in [Luo et al. \geq 2018a;

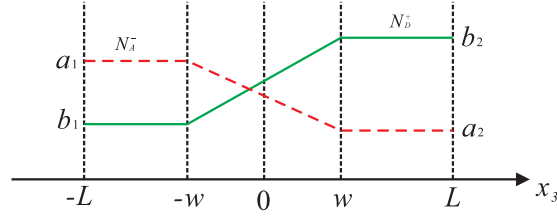


Figure 2. Piecewise linear doping.

$\geq 2018b]$, respectively. In this section we show that PN junctions in a piezoelectric semiconductor rod can be produced by nonuniform doping. Consider the case when the left half of the rod is mainly p -doped and the right half mainly n -doped. Between the two halves there is a finite transition zone of width $2w$ in which the doping varies linearly as shown in Figure 2. Because of diffusion of the holes and electrons related to the doping, a PN junction may form in and near the transition zone. The PN junctions studied in [Luo et al. $\geq 2018a$; $\geq 2018b]$ do not have a finite transition zone and effectively correspond to the special case of $w = 0$ in Figure 2, which is an ideal case simplified for theoretical analysis. In real applications usually there is a transition zone with a nonzero w .

Quantitatively, the doping profile in Figure 2 is described by

$$N_A^- = \begin{cases} a_1 & -L < x_3 < -w, \\ a_1 + \frac{a_2 - a_1}{2w}(x_3 + w) & |x_3| < w, \\ a_2 & w < x_3 < L, \end{cases} \quad (36)$$

and

$$N_D^+ = \begin{cases} b_1 & -L < x_3 < -w, \\ b_1 + \frac{b_2 - b_1}{2w}(x_3 + w) & |x_3| < w, \\ b_2 & w < x_3 < L. \end{cases} \quad (37)$$

Then,

$$N_D^+ - N_A^- = \begin{cases} d_1, & -L < x_3 < -w, \\ d_3 + d_4 x_3, & |x_3| < w, \\ d_2, & w < x_3 < L, \end{cases} \quad (38)$$

where

$$d_1 = b_1 - a_1, \quad d_2 = b_2 - a_2, \quad d_3 = \frac{b_1 - a_1}{2} + \frac{b_2 - a_2}{2}, \quad d_4 = \frac{b_2 - b_1}{2w} - \frac{a_2 - a_1}{2w}. \quad (39)$$

PN junctions are local. It is sufficient to consider the special and relatively simple case when $L = \infty$. In this case, from (21), (20), (16), and (23), we have, for $x_3 < -w$,

$$\begin{aligned} \varphi^p &= \frac{q}{\varepsilon_{33}\kappa^2}d_1, \quad \varphi = C_1 \exp \kappa(x_3 + w) + \frac{q}{\kappa^2\varepsilon_{33}}(p_0 - n_0) + \varphi^p(x_3), \\ p &\cong p_0 \left(1 - \frac{q}{k_B T} \varphi\right), \quad n \cong n_0 \left(1 + \frac{q}{k_B T} \varphi\right), \quad u_3 = -\frac{\bar{e}_{33}}{\bar{c}_{33}} \varphi + C_2, \\ D_3 &= -\varepsilon_{33}\varphi_{,3}, \quad T_3 = 0, \quad J_3^p = 0, \quad J_3^n = 0, \end{aligned} \quad (40)$$

and, similarly for $w < x_3$,

$$\begin{aligned}\varphi^p &= \frac{q}{\varepsilon_{33}\kappa^2}d_2, \quad \varphi = C_3 \exp \kappa(w - x_3) + \frac{q}{\kappa^2\varepsilon_{33}}(p_0 - n_0) + \varphi^p(x_3), \\ p &\cong p_0\left(1 - \frac{q}{k_B T}\varphi\right), \quad n \cong n_0\left(1 + \frac{q}{k_B T}\varphi\right), \quad u_3 = -\frac{\bar{e}_{33}}{\bar{c}_{33}}\varphi + C_4, \\ D_3 &= -\varepsilon_{33}\varphi_{,3}, \quad T_3 = 0, \quad J_3^p = 0, \quad J_3^n = 0.\end{aligned}\tag{41}$$

Equation (40) and (41) show that κ describes the exponentially decaying rate of the fields from the edges of the transition zone. Inside the transition zone where $|x_3| < w$, we have

$$\begin{aligned}\varphi^p &= \frac{q}{\varepsilon_{33}\kappa^2}(d_3 + d_4x_3), \quad \varphi = C_5 \sinh \kappa(x_3 + w) + C_6 \sinh \kappa(x_3 - w) + \frac{q}{\kappa^2\varepsilon_{33}}(p_0 - n_0) + \varphi^p(x_3), \\ p &\cong p_0\left(1 - \frac{q}{k_B T}\varphi\right), \quad n \cong n_0\left(1 + \frac{q}{k_B T}\varphi\right), \quad u_3 = -\frac{\bar{e}_{33}}{\bar{c}_{33}}\varphi + C_7, \\ D_3 &= -\varepsilon_{33}\varphi_{,3}, \quad T_3 = 0, \quad J_3^p = 0, \quad J_3^n = 0.\end{aligned}\tag{42}$$

The boundary and continuity conditions are (24) when $L = \infty$, and

$$\begin{aligned}T_{33}(\pm w^-) &= T_{33}(\pm w^+), \quad J_3^p(\pm w^-) = J_3^p(\pm w^+), \\ J_3^n(\pm w^-) &= J_3^n(\pm w^+), \quad D_3(\pm w^-) = D_3(\pm w^+),\end{aligned}\tag{43}$$

as well as

$$\begin{aligned}u_3(\pm w^-) &= u_3(\pm w^+), \quad \varphi(\pm w^-) = \varphi(\pm w^+), \\ p(\pm w^-) &= p(\pm w^+), \quad n(\pm w^-) = n(\pm w^+).\end{aligned}\tag{44}$$

Equation (24) when $L = \infty$ and (43)₁₋₃ are already satisfied. Equation (44)₂ implies (44)_{3,4}. From (43)₄ and (44)_{1,2}, we have six conditions left. With (26)–(28) where $L = \infty$, there are nine equations for C_1 – C_7 , p_0 , and n_0 . They are solved on a computer.

As a numerical example, consider a ZnO rod whose material constants can be founded in [Auld 1973]:

$$\varepsilon_{33} = 12.64\varepsilon_0 = 1.119 \times 10^{-10} \text{ F/m}, \quad c_{33} = 21.09 \times 10^{10} \text{ N/m}^2, \quad e_{33} = 1.32 \text{ C/m}^2,\tag{45}$$

where the dielectric constant of free space is $\varepsilon_0 = 8.8537 \times 10^{-12} \text{ F/m}$. At room temperature, we have [Pierret 1996]

$$\frac{\mu_{33}^n}{D_{33}^n} = \frac{\mu_{33}^p}{D_{33}^p} = \frac{q}{k_B T} = 38.46 \text{ V}^{-1}.\tag{46}$$

We consider the following case with some symmetry or antisymmetry:

$$a_1 = b_2 = 1.0 \times 10^{21} \text{ m}^{-3}, \quad a_2 = b_1 = 0.8a_1, \quad w = 0.1 \mu\text{m}.\tag{47}$$

In this case, it is found that

$$p_0 = n_0 = 0.9 \times 10^{21} \text{ m}^{-3} = \frac{1}{2}(a_1 + a_2) = \frac{1}{2}(b_1 + b_2).\tag{48}$$

From (19),

$$\frac{1}{\kappa} = 1.005 \times 10^{-7} \cong 0.1 \mu\text{m},\tag{49}$$

which is a characteristic length of the exponentially varying fields. Numerical results show that in this case,

$$\frac{q}{k_B T} \varphi \cong 0.1154. \quad (50)$$

Hence the linear approximation in (16) is valid.

Figure 3 shows the contour plots of various electromechanical fields inside and near the transition zone. The diameter d of the rod in the figure is symbolic only and is immaterial for a one-dimensional model. Figures 3a and 3b are the concentrations of holes and electrons which were initially determined by the piecewise linear functions in Figure 2 but are now smooth because of diffusion. They are monotonically changing along the rod, more rapidly in the transition zone. Figure 3c shows essentially the net or total charge which localizes within and near the transition zone, and has a sign change there (the formation of a PN junction). Figure 3d shows the local electric field produced by the charges in the PN junction (the so-called built-in field), which is negative (pointing to the left) as expected from the signs of the charges in 3c. Figure 3e is the electric potential (the so-called built-in potential) corresponding to the electric field in Figure 3d. The potential in Figure 3e rises from left to right monotonically. It changes rapidly within the transition zone and is essentially constant far away from there. Since $x_3 = 0$ is chosen as a reference where potential is zero, the potential is negative on the left and positive on the right. The material is piezoelectric. Therefore, the electric field in Figure 3d causes mechanical fields. The displacement field is shown in Figure 3f, which is qualitatively similar to the electric potential. The strain field is shown in Figure 3g, which is localized within and near the transition zone.

Figure 4 shows the effects of $2w$, i.e., the width of the transition zone, on various electromechanical fields. As $2w$ decreases, the transition zone is narrower and all fields change more rapidly there. The total charge in Figure 4c becomes more concentrated. The intensities of the total charge in Figure 4c, the electric field in Figure 4d, and the strain field in Figure 4g all increase. Therefore, in the cases studied in [Luo et al. \geq 2018a; \geq 2018b] where the width of the transition zone $2w = 0$, the intensity or strength of the fields at the PN junction represents that of an ideal or limit case significantly larger than what happens when $2w$ is finite. At far fields away from the transition zone, the concentrations of holes in Figure 4a, electrons in Figure 4b, electric potential in Figure 4e, and displacement in Figure 4f are insensitive to w .

In Figure 5, $w = 0.1 \mu\text{m}$ is fixed. The difference of N_D^+ and N_A^- is varied by choosing different values of λ according to

$$a_0 = 10^{21} \text{ m}^{-3}, \quad a_1 = b_2 = a_0 + \lambda a_0, \quad a_2 = b_1 = 0.8a_0 - \lambda a_0. \quad (51)$$

It can be verified from (36) and (37) that under (51) the sum of N_D^+ and N_A^- is fixed. As λ increases, the gradients of the carrier concentrations increase as seen from Figures 5a and 5b. As a consequence, overall the fields change more rapidly or become stronger inside and near the transition zone, which is as expected.

In Figure 6, $w = 0.1 \mu\text{m}$ is fixed. The sum of N_D^+ and N_A^- is varied by choosing different values of λ according to

$$a_0 = 10^{21} \text{ m}^{-3}, \quad a_1 = b_2 = a_0 + \lambda a_0, \quad a_2 = b_1 = 0.8a_0 + \lambda a_0. \quad (52)$$

It can be verified from (38) that under (52) the difference of N_D^+ and N_A^- is fixed. As λ increases, a_1 , a_2 , b_1 , and b_2 all increase. From (48), p_0 and n_0 increase and hence there are more holes and electrons.

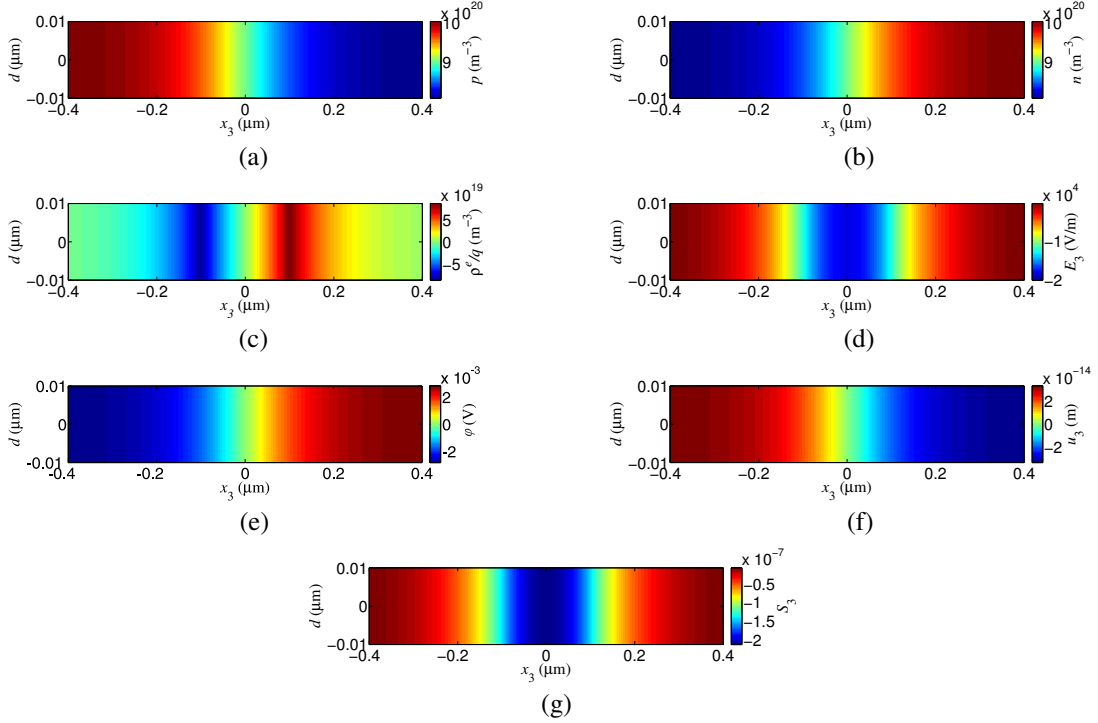


Figure 3. Fields inside and near the transition zone: (a) $p(x_3)$ for holes; (b) $n(x_3)$ for electrons; (c) ρ^e/q for the total charge (PN junction); (d) $E_3(x_3)$ for the electric field; (e) $\varphi(x_3)$ for the electric potential; (f) $u_3(x_3)$ for the displacement; (g) $S_3(x_3)$ for the strain.

This can be seen in Figures 6a and 6b. It can be shown that the coefficients of various fields, C_1 , C_3 , C_5 , and C_6 , are inversely proportional to κ^3 . This contributes to the reduction of fields in Figure 6c–d as λ , and hence $p_0 + n_0$ as well as κ , increase.

For a qualitative comparison, the results of the PN junction charge and electric field distributions in [Pierret 1996] are shown in Figures 7, left, and 7, right, respectively. Comparing Figures 3c, 4c, 5c and 6c with Figure 7, left, we can see that the piecewise constant charge distribution in Figure 7, left, can be viewed as averages of the gradually changing charge distributions obtained in the present paper, which are more realistic. In obtaining the results in Figure 7, the charge distribution is assumed known so that only the charge equation of electrostatics is needed to calculate the electric field. However, in the present paper coupled equations need to be solved to obtain all fields simultaneously. There is a more fundamental difference between the results obtained in the present paper and that in Figure 7, left. In the assumed charge distribution in Figure 7, left, the impurity N_A^- left by holes alone is responsible for the net charge to the left of the junction and hence the name “depletion region”. However, our more sophisticated and coupled-field analysis shows that in fact both the N_A^- left by the holes and the electrons diffused from the right part of the junction together contribute to the net charge to the left of the junction. The situation to the right of the junction is similar. Comparing Figures 3d, 4d, 5d and 6d with Figure 7, right, we see that the axial electric field obtained in the present paper is smoothly changing and hence

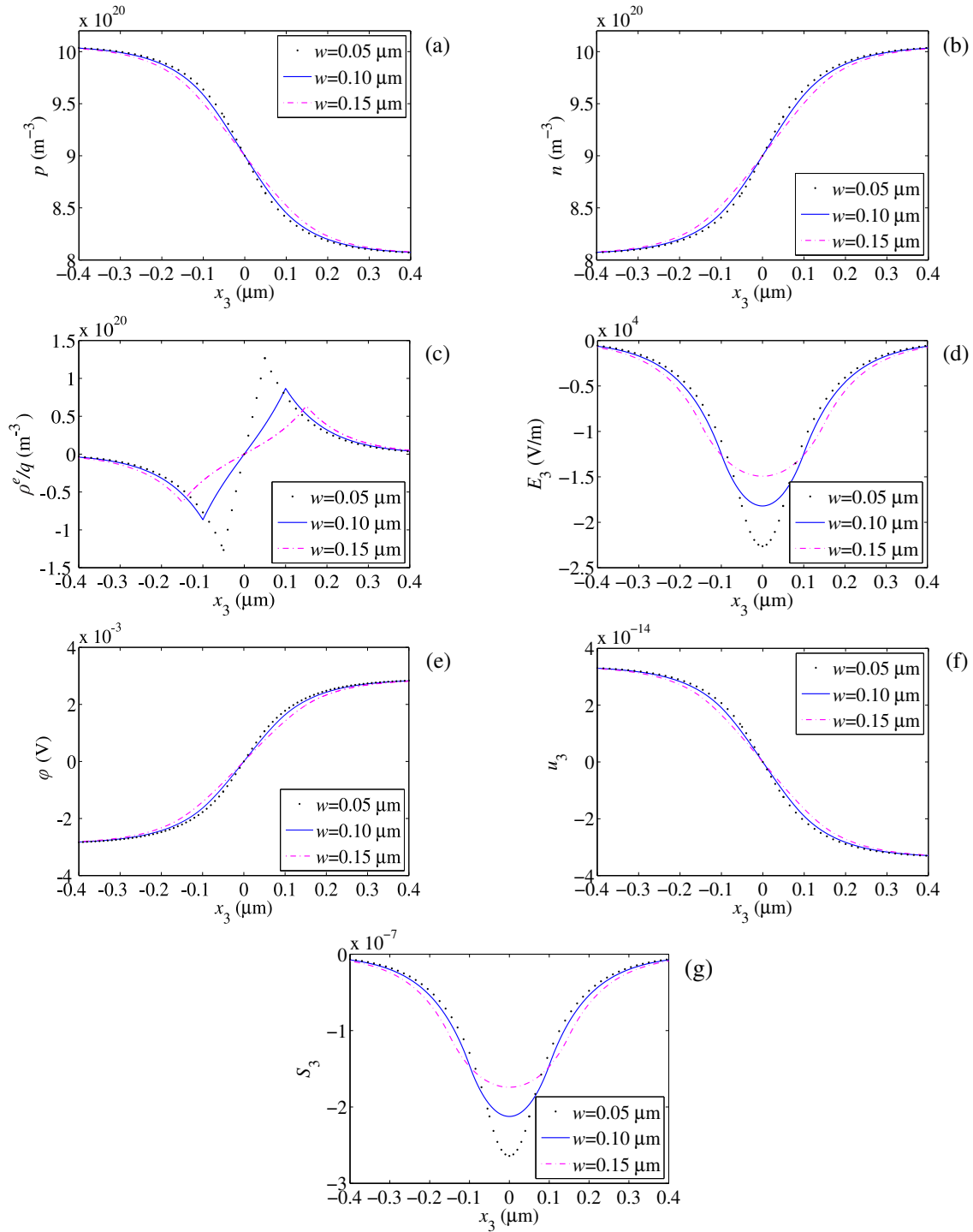


Figure 4. Effects of $2w$, the width of the transition zone: (a) $p(x_3)$ for holes; (b) $n(x_3)$ for electrons; (c) ρ^e/q for the total charge (PN junction); (d) $E_3(x_3)$ for the electric field; (e) $\varphi(x_3)$ for the electric potential; (f) $u_3(x_3)$ for the displacement; (g) $S_3(x_3)$ for the strain.

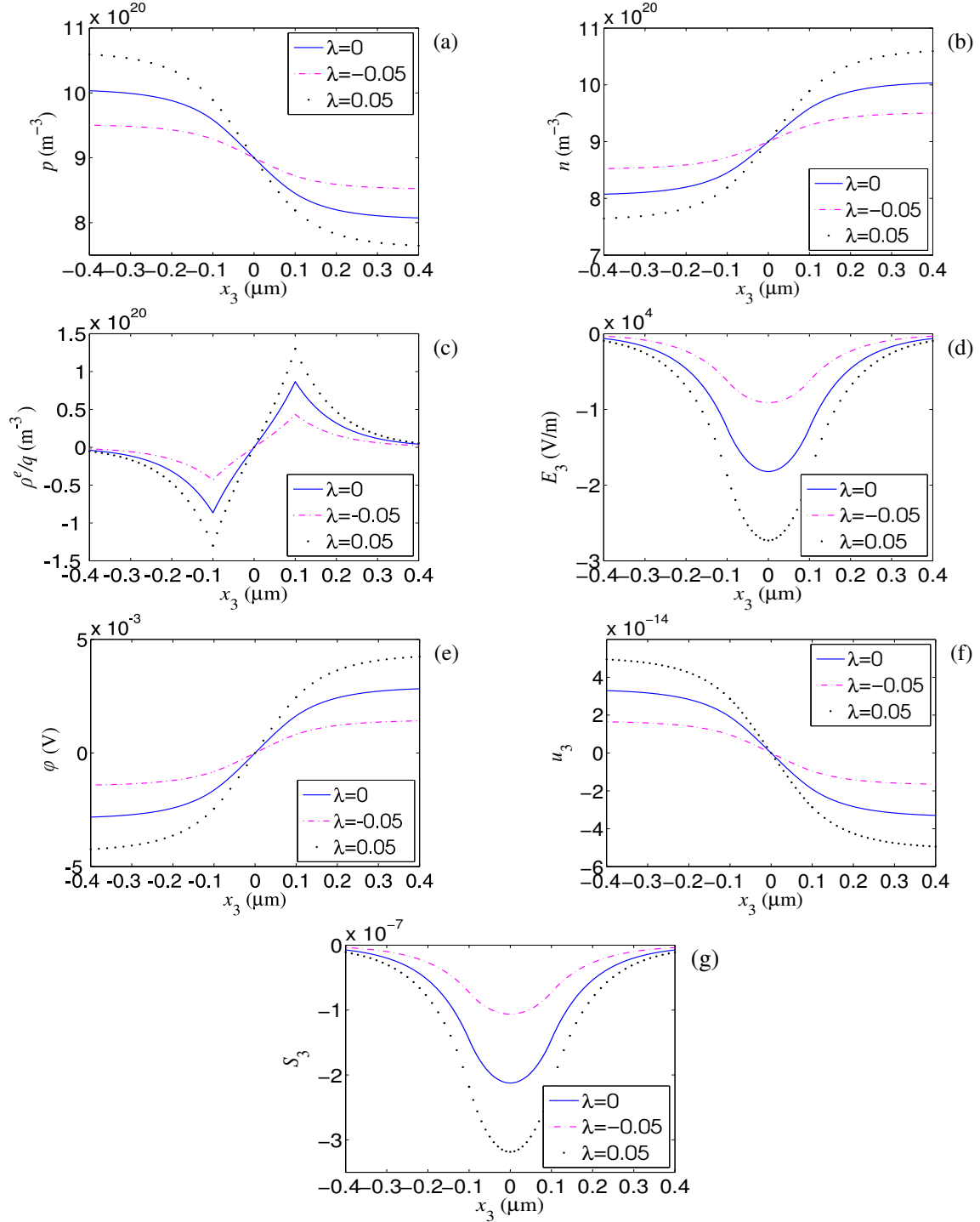


Figure 5. Effects of doping concentration difference: (a) $p(x_3)$ for holes; (b) $n(x_3)$ for electrons; (c) ρ^e/q for the total charge (PN junction); (d) $E_3(x_3)$ for the electric field; (e) $\varphi(x_3)$ for the electric potential; (f) $u_3(x_3)$ for the displacement; (g) $S_3(x_3)$ for the strain.

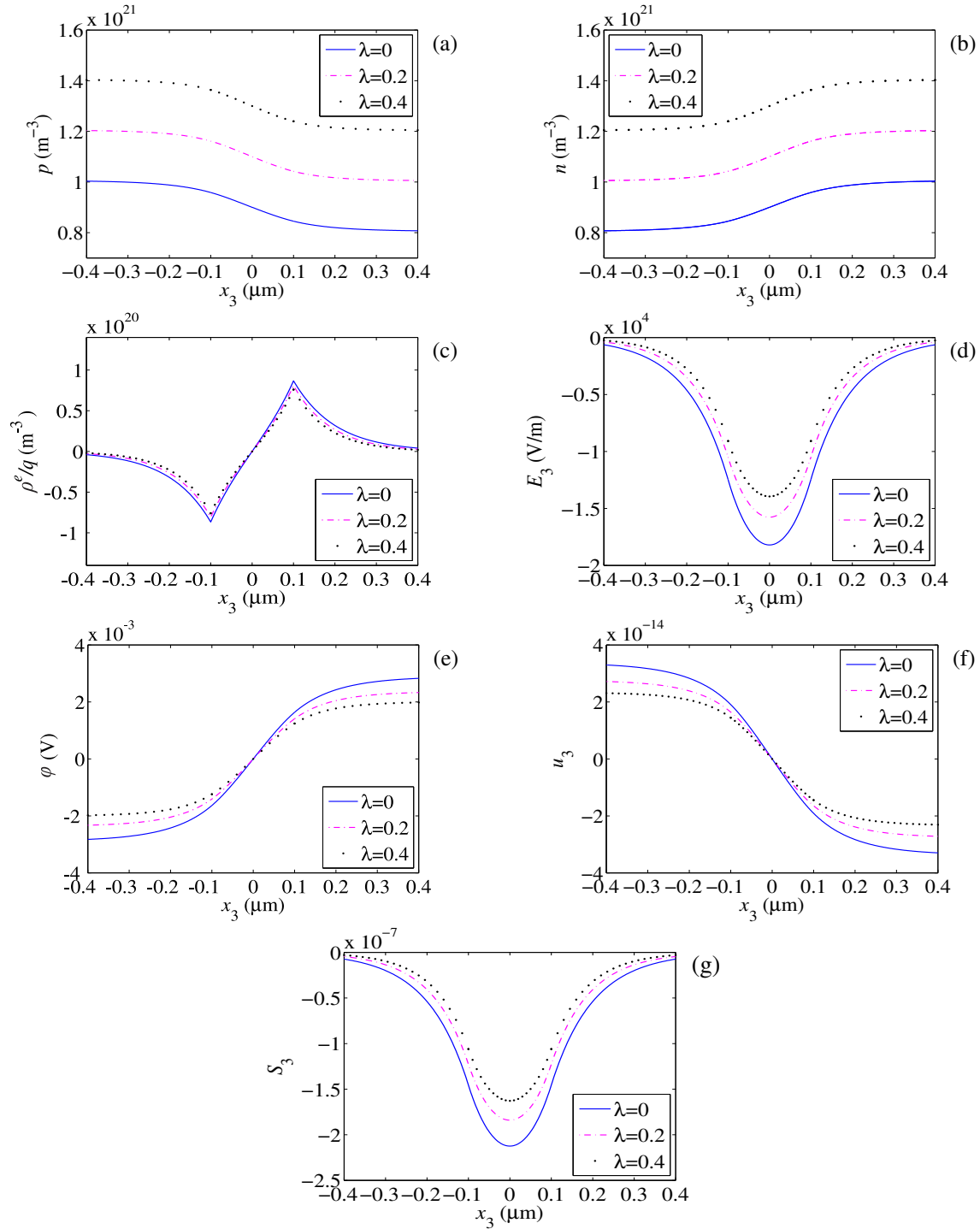


Figure 6. Effects of doping concentration difference: (a) $p(x_3)$ for holes; (b) $n(x_3)$ for electrons; (c) ρ^e/q for the total charge (PN junction); (d) $E_3(x_3)$ for the electric field; (e) $\phi(x_3)$ for the electric potential; (f) $u_3(x_3)$ for the displacement; (g) $S_3(x_3)$ for the strain.

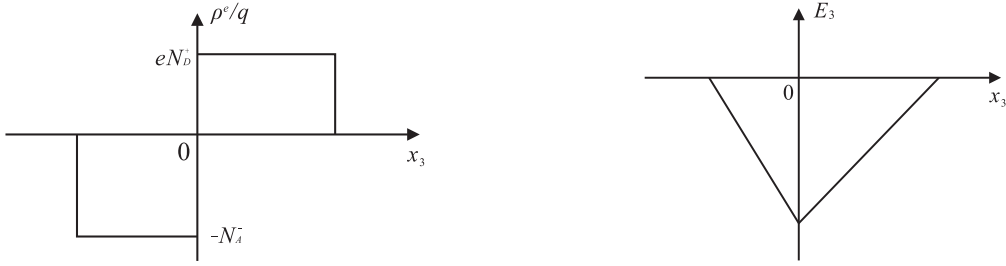


Figure 7. Fields in a PN junction with assumed charge distribution. Left: charge distribution. Right: electric field.

is more realistic. The potential fields obtained in the present paper are qualitatively similar to those in [Pierret 1996], which are not presented here.

7. Sinusoidal doping

In this section we consider the effect of a periodically varying doping described by

$$N_A^-(x_3) = a_1 + b_1 \sin \lambda x_3, \quad N_D^+(x_3) = a_2 + b_2 \sin \lambda x_3. \quad (53)$$

Hence,

$$N_D^+(x_3) - N_A^-(x_3) = a + b \sin \lambda x_3, \quad a = a_2 - a_1, \quad b = b_2 - b_1. \quad (54)$$

In this case, for the particular solution of (21) we have

$$\varphi^p = \frac{q}{\varepsilon_{33}} \left[\frac{a}{\kappa^2} + \frac{b}{\kappa^2 + \lambda^2} \sin \lambda x_3 \right]. \quad (55)$$

From (27) and (28), the two equations for determining p_0 and n_0 take the following form:

$$p_0 - n_0 + a = 0, \quad p_0 = \frac{n_0 a_1}{2n_0 - a_2}. \quad (56)$$

In the special case when $a_2 = a_1$, (54) implies that $a = 0$. Then, from (56), we obtain $p_0 = n_0 = a_1$. For a numerical example, we consider the case when $a_1 = 10^{21} \text{ m}^{-3}$, $b_1 = 0.2a_1$, $b_2 = -b_1$, and $\lambda = 0.2\kappa$. Then $2\pi/\lambda \cong 3\mu\text{m}$, which can be viewed as some wavelength of the doping. We choose $2L = 30\mu\text{m}$ which is about ten times the doping wavelength $2\pi/\lambda$. The electromechanical fields in this case are shown in Figure 8. They are essentially periodic except at $x_3 = \pm L$ where there are some end effects. It can be seen that under a periodic doping, p and n in Figure 8a vary similarly but are out of phase. The total charge ρ^e in Figure 8b oscillates and has some concentration near the ends. The concentration of carriers near the ends of a rod was also observed in [Zhang et al. 2016a; 2017a]. The periodic doping produces essentially the same periodic electric field in Figure 8c, potential in Figure 8d, displacement in Figure 8e, and strain in Figure 8f. Effectively a periodic doping produces a series of PN junctions. The fields in Figure 8 can be explored for possible applications. For example, if an acoustic wave propagates in the rod with the presence of the periodic strain field in Figure 8f, does the strain field acts as an initial or biasing field and does it affect the waves like a phononic crystal?

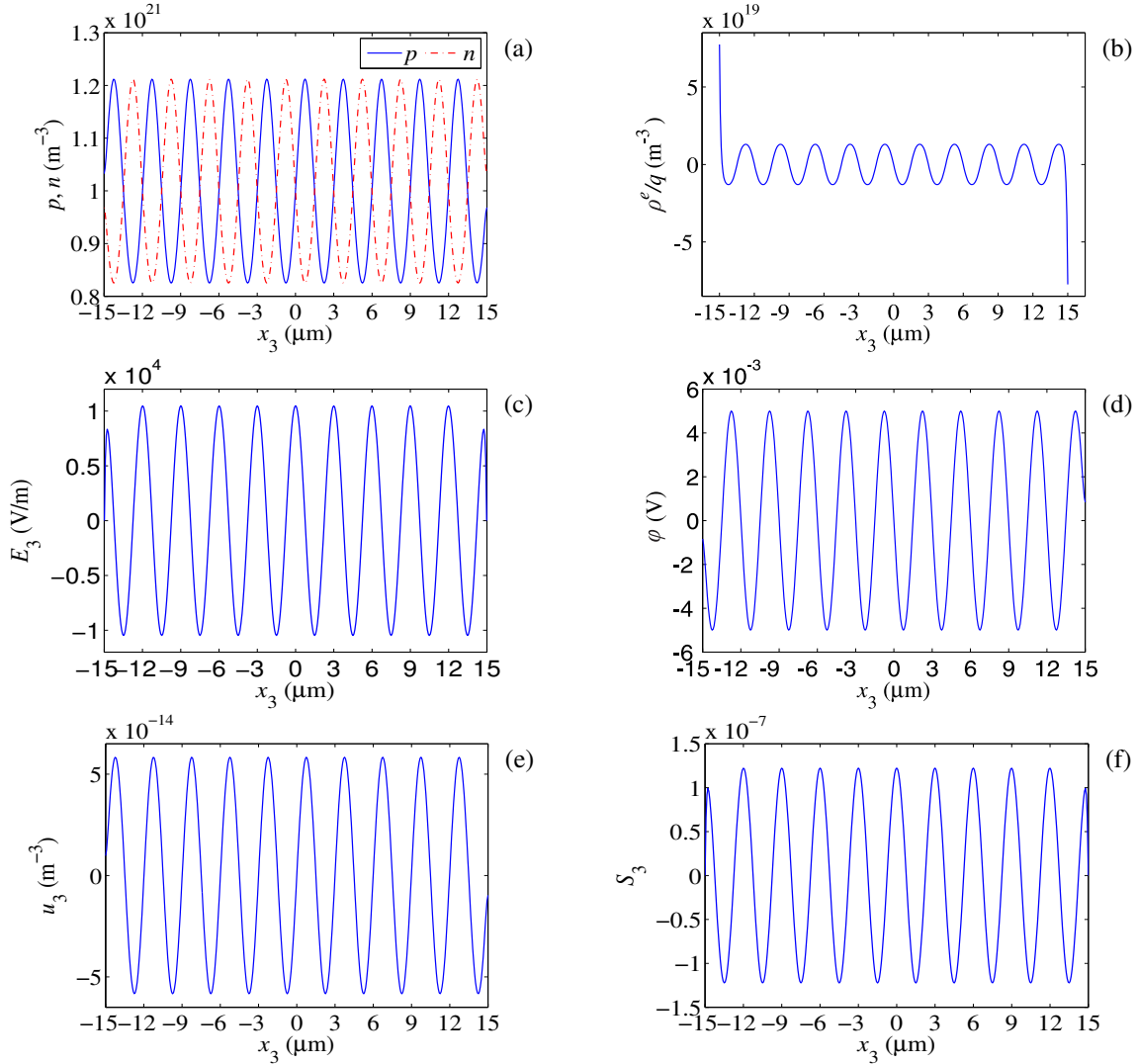


Figure 8. Effects of sinusoidal doping: (a) $p(x_3)$ and $n(x_3)$; (b) ρ^e/q for the total charge; (c) $E_3(x_3)$ for the electric field; (d) $\varphi(x_3)$ for the electric potential; (e) $u_3(x_3)$ for the displacement; (f) $S_3(x_3)$ for the strain.

8. Conclusions

For low values of the electric potential, the governing equations of an isolated piezoelectric semiconductor rod can be linearized and reduced to a single equation for the potential which is valid for small carrier concentration variations. Solutions of the equation show that a uniform or linear doping makes a uniform or linear contribution to the electric potential and carrier concentrations. PN junctions can be realized through nonuniform doping. Near the transition zone between a p -doped region and an n -doped region, there are local charges producing a local electric field and thus forming a PN junction. In the

so-called depletion regions near a PN junction, in fact both impurities and mobile charges contribute to the net charges. The intensity or strength of the charge and field distributions at the junction is sensitive to the width of the transition zone of the piecewise linear doping. When its width becomes narrower, the electric field in the PN junction becomes stronger. The electric field in the junction also becomes stronger when the doping difference increases. A sinusoidal doping produces periodic distributions of charges and an electric field which can be explored for device applications. Since the material is piezoelectric, there exist mechanical fields associated with the electric fields.

Acknowledgments

This work was supported by the National Natural Science Foundation of China (Nos. 11672141 and 11372145), the Y. K. Pao Visiting Professorship at Ningbo University, and the K. C. Wong Magana Fund through Ningbo University.

References

- [Araneo et al. 2012] R. Araneo, G. Lovat, P. Burghignoli, and C. Falconi, “Piezo-semiconductive quasi-1D nanodevices with or without anti-symmetry”, *Adv. Mater.* **24**:34 (2012), 4719–4724.
- [Asthana et al. 2014] A. Asthana, H. A. Ardakani, Y. K. Yap, and R. S. Yassar, “Real time observation of mechanically triggered piezoelectric current in individual ZnO nanobelts”, *J. Mater. Chem. C* **2**:20 (2014), 3995–4004.
- [Auld 1973] B. A. Auld, *Acoustic fields and waves in solids, I*, Wiley, New York, 1973.
- [Büyükköse et al. 2014] S. Büyükköse, A. Hernández-Mínguez, B. Vratzov, C. Somaschini, L. Geelhaar, H. Riechert, W. G. van der Wiel, and P. V. Santos, “High-frequency acoustic charge transport in GaAs nanowires”, *Nanotechnology* **25**:13 (2014), art. id. 135204.
- [Chen et al. 2007] T. T. Chen, C. L. Cheng, S.-P. Fu, and Y. F. Chen, “Photoelastic effect in ZnO nanorods”, *Nanotechnology* **18**:22 (2007), art. id. 225705.
- [Choi et al. 2009] M.-Y. Choi, D. Choi, M.-J. Jin, I. Kim, S.-H. Kim, J.-Y. Choi, S. Y. Lee, J. M. Kim, and S.-W. Kim, “Mechanically powered transparent flexible charge-generating nanodevices with piezoelectric ZnO nanorods”, *Adv. Mater.* **21**:21 (2009), 2185–2189.
- [Chung et al. 2012] S. Y. Chung, S. Kim, J.-H. Lee, K. Kim, S.-W. Kim, C.-Y. Kang, S.-J. Yoon, and Y. S. Kim, “All-solution-processed flexible thin film piezoelectric nanogenerator”, *Adv. Mater.* **24**:45 (2012), 6022–6027.
- [Collet 2008] B. Collet, “Acoustic wave propagation in cubic piezoelectric semiconductor plates”, *J. Acoust. Soc. Am.* **123**:5 (2008), 3694.
- [Fan et al. 2016] C. Y. Fan, Y. Yan, G. T. Xu, and M. H. Zhao, “Piezoelectric-conductor iterative method for analysis of cracks in piezoelectric semiconductors via the finite element method”, *Eng. Fract. Mech.* **165** (2016), 183–196.
- [Fan et al. 2017] S. Fan, Y. Liang, J. Xie, and Y. Hu, “Exact solutions to the electromechanical quantities inside a statically-bent circular ZnO nanowire by taking into account both the piezoelectric property and the semiconducting performance, I: linearized analysis”, *Nano Energy* **40** (2017), 82–87.
- [Gao and Wang 2007] Y. Gao and Z. L. Wang, “Electrostatic potential in a bent piezoelectric nanowire: the fundamental theory of nanogenerator and nanopiezotronics”, *Nano Lett.* **7**:8 (2007), 2499–2505.
- [Gao and Wang 2009] Y. Gao and Z. L. Wang, “Equilibrium potential of free charge carriers in a bent piezoelectric semiconductive nanowire”, *Nano Lett.* **9**:3 (2009), 1103–1110.
- [Gao et al. 2007] P. X. Gao, J. Song, J. Liu, and Z. L. Wang, “Nanowire piezoelectric nanogenerators on plastic substrates as flexible power sources for nanodevices”, *Adv. Mater.* **19**:1 (2007), 67–72.
- [Gu and Jin 2015] C. Gu and F. Jin, “Shear-horizontal surface waves in a half-space of piezoelectric semiconductors”, *Philos. Mag. Lett.* **95**:2 (2015), 92–100.

- [Hickernell 2003] F. S. Hickernell, "The piezoelectric semiconductor and acoustoelectronic device development in the sixties", pp. 1012–1020 in *Proc. 2003 IEEE International Frequency Control Symposium and PDA Exhibition* (Tampa), IEEE, Piscataway, NJ, 2003.
- [Hu et al. 2007] Y. Hu, Y. Zeng, and J. Yang, "A mode III crack in a piezoelectric semiconductor of crystals with 6 mm symmetry", *Int. J. Solids Struct.* **44**:11-12 (2007), 3928–3938.
- [Hu et al. 2010] Y. Hu, Y. Chang, P. Fei, R. L. Snyder, and Z. L. Wang, "Designing the electric transport characteristics of ZnO micro/nanowire devices by coupling piezoelectric and photoexcitation effects", *ACS Nano* **4**:2 (2010), 1234–1240.
- [Hutson and White 1962] A. R. Hutson and D. L. White, "Elastic wave propagation in piezoelectric semiconductors", *J. Appl. Phys.* **33**:40 (1962), 40–47.
- [Ji et al. 2013] J. Ji, Z. Zhou, X. Yang, W. Zhang, S. Sang, and P. Li, "One-dimensional nano-interconnection formation", *Small* **9**:18 (2013), 3014–3029.
- [Kumar and Kim 2011] B. Kumar and S.-W. Kim, "Recent advances in power generation through piezoelectric nanogenerators", *J. Mater. Chem.* **21**:47 (2011), 18946–18958.
- [Lee et al. 2012] K. Y. Lee, B. Kumar, J.-S. Seo, K.-H. Kim, J. I. Sohn, S. N. Cha, D. Choi, Z. L. Wang, and S.-W. Kim, "P-type polymer-hybridized high-performance piezoelectric nanogenerators", *Nano Lett.* **12**:4 (2012), 1959–1964.
- [Lee et al. 2014] K. Y. Lee, J. Bae, S. M. Kim, J.-H. Lee, G. C. Yoon, M. K. Gupta, S. Kim, H. Kim, J. Park, and S.-W. Kim, "Depletion width engineering via surface modification for high performance semiconducting piezoelectric nanogenerators", *Nano Energy* **8** (2014), 165–173.
- [Li et al. 2015] P. Li, F. Jin, and J. Yang, "Effects of semiconduction on electromechanical energy conversion in piezoelectrics", *Smart Mater. Struct.* **24** (2015), art. id. 025021.
- [Li et al. ≥ 2018] P. Li, F. Jin, and J. X. Ma, "The one-dimensional dynamic equations for piezoelectric semiconductor beams with rectangular cross sections and its applications in static and dynamic characteristics analysis", to appear in *Appl. Math. Mech.*
- [Liao et al. 2014] Q. Liao, Z. Zhang, X. Zhang, M. Mohr, Y. Zhang, and H.-J. Fecht, "Flexible piezoelectric nanogenerators based on a fiber/ZnO nanowires/paper hybrid structure for energy harvesting", *Nano Res.* **7**:6 (2014), 917–928.
- [Luo et al. ≥ 2018a] Y. X. Luo, C. L. Zhang, W. Q. Chen, and J. S. Yang, "An analysis of PN junctions in piezoelectric semiconductors", to appear in *J. Appl. Phys.*
- [Luo et al. ≥ 2018b] Y. X. Luo, C. L. Zhang, W. Q. Chen, and J. S. Yang, "Electromechanical fields near a circular PN junction between two piezoelectric semiconductors", to appear in *Acta Mech. Solida Sin.*
- [Pierret 1983] R. F. Pierret, *Semiconductor fundamentals*, Modular Series on Solid State Devices **1**, Addison-Wesley, Reading, MA, 1983.
- [Pierret 1996] R. F. Pierret, *Semiconductor device fundamentals*, Addison-Wesley, Reading, MA, 1996.
- [Romano et al. 2011] G. Romano, G. Mantini, A. Di Carlo, A. D'Amico, C. Falconi, and Z. L. Wang, "Piezoelectric potential in vertically aligned nanowires for high output nanogenerators", *Nanotechnology* **22**:46 (2011), art. id. 465401.
- [Shen et al. 2010] Y. Shen, J.-I. Hong, S. Xu, S. Lin, H. Fang, S. Zhang, Y. Ding, R. L. Snyder, and Z. L. Wang, "A general approach for fabricating arc-shaped composite nanowire arrays by pulsed laser deposition", *Adv. Funct. Mater.* **20**:5 (2010), 703–707.
- [Sladek et al. 2014a] J. Sladek, V. Sladek, E. Pan, and M. Wünsche, "Fracture analysis in piezoelectric semiconductors under a thermal load", *Eng. Fract. Mech.* **126** (2014), 27–39.
- [Sladek et al. 2014b] J. Sladek, V. Sladek, E. Pan, and D. L. Young, "Dynamic anti-plane crack analysis in functional graded piezoelectric semiconductor crystals", *Comput. Model. Eng. Sci.* **99**:4 (2014), 273–296.
- [Wang 2003] Z. L. Wang, "Nanobelts, nanowires, and nanodiskettes of semiconducting oxides: from materials to nanodevices", *Adv. Mater.* **15**:5 (2003), 432–436.
- [Wang 2010] Z. L. Wang, "Piezopotential gated nanowire devices: piezotronics and piezo-phototronics", *Nano Today* **5**:6 (2010), 540–552.

- [Wang et al. 2006] X. Wang, J. Zhou, J. Song, J. Liu, N. Xu, and Z. L. Wang, “Piezoelectric field effect transistor and nanoforce sensor based on a single ZnO nanowire”, *Nano Lett.* **6**:12 (2006), 2768–2772.
- [Wauer and Suherman 1997] J. Wauer and S. Suherman, “Thickness vibrations of a piezo-semiconducting plate layer”, *Int. J. Eng. Sci.* **35**:15 (1997), 1387–1404.
- [Xue et al. 2010] H. Xue, N. Pan, M. Li, Y. Wu, X. Wang, and J. G. Hou, “Probing the strain effect on near band edge emission of a curved ZnO nanowire via spatially resolved cathodoluminescence”, *Nanotechnology* **21**:21 (2010), art. id. 215701.
- [Yang 2005] J. Yang, “An anti-plane crack in a piezoelectric semiconductor”, *Int. J. Fract.* **136**:1-4 (2005), L27–L32.
- [Yang and Zhou 2005] J. S. Yang and H. G. Zhou, “Amplification of acoustic waves in piezoelectric semiconductor plates”, *Int. J. Solids Struct.* **42**:11-12 (2005), 3171–3183.
- [Yang et al. 2005] J. Yang, X. Yang, and J. A. Turner, “Amplification of acoustic waves in piezoelectric semiconductor shells”, *J. Intell. Mater. Syst. Struct.* **16**:7-8 (2005), 613–621.
- [Yang et al. 2006] J. S. Yang, Y. C. Song, and A. K. Soh, “Analysis of a circular piezoelectric semiconductor embedded in a piezoelectric semiconductor substrate”, *Arch. Appl. Mech.* **76**:7-8 (2006), 381–390.
- [Yoo et al. 2009] J. Yoo, C.-H. Lee, Y.-J. Doh, H. S. Jung, and G.-C. Yi, “Modulation doping in ZnO nanorods for electrical nanodevice applications”, *Appl. Phys. Lett.* **94**:22 (2009), art. id. 223117.
- [Yu et al. 2010] J. Yu, S. J. Ippolito, W. Wlodarski, M. Strano, and K. Kalantar-Zadeh, “Nanorod based Schottky contact gas sensors in reversed bias condition”, *Nanotechnology* **21**:26 (2010), art. id. 265502.
- [Zhang and Hu 2014] J. Zhang and Y.-T. Hu, “Analysis on the anti-plane deformations of a piezoelectric semiconductor plate with a hole”, pp. 106–109 in *Proc. 2014 Symposium on Piezoelectricity, Acoustic Waves, and Device Applications* (Beijing), edited by X. Wang et al., IEEE, Piscataway, NJ, 2014.
- [Zhang et al. 2016a] C. L. Zhang, X. Y. Wang, W. Q. Chen, and J. S. Yang, “Carrier distribution and electromechanical fields in a free piezoelectric semiconductor rod”, *J. Zhejiang Univ. Sci. A* **17**:1 (2016), 37–44.
- [Zhang et al. 2016b] C. L. Zhang, X. Y. Wang, W. Q. Chen, and J. S. Yang, “Propagation of extensional waves in a piezoelectric semiconductor rod”, *AIP Adv.* **6**:4 (2016), art. id. 045301.
- [Zhang et al. 2017a] C. Zhang, X. Wang, W. Chen, and J. Yang, “An analysis of the extension of a ZnO piezoelectric semiconductor nanofiber under an axial force”, *Smart Mater. Struct.* **26**:2 (2017), art. id. 025030.
- [Zhang et al. 2017b] C. L. Zhang, Y. X. Luo, R. R. Cheng, and X. Y. Wang, “Electromechanical fields in piezoelectric semiconductor nanofibers under an axial force”, *Mater. Res. Soc. Adv.* **2**:56 (2017), 3421–3426.
- [Zhang et al. ≥ 2018] C. L. Zhang, X. Y. Wang, W. Q. Chen, and J. S. Yang, “Bending of a cantilever piezoelectric semiconductor fiber under an end force”, under review.
- [Zhao et al. 2016a] M. H. Zhao, Y. Li, Y. Yan, and C. Y. Fan, “Singularity analysis of planar cracks in three-dimensional piezoelectric semiconductors via extended displacement discontinuity boundary integral equation method”, *Eng. Anal. Bound. Elem.* **67** (2016), 115–125.
- [Zhao et al. 2016b] M. H. Zhao, Y. B. Pan, C. Y. Fan, and G. T. Xu, “Extended displacement discontinuity method for analysis of cracks in 2D piezoelectric semiconductors”, *Int. J. Solids Struct.* **94** (2016), 50–59.

Received 2 Sep 2017. Revised 24 Sep 2017. Accepted 29 Sep 2017.

GUANGYING YANG: 1501081004@nbu.edu.cn
 Mechanical Engineering and Mechanics, Ningbo University, Ningbo, China

JIANKE DU: dujianke@nbu.edu.cn
 Mechanical Engineering and Mechanics, Ningbo University, Ningbo, China

JI WANG: wangji@nbu.edu.cn
 Mechanical Engineering and Mechanics, Ningbo University, Ningbo, China

JIASHI YANG: jyang1@unl.edu
 Mechanical and Materials Engineering, University of Nebraska – Lincoln, NE, United States

RESEARCH ON ACCUMULATIVE PLASTIC DAMAGE FOR LOW-CYCLE FATIGUE ANALYSIS OF HULL NOTCHED PLATE

JUNLIN DENG, PING YANG, YUAN CHEN AND JIN HAN

Ship plates suffer from both low-cycle fatigue damage and accumulative plastic damage under asymmetric low-cycle fatigue loading. The accumulative plastic damage under asymmetric low-cycle fatigue loading was investigated using the Chaboche model for numerical analysis, during which the accumulative plastic deformation localized around the region of the notch root was taken as the control parameter. The corresponding experiments were conducted and compared with the results of theoretical analysis in this paper. Based on a series of calculations by finite element simulation, the influence of stress amplitude, mean stress, stress ratio, and initial notch radius on the accumulative plastic strain were investigated and discussed. Based on the fatigue fracture toughness at the root of the ship plate, this paper presents a new assessment approach for additional damage caused by plastic deformation under asymmetrical low cycles.

A list of symbols can be found on page 137.

1. Introduction

Ship hull structures suffer from cyclic loading in navigation conditions, and the phenomenon of accumulative plastic deformation can happen in the ship's structural material under large asymmetric cyclic loads with nonzero mean stress, and as a result, damage to the hull structure will occur [Fukumoto and Kusama 1985; Fujita et al. 1984; Yao and Nikolov 1990]. This kind of damage is called accumulative plastic damage. In fact, a ship's plate under asymmetric low-cycle fatigue loading will produce gradual cumulative damage comprising inelastic deformation and low-cycle fatigue damage.

Accumulative plastic damage is caused by a load that exceeds the tensile ultimate stress or critical compression stress of the plate panels. Fukumoto and Kusama [1985] pointed out that maritime ships should withstand not only static loads but also alternating loads due to the waves encountered during a voyage, and if the alternating loads are large enough, the form of the structural damage to a ship comprises the accumulative plastic damage. The increasing plastic deformation would appear after each load cycle. While the plastic deformation is small in each cycle, it will increase gradually until it reaches the limits of the ductility of the hull steel, which leads to a loss of material ductility and then destruction. According to analysis of the accident on the Japanese ship, the "Onomichi Maru", Fujita et al. [1984] reviewed the problem of accumulative plastic damage around the hull structure, and thought the ship's accident was a typical case of accumulative plastic damage. Yao and Nikolov [1990] also pointed out that the hull structure under large enough alternating loads would undergo buckling or yield failure, resulting in a decrease in the load-bearing capacity of the ship's hull, and consequently leading to overall

Ping Yang is the corresponding author.

Keywords: low cycle fatigue load, notched plate, Chaboche kinematic hardening model, accumulative plastic damage.

fracture failure of the hull structure. In order to prevent a fracture failure caused by accumulative plastic deformation, it is necessary to investigate the accumulative plastic damage of the hull structure caused by asymmetrical loading cycles. Moreover, the existing researches have shown that accumulative plastic deformation has a significant influence on the low-cycle fatigue strength of structural materials under a stress cycle [Lim et al. 2009; Kang et al. 2008], and a coupling interaction in the structural materials between accumulative plastic damage and low-cycle fatigue damage exists. Therefore, it is necessary to study the accumulative plastic damage subjected to low-cycle fatigue loading for ship hull structures in depth.

Studies [Taleb 2013; Hassan and Kyriakides 1994] have shown that the accumulative plastic behavior of structural materials clearly depends on the characteristics of cyclic deformation. Under asymmetric stress loading cycles, the stress-strain curve is not closed, and the plastic strain gradually accumulates. A cumulative plastic damage of the structural materials will occur, which is also called the ratcheting effect. This is one of the most important phenomena of plastic deformation, occurring when the structural materials are subjected to asymmetric stress loading cycles [Hassan and Kyriakides 1994]. It was found that different structural materials exhibit different accumulative plastic behaviors according to test reports on 1070 steel [Jiang and Huseyin 1994] and 1045 steel [Jixi and Jiang 2005].

In addition to experimental studies on accumulative plastic damage, the cyclic constitutive model, which has been widely used to describe the ratcheting effect, is mainly based on the A–F nonlinear kinematic hardening model [Armstrong and Frederick 1968]. It was developed and improved by Chaboche [1989b], Ohno [1990], and Jiang and Sehitoglu [1996]. Chen et al. [2009] analyzed the mean stress, stress amplitude, and load history on the impact of the HNS ratcheting effect and found that the material had a very strong memory in multistep loading. Kang et al. [2006] studied SS304 stainless steel and found the generation of accumulated plastic strain makes the low-cycle fatigue life of the structural materials decline, and mean stress, stress amplitude, and stress ratio play an important role in the low-cycle fatigue life. Tyfour and Kapoor [1995] indicated that steel under a nonsymmetric stress cycle would have an accumulative incremental deformation, which can cause the loss of steel ductility and material stiffness, and finally result in crack initiation when the accumulated plastic strain reaches a critical value.

However, the existing studies on accumulative plastic failure are almost all confined to material properties, or in a way to conduct research on the fatigue crack initiation of notched specimens. For example, Li et al. [2015] proposed an approach for predicting fatigue crack initiation of a notched specimen with polycrystalline materials through CPFEE simulations. In this approach, a CPFEE simulation was performed to identify the weakest site and to determine the energy efficiency factor to easily capture the strain inhomogeneity of individual grains. Payne et al. [2010a; 2010b] observed on a notched specimen with an aluminum alloy (AA) 7075 that the initiation of a fatigue crack is significantly influenced by the local deformation, and they emphasized the important role of accumulated plastic deformation near the notch root in fatigue crack initiation. Ranganathan et al. [2011] proposed a short crack approach to determine the fatigue crack initiation life at the notch tip and then they gave acceptable predictions compared with the experiments. There is little research focusing on accumulative plastic damage of notched plate specimens under asymmetrical stress loading cycles.

Therefore, based on experiments on a ship's notched plate, a theoretical analysis of accumulative plastic damage was conducted, and the effect of mean stress and stress amplitude were analyzed by numerical simulation.

2. Theoretical analysis

2.1. Plastic strain field at the notch root of a notched plate. Under low-cycle fatigue loading, since the plastic deformation is the main part, the elastic strain can be omitted in the actual calculation. Then the stress-strain relationship of the notched plate in an $(n + 1)$ cycle's load cycle can be expressed as [Deng et al. 2016]:

$$\begin{aligned}\Delta\sigma_{eq(n+1)} &= \sqrt{(\Delta\sigma_{x(n+1)}^p)^2 - \Delta\sigma_{x(n+1)}^p \Delta\sigma_{y(n+1)}^p + (\Delta\sigma_{y(n+1)}^p)^2}, \\ \Delta\varepsilon_{x(n+1)}^p &= \frac{f(\Delta\sigma_{eq(n+1)})}{\Delta\sigma_{eq(n+1)}} \left(\Delta\sigma_{x(n+1)}^p - \frac{1}{2} \Delta\sigma_{y(n+1)}^p \right), \\ \Delta\varepsilon_{y(n+1)}^p &= \frac{f(\Delta\sigma_{eq(n+1)})}{\Delta\sigma_{eq(n+1)}} \left(\Delta\sigma_{y(n+1)}^p - \frac{1}{2} \Delta\sigma_{x(n+1)}^p \right), \\ f(\Delta\sigma_{eq(n+1)}) &= \left(\frac{\Delta\sigma_{eq(n+1)}}{K'} \right)^{1/n'},\end{aligned}\quad (1)$$

where $\Delta\sigma_{x(n+1)}^p$, $\Delta\sigma_{y(n+1)}^p$, $\Delta\varepsilon_{x(n+1)}^p$, $\Delta\varepsilon_{y(n+1)}^p$ are the local plastic stress and strain at the notch area, n' is the material cyclic hardening coefficient, and K' is the cyclic strength coefficient.

The ship's hull plate is generally under a plane stress state, and the elasto-plastic stress-strain constitutive relation of the notch root is obtained by the stress-strain curve combined with elasticity and plasticity theory. Under low-cycle fatigue loading, combined with the Hencky degeneration equation, the equation can be expressed using an amplitude form as follows [Deng et al. 2017]:

$$\Delta\varepsilon_{ij} = \frac{1+\nu}{E} \Delta\sigma_{ij} - \frac{\nu}{E} \Delta\sigma_{kk} \delta_{ij} + \frac{3}{2} \frac{f(\Delta\sigma_{eq}/2)}{\Delta\sigma_{eq}} S_{ij}, \quad (2)$$

where

$$\begin{aligned}\Delta\sigma_{ij} &= (\sigma_{ij})_{\max} - (\sigma_{ij})_{\min}, & \Delta\varepsilon_{ij} &= (\varepsilon_{ij})_{\max} - (\varepsilon_{ij})_{\min}, \\ \Delta S_{ij} &= \Delta\sigma_{ij} - \frac{1}{3} \Delta\sigma_{kk} \delta_{ij}, & \Delta\sigma_{eq} &= \sqrt{\frac{3}{2} \Delta S_{ij} \Delta S_{ij}},\end{aligned}$$

where ν is Poisson's ratio, E is the elastic modulus, ε_{ij} is the strain component, σ_{ij} is the stress component, ε_{ij}^p is the equivalent plastic strain, σ_{eq} is the equivalent stress, and S_{ij} is the stress deviator.

2.2. Accumulated incremental plastic strain at the notch root of a notched plate. The basic form of the Chaboche model can be determined according to the literature [Chaboche 1989a; Tong et al. 2013]. Because the strain fatigue of the notched plate under cyclic loading is the main subject under discussion in the paper, the elastic strain can be ignored to focus on the plastic strain problem.

Adopting the Chaboche model [1989a] for the material, the yield function is

$$f_1(\sigma, \chi, R_0, k) = J(\sigma - \chi) - R_0 - k \leq 0, \quad (3)$$

where χ is the nonlinear kinematic hardening variable, R_0 is the isotropic hardening variable, k is the yield surface of the initial radius, J is the deviatoric stress space in the von Mises distance, and

$$J(\sigma - \chi) = \sqrt{\frac{3}{2} (\sigma' - \chi') : (\sigma' - \chi')}, \quad (4)$$

where σ' and χ' are, respectively, the deviators of σ and χ .

The plastic flow conditions are

$$f_1 = 0 \quad \text{and} \quad \frac{\partial f_1}{\partial \sigma} : \dot{\sigma} > 0. \quad (5)$$

The nonlinear kinematic hardening χ and isotropic hardening variable R_0 can be expressed as:

$$\begin{aligned} \dot{\chi} &= \dot{\chi}_1 + \dot{\chi}_2, & \dot{\chi}_1 &= C_1(a_1 \dot{\varepsilon}_p - \chi_1 \dot{\varepsilon}_p), \\ \dot{R}_0 &= b(Q - R_0) \dot{\varepsilon}_p, & \dot{\chi}_2 &= C_2(a_2 \dot{\varepsilon}_p - \chi_2 \dot{\varepsilon}_p), \end{aligned} \quad (6)$$

where C_1, a_1, C_2, a_2, Q, b are material constants, and they are determined by experiment; $\dot{\varepsilon}_p$ is the accumulative plastic strain rate.

According to the study discussing the Chaboche model [Tong et al. 2013], from the differential relationship between the plastic strain and the accumulated plastic strain, the accumulative plastic strain at the notch root of the notch plate in the $(n + 1)$ cycle can be

$$d\varepsilon_{p,n+1} = \left\langle \frac{f_1}{Z} \right\rangle^n = \sqrt{\frac{2}{3}} d\varepsilon_{n+1}^p : d\varepsilon_{n+1}^p. \quad (7)$$

Here, $d\varepsilon_{n+1}^p$ is the equivalent plastic strain increment at the notch root of the notch plate after the first $n + 1$ load cycle, which can be obtained through the Newton–Raphson iteration by the stress-strain relationship (1) of the notch plate in the $n + 1$ load cycle.

Substituting (1) and (7) into the Newton–Raphson iteration as in [Budiansky and Hutchinson 1978], the plastic strain increment at the notch root of the notched plate $d\varepsilon_{n+1}^p$ after the $n + 1$ cycle can be obtained. In addition, the corresponding incremental plastic strain increment can be obtained too; update the corresponding parameters in turn, and the corresponding incremental plastic strain increment can be obtained for the i -th cycle.

The notched plates are only subjected to uniaxial loading cycles in this paper; therefore, we can obtain the accumulated plastic strain increments after the $N + 1$ cycle under uniaxial cyclic loading as

$$\Delta\varepsilon_{p,n+1} = \sum_{i=1}^{n+1} d\varepsilon_{p,n+1} = \sum_{i=1}^{n+1} \left\langle \frac{f_1}{Z} \right\rangle^n = \sum_{i=1}^{n+1} \sqrt{\frac{2}{3}} d\varepsilon_i^p : d\varepsilon_i^p. \quad (8)$$

Equation (8) is the expression for the value of the accumulated incremental plastic strain at the notch root of the notch plate after an $n + 1$ cycle.

2.3. The stiffness matrix variation of the notch root region. Assuming that all the variables in step n and the strain increment in step $n + 1$ are known, the stress increment in step $n + 1$ can be obtained by the Newton–Raphson iteration. At the beginning, assume that the incremental plastic strain can be ignored, so the stress in $n + 1$ step can be written by the generalized Hooke’s law as

$$\sigma_{n+1}^{\text{tr}} = D^e : (\varepsilon_{n+1} - \varepsilon_n^p), \quad (9)$$

where σ is a second-order Cauchy stress tensor and D^e is a fourth-order isotropic elastic tensor.

With the Bauschinger effect (the move of the yield surface center) and the evolution equation of the nonlinear kinematic hardening rate of the structural materials [Jerome et al. 1983], the back stress in the

$n + 1$ step is

$$\alpha_{n+1} = \sum_{k=1}^M \theta_{n+1}^k (\alpha_n^{(k)} + C_k a_k \Delta \varepsilon_{n+1}^p), \quad (10)$$

where $\theta_{n+1}^k = 1/(1 + C_k \Delta p_{n+1})$, $0 \leq \theta_{n+1}^k \leq 1$; a_k and C_k are material constants which describe the material hardening properties, and M represents the number of back stress force components.

After finding out δ_{n+1} , ε_{n+1} , ε_{n+1}^p and other variables at the $n + 1$ cycle, the differential equation of the constitutive equation can be pushed to the stiffness matrix of the current moment. According to (9), differential equations can be obtained as follows:

$$d\Delta\delta_{n+1} = D^e : (d\Delta\varepsilon_{n+1} - d\Delta\varepsilon_{n+1}^p). \quad (11)$$

By differential calculation, (12) can be obtained as follows:

$$d\Delta\varepsilon_{n+1}^p = L_{n+1}^{-1} : J_{n+1}^0 : 2GI_d : d\Delta\varepsilon_{n+1}, \quad (12)$$

where

$$\begin{aligned} L_{n+1} &= n_{n+1} \otimes n_{n+1} - J_{n+1}^0 : H_{n+1}; & J_{n+1}^0 &= \sqrt{\frac{3}{2}} \Delta p_{n+1} J_{n+1}, \\ H_{n+1} &= \left(2G + \sum_{k=1}^m \theta_{n+1}^k C_k \alpha_k \right) I - n_{n+1} \otimes \left(\frac{2}{3} \sum_{k=1}^m C_k \theta_{n+1}^{(k)} \alpha_{n+1}^{(k)} \right), & I_d &= I - \frac{1}{3} \delta \otimes \delta. \end{aligned}$$

Here, I_d is the fourth-order tensor, and δ is the second-order tensor.

Furthermore, $J_{n+1} = (I - n_{n+1} \otimes n_{n+1}) / \|S_{n+1} - \alpha_{n+1}\|$, I is the fourth-order tensor, $I_{ijkl} = \frac{1}{2}(\delta_{ik}\delta_{jl} + \delta_{jk}\delta_{il})$; and $n_{n+1} = (S_{n+1} - \alpha_{n+1}) / \|S_{n+1} - \alpha_{n+1}\|$. S_{n+1} , α_{n+1} are the partial stress tensor and back stress tensor, respectively, and p_{n+1} is the equivalent accumulative plastic strain at the notch root in the $n + 1$ step.

Finally, substituting (12) into (11), the stiffness matrix of the models is as follows:

$$\frac{d\Delta\delta_{n+1}}{d\Delta\varepsilon_{n+1}} = D^e - 4G^2(L_{n+1}^{-1} : J_{n+1}^0) : I_d. \quad (13)$$

Substituting (13) into (9), the variation of the plastic deformation at the notch root region can be obtained in the $n + 1$ cycle because the accumulative plastic deformation stiffness is reduced. Using the Newton–Raphson iteration method, the variation of plastic deformation at the notch root can be obtained in the corresponding cycles.

2.4. The accumulated plastic damage life. The accumulative plastic strain can produce additional damage in the stress control loop. When the average stress is that of nonzero asymmetrical stress cycles, in order to consider the effect of accumulative plastic strain, the accumulative plastic strain failure cycles can be calculated using the model proposed by [Xia and Kujawki 1996]. Then

$$\sigma_{\max} \dot{\varepsilon}_r^p = \kappa_r N_r^\beta. \quad (14)$$

Then

$$N_r = \left(\frac{\sigma_{\max} \dot{\varepsilon}_r^p}{\kappa_r} \right)^{1/\beta}, \quad (15)$$

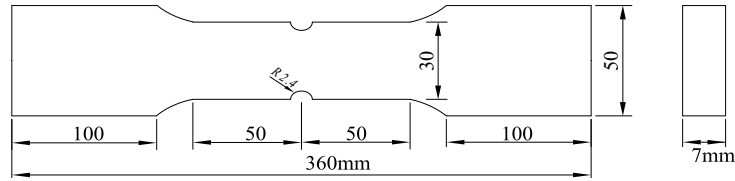


Figure 1. A notched plate specimen (the notch diameter is 4.8 mm, thickness is 7 mm).



Figure 2. Testing rigs and the locations of the strain gage and extensometer for strain measurements.

where ε_r^p is the accumulative plastic strain, $\dot{\varepsilon}_r = d\varepsilon_r^p/dN$, which is obtained by (8), is the accumulative plastic strain rate when the accumulative plastic strain steadily develops, and κ_r , β are the corresponding material constants, which are obtained by fitting the experimental measurements.

Equation (15) is the expression for the value of the accumulated plastic damage life of the hull notched plate.

3. Experimental investigations

3.1. Experimental setup. In order to investigate the local cumulative plastic damage characteristics of the hull notched plate under asymmetric stress loading cycles, a series of experiments were carried out and the properties of the materials studied. The accumulative plastic damage experiments were conducted on a 7 mm thick hull, and notched plate specimens with other dimensions as shown in Figure 1. The tests were performed in air and at room temperature using a computer-controlled MTS322 servo-hydraulic testing machine. The MTS fatigue testing machine and data processing program were used in the tests. The specimen and the test setup are shown in Figure 2.

The Q235 steel is low carbon steel, which is widely used in hull structures. It was employed in the tests where the uniaxial tensile stress-strain curve of the steel was obtained by tensile tests as shown in Figure 3. The basic material and mechanical properties of the Q235 steel were obtained by tensile tests as shown in Table 1. The chemical composition (in % wt) of this material is C-0.17; Mn-0.49; Si-0.23; P-0.026; and S-0.025. Sinusoidal loading with stress control was adopted in the tests. A 0.25 Hz frequency was chosen based on other low-cycle fatigue test results available in the literature.

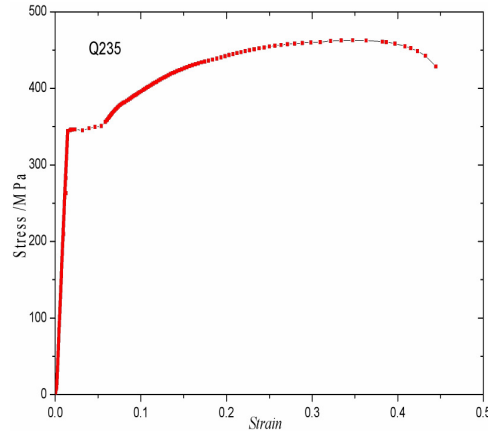


Figure 3. The uniaxial tensile stress-strain curve.

The notched plate specimens were subjected to stress- or strain-controlled fully reversed low-cycle fatigue loading. In the strain-controlled test, the strain range measured by an extensometer attached at the back face was controlled so that it kept the objective value. The extensometer had a 25 mm gage length, and ± 1 mm range, in order to reduce the influence of the notch geometry on the strain measurement, and a 0.01% extensometer strain control accuracy whose operating temperature range was -80°C to 200°C . The accumulative plastic strain at the notched root region was simultaneously measured by a strain gage attached 3 mm away from the notch root as shown in Figure 2. The strain range measured by the strain gage was referred to as the accumulative plastic strain at the notch root and used for (15) to calculate the accumulative plastic damage life of the notched plate specimen.

The tests were conducted under constant amplitude loading with different mean stresses and stress amplitudes to study the effect on the accumulative plastic strain deformation of the hull notched plate. The real-time information such as time, load, and extensometer strain were recorded. After the accumulative plastic failure, fractographs and microscopic changes were examined using a LEO Electron Microscopy 1530 VP field emission scanning electron microscope (FESEM) to analyze the failure mechanisms. The loading conditions and experimental results of the Q235 steel are summarized in Table 2. An example of the appearance of accumulative plastic damage is shown in Figure 4 and the damage morphologies are shown in Figure 5.

3.2. Observation of the damage morphology. Figure 4 shows an example of the appearance of accumulative plastic damage at the notched root region of the specimen from Q235 steel inspected during an accumulative plastic damage test with a stress amplitude of $\sigma_a = 260$ MPa and mean stress of $\sigma_m = 60$ MPa. Observation of the notched root region in the test did detect the corresponding plastic deformation phenomenon at the notched root region under low-cycle fatigue loading.

Figure 5 shows examples of the accumulative plastic damage morphology of the notched plate of Q235 steel under the stress loading cycle with the same mean stress of $\sigma_m = 60$ MPa, where the stress amplitude (σ_a) was 240 MPa in No. 1; 260 MPa in No. 2, and 280 MPa in No. 3. An observation of the notch root region in the test detected the corresponding plastic deformation phenomenon under the fatigue loading stress cycle with the same mean stress of $\sigma_m = 60$ MPa. There was an obvious plastic

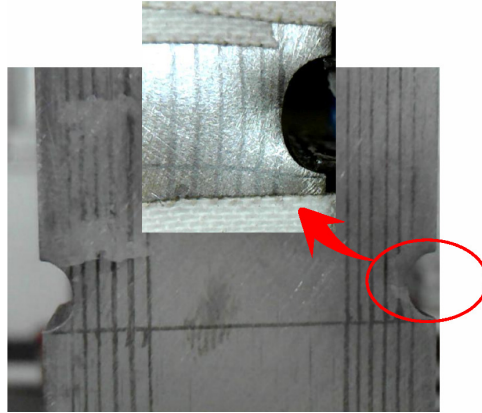


Figure 4. Accumulative plastic damage morphology of the notched plate specimen.

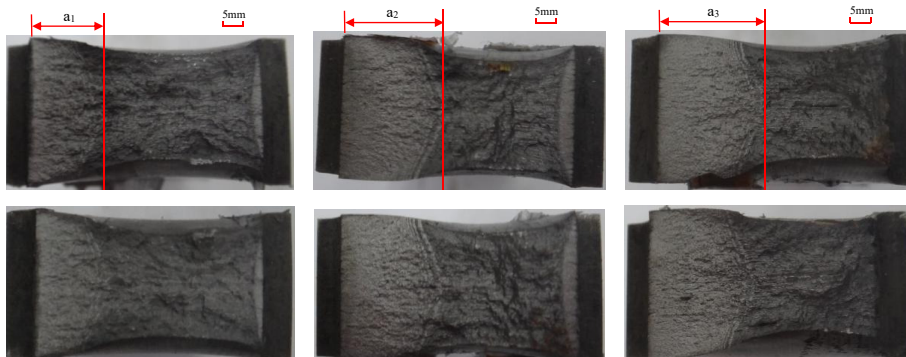


Figure 5. Accumulative plastic damage morphology of the notched plate specimens: No. 1 (left column); No. 2 (middle column); No. 3 (right column).

deformation at the root region of the specimen after the low-cycle fatigue loading. The tests showed that the irregularity on the fracture surface was more significant in the accumulative plastic damage test with the constant mean stress but gradual increase in stress amplitude. The fracture morphologies show obvious accumulative plastic damage and a transgranular fracture. It can be found that the accumulation of plastic deformation at the notch root is obvious in the case of higher stress amplitude. Greater plastic damage was produced in the asymmetric stress loading-cycle process, which led to a decrease in the ability to resist deformation of the material. With the increase in stress amplitude, a larger accumulative plastic deformation will lead to earlier fracture failure.

Therefore, it is necessary to consider the effect of accumulative plastic damage in low-cycle fatigue problems under asymmetric stress loading cycles.

3.3. Experimental result and discussion. The stress-strain curve of Q235 steel based on experiments under uniaxial tensile loads is shown in Figure 3. The Q235 steel sample mechanical performance parameters were obtained according to the MTS fatigue testing machine data collection system and

material	E (GPa)	K (MPa)	σ_y (MPa)	σ_b (MPa)
Q235	206	1193	310	475

Table 1. The mechanical properties of Q235.

stress amplitude (MPa)	specimen number	mean stress (MPa)	accumulated plastic damage life (N)
240	No. 01	0	2667
	No. 02	20	2376
	No. 03	40	2212
	No. 04	60	2024
260	No. 05	0	2435
	No. 06	20	2168
	No. 07	40	1800
	No. 08	60	1971
280	No. 09	0	2530
	No. 10	20	2329
	No. 11	40	1875
	No. 12	60	1147

Table 2. Accumulated plastic damage life at the notched root for Q235 steel.

numerical fitting with Origin software based on a static load in the tensile test results. The parameters are shown in Table 1.

The specimens were tested for stress amplitude ($\sigma_a = 240$ MPa, 260 MPa, 280 MPa) and mean stress ($\sigma_m = 0$ MPa, 20 MPa, 40 MPa, 60 MPa) under asymmetrical stress loading cycles. According to the strain gage, which is arranged at the notched root of the specimen, the accumulative plastic damage life of the notched plate under asymmetrical cyclic loading is shown in Table 2.

Since it is known that if the mean stress is larger, the notched root mainly appears with accumulative plastic damage under asymmetrical cyclic loading, the mean stress (which is relatively large in Table 2) was chosen to be combined with (14) for fitting the Q235 steel material parameters. The corresponding results are listed in Table 3.

When the mean stress is large enough, the accumulative plastic damage may primarily be produced at the notch root under the asymmetrical stress cyclic loading [Kang et al. 2002]; therefore, the specimens with relatively higher mean stresses, as shown in Table 2, were chosen for numerical fitting. Combined with the selected experimental results in Table 3 and the material parameters, the numerical fitting was performed for (8), and the parameter values of $K_r = 200.83$ and $\beta = -1.37$ were obtained.

4. Numerical analysis and discussion

In the present study, the commercial finite element software ANSYS was employed, and in the material model, the von Mises yield function, associated flow rule, and Chaboche kinematic hardening model

stress amplitude	mean stress	specimen number	accumulative plastic damage life (N)	accumulative plastic rates ($\dot{\epsilon}_r$)
240	60	No. 04	2024	0.0011
260	60	No. 08	1971	0.0019
280	60	No. 12	1147	0.0036
280	40	No. 11	1875	0.0029
280	20	No. 10	2329	0.0014

Table 3. Loading conditions and experimental results for Q235 steel.

E (Gpa)	ν	Q	b	k	–
206	0.3	162	8.5	145	–
C_1	α_1	C_2	α_2	C_3	α_3
140000	8750	75000	238	1950	0

Table 4. Values for the material parameters of Q235 steel for a viscoplastic constitutive material model.

were used. The Chaboche kinematic hardening model is an advanced material model that is capable of capturing basic cyclic plastic responses of materials such as the Bauschinger effect, plastic shakedown, ratcheting resulting from asymmetric stress cycles, and mean stress relaxation resulting from asymmetric strain cycles. The constitutive equations contain 11 material parameters, namely, E , ν , k , b , Q , C_1 , α_1 , C_2 , α_2 , C_3 , α_3 . The kinematic hardening behavior is described by C_1 , α_1 , C_2 , α_2 , C_3 , and α_3 , where α_1 , α_2 , and α_3 are the saturated values of the kinematic hardening variables, and C_1 , C_2 , and C_3 indicate the speed with which the saturation is reached. The isotropic hardening is depicted by Q and b , the initial size of the yield surface is represented as k , E is the Young's modulus, and ν is Poisson's ratio. The parameter values, optimized from the uniaxial test data of Q235 at room temperature, are listed in Table 4. The above material model is adopted in the finite element software ANSYS. Comparisons of the experimental result and the model simulations are given in Figure 6 for the stress-controlled cyclic test.

A notched plate specimen was considered and the finite element meshes for the specimen are shown in Figure 7. Moreover, the APDL language was adopted to establish the finite element model in order to improve the data processing efficiency. Because of the thin thickness and loading conditions, finite element modeling of the notched plate specimen was treated as a plane stress case. Due to the symmetry, only a quarter of the specimen was considered. The plane 182 element type in ANSYS was used in the FE mesh model. To simulate the high stress and strain gradients, refined mesh elements were used for the region near the notch root. The element size in the notch root region was chosen as 0.05 mm to obtain a relatively high accurate stress-strain response.

4.1. Stress-strain curve at the notched root of specimen. Finite element computations were carried out on the hull notched plate specimen to study the detailed accumulative plastic deformation response. For consistency within the experiment, the same loading condition was adopted in the numerical model. With the sinusoidal cyclic loads applied on the quarter of the finite element model in Figure 7, combined with the fitting material with the model of coefficients in Table 3 (based on the Chaboche nonlinear

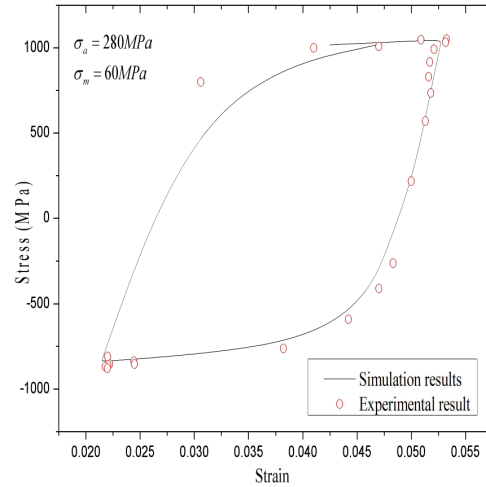


Figure 6. Stress and strain hysteresis loop for the notched plate.

kinematic hardening model), finite element analysis was carried out under low-cycle fatigue loading, and we obtained a stress-strain hysteresis loop at the notched root under asymmetrical stress cycling loads, which is shown in Figure 8.

Finite element computations were carried out for over 40 cycles at the selected asymmetrical stress loading cycles. The normal stress-strain response for mean stress ($\sigma_m = 20 \text{ MPa}$, 40 MPa , 60 MPa) is shown in Figure 8 for a Gauss integration point just ahead of the notched root. The Gauss integration point is located most closely to the notched root with a polar coordinate of ($r = 3.8 \mu\text{m}$, $\theta = 45^\circ$). The stress-strain response exhibits a progressive shift in the direction of increasing tensile strain, a phenomenon known as ratcheting, which means the plastic strain clearly accumulates at the notched root under asymmetrical stress loading cycles, but also no obvious mean stress relaxation is observed from Figure 8. After several loading cycles, the accumulative plastic strain rate tends to be insignificant, which means that the stabilized stress-strain responses are reached. Figure 8 shows that with a plate undergoing asymmetrical stress loading cycles, the notched root appeared with the accumulation of plastic strain, the accumulating growth of initial plastic deformation increases faster, and then it gradually reduces and tends to be stable. What can be seen from the figure is that the stress-strain hysteresis loop of Q235 steel does not change significantly in shape, which is obviously different from [Kang et al. 2002], which reported that the stress-strain hysteresis loop of cyclic softening materials gradually increases.

The peak cyclic loading case with the stress amplitude of 280 MPa and mean stress of 60 MPa were, respectively, applied to the finite element model. The stress and strain contours are obtained, respectively, as shown in Figure 9. It can be seen in Figure 9 that the stress at the notch root of the notched plate specimen is obviously higher than the yield stress. The plastic deformation is relatively large.

Combined with Figure 8, it can be observed that the plastic deformation clearly accumulates with the increase in the cyclic numbers under asymmetric loading cycles. In the initial cycles, the accumulated plastic strain increments grow rapidly with the increasing number of cycles; the accumulated plastic strain increment rate is gradually decreased, and then becomes stable. Therefore, the additional damage caused

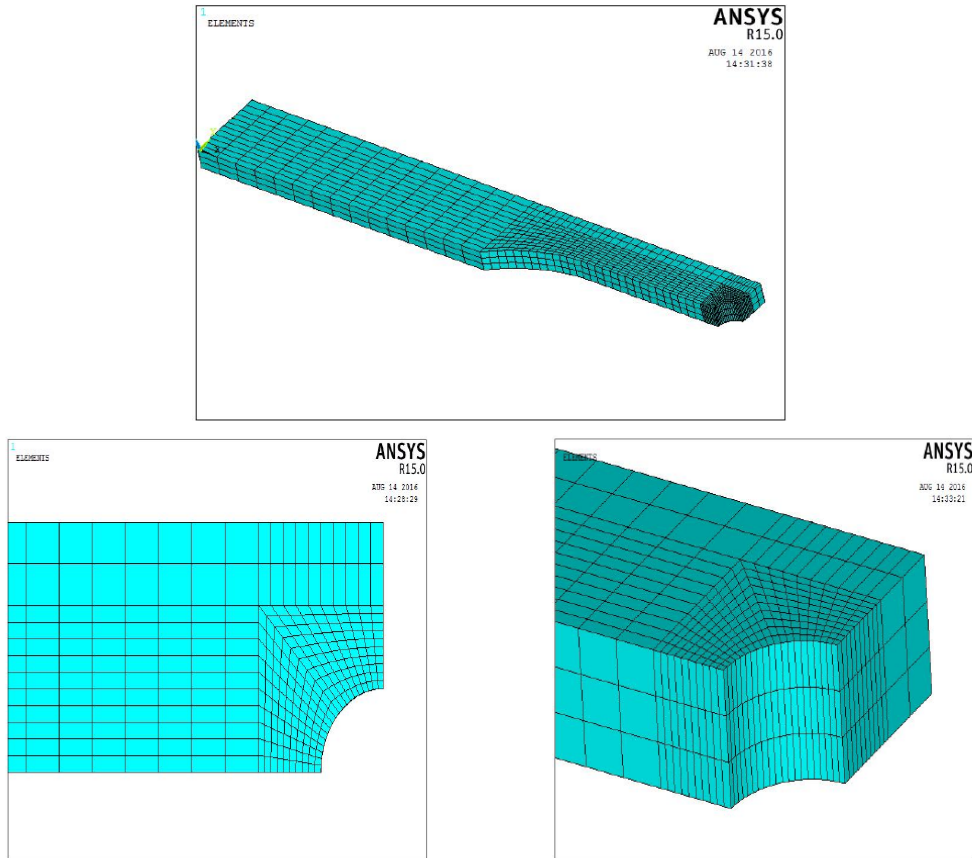


Figure 7. A quarter of the finite element model for the notched plate specimen and the refined mesh for the notch root.

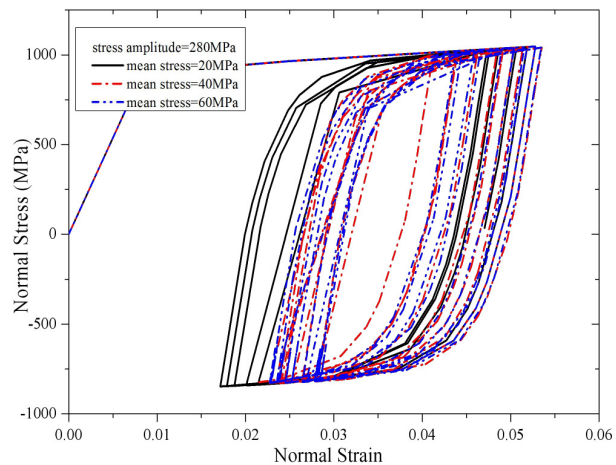


Figure 8. The stress-strain curve at the root of the notched plate.

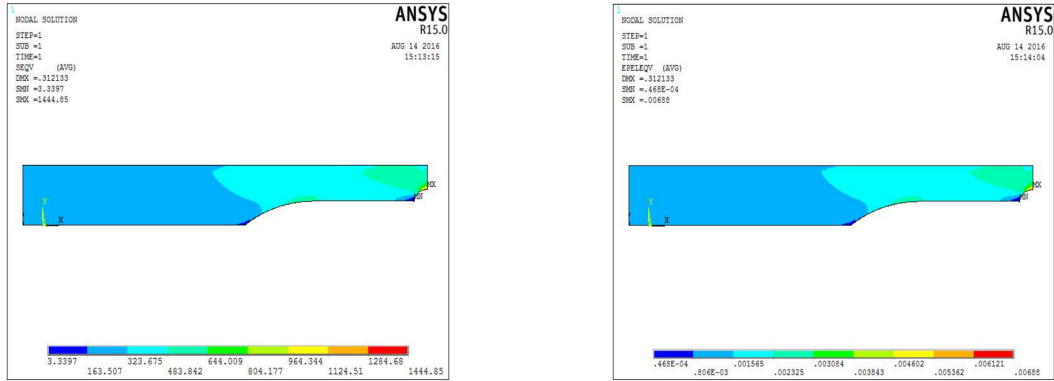


Figure 9. The stress and strain contours under the 280 MPa stress amplitude and 60 MPa mean stress of the peak cyclic loading case: Stress contour (left); Strain contour (right).

by plastic deformation should be considered when evaluating fracture toughness under asymmetric low-cycle fatigue cyclic loading.

In the present work, the accumulative plastic strain is examined and the results are plotted against the number of cycles as shown in Figures 10 and 11, left. Obviously the accumulative plastic strain increases with the increase in the stress ratio for a given stress amplitude. The results determined that the stress-strain response near the notched root remains fairly constant during the cyclic loading, and the accumulative plastic strain increases with the increase in mean stress. The continuous increase in accumulative plastic strain may eventually lead to a material separation near the notched root, and hence crack initiation and propagation.

4.2. The effect of mean stress and stress amplitude. As shown in Figure 10, left, the results from the

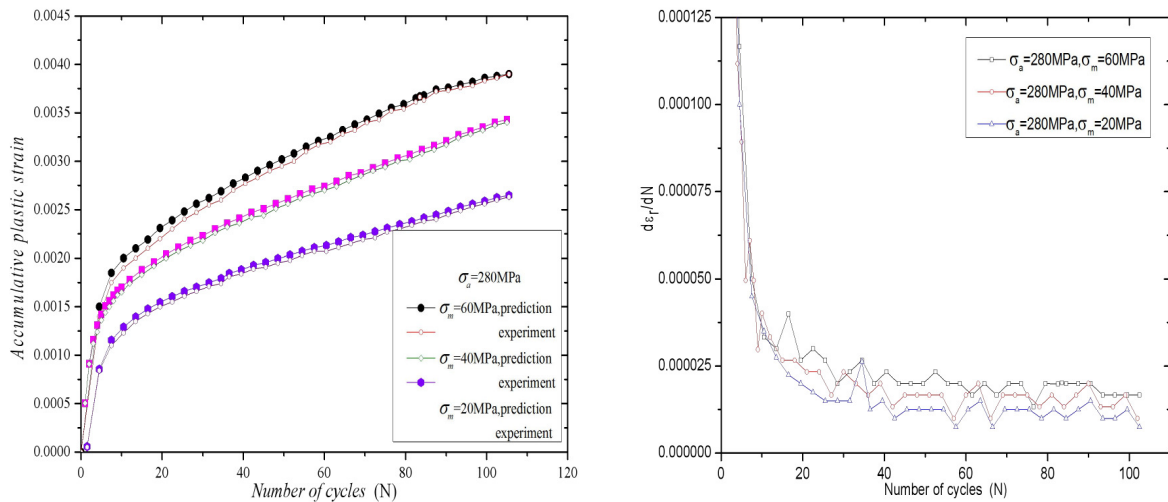


Figure 10. Accumulative plastic strains (left) and strain rates (right) versus cyclic numbers for different mean stresses.

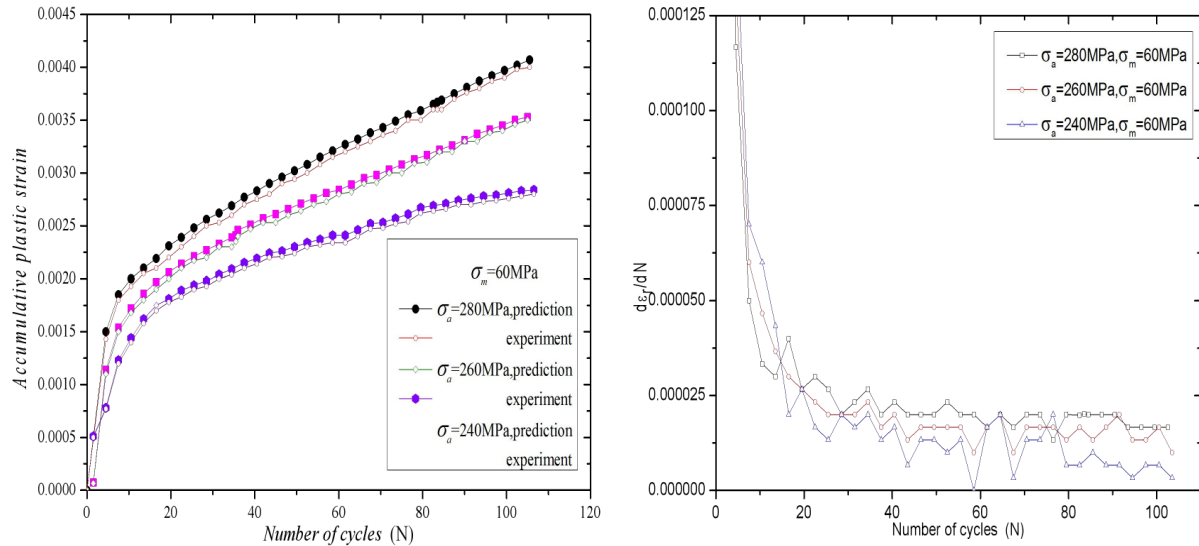


Figure 11. Accumulative plastic strains (left) and strain rates (right) versus cyclic numbers for different stress amplitudes.

predictive model obviously agree well with the experiments. Due to the existence of the mean stress, the notch root of the hull notched plate has an accumulated incremental plastic deformation in the mean stress direction. The accumulated incremental plastic deformation accumulates quickly in the initial stage, and the mean stress is bigger; the accumulative plastic deformation is also relatively larger, and as the accumulated incremental plastic deformation increases, the accumulated incremental plastic deformation rate at the notch root of the hull notched plate specimen decreases gradually and tends to a nonzero constant steady state in Figure 10, right. These trend results are basically the same as in [Satyadevi et al. 2007].

As shown in Figure 11, left, the results from the predictive model obviously agree well with the experiments. Under the same mean stress and different stress amplitude cyclic loadings, the notch root of accumulated plastic strain gradually increased with the increase in stress amplitude. When the stress amplitude is larger, the accumulated incremental plastic deformation is also relatively larger, and the stress amplitude is higher, and the material quickly progresses into the accumulated incremental plastic deformation stage. The trend in this kind of change is similar to that of [Paul et al. 2010]. Due to the existence of the stress amplitude, the accumulated incremental plastic damage occurred in the axial direction of the notched specimen. The accumulated incremental plastic deformation of the notch root is quickly accumulated in the initial cycle, and the rate of plastic change tends to be a nonzero constant.

Finally, according to the test results and the calculation results of Figures 10 and 11, right, the accumulative plastic damage values at the notch root are solved by selecting the accumulative plastic deformation rate curve at a stable level under asymmetric low-cycle fatigue loading.

4.3. Accumulative plastic damage life. Considering the accumulative plastic damage effect, the accumulative plastic damage life of a notched plate should be analyzed under asymmetrical stress loading cycles; this paper predicts numerical results and experimental results; then the calculation results of Neuber's empirical approach [1961] based on the determination of local strain amplitudes in the vicinity

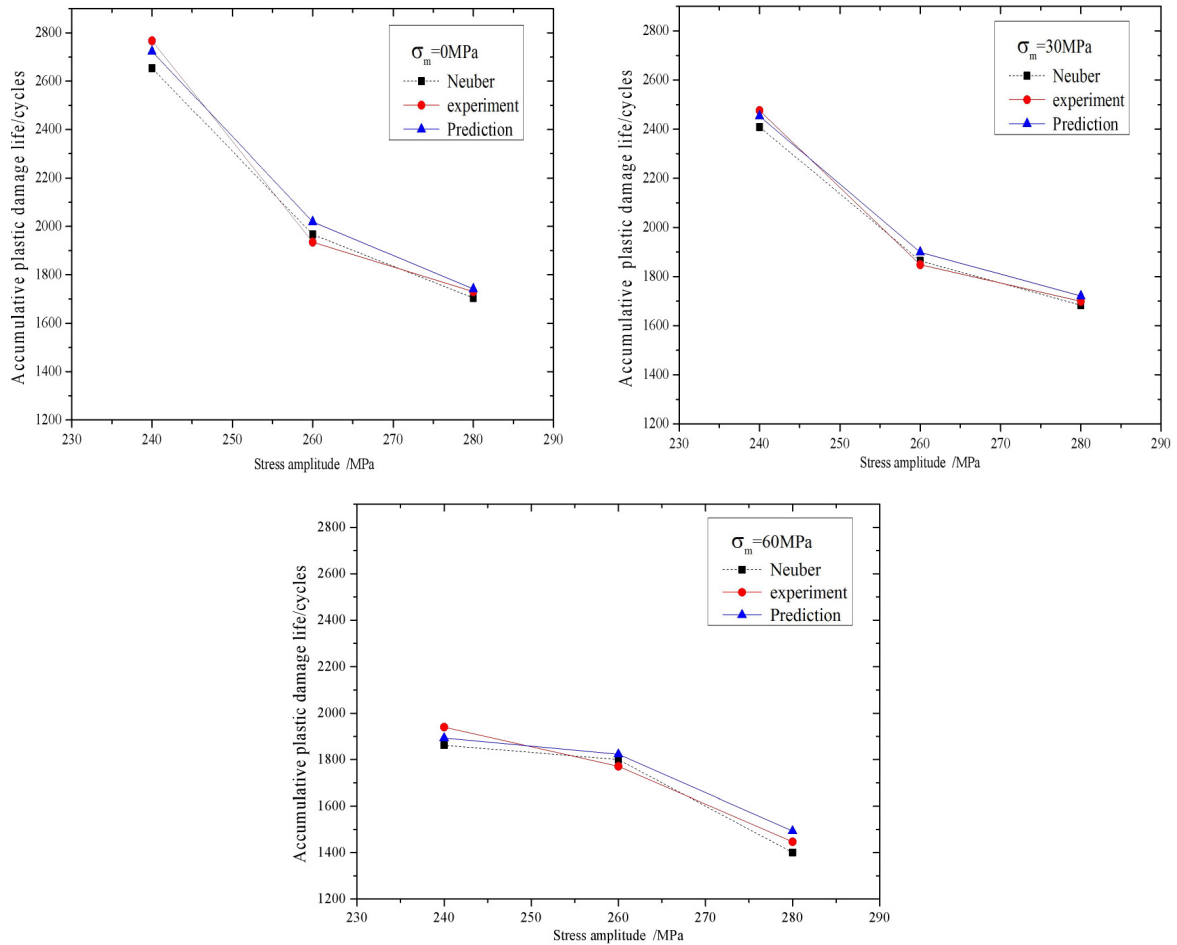


Figure 12. The comparison of prediction models and experimental measurements under different stress amplitudes.

of a notch are compared with the above results. Combined with the first part of the study, under different mean stresses and stress amplitudes, the accumulative plastic damage life of the notched plate are shown in Figure 12.

Figure 12 shows the accumulative plastic damage life of the hull notched plate under the same mean stresses at different stress amplitudes, so the damage life is related to the change in stress amplitude. Figure 11, left, shows that when the stress amplitude is high, the accumulative plastic deformation of the hull notched plate steadily develops, and it will eventually produce large accumulative plastic damage. At the same time, the larger accumulative plastic deformation of the notched root is the main form of the hull notched plate damage. Figure 11, right, shows that the accumulative plastic strain rate increases with the increase of stress amplitude; therefore, the accumulated incremental plastic damage life of the hull notched plate decreases with the increase of stress amplitude. Due to the damage caused by the accumulative plastic damage under the same mean stress, the greater the stress amplitude is, the shorter the accumulative plastic damage life is. The nonzero average stress accumulative plastic failure life of the

specimen is significantly shorter than that with average stress, which is equal to zero. With the increase of stress amplitude, the accumulative plastic damage life is significantly reduced, indicating that under the same average stresses and different stress amplitudes, the accumulative plastic deformation caused by the notch root of the ship's hull is an additional damage, which reduces the accumulative plastic damage life of the hull notched plate.

In addition, to illustrate the relationship between the accumulative plastic damage life and the accumulative plastic strain, (14) is fitted to the experimental data resulting in $K_r = 200.83$ and $\beta = -1.37$ for mean stress and stress amplitude, respectively. From the three respective results, the errors, based on a comparison with the predicted results of accumulative plastic damage life at the hull notched plates, the experimental results, and the Neuber rule, are in the acceptable range. This shows that the prediction model of the fitting parameter K_r and β is capable of forecasting the accumulative plastic damage life of a hull notched plate under low-cycle fatigue asymmetrical stress loading cycles.

5. Conclusion

The accumulative plastic deformation at the notch root of a hull notched plate under asymmetric cyclic loading is theoretically analyzed by adopting the Newton–Raphson iterative method. Through the experiment and finite element simulation, the accumulative plastic damage life of the notched plate under low-cycle fatigue loads is studied and the following conclusions can be drawn:

- (1) Combined with the Newton–Raphson iterative method to deduce the accumulative plastic deformation's theoretical solution under low-cycle high-stress asymmetrical cyclic loading, a significant accumulative plastic damage will be produced at the notch root of the hull notched plate under low-cycle fatigue loading, and the accumulative plastic damage depends on mean stress and the stress amplitude of asymmetric cyclic loading. The increase of the accumulative plastic deformation at the notch root is relatively large in the beginning stages, then gradually tends to stabilize.
- (2) The theoretical solutions of the tangent stiffness at the notch root of the notched plate are derived. The accumulative plastic deformation at the notch root significantly reduces the tangent stiffness at the notch root, and the decrease of the stiffness of the notch root is further aggravated by the accumulation of plastic deformation. With the increase of the number of cycles, the accumulative plastic deformation at the notched root gradually increases and eventually leads to the depletion of the notched plate material.
- (3) The assessment model for the accumulative plastic damage life for the hull notched plate is established under low-cycle fatigue loading, and based on the theoretical analysis and numerical simulation, the results of the relevant model parameters are fitted with the experimental results. Compared to the experimental results, the model can estimate the accumulative plastic damage life of the hull notched plate under low-cycle fatigue loads well.

Acknowledgements. The authors are indebted to the National Natural Science Foundation of China (Grant No. 51479153) and the Provincial Natural Science Foundation of Guangxi for financial support (Grant No. 2016GXNSFAA380033) and the basic ability promotion program for young and middle-aged teacher of University in Guangxi (No. 2017KY0809).

List of symbols

K'	hardening modulus (MPa)	n'	hardening exponent
ν	Poisson's ratio	E	Young's modulus (MPa)
σ	local stress (MPa)	ε	local strain
σ_{ij}	stress component	ε_{ij}	strain component
$\Delta\sigma_{x(n+1)}^p$	x -direction plastic stresses in $n + 1$ cycle		
$\Delta\sigma_{y(n+1)}^p$	y -direction plastic stresses in $n + 1$ cycle		
$\Delta\varepsilon_{x(n+1)}^p$	x -direction plastic strains in $n + 1$ cycle		
$\Delta\varepsilon_{y(n+1)}^p$	y -direction plastic strains in $n + 1$ cycle		
σ_{eq}	equivalent stress	ε_{eq}^p	equivalent plastic strain
χ	nonlinear kinematic hardening variable	R_0	isotropic hardening variable
k	yield surface of the initial radius	J	deviatoric stress space in the von Mises distance
S_{ij}	stress deviator	S_{n+1}	partial stress tensor
α_{n+1}	back stress tensor	p_{n+1}	equivalent accumulative plastic strain
D^e	fourth-order isotropic elastic tensor	σ_{max}	maximum stress (MPa)
ε_r^p	accumulative plastic strain	$d\varepsilon_r^p/dN$	accumulative plastic strain rate
κ_r	material constant	β	material constant
N_r	accumulative plastic damage life (cycles)		
σ_y	yield stress (MPa)	σ_b	tensile stress (MPa)
σ_n	nominal stress (MPa)	ε_n	nominal strain
ε_a	local strain amplitude	σ_m	effective mean stress (MPa)

References

- [Armstrong and Frederiek 1968] P. J. Armstrong and C. O. Frederiek, "A mathematical representation of the multiaxial Bauschinger effect", Report RD/B/N 731, Central Electricity Generating Board, 1968.
- [Budiansky and Hutchinson 1978] B. Budiansky and J. W. Hutchinson, "Analysis of crack closure in fatigue crack growth", *J. Appl. Mech.* **45** (1978), 267–276.
- [Chaboche 1989a] D. Chaboche, J. L. Nouailhas, "Constitutive modeling of ratchetting effects, part I: Experimental facts and properties of the classical models", *J. Eng. Mater. Technol.* **111**:4 (1989), 384–392.
- [Chaboche 1989b] J. L. Chaboche, "Constitutive equations for cyclic plasticity and cyclic viscoplasticity", *Int. J. Plast.* **5** (1989), 247–302.
- [Chen et al. 2009] G. Chen, S.-C. Shan, X. Chen, and H. Yuan, "Ratcheting and fatigue properties of the high-nitrogen steel X13CrMnMoN18-14-3 under cyclic loading", *Comput. Mater. Sci.* **46**:3 (2009), 572–578.
- [Deng et al. 2016] J. Deng, B. Du, and P. Yang, "Research on the fracture toughness for ship cracked plates based on the accumulative increment plastic deformation", *J. Ship Mech.* **20**:6 (2016), 748–757.
- [Deng et al. 2017] J. L. Deng, P. Yang, and Y. Chen, "Low-cycle fatigue crack initiation life of hull-notched plate considering short crack effect and accumulative plastic damage", *Appl. Ocean Res.* **68** (2017), 65–76.
- [Fujita et al. 1984] Y. Fujita, T. Nomoto, and K. Yuge, "Behavior of deformation of structural members under compressive and tensile loads (1st report) on the buckling of a column subjected to repeated loading", *J. Soc. Naval Arch Japan* **156** (1984), 346–354.
- [Fukumoto and Kusama 1985] Y. Fukumoto and H. Kusama, "Cyclic behaviour of plates under in plane loading", *Eng. Struct.* **7** (1985), 56–63.
- [Hassan and Kyriakides 1994] T. Hassan and S. Kyriakides, "Ratcheting of cyclically hardening and softening materials, I: Uniaxial behavior", *Int. J. Plast.* **10**:2 (1994), 149–184.

- [Jerome et al. 1983] S. P. Jerome, A. Dinsenhacher, and E. B. Jeffrey, "A method for estimating life time loads and fatigue lives for Swath and conventional monohull ships", *Naval Eng. J.* **95**:3 (1983), 63–85.
- [Jiang and Huseyin 1994] Y. Jiang and S. Huseyin, "Cyclic ratcheting of 1070 steel under multiaxial stress states", *Int. J. Plast.* **10** (1994), 608–679.
- [Jiang and Sehitoglu 1996] Y. Jiang and H. Sehitoglu, "Modeling of cyclic ratcheting plasticity, part I: Development of constitutive relations", *J. Appl. Mech.* **63** (1996), 720–725.
- [Jixi and Jiang 2005] Z. Jixi and Y. Jiang, "An experimental study of inhomogeneous cyclic plastic deformation of 1045 steel under multiaxial cyclic loading", *Int. J. Plast.* **21** (2005), 2174–2190.
- [Kang et al. 2002] G. Kang, Q. Gao, L. Cai, and Y. Sun, "Experimental study on the uniaxial and nonproportionally multiaxial of SS304 stainless steel at room and high temperatures", *Unclear Eng. Design* **216** (2002), 13–26.
- [Kang et al. 2006] G. Kang, J. Kan, Q. Zhang, and Y. Sun, "Time-dependent ratchetting experiments of SS304 stainless steel", *Int. J. Plast.* **22** (2006), 858–894.
- [Kang et al. 2008] G. Kang, Y. Liu, and J. Ding, "Multiaxial ratcheting-fatigue interactions of annealed and tempered 42CrMo steels: experimental observations", *Int. J. Fatigue* **30** (2008), 2104–2118.
- [Li et al. 2015] L. Li, L. Shen, and G. Proust, "Fatigue crack initiation life prediction for aluminium alloy 7075 using crystal plasticity finite element simulations", *Mech. Mater.* **81** (2015), 84–93.
- [Lim et al. 2009] C. B. Lim, K. S. Kim, and J. B. Seong, "Ratcheting and fatigue behavior of a copper alloy under uniaxial cyclic loading with mean stress", *Int. J. Fatigue* **31**:3 (2009), 501–507.
- [Neuber 1961] H. Neuber, "Theory of stress concentration for shear-strained prismatical bodies with arbitrary nonlinear stress-strain law", *J. Appl. Mech. (ASME)* **28**:4 (1961), 544–560.
- [Ohno 1990] N. Ohno, "Recent topics in constitutive modeling of cyclic plasticity and viscoplasticity", *Appl. Mech. Rev.* **43**:11 (1990), 283–295.
- [Paul et al. 2010] S. K. Paul, S. Sivaprasad, and S. Dhar, "Ratcheting and low cycle fatigue behavior of SA333 steel and their life prediction", *J. Nuclear Mater.* **401** (2010), 17–24.
- [Payne et al. 2010a] J. Payne, G. Welsh, R. J. Christ Jr., and J. Nardiello, "Observations of fatigue crack initiation in 7075-T651", *Int. J. Fatigue* **32** (2010), 247–255.
- [Payne et al. 2010b] J. Payne, G. Welsh, R. J. Christ Jr., J. Nardiello, and J. M. Papazian, "Observations of fatigue crack initiation in 7075-T651", *Int. J. Fatigue* **32** (2010), 247–255.
- [Ranganathan et al. 2011] N. Ranganathan, H. Aldroe, F. Lacroix, F. Chalon, R. Leroy, and A. Tougui, "Fatigue crack initiation at a notch", *Int. J. Fatigue* **33** (2011), 492–499.
- [Satyadevi et al. 2007] A. Satyadevi, S. M. Sivakumar, and S. S. Bhattacharya, "A new failure criterion for materials exhibiting ratcheting during very low cycle fatigue", *Mater. Sci. Eng. A* **452-453** (2007), 380–385.
- [Taleb 2013] L. Taleb, "About the cyclic accumulation of the inelastic strain observed in metals subjected to cyclic stress control", *Int. J. Plast.* **43** (2013), 1–19.
- [Tong et al. 2013] J. Tong, L. G. Zhao, and B. Lin, "Ratcheting strain as a driving force for fatigue crack growth", *Int. J. Fatigue* **46** (2013), 49–57.
- [Tyfour and Kapoor 1995] W. R. Tyfour and A. Kapoor, "The steady state wear behaviour of pearlitic rail steel under dry rolling-sliding contact conditions", *Wear* **180** (1995), 79–89.
- [Xia and Kujawki 1996] Z. Xia and D. Kujawki, "Effect of mean stress and ratcheting strain on fatigue life of steel", *Int. J. Fatigue* **18** (1996), 335–341.
- [Yao and Nikolov 1990] T. Yao and P. I. Nikolov, "Buckling/plastic collapse of plates under cyclic loading", *J. Soc. Naval Arch Japan* **168** (1990), 449–462.

JUNLIN DENG: junlin.deng@163.com

School of Transportation, Wuhan University of Technology, Heping street #1178, Wuchang District, Wuhan, 430063, China

PING YANG: pyangwhut@163.com

School of Transportation, Wuhan University of Technology, Heping street #1178, Wuchang District, Wuhan, 430063, China

YUAN CHEN: yuanc0801@163.com

School of Transportation, Wuhan University of Technology, Heping street #1178, Wuchang District, Wuhan, 430063, China

JIN HAN: wulihanjin@163.com

School of Transportation, Wuhan University of Technology, Heping street #1178, Wuchang District, Wuhan, 430063, China

SUBMISSION GUIDELINES

ORIGINALITY

Authors may submit manuscripts in PDF format online at the Submissions page. Submission of a manuscript acknowledges that the manuscript is original and has neither previously, nor simultaneously, in whole or in part, been submitted elsewhere. Information regarding the preparation of manuscripts is provided below. Correspondence by email is requested for convenience and speed. For further information, write to contact@msp.org.

LANGUAGE

Manuscripts must be in English. A brief abstract of about 150 words or less must be included. The abstract should be self-contained and not make any reference to the bibliography. Also required are keywords and subject classification for the article, and, for each author, postal address, affiliation (if appropriate), and email address if available. A home-page URL is optional.

FORMAT

Authors can use their preferred manuscript-preparation software, including for example Microsoft Word or any variant of $\text{T}_{\text{E}}\text{X}$. The journal itself is produced in $\text{L}^{\text{A}}\text{T}_{\text{E}}\text{X}$, so accepted articles prepared using other software will be converted to $\text{L}^{\text{A}}\text{T}_{\text{E}}\text{X}$ at production time. Authors wishing to prepare their document in $\text{L}^{\text{A}}\text{T}_{\text{E}}\text{X}$ can follow the example file at www.jomms.net (but the use of other class files is acceptable). At submission time only a PDF file is required. After acceptance, authors must submit all source material (see especially Figures below).

REFERENCES

Bibliographical references should be complete, including article titles and page ranges. All references in the bibliography should be cited in the text. The use of $\text{BibT}_{\text{E}}\text{X}$ is preferred but not required. Tags will be converted to the house format (see a current issue for examples); however, for submission you may use the format of your choice. Links will be provided to all literature with known web locations; authors can supply their own links in addition to those provided by the editorial process.

FIGURES

Figures must be of publication quality. After acceptance, you will need to submit the original source files in vector format for all diagrams and graphs in your manuscript: vector EPS or vector PDF files are the most useful. (EPS stands for Encapsulated PostScript.)

Most drawing and graphing packages—Mathematica, Adobe Illustrator, Corel Draw, MATLAB, etc.—allow the user to save files in one of these formats. Make sure that what you're saving is vector graphics and not a bitmap. If you need help, please write to graphics@msp.org with as many details as you can about how your graphics were generated.

Please also include the original data for any plots. This is particularly important if you are unable to save Excel-generated plots in vector format. Saving them as bitmaps is not useful; please send the Excel (.xls) spreadsheets instead. Bundle your figure files into a single archive (using zip, tar, rar or other format of your choice) and upload on the link you been given at acceptance time.

Each figure should be captioned and numbered so that it can float. Small figures occupying no more than three lines of vertical space can be kept in the text (“the curve looks like this:”). It is acceptable to submit a manuscript with all figures at the end, if their placement is specified in the text by means of comments such as “Place Figure 1 here”. The same considerations apply to tables.

WHITE SPACE

Forced line breaks or page breaks should not be inserted in the document. There is no point in your trying to optimize line and page breaks in the original manuscript. The manuscript will be reformatted to use the journal's preferred fonts and layout.

PROOFS

Page proofs will be made available to authors (or to the designated corresponding author) at a Web site in PDF format. Failure to acknowledge the receipt of proofs or to return corrections within the requested deadline may cause publication to be postponed.

Journal of Mechanics of Materials and Structures

Volume 13, No. 1

January 2018

- Studies on performance and failure mode of T-shaped diaphragm-through connection under monotonic and cyclic loading** **BIN RONG, CHANGXI FENG, RUOYU ZHANG, SHUAI LIU and GUANGCHAO YOU** **1**
- Multimodal piezoelectric device for energy harvesting from engine vibration** **CLAUDIO D. GATTI, JOSÉ M. RAMIREZ, MARIANO FEBBO and SEBASTIÁN P. MACHADO** **17**
- Numerical and experimental study on incremental forming process of Al/Cu bimetals: influence of process parameters on the forming force, dimensional accuracy and thickness variations** **MOHAMMAD HONARPISHEH, MORTEZA KEIMASI and IMAN ALINAGHIAN** **35**
- Ordinary state-based peridynamics for open-hole tensile strength prediction of fiber-reinforced composite laminates** **XIAO-WEI JIANG and HAI WANG** **53**
- Stability of Cosserat solids: size effects, ellipticity and waves** **RODERIC S. LAKES** **83**
- Extreme Cosserat elastic cube structure with large magnitude of negative Poisson's ratio** **CARLOS ANDRADE, CHAN SOO HA and RODERIC S. LAKES** **93**
- Electromechanical fields in a nonuniform piezoelectric semiconductor rod** **GUANGYING YANG, JIANKE DU, JI WANG and JIASHI YANG** **103**



1559-3959(2018)13:1;1-0